FePt based advanced magnetic recording media

A DISSERTATION
SUBMITTED TO THE FACULTY OF THE GRADUATE SCHOOL
OF THE UNIVERSITY OF MINNESOTA
BY

HAO WANG

IN PARTIAL FULFILLMENT OF THE REQUIREMENTS
FOR THE DEGREE OF
DOCTOR OF PHILOSOPHY

JIAN-PING WANG, ADVISOR

FEBRUARY, 2013

Acknowledgements

I am very much delighted to have this chance to thank those people who supported and helped me. First of all, I would like to thank my advisor, Professor Jian-Ping Wang, for his sharing of scientific mind, introducing me to the research field of magnetic materials and supervising me to do this exciting project. The discussion with him was invaluable and guided me to passionately explore amazing science in this topic.

I would also like to acknowledge the input and advice from Professor Randall Victora, Beth Stadler and Jack Judy during my work and stay in the center for Micromagnetic and Information Technologies (MINT), which builds a solid foundation for me in the field of magnetism and magnetic materials.

I am thankful to my dissertation committee members Professor Anand Gobinath, Beth Stadler, Andre Mkhoyan, Stephen Campbell, and Richard D. James for their time, help and effort of serving in my committee.

Parts of this work were carried out using the Characterization Facility which receives partial support from NSF through the NSF Minnesota MRSEC Program under Award Number DMR-0819885 and NNIN program.

It has been an enjoyable experience with the past and current members of Professor Wang's group. I would like to thank Mr. Haibao Zhao, Dr. Bin Ma, Dr. Xiaoqi Liu, Dr. Jingzhi Han, Dr. Xiaomin Cheng, Mr. Shaoqian Yin, Ms. Meiyin Yang, Mr. Patrick Quarterman, and all the other group members and visiting scholars for their valuable discussion and collaboration.

Finally, I would like to express my love and thanks to my parents and my friends. Without their love, support and advice, I would have never gone so far.

Dedication

With gratitude to my parents.

Abstract

In future extremely high density magnetic recording, FePt is considered as a promising candidate for future recording media materials. In this thesis work, FePt media with composite structure have been systematically studied in the forms of both granular media and bit patterned media (BPM).

Continuous FePt films with surface roughness of less than 0.3 nm are achieved in FePt hard magnetic films, exchanged coupled composite (ECC) films and graded films. Nanoimpriting and block-copolymer lithography are employed to fabricate BPM. The switching field distribution (SFD) broadening and degradation of FePt BPM are studied. The reduction of SFD has been achieved using a post-annealing process. Both ECC and graded FePt BPM with sub-30 nm dot size have been experimentally demonstrated on large substrates for the first time. It is confirmed that the patterned graded BPM sample has smaller switching field and larger thermal energy barrier than the ECC sample does.

Ultra-thin FePt granular media with graded composition was directly fabricated using a spontaneous layer diffusion process between the FePt and Pt layers during film deposition. A large gain factor of 3.74 was found in this spontaneously formed FePt graded granular media.

A nanopatterning process, named as the Embedded Mask Patterning (EMP), is proposed and experimentally demonstrated based on the FePt magnetic recording media. In this process the granular structure is defined by a sputtering-deposited mask layer, while the magnetic properties are determined by the FePt continuous film. Grain size can be decreased by optimizing the mask layer only.

A non-ideal surface anisotropy effect has been observed on the magnetization reversal process of both $L1_0$ phase FePt nanoparticles, and (001) textured $L1_0$ FePt thin film with island structure. The broken symmetry of the surface creates surface anisotropy and also weakens the exchange coupling. The elimination of the surface effect has been experimentally demonstrated by epitaxially capping a Pt layer on FePt. After being embedded in a Pt matrix, the exchange coupling between the surface portion and internal portion of FePt islands was enhanced.

Table of contents

Acknowledgements i

Dedication ii

Abstract iii

Table of contents iv

List of Figures vii

List of Tables xvi

Chapter 1. Introduction 1

1.1 Magnetism *1*

1.2 Basics of magnetic recording *3*

1.2.1 Magnetic recording 3

1.2.2 Record and play back process 6

1.2.3 Longitudinal recording 6

1.2.4 Perpendicular recording 7

1.2.5 Issues in future ultra-high density magnetic recording 8

1.3 Magnetic materials for high density recording media *12*

1.3.1 Current hexagonal Co-alloys 12

1.3.2 $SmCo_5$ 13

1.3.3 $L1_0$ FePt 14

1.4 Thin film fabrication technology *17*

1.4.1 Vacuum system 17

1.4.2 Plasma and glow discharge 18

1.4.3 Sputtering system 20

1.4.4 Thin film growth 23

1.5 Thin film characterization techniques *25*

1.5.1 X-ray diffraction 25

1.5.2 Magnetic measurements 26

1.5.3 Electron Microscopy 27

1.5.4 Surface analysis 31

1.5.5 Composition analysis 33

1.6 Scope of this thesis *35*

Chapter 2. Progress on FePt recording media 38

2.1 Introduction *38*

2.2 Low temperature chemical ordering *38*

2.3 Grain size and distribution control for heat assisted magnetic recording. *40*

2.4 Bit patterned media *42*

2.5 Exchange coupled composite structure *45*

2.6 Graded media *48*

2.7 Conclusion *51*

Chapter 3. FePt thin film fabrication and composite structure **54**

3.1 Introduction *54*

3.2 Core-shell type FePt ECC media *57*
3.2.1 Experiment 57
3.2.2 Results and discussion 60
3.2.3 Tilted axis 67

3.3 Spontaneously formed FePt graded granular media *71*
3.3.1 Experiment 72
3.3.2 Results and discussion 73

3.4 Conclusion *79*

Chapter 4. FePt bit patterned media **82**

4.1 Introduction *82*

4.2 Patterning process *83*
4.2.1 Nanoimprinting 83
4.2.2 Block copolymer self-assemble 89

4.3 $L1_0$ FePt type bit patterned media *91*
4.3.1 Development of FePt continuous film 91
4.3.2 FePt BPM fabricated using nanoimpringting lithography 94
4.3.3 FePt BPM fabricated using block copolymer self-assemble 102

4.4 Conclusion *108*

Chapter 5. FePt type ECC and graded bit patterned media **111**

5.1 Introduction *111*

5.2 Development of FePt type continuous film with composite structure *113*

5.3 FePt type ECC and graded bit patterned media *119*

5.4 Conclusion *124*

Chapter 6. Embedded mask patterning: a nanopatterning process to fabricate FePt granular **126**

6.1 Introduction *126*

6.2 Experiments and discussion *128*

6.3 Conclusion *136*

Chapter 7. Surface anisotropy effect in $L1_0$ FePt nanoparticles **138**

7.1 Introduction *138*

7.2 Experiments and discussion *139*

7.3 Conclusion *149*

Chapter 8. Conclusion and outlook **152**

8.1 Conclusion *152*

8.2 Outlook 154

Conference presentations 155

Patent 156

Publications 157

Reference list 159

List of Figures

Figure 1.1 a typical hysteresis loop of ferromagnetic materials 2

Figure 1.2 Roadmap of areal density evolution of hard disk drive. 4

Figure 1.3 Basic mechanical structure and components of a hard disk drive. 4

Figure 1.4 Schematic figure of the granular structure of recording media and bit. 5

Figure 1.5 Schematic of longitudinal recording. 6

Figure 1.6 Schematic of perpendicular recording.[4] 7

Figure 1.7 Trilemma of future high density magnetic recording 8

Figure 1.8 Slater-Pauling cure. 11

Figure 1.9 Phase diagram of Sm-Co binary alloy. 13

Figure 1.10 Lattice structure of $SmCo_5$ 14

Figure 1.11 Phase diagram of Fe-Pt binary alloy. 15

Figure 1.12 Lattice structure of (up) A1 phase FePt and (down) $L1_0$ phase FePt. 16

Figure 1.13 Structure of a DC glow discharge with corresponding potential, ion density and electron density. 19

Figure 1.14 Schematic of magnetron sputtering 20

Figure 1.15 8-target magnetron sputtering 21

Figure 1.16 Structure diagram of 8-target magnetron sputtering system. 22

Figure 1.17 Schematic figure of main chamber of the 8-target magnetron sputtering system. 23

Figure 1.18 Thornton's Zone model for sputter deposited metal films 23

Figure 1.19 Schematic illustration of three common epitaxial growth modes 24

Figure 1.20 Schematic of X-ray diffractometer. 25

Figure 1.21 Schematic of vibration sample magnetometer. 27

Figure 1.22 Schematic figure of a scanning electron microscopy. 28

Figure 1.23 Schematic figure of a transmission electron microscopy 29

Figure 1.24 Schematic of AFM working principle 31

Figure 1.25 Schematic configuration of electron energy loss spectrum. 34

Figure 2.1 (a) How the out-of-plane coercivity, in-plane coercivity and lattice misfit between CrRu and FePt change with the Ru content. (b) displays the XRD spectra of $Cr_{91}Ru_9$/Pt/FePt films with different deposition temperature. [Ref. 6] 39

Figure 2.2 (a) plan-view TEM image, (b) cross-sectional TEM image, (c) in-plane and out-of-plane hysteresis loops of FePtAg-C granular media. [Ref. 21] 41

Figure 2.3 Comparison of (left) conventional media and (right) bit patterned media. [Ref. 25] 43

Figure 2.4 SEM plan-view image of FePt BPM fabricated using BCP. [Ref. 33] 44

Figure 2.5 magnetization reversal in an ECC grain. [Ref. 39] 46

Figure 2.6 TEM cross sectional image of a patterned ECC dots with structure of FePt/Fe/Ru(capping). 48

Figure 2.7 Schematic comparison of an ECC grain and a graded grain. 49

Figure 2.8 (a) Cross-sectional STEM annular dark field image of sample Pt(7 nm)/FePt(6 nm) rotated by 90 degree counterclockwise (left: film top). (b) A schematic of how the Fe composition changes with position, in which the higher the brightness, the more the Fe. (c) EELS line scan analysis of Fe content in one columnar grain along the film normal. The curve of Fe-L_3 edge areal density vs. position was plotted in (c) with associated position in (a) and (b). [Ref. 59] 50

Figure 3.1 schematic comparison between conventional structure and ECC structure 55

Figure 3.2 Different configurations of ECC structure (Ref. 5) 56

Figure 3.3 Micromagnetic simulation model in Ref. 13. 58

Figure 3.4 schematic figure of the morphology of FePt and FePt/Fe films on MgO substrate. 59

Figure 3.5 XRD θ-2θ scan spectra of the core-shell type ECC samples. 60

Figure 3.6 TEM cross-sectional images of (a) FePt and (b) FePt/Fe(3nm); (c), (d) schematic figures of core-shell structure 61

Figure 3.7 hysteresis loop of pure FePt film. 62

Figure 3.8 The Fe layer thickness dependence of magnetic properties: (a) the saturation magnetization. The inset is the square ratio of magnetization; (b) the coercivities. 63

Figure 3.9 The recoil curves of FePt/Fe (3nm) nanocomposite: (a) Out-of-plane, and (b) In-plane. The fields labeled in the figures are the applied fields that start the measurements. 64

Figure 3.10 Time dependence of reverse applied field of FePt/Fe (3 nm) ECC media. The field applied opposed to saturation state, is a little smaller than coercivity measured at the normal sequense. The time is the duration through which the net magnetization is zero. 66

Figure 3.11 high-resolution cross-section TEM image of an FePt/Fe(3 nm) core-shell type composite island..... 67

Figure 3.12 the remanence curves of the core-shell type FePt/Fe with Fe thickness of (a) 3 nm and (b) 4 nm. 68

Figure 3.13 The dependence of remanent magnetization on the angle between the film normal and the direction of magnetic field in a VSM: (a) FePt/Fe(3 nm) nanocomposite; (b) FePt/Fe(5 nm) nanocomposite. The sample rotates against the magnet, and no field is applied. M_X represents the normalized magnetization along the film normal, and M_Y represents the normalized in-plane magnetization. Besides, the weak variation of total magnetization M is due to the calibration error between X and Y coils. The original direction of the film normal is set as 0. The easy axis direction is marked by the red arrow in both figures. 69

Figure 3.14 The dependence of remanent coercivity H_{CR} (left column) and magnetization M_R (right column) on the angle between the film normal and applied field, for FePt/Fe(3nm) (up row) and FePt/Fe(4nm) nanocomposite (loe row): (a) H_{CR} of FePt/Fe(3nm); (b) M_R of FePt/Fe(3nm); (c) H_{CR} of FePt/Fe(4nm); (d) M_R of FePt/Fe(4nm). 70

Figure 3.15 (a) XRD spectrum and (b) Out-of-plane hysteresis loop of the sample Pt(7 nm)/FePt(6 nm); (c) Coercivity vs. FePt thickness while keeping Pt as 7 nm; (d) coercivity vs. Pt thickness while keeping FePt as 6 nm. We only listed the magnetic layer in figure captions..... 73

Figure 3.16 (a) TEM plan-view image of the sample Pt(7 nm)/FePt(6 nm). The mean diameter of the grains is around 12 nm. (b) Bright field cross-sectional image clearly shows the granular structure and the different layers except the Cu capping layer. (c) STEM annular dark field cross-sectional image shows the entire layer structure including the Cu capping layer. The thicknesses of corresponding layers are: RuAl (20 nm), Pt (7 nm), FePt (6 nm), Cu (1 nm)..... 75

Figure 3.17 (a) Cross-sectional STEM annular dark field image of sample Pt(7 nm)/FePt(6 nm) rotated by 90 degree counterclockwise (left: film top). (b) A schematic of how the Fe composition changes with position, in which the higher the brightness, the more the Fe. (c) EELS line scan analysis of Fe content in one columnar grain along the film normal. The curve of Fe-L_3 edge areal density vs. position was plotted in (c) with associated position in (a) and (b). 77

Figure 3.18 (a) Delta M curve of sample Pt(7 nm)/FePt(6 nm). The negative peak at 5 kOe field indicates the dominant dipole interaction of FePt grains. Thermal decay measurement was performed and the experimental data were shown in (b) as the scattered dots. The line was obtained by fitting the experimental data to the Sharrock equation. The thermal barrier is 160 k_BT. 78

Figure 4.1 Comparison of (left) conventional media and (right) bit patterned media. 82

Figure 4.2 Baseic steps of nanoimprint lithography 84

Figure 4.3 Schematic figure of the thermal type NIL process 85

Figure 4.4 schematic figure of the UV-type NIL 86

Figure 4.5 Phase transformation and nanodot array formation of block copolymer 89

Figure 4.6 Schematic diagram of fabrication process of block-copolymer lithography 90

Figure 4.7 The AFM images of FePt continuous film, with surface roughness of 0.218 nm 92

Figure 4.8 (a) XRD spectra and (b) Out-of-plane hysteresis loop of FePt continuous film. Its H_C value is 3.82 kOe. 93

Figure 4.9 Schematic drawing of the fabrication of FePt patterned structure by using anodize alumina (AAO) mold. (a) deposition of Al film on Si wafer, (b) fabrication of AAO and coated it with thin SiO_2 and SAM layer, (c) spin coating of the resist on FePt thin film, (d) nanoimprinting, (e) demolding, (f) removal of the residual layer by reactive

ion etching (RIE) and transfer the pattern into FePt film by Ar ion milling (f) removal of the resist to leave the FePt pillars on substrate. 96

Figure 4.10 SEM plane -view images of (a) AAO mold, (b) as-imprinted image of resist by using mold without SiO_2 coating, inset is the magnified view of the indicated area, and SEM cross-sectional image of (c) as-imprinted image of resist pillars by using the mold with thin ~ 2-3 nm SiO_2 coating. 98

Figure 4.11 SEM plane view images of (a) AAO mold coated with thin SiO2 layer. The average hole diameter is about 75 nm. (b) the cross-sectional SEM image of as-imprinted resist pillars. Some pillars with smaller height are indicated by white arrows and (c) plan-e view SEM image of FePt dots on Si wafer. Some dots with reduced height are indicated by black arrows. 101

Figure 4.12 SEM plan-view image of FePt BPM fabricated using BCP. 103

Figure 4.13 TEM cross-sectional image of FePt BPM fabricated using BCP. 103

Figure 4.14 (a) XRD spectra, (b) out-of-plane hysteresis loop and recoil loop of the as-patterned FePt BPM. The inset in (a) is FePt (001) rocking curve, whose FWHM is 7.26º. The ordering parameter of FePt is 0.48, and coercivity is 16.0 kOe. Delta H_C is 7.3 kOe and SFD is 34%. 105

Figure 4.15 (a) The XRD spectra, (b) out-of-plane hysteresis loop and recoil loop of the annealed FePt BPM. The inset in (a) is FePt (001) rocking curve. The ordering parameter of FePt is 0.57, the FWHM of the rocking curve is 6.81º, and coercivity is 17.1 kOe. Delta HC is 3.4 kOe and SFD is 15%. 107

Figure 5.1 Major stages and trilemma of FePt ECC or graded BPM fabrication 112

Figure 5.2 Formation of FePt/Fe graded interface. 113

Figure 5.3 The AFM images of (a) ‘Hard I’, (b) ‘Hard II’, (c) ‘ECC’, (d) ‘Graded I-300’, (e) ‘Graded II’ and (f) ‘Graded III’. (e) Surface roughness of all continuous films. 116

Figure 5.4 (a) XRD spectra of sample ‘Hard I’; (b) Out-of-plane hysteresis loops of the continuous films sample ‘Hard I’, ‘Hard II’, ‘ECC’, ‘Graded I-200’, ‘Graded I-300’, ‘Graded II’ and ‘Graded III’. Their HC values are 2.28 kOe, 1.38 kOe, 0.66 kOe, 0.59 kOe, 0.52 kOe, 1.18 kOe, and 1.62 kOe respectively. 118

Figure 5.5 SEM plan-view image of the patterned ‘ECC’ film. The inset is a cross-sectional TEM image of a single ECC dot..... 120

Figure 5.6 The out-of-plane hysteresis loops of (a) patterned ‘Hard I’ and ‘Hard II’, (b) patterned ‘Graded II’ and ‘Graded III’, (c) patterned ‘ECC’, ‘Graded I-200’, and ‘Graded I-300’. Their H_C are 16 kOe, 13 kOe, 1.3 kOe, 12.1 kOe, 4.64 kOe, 4.47 kOe and 5.08 kOe, respectively..... 121

Figure 5.7 (a) DCD curve obtained from MFM images of patterned ‘ECC’ sample, and MFM images with different remanent states: after applied reverse field (b) -1 kOe, (c) -6 kOe and (d) -9 kOe, respectively. The DCD curve was plotted by counting the number of the reversed magnetic islands under different remanent states from MFM images. 123

Figure 6.1 The schematic drawing of the EMP process. Step one: Highly $L1_0$ ordered FePt continuous layer was deposited on the substrate; Step two: The embedded mask layer (Ru-SiO_2) with a fine granular structure was deposited on the $L1_0$ ordered FePt continuous film. Step three: The SiO_2 of hard mask layer was removed using a reactive ion etching process (RIE). Step four: The Ru dots array pattern was transferred to FePt layer using a RIE process. All four steps could be done in vacuum. 128

Figure 6.2 (a) TEM plan-view image of Ru-SiO_2 mask layer on the carbon film of a TEM grid; (b) the out-of-plane hysteresis loop of FePt continuous film of the sample with full structure..... 130

Figure 6.3 The out-of-plane hysteresis loops of the (a) continuous film, (b) as-etched film, and (c) annealed film with coercivity of 2.8 kOe, 350 Oe and 2 kOe, respectively. 131

Figure 6.4 XRD spectra of the (a) as-prepared continuous film, (b) as-patterned film, and (c) annealed film. 133

Figure 6.5 Hysteresis loops of as-patterned and annealed 12nm-thick FePt sample. 135

Figure 6.6 TEM plan-view image of the annealed 5nm-thick FePt sample. The grain size is 4.6 nm and the center to center distance is 6.3 nm..... 136

Figure 7.1 Directly ordered $L1_0$ FePt nanoparticles prepared using a gas-phase aggregation technique at room temperature. (Ref. 12) (a) TEM image of one chemically ordered particle with its c-axis (the magnetic easy axis) lying in-plane; (b) a 3-D atomic reconstruction of the $L1_0$ FePt particle. (c) Hysteresis loop of 30 layers of mono-dispersed $L1_0$ FePt nanoparticles, with a coercivity of 33.4 kOe at temperature of 5 Kelvin. (d) The remanence state of one octahedral $L1_0$ FePt nanoparticle. Here arrows represent the spins from iron atoms and all platinum atoms have been omitted for clarity. Red arrows are surface spins and black arrows are interior spins, respectively. 140

Figure 7.2 (a) The schematic of an FePt island with (001) texture. (b) The FePt island is covered by Pt atoms epitaxially. 143

Figure 7.3 (a) The TEM cross-section image of $L1_0$ FePt island-structural film. The plan-view image of the island-like structure is shown in the SEM image inset. (b) The zoom-in cross-section image of a single FePt island, which exactly matches the model in Figure 7.2 (a). 144

Figure 7.4 (a) The TEM cross-section image of FePt/Pt(8nm) island-structural film. (b) The zoom-in cross-section image of a single FePt/Pt(8nm) island. The region 1 and region 2 are located at the top and side wall of an FePt island, respectively. The enlarged and filtered images are shown in (c) region 1 (top part) and (d) region 2 (side wall), to confirm the epitaxial growth and lattice match of Pt on FePt..... 145

Figure 7.5 (a) XRD spectra of FePt, FePt/Pt(3nm), and FePt/Pt(8nm) samples. All of them show good (001) texture and $L1_0$ ordering of FePt. Pt layer has both (200) texture

and (111) texture. (b) The hysteresis loops of all three samples. The coercivity of FePt, FePt/Pt(3nm), and FePt/Pt(8nm) are 13.5 kOe, 15 kOe and 17 kOe, respectively. A kink is obviously visible in FePt sample, but weaker in FePt/Pt(3nm), and disappears in FePt/Pt(8nm). 147

List of Tables

Table 1.1 High K_U magnetic materials. 12

Table 1.2 Vacuum range and pressure. 17

Table 2.1 A brief summary of FePt granular media fabrication 42

Table 2.2 Results summary of continuous film, as-patterned BPM and annealed BPM [Ref. 38] 45

Table 3.1 The magnetic properties and gain factors of FePt/Fe bilayers. Two kinds of gain factor ξ are obtained. $\xi_{\Delta E}$ by measured energy barrier, and ξ' by the modified formula 71

Table 4.1 Results summary of continuous film, as-patterned BPM and annealed BPM 108

Table 5.1 The recording layer structure and fabrication condition of all continuous films 113

Table 5.2 Surface energy of $L1_0$ FePt and bcc Fe 117

Table 5.3 H_C and ΔE of patterned 'ECC', 'GRADED I-200' and 'GRADED I-300' 122

Table 6.1 A brief summary of FePt granular media fabrication 127

Chapter 1. INTRODUCTION

1.1 Magnetism

Even in ancient times, magnetism has been widely studied and utilized in modern human society. Magnetic data storage, permanent magnets and magnetic resonance imaging are three most important applications of magnetic technology. In magnetic materials, the spin and orbital angular motion of electrons generate magnetization and magnetic moment. Their several types of magnetism, which are classified by their response to applied magnetic field and interaction with neighboring atoms.

A. Diamagnetism

With diamagnetic behavior, the magnetic moments tend to be aligned anti-parallel to the applied field. All materials experience diamagnetism, but its effect is very weak. Therefore it only dominates in nonmagnetic materials.

B. Paramagnetism

In a paramagnetic material, the magnetic moments can be aligned by external field and be saturated if the field is very strong. However, after removing the external field, the alignment of the moments will become random and net magnetization will decrease to zero.

C. Ferromagnetism

From the view of application, ferromagnetism is the most important type of magnetism. In ferromagnetic materials, the magnetic moments of neighboring atoms are strongly coupled together, and response to external fields. But unlike paramagnetic materials, a ferromagnetic material show hysteresis, because it has nonzero remanence (remanent magnetization) at zero field.

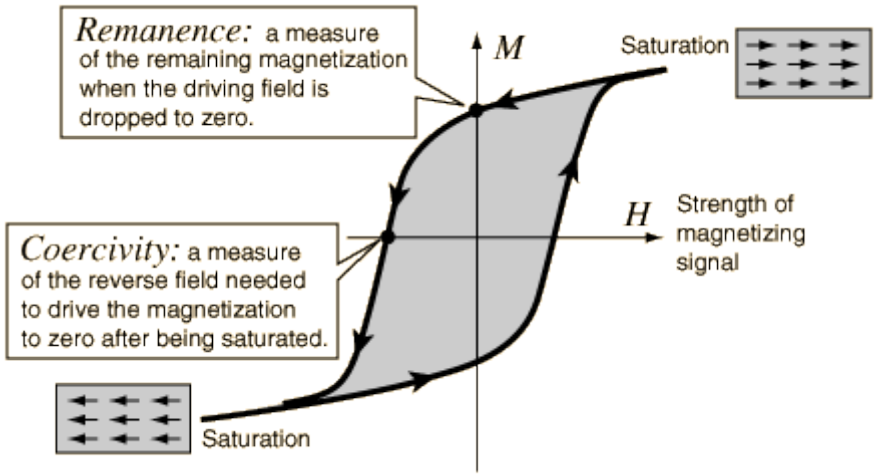

Figure 1.1 a typical hysteresis loop of ferromagnetic materials[1]

Figure 1.1 shows a typical hysteresis loop of ferromagnetic materials. It recorded how the magnetization changed with magnetic field. When the field is sufficiently large, it saturates the magnetic material and all the magnetic moments are aligned parallel to external field. After removing the field, the exchange coupling among the moments tends to keep the alignment even after removing the external field, and leads to a net magnetization at zero field. To achieve zero net magnetization, an opposite field is required applying to the material. The value of this opposite field is called coercivity.

When a ferromagnetic magnet is extremely small, the thermal effect becomes dominant. Similar to paramagnetism, in this condition the magnetic moments tend to be randomly aligned and net magnetization is zero without external field. This phenomena is called superparamagnetism. It is one of the most important limitations to prevent further increasing the density of magnetic recording.

D. Antiferromagnetism

In an antiferromagnetic material, the magnetic moments tend be aligned anti-parallel to their adjacent moments. The atoms are coupled by a negative molecular field and the moments of two neighbors point to opposite directions. The net magnetization of antiferromagnetic materials is zero. Typically, antiferromagnetic materials are ionic compounds, such as oxides.

E. Ferrimagnetism

Similar to antiferromagnetism, in ferromagnetic materials, the neighboring pairs of electrons tend to point opposite direction. However, the magnetizations of two sublattices are different. Therefore, the net magnetization of ferrimagnetism is nonzero.

1.2 Basics of magnetic recording

1.2.1 Magnetic recording

With the invention of magnetic tape and hard disk drive, magnetic recording technology has made significant progress in the past decades, and has become a core technology in this information society. The first commercialized hard disk drive, which was named 350 RAMAC (Random Access Method of Accounting and Control), was demonstrated by IBM in September 1956. It contained fifty 24-inch disks and weighed hundreds of kilograms. Its areal density was only 5 Kbit/in^2 and capacity was only 5 MB, but it successfully realized random access by moving its magnetic head to any storage area on the disk. In 1968, IBM first proposed Winchester technology; its disk packs, head and arm assembly were sealed. As a prototype of the most modern hard disk drive, the IBM 3340 was introduced in 1973 based on Winchester technology. Then, with the invention of thin film head, the volume of hard disk drive was tremendously reduced. Today, the areal density of magnetic recording media is approaching 1 Tbit/in^2, and commercialized hard disk drive with capacity up to 4 TB is available for personal computer. Figure 1.2 shows the evolution of areal density of hard disk from the period of first commercialized product to the future.

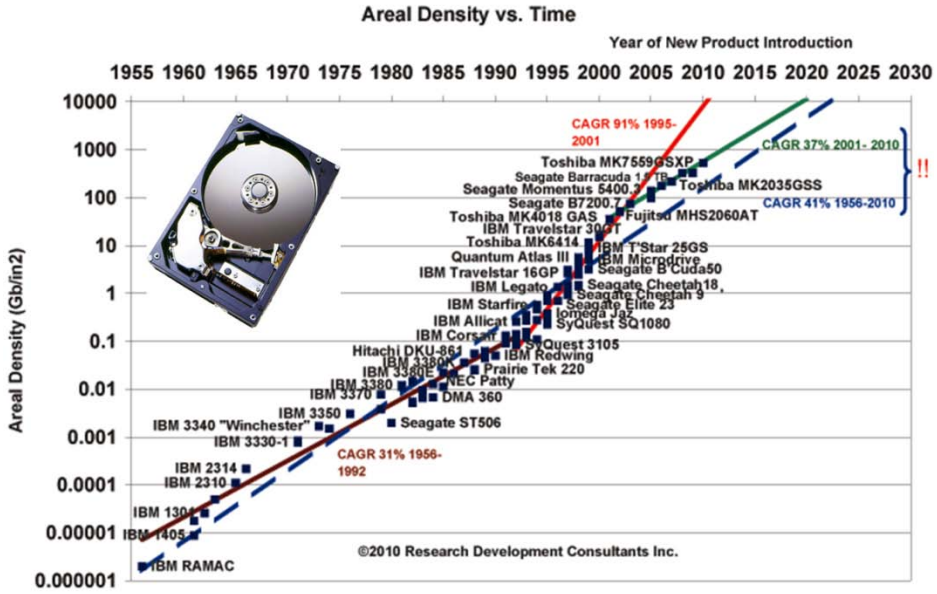

Figure 1.2 Roadmap of areal density evolution of hard disk drive.[2]

As can be seen in the figure, the annual growth rate of areal density reached a maximum value of around 60 percentages in the 1990s. Then the growth became slower because the magnetic recording was believed to approach physical limitation. Now, the areal density has increased 9 orders from 1950s.

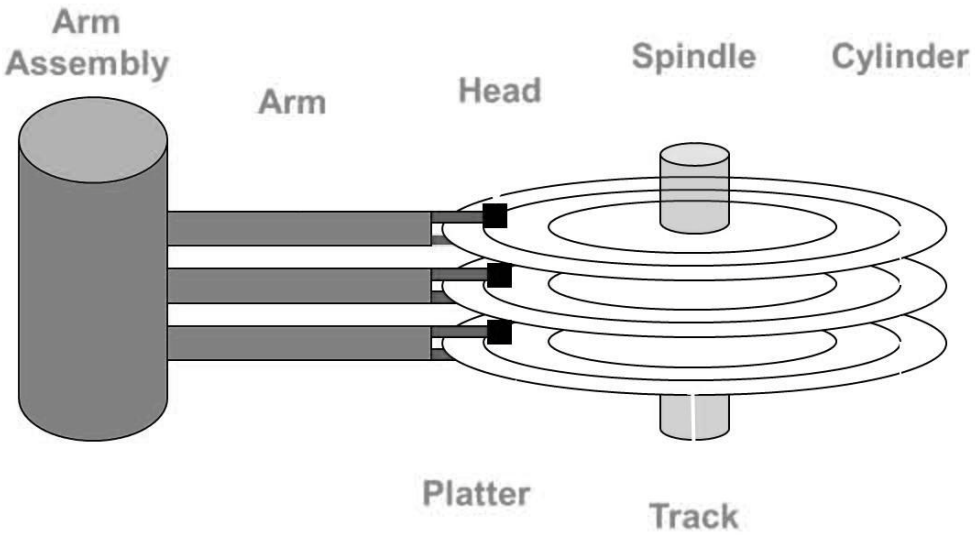

Figure 1.3 Basic mechanical structure and components of a hard disk drive.

Figure 1.3 shows the basic structure and components of a hard disk drive. Data are stored in a stack of disks. The disks are rotated by the spindle. The spin speed ranges

from a few thousand RPM to more than 10 thousand RPM. The faster the rotation is, the shorter the accessing time. The head is used to read and write data to and from the disks. With the rotation of disk and movement of the arm, head can access any area on the disk. A hard disk drive also has complicated electronics components which operate the recording process, convert the reading back signal to digital data and set appropriate current of head to record digital information in disks. The disks are formatted to have a lot of tracks, which are concentric circles. The data is only stored on the tracks. However, the tracks are not physically divided, but marked with different magnetic states. All the data is recorded in a magnetic thin film with granular structure on top of the disks.

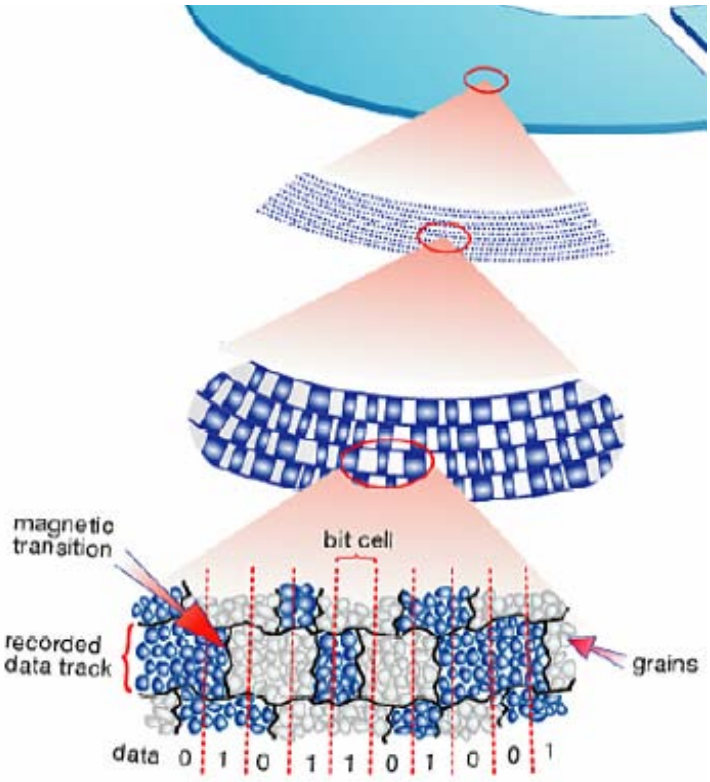

Figure 1.4 Schematic figure of the granular structure of recording media and bit.[3]

As shown in the bottom of Figure 1.4, the recording media is composed of countless tiny grains. The grain size is less than 10 nm. All grains are ferromagnetic material and isolated by non-magnetic materials, such as oxides. A bunch of grains are used to record a single bit and exchange coupled together as ferromagnetic materials. Each bit can be

magnetized by a writing head (writer) and its magnetization can be sensed by a reading head (reader). This is how the information data been accessed.

1.2.2 Record and play back process

A. Record process

In a recording process, writing current is generated according to the information to be stored. The current magnetizes the writer and produces magnetic field towards media. In a region on the recording media, where the magnetic field is larger than the switching field, the magnetization of recording bit is reversed. Thus, the information is recorded.

B. Play back process

The reader has a magnetoresistive (MR) unit, the resistance of which changes with its magnetization status. With the MR component, reader can detect magnetic flux. As the disk rotated and the reader moves along the tracks and bit transitions, the change of the magnetization flux is sensed by the reader and induced a voltage which can be recognized by the electronic part.

1.2.3 Longitudinal recording

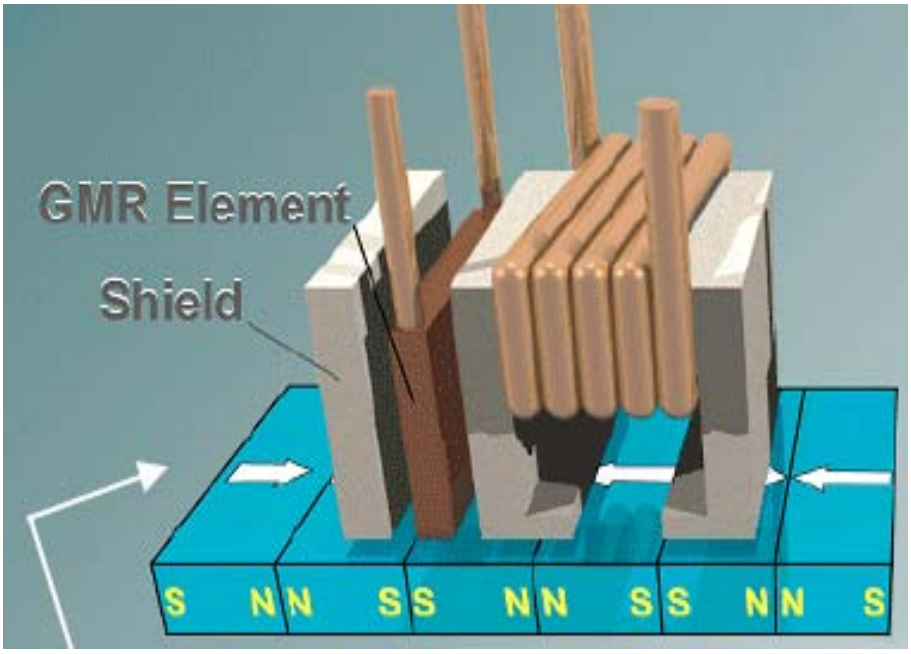

Figure 1.5 Schematic of longitudinal recording.[4]

In a longitudinal recording system, the magnetization of the bits lies in the plane. The stray field generated from a ring head was used to write data. Figure 1.5 demonstrates a schematic of longitudinal recording system. It was widely used for decades but became seriously flawed when people wanted to further increase the areal density. At the transition, the magnetization of two adjacent bits point toward together. A bit which experiences the demagnetization field from its neighbor becomes unstable and its magnetization could be changed with thermal fluctuation effect. The transition between two bits will become broader and lower the signal to noise ratio. Another drawback is that the writing field is the stray field of a ring head. It is not sufficient large to write recording media with high coercivity and high thermal stability. These disadvantages prevent the longitudinal recording being used in high density recording strategy. Then, perpendicular recording emerges as times require.

1.2.4 Perpendicular recording

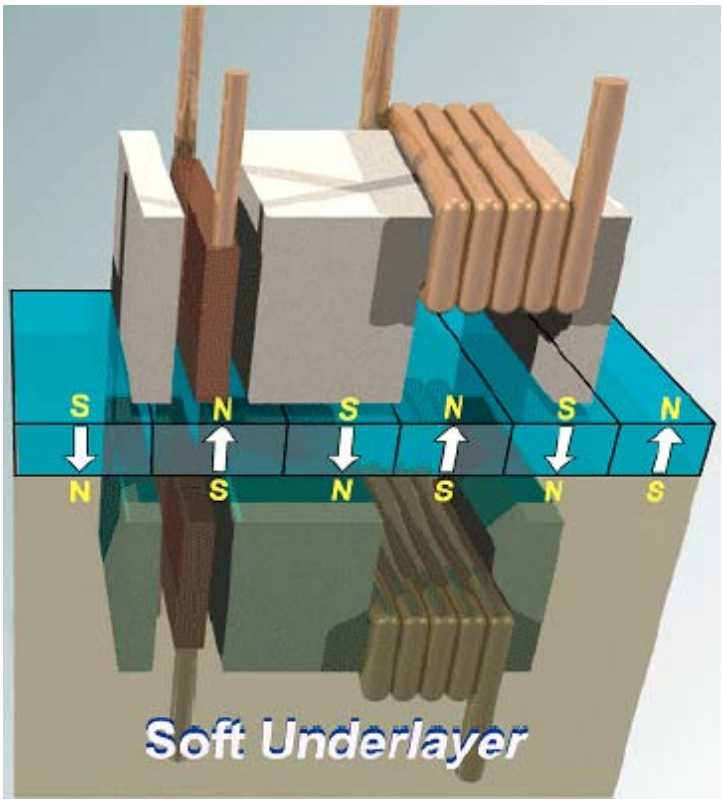

Figure 1.6 Schematic of perpendicular recording.[4]

As the name suggests, in perpendicular recording, the magnetization of recording bits point out-of -plane. It was first proposed by S. Iwasaki in 1977[5]. Figure 1.6 shows the schematic of perpendicular recording, with this configuration, the magnetization of adjacent bits does not point each other. Its grains are much more stable compared to the longitudinal recording. Hence the grain can be further shrunk to increase areal density. A Ring head is no longer used in perpendicular recording and replaced by single pole head. The pole head can generate stronger magnetic field than the ring head does. In addition, a soft underlayer was put beneath the recording layer. This layer can mirror the writer and enhance the field. With the existence of stronger field, high anisotropy magnetic materials can be used to fabricate the recording media to form small and thermally stable grains.

1.2.5 Issues in future ultra-high density magnetic recording

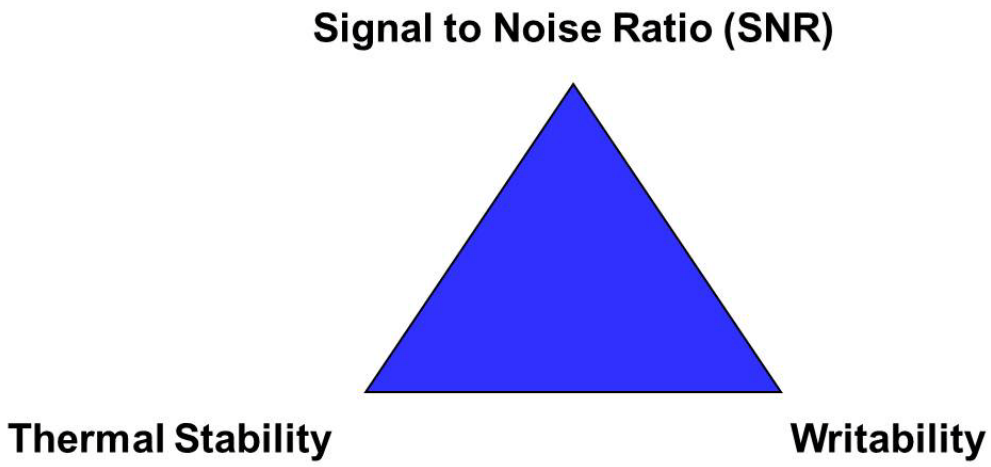

Figure 1.7 Trilemma of future high density magnetic recording

As described before, the growth of areal density has slowed down in the past ten years. Some inevitable issues have to be faced and solved before further pushing forward the increase of recording density. From the perspective of recording media, there are three fundamental requirements: signal to noise ratio (SNR), thermal stability and writability. High SNR makes the information detectable to reader. High thermal stability insures the bit has a stable state with small grain size. A writable bit means that its

switching field is smaller than the writing field. However, it is very difficult to fulfill all these three requirements. Figure 1.7 demonstrates this so called trilemma.

A. SNR

There are several kinds of noise in magnetic recording system. Reader generates noise voltage due to the resistance of MR element. It can be expressed as:

$$NV = \sqrt{4kTR\Delta f} \tag{1.1}$$

where k is Boltzmann constant, T is absolute temperature, R is resistance and Δf is the band width. And the SNR can be written as:

$$SNR = \frac{J^2 \rho DWt}{64kT\Delta f}\left(\frac{\Delta\rho}{\rho}\right) \tag{1.2}$$

where J is current density, D and W are the dimension of MR element. $\frac{\Delta\rho}{\rho}$ is the change of resistivity.

From the view of media, transition noise is dominant. Media SNR can be written as:

$$SNR = \frac{0.31PW_{50}BW}{a^2 s} \tag{1.3}$$

where PW_{50} is the pulse width of read back process, B is bit length, W is track width, a is transition parameter and s is cross track correlation width. Both a and s are associate with the grain size of media. If grain size decreases, both a and s are reduced. Then, the SNR will be increased. Therefore, the media grain size has to be decreased to maintain sufficient SRN while increasing the areal density.

B. Thermal stability

The magnetization of a magnetic particle has a chance to flip even without any external field. This is called thermal fluctuation. The possibility of a particle to be swathed in time t can be expressed as:

$$p = tv^0 e^{-\Delta E/k_B T} \tag{1.4}$$

where ΔE is the energy barrier to prevent the switching and v^0 is a constant value of 10^9-10^{10} Hz. Set p as 0.5, ΔE can be written as:

$$\Delta E/k_B T = ln(2tv^0)$$

(1.5)

For magnetic recording, the data are supposed to be stable in 10 years, which means t=10 years. Therefore, $\Delta E/k_B T=60$, which is a typical value to evaluate the thermal stability of recording media. A grain in the media can be treated as a single domain particle and its thermal energy barrier can be estimated as

$$\Delta E = K_u V$$

(1.6)

where V is the volume of a single grain and K_U is the magnetocrystalline anisotropy of the media material. While increasing the real density, V has to be reduced. Therefore, High K_U materials are required to maintain the thermal stability, otherwise the energy barrier will be too low and the particle will be switched by thermal fluctuation. In this case, the ferromagnetic particle becomes superparamagnetic. This issue is called the 'superparamagnetic limitation'.

Another way to increase thermal stability is bit patterned media (BPM)[6]. In BPM, the media is no long granular configuration, but a continuous film followed by a patterning process. Unlike the conventional media, in which a bit is composed of a bunch of grains, BPM is patterned to dot array and a single dot acts as a bit. Since the volume of a dot in BPM is much larger than a grain in conventional media, it is thermally stable even with high areal density.

C. Writability

As mentioned before, to reverse the magnetization of a bit and record information, the writing field has to be larger than the switching field of media. However, the writing field is limited. It is proportional to the saturation magnetization (M_S) of the writing materials. The Slater-Pauling curve in Figure 1.8 shows the magnetic moment of common magnetic materials. From this figure, we can see that FeCo has the highest moment among all known materials. Its saturation magnetization is 2.45 T.[7] This is also the highest available writing field.

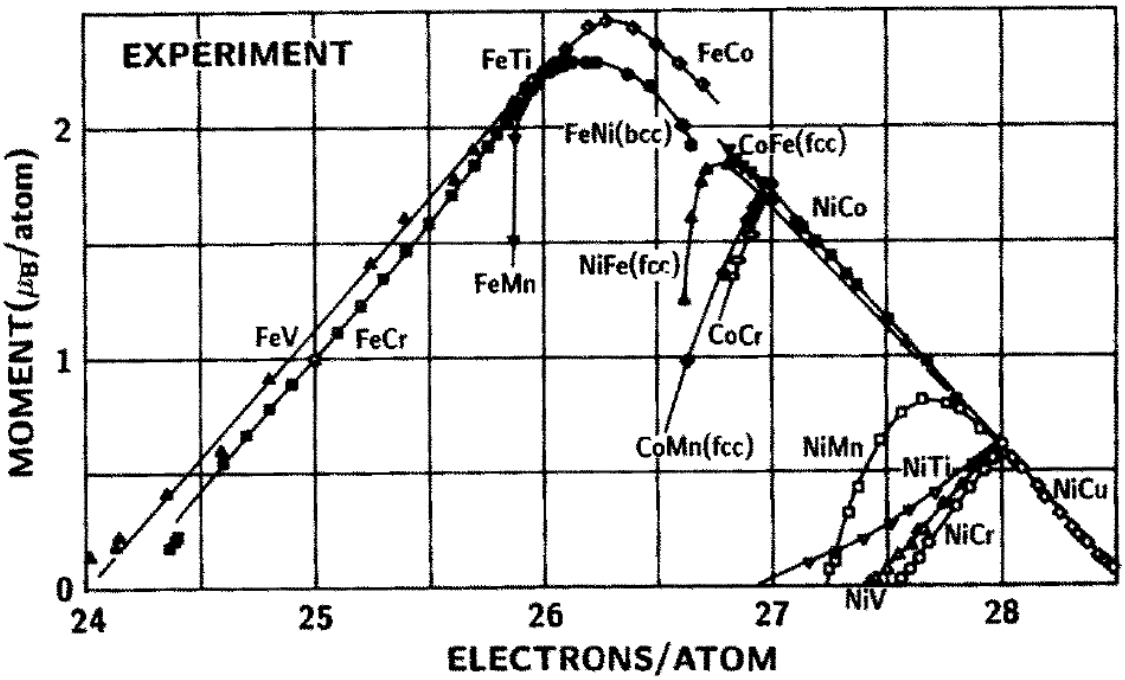

Figure 1.8 Slater-Pauling cure.[8]

Since the writing field is limited, the switching field of media has to be engineered to be lower than the writing field. However, since the high K_U materials are required to in high density recording media to maintain thermal stability, it is inevitable to use media material whose coercivity is higher than the writing field. Two strategies were proposed to solve this writability issue. One is heat assisted magnetic recording (HAMR).[9,10] Usually, the coercivity of a ferromagnetic material will be reduced at high temperature and approach zero when the temperature is near a certain value, called Curie temperature (T_C). In a HAMR system, the bit to be recorded is locally heated to reduce its switching field before writing. This allows HAMR media to overcome the superparamagnetic limitation. The second strategy is composite media. At first, exchange coupled composite (ECC) media, which has two exchange-coupled magnetic regions with different switching fields in individual recording grains, was modeled and experimentally demonstrated to address the writability and adjacent track erasure issues[11,12]. In ECC media, the switching field is lowered with the help of a soft magnetic region, and its thermal stability is maintained by the hard magnetic region. Then, graded media, in which the magnetic anisotropy gradually changes along the grain columnar direction, was proposed to further reduce the switching field.[13,14]

1.3 Magnetic materials for high density recording media

1.3.1 Current hexagonal Co-alloys

Table 1.1 High K_U magnetic materials.[15]

type	material	K_u (10^7erg/cm^3)	M_s (emu/cm^3)	H_k(kOe)	T_c(K)	D_p(nm)
Co alloys	CoCrPt	0.20	298	13.7	--	10.4
	Co	0.45	1400	6.4	1401	8.0
	Co_3Pt	2.0	1100	35	--	4.8
$L1_0$ alloys	FePd	1.8	1100	33	760	5.0
	FePt	6.6-10	1140	116	750	3.3-2.8
	CoPt	4.9	800	123	840	3.6
	MnAl	1.7	560	69	650	5.1
Rare-earth transition metals	$Fe_{14}Nd_2B$	4.6	1270	73	585	3.7
	$SmCo_5$	11-20	910	240-400	1000	2.7-2.2

Table 1.1 lists the common high K_U materials which are currently used or could be potentially used in recording media. In the table, K_U is the magnetocrystalline anisotropy, M_S is the saturation magnetization, H_K is the anisotropy field, T_C is the Curie temperature and D_P is the minimum stable particle size.

Co based hexagonal close packed (hcp) alloys are widely used in commercial hard disk drive as recording media materials. Co-alloys have uniaxial anisotropy and the easy axis is along the c direction. Although Co has higher K_U value than CoCrPt does, it is CoCrPt not Co which is used in recording media. There are two reasons:

1. In a magnetic recording media, the magnetic grains have to be isolated by nonmagnetic materials, to make the adjacent grains exchange-decouple. Doping Cr element into Co-alloy can separate the Co grains. Some of the Cr atoms diffuse in to Co grains, but more Cr form grain boundary and exchange decoupled the Co grains.
2. The magnetocrystalline anisotropy can be enhanced by doping Pt. Generally, high coercivity and thermal stability are reqired in recording media.

Since Co-alloy does not have high anisotropy, its minimum stable particle size is as large as 10 nm, which is much larger than the required size for future high density recording. Therefore, ultra-high K_U materials, such as $SmCo_5$ and FePt became more

popular, and finally FePt was considered to be the best candidate because of its desireable magnetic stability and chemical stability.

1.3.2 $SmCo_5$

As shown in Table 1.1, $SmCo_5$ has the largest K_U value among all magnetic materials. Its K_U value can be as high as $2x10^8$ erg/cc, and a SmCo5 magnetic particle can be thermally stable, even it is as small as 2.5 nm. However, $SmCo_5$ has a very serious corrosion issue. It is not chemically stable and very easilycorroded, even in normal environment, because it contains a rare earth element.

Figure 1.9 shows the diagram of Sm-Co binary alloy. $SmCo_5$ phase just has a small window in the phase diagram. Therefore the fabrication and composition are critical to achieve $SmCo_5$ phase. In fact, the Sm_2Co_{17} phase, which has smaller K_U value than the $SmCo_5$ phase, will be mixed into $SmCO_5$ if the fabrication is not well controlled.

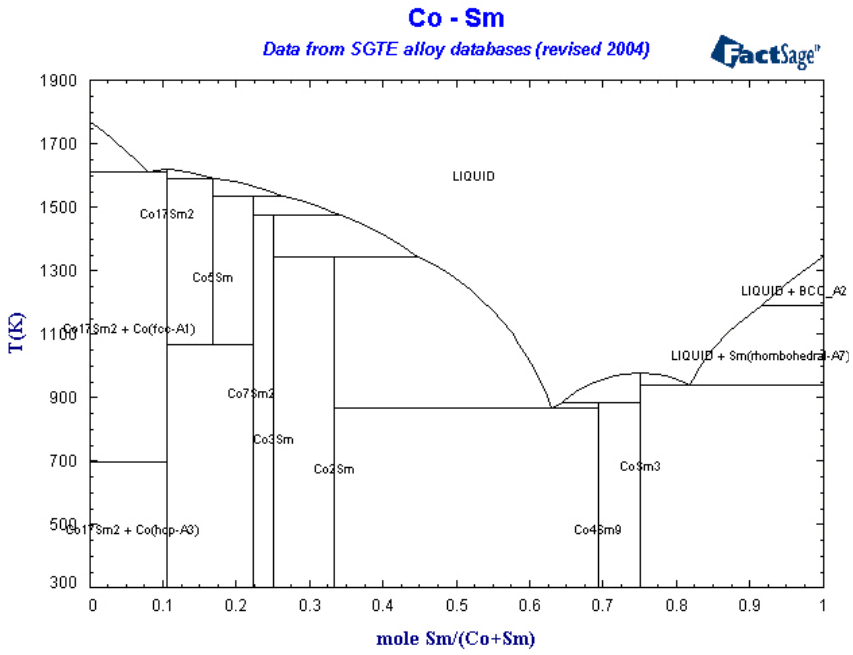

Figure 1.9 Phase diagram of Sm-Co binary alloy.[16]

Figure 1.10 show the lattice structure of SmCo5. It has a super lattice structure, in which pure Co atomic layer and Co-Sm mixed atomic layer are alternatively arranged.

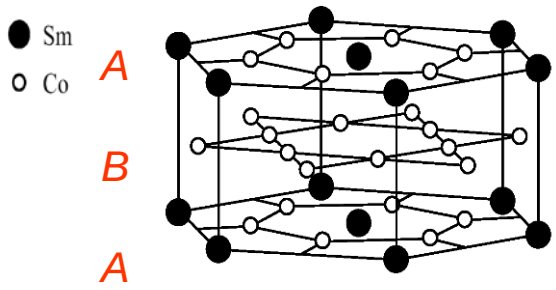

Figure 1.10 Lattice structure of $SmCo_5$[17]

1.3.3 $L1_0$ FePt

As shown in Table 1.1, $L1_0$ phase FePt has the second largest magnetocrystalline anisotropy of all common magnetic materials. But, unlike $SmCo_5$, it is not only magnetically stable, but also chemically stable. An $L1_0$ ordered FePt magnetic particle is thermally stable even its size is as small as 3 nm. Therefore, it was considered as the most promising candidate for future extremely high density magnetic recording media material, especially for the HAMR media.

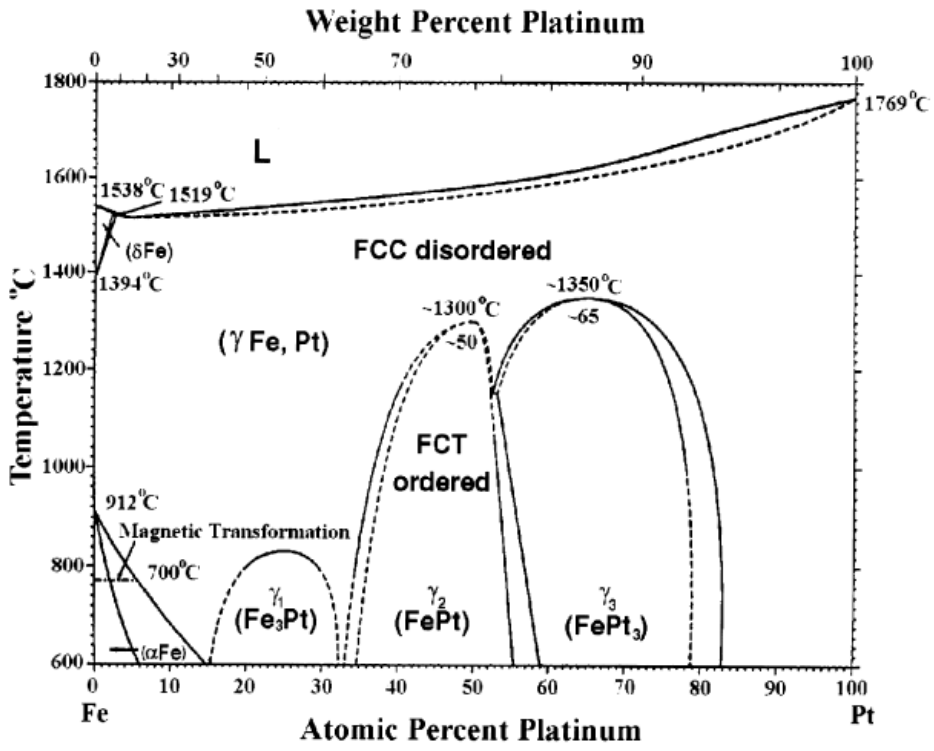

Figure 1.11 Phase diagram of Fe-Pt binary alloy.[18]

Figure 1.11 shows the phase diagram of FePt binary alloy. In FePt solid alloy, when the atom ration of Fe to Pt is around 1 to 1, there are two phases. One is disordered phase with FCC structure, and the other one is ordered phase with FCT structure. Figure 1.12 demonstrates the lattice structure of these two phases. To transform A1 phase to $L1_0$ phase, we can either anneal the disordered FePt at high temperature or increase the fabrication of FePt thin film during deposition.

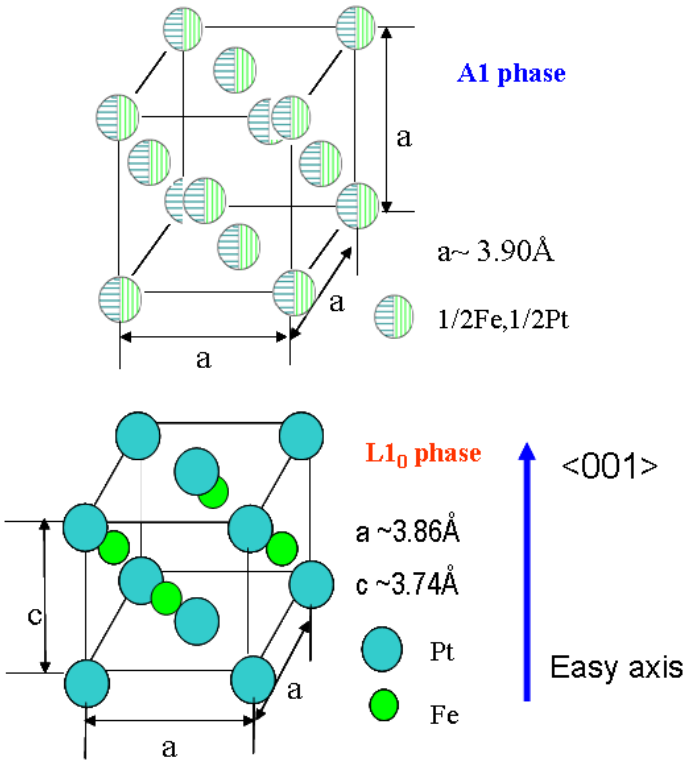

Figure 1.12 Lattice structure of (up) A1 phase FePt and (down) $L1_0$ phase FePt.

The disordered phase is called the A1 phase. Its lattice structure is face centered cubic (FCC), with a lattice constant a around 0.39 nm. In A1 phase, Fe and Pt atoms are randomly arranged. Its anisotropy is low, and it cannot be used to store data. In $L1_0$ ordered phase FePt, the Fe and Pt atoms are arranged layer by layer. The c axis of its unit cell is shorter than a and b axis. The asymmetry of unit cell makes the $L1_0$ FePt has uniaxial magnetocrystalline anisotropy. The easy axis is along c axis. $L1_0$ phase FePt has very large magnetocrystalline anisotropy. Shima experimentally demonstrated coercivity as high as 105 kOe in FePt thin film, by depositing FePt onto single crystal MgO substrate at 780 ^{o}C, and measuring the sample at 4.5 K[19].

In this thesis work, FePt is the primary magnetic material to demonstrate advanced recording media.

1.4 Thin film fabrication technology

1.4.1 Vacuum system

Vacuum systems are widely employed in nanotechnology. Lots of characterization methods and almost all fabrication processes of thin film materials have to be carried out in vacuum. Vacuum is evaluated by pressure. Depends on the pressure value, the quality of vacuum is divided into the following ranges (as shown in Table 1.2):

Table 1.2 Vacuum range and pressure.

	pressure (Torr)
Atmospheric pressure	760
Low vacuum	760 to 25
Medium vacuum	25 to 1×10^{-3}
High vacuum	1×10^{-3} to 1×10^{-9}
Ultra high vacuum	1×10^{-9} to 1×10^{-12}
Extremely high vacuum	$<1\times10^{-12}$

Typically, a vacuum system used for thin film deposition is in the high vacuum range. A molecular beam epitaxy system, which is used to deposit single crystal thin films, requires ultra high vacuum level. Another important parameter related to vacuum is mean free path λ_{mfp}. It stands for the distance of a molecular has to travel until it collides with another one. A simple calculation of mean free path can express as follows,

$$\lambda_{\mathrm{mfp}} = 5 \times 10^{-3}/\mathrm{P} \quad (1.7)$$

where P stands for pressure. In a high vacuum system, the mean free path is larger than the chamber size, which means that molecules collide only with the wall. Vacuum pumps are employed to pump down a vacuum chamber from atmosphere to vacuum. In fact, every vacuum chamber is leaking, though the leakage may be extremely small. The pumps have to keep pumping the system all the time. At least two levels of pumps are required to achieve and maintain vacuum. The first stage is using a roughing pump, usually a rotary mechanical pump, to pump down the chamber from atmosphere to low

vacuum. Then, a high vacuum pump will be started to continuing pump the chamber down to high vacuum range, and the roughing pump is switched to pump the outlet of the high vacuum pump as a backing pump.

In thin film deposition or characterization vacuum system, there are several common high vacuum pumps: diffusion pump, turbomolecular pump, cryo-pump and ion pump.

The maintenance of vacuum system is very important and skillful. And the most common procedure of maintenance is leak detecting. The most difficult step is to locate the leaking point. A helium leak detector, which indicates the helium flow rate, can significantly reduce the period of leakage detection. First, attach a helium leak detector to the leaked vacuum system; Then, the chamber can be pumped down using the pumping system integrated in the leak detector. Third, blow helium gas to the suspected leakage points. If the point is leaking, helium flow rate displayed on the leak detector will increase.

1.4.2 Plasma and glow discharge

Plasmas are weakly ionized gases which contain electrons, ions, natural atoms and molecular. Low pressure plasmas are widely used in thin film related technology. There are several types of low pressure plasmas in low pressure condition: glow discharge plasma, capacitively coupled plasma (CCP), cascaded arc plasma source, inductively coupled plasma (ICP), and wave heated plasma. Different types are used in different applications. For example, glow discharge and CCP are used to in DC and RF sputtering process, respectively. CCP and ICP are used to enhance the reactive ion etching (RIE).

Take the glow discharge for example. To generate plasma in a vacuum chamber, two metal electrodes have to be integrated. Then a purge noble gas, which is usually Ar in a sputtering process, is added into the chamber with an appropriate flow rate to maintain a low pressure gas environment. The discharge can be initiated by applying a sufficiently high DC voltage between two electrodes.

At the beginning, an electron near the cathode is accelerated toward the anode by the applied electric field. The electron collides with a new atom of the noble gas and turns it

into a positive ion and an electron. This process can be expressed using the following equation,

$$e^- + A = 2e^- + A^+$$

(1.8)

Now there are two electrons and one positive ion. The electrons will bombard the other neutral gas atoms and generate more and more positive ions and electrons. The positive atoms will be accelerated toward the cathode and bombard the cathode. This effect continues until an avalanche current causes the gas to breakdown. The distance between electrodes has to be long enough and the gas pressure has to be low enough in order to ensure the electrons can get sufficient energy before collision.

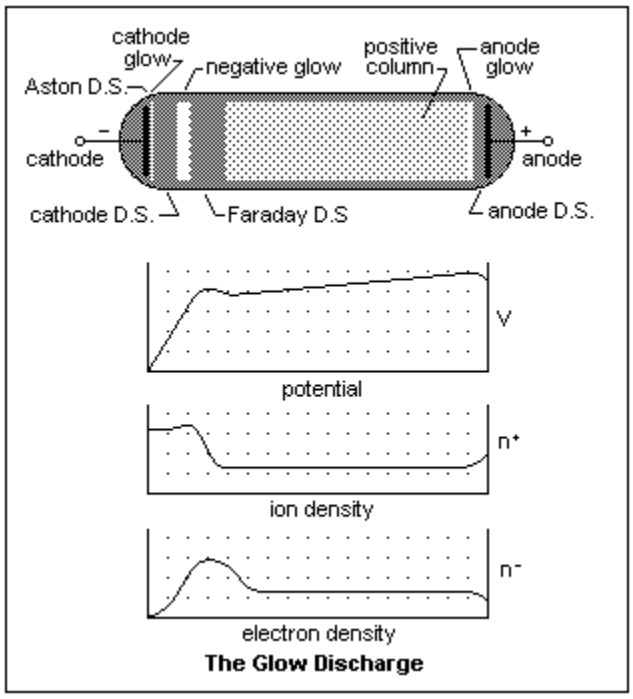

Figure 1.13 Structure of a DC glow discharge with corresponding potential, ion density and electron density.[20]

Figure 1.13 shows the structure of a DC glow discharge and corresponding potential, ion density and electron density. Near the surface of cathode, there is a dark space called Aston Dark Space (Aston D. S.). Both low energy electrons nd high energy positive ions are contained in this thin area. Cathode glow appears beyond the Aston D. S.. It is a highly luminous layer. Next to the cathode glow, it is dark area called cathode dark space. In this area some electrons are accelerated to begin collision, some others collides with natural atoms without produce ion. The next is negative glow, in which the visible

emission is generated by the interactions between assorted secondary electrons and neutrals with attendant excitation and de-excitation. The following regions are Faraday dark space, and positive column. These regions are not used in sputtering process. During sputtering, the substrate is placed inside the negative glow, so the regions beyond negative glow do not appear. The target is placed at the cathode so that it will be bombarded by the accelerated positive ions. As shown in the other charts of Figure 1.13, the potential, ion density and electron density are highly nonlinear, and the sputtering regions have largest ion density.

1.4.3 Sputtering system

In this work, sputtering is the main process used to fabricate magnetic thin films, but unlike a simple cathode-anode pair which is used to generate plasma, a set of magnets are placed at the back side of the cathode. This configuration is called magnetron sputtering.

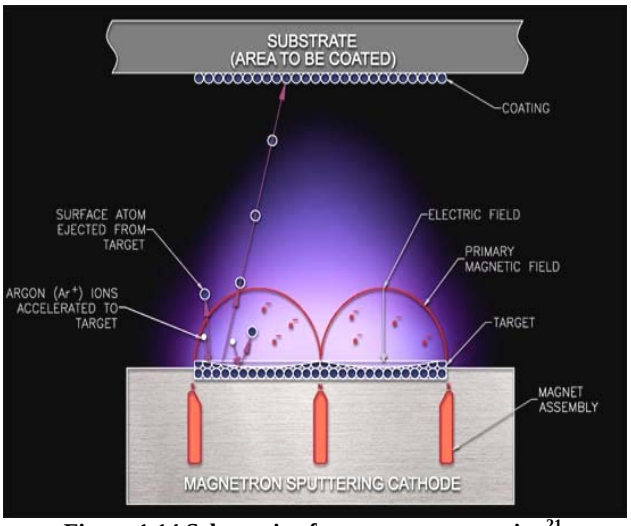

Figure 1.14 Schematic of magnetron sputtering[21]

As shown in Figure 1.14, magnetic fields are generated from the side magnets, then penetrate the target, and finally return to the central magnet. The electrons will be trapped near the surface of target by magnetic fields and continue rotating around in circular motion. The plasma near the target surface will be significantly enhanced because more and more electrons increase the possibility of collision and ionization. With same voltage, one to two orders of magnitude more current is drawn in magnetron sputtering compared to simple discharges. In other words, compared to simple sputtering, a magnetron sputtering configuration can have higher deposition rate and lower operation voltage. The

required operation pressure of working gas also can be reduced, because the magnetic fields can maintain high density of electrons in plasma.

In thin film deposition, many kinds of materials are expected to be sputtered. DC sputtering works very well with the conductive materials. However, when working with nonconductive materials, DC sputtering will not work. When sputtering nonconductive materials, for example SiO_2, after the positive ions are accelerated and bombard the target, positive charges accumulate at the target surface and will not be neutralized. In this case, RF sputtering, which is an AC sputtering with radio frequency, is required. At high frequency, the current can pass through dielectric materials, as well as the charges on the target surface, but in order to make ions bombard the target not the substrate, a negative target self-bias is required to direct the positive ions to target.

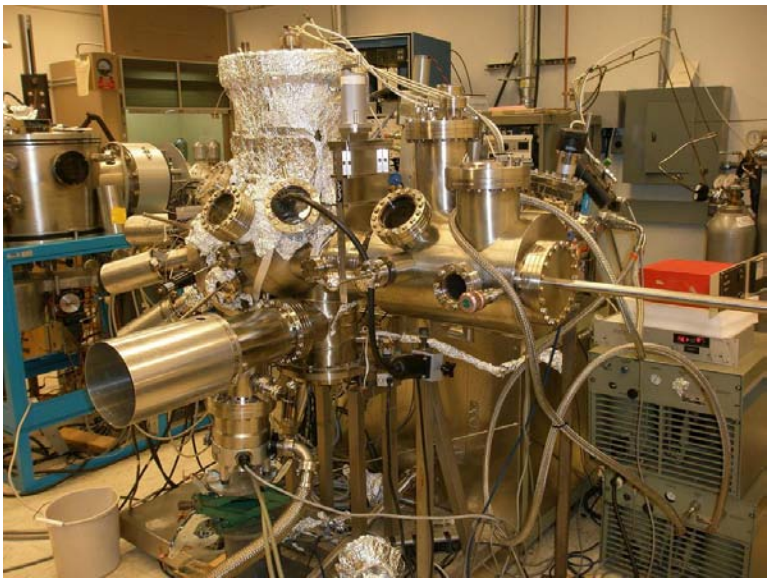

Figure 1.15 8-target magnetron sputtering

In this thesis work, an eight-target magnetron sputtering system, shown in Figure 1.15, is used. It was modified from a MBE system. Therefore it is mainly sealed using CF flanges and can maintain a vacuum with base pressure around $4x10^{-8}$ torr. Its structure diagram is shown in Figure 1.16

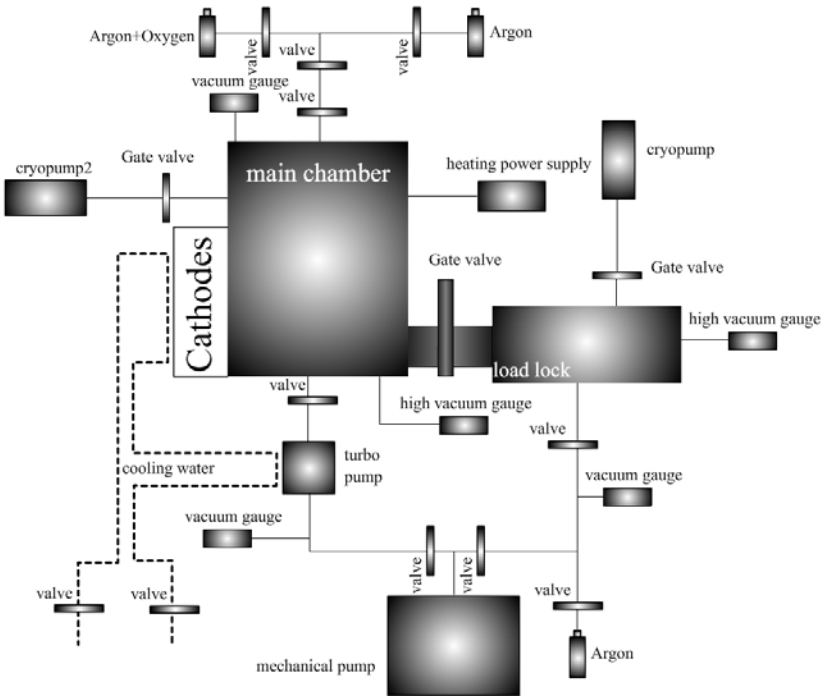

Figure 1.16 Structure diagram of 8-target magnetron sputtering system.

As shown in Figure 1.16, this sputtering system contains two vacuum chambers. One is load-lock which can store 5 substrate holders. The other one is main chamber which has 8 magnetron sputtering guns and is used for thin film deposition. The load-lock chamber is pumped by a cryopump. The main chamber is pumped by cryopump and a turbo pump, which is backed by a mechanical rotary pump. During sputtering, the main chamber is only pumped by the turbo pump, and the working pressure is controlled by adjusting the valve between turbo pump and main chamber. The mechanical pump is also used to pump down both chambers from atmosphere to low vacuum.

A heater is equipped in the main chamber and placed at the back side of the substrate holder. It can be used not only to heat the substrate before and during sputtering, but also to anneal samples. The maximum temperature is around 550 ^{o}C.

Usually, the working gas is pure Ar, but O_2 gas also can be mixed into Ar to perform reactive sputtering.

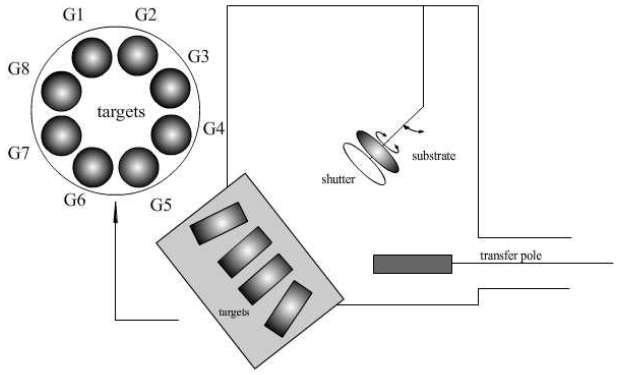

Figure 1.17 Schematic figure of main chamber of the 8-target magnetron sputtering system.

Figure 1.17 demonstrates the schematic of main chamber. 8 magnetron sputtering guns are arranged on a circle. The substrate holder and its shutter are placed on the rotation stage, which is at the con-focal point of the 8 guns.

1.4.4 Thin film growth

One of the key points of this work is to control the microstructure of thin films. Typically the thin films used in magnetic recording media are polycrystalline films. The granular structure and surface morphology are very critical and substantially determine the performance of recording media.

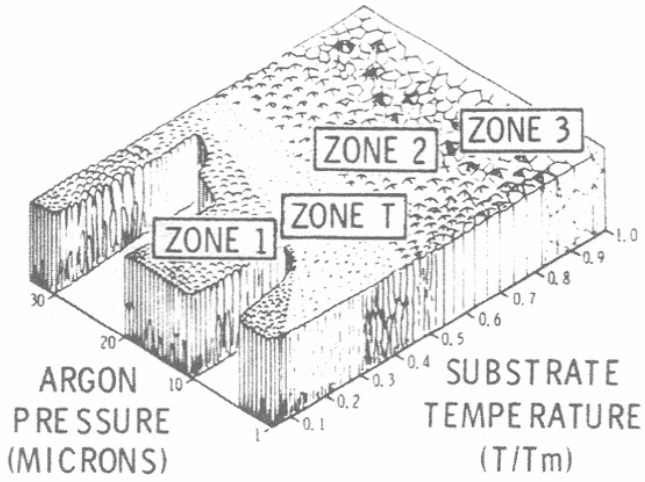

Figure 1.18 Thornton's Zone model for sputter deposited metal films[22]

Figure 1.18 displays the schematic of sputtered-film structures as Thornton's zone model. The microstructure of a sputtered-film largely depends on the fabrication condition and sputtering parameters. Both argon pressure and substrate temperature are important to control the grain size of a thin film. Basically, higher temperature leads to larger grain size.

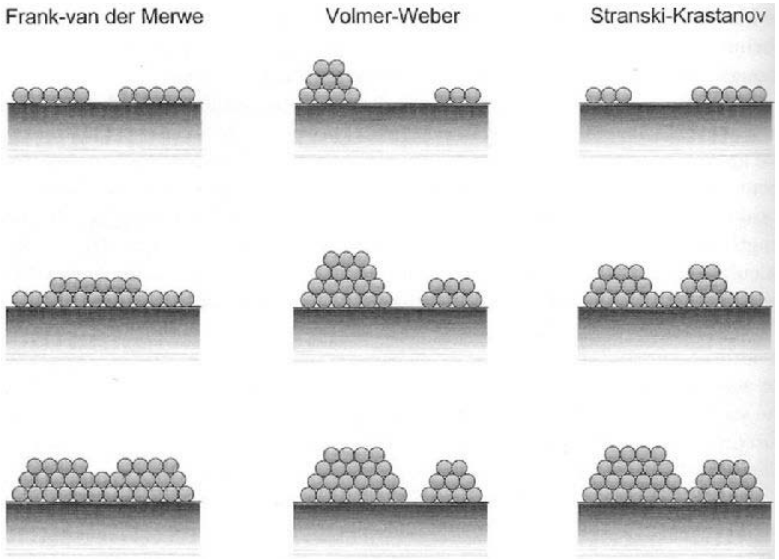

Figure 1.19 Schematic illustration of three common epitaxial growth modes[23]

As shown in Figure 1.19, in the morphological view, the film growth also has different moes:

1) Frank-van der Merwe mode:

The adatoms take priority to fill up the edge of step until the lower step is filled up. Thus, the film is deposited layer by layer.

2) Volmer-Weber mode:

The adatoms nucleate at a few points and pile up as islands.

3) Stranski-Krastanov mode:

It is the combination of the above two modes. At the beginning, the film is deposited layer by layer, and then islands will be formed at top.

1.5 Thin film characterization techniques

1.5.1 X-ray diffraction

X-ray diffraction (XRD) is one of the basic tools to study the crystalline structure and texture of materials. Its working principle can be expressed in Bragg's law (eq. 1.9),

$$n\lambda = 2d \sin\theta \quad (1.9)$$

where n is the order of reflection, λ is the wave length of x-ray, d is spacing between adjacent diffraction planes in lattice, and θ is the angle between incident x-ray and diffraction plane. The value of λ depends on the x-ray source. The most common x-ray source is Cu, and the wave length of Cu k_α radiation is 1.54 Å. However some materials tend to absorb x-rays with wave length in this range and make the detected intensity very low. In this case, other types of x-ray source, such as Co, can be used to improve the signal.

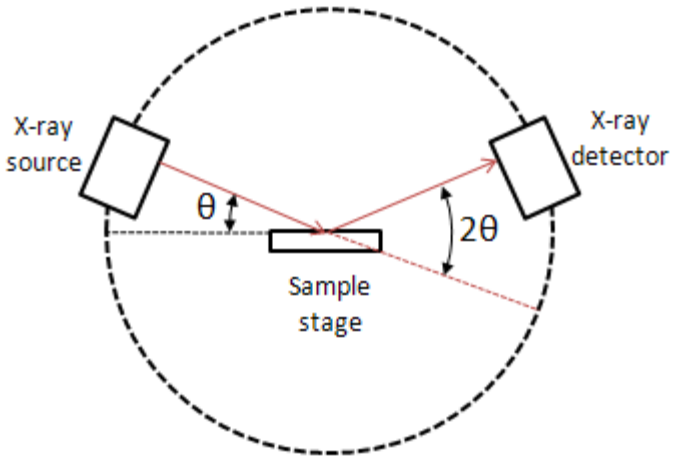

Figure 1.20 Schematic of X-ray diffractometer.[24]

Figure 1.20 shows the schematic of an x-ray diffractometer. It contains three basic components, which are x-ray source, sample stage and x-ray detector. Depending on the configuration and design of x-ray diffractometer itself, two of the three components rotate during operation. No matter how they rotate, the detector and source have same

included angle (θ) with sample plane. The machine records the reflected x-ray intensity while scan θ in certain range. The XRD spectrum is drawn based on intensity vs. 2θ. When θ matches any diffraction plane according to Bragg's law (eq. 1.9), the intensity will increase and a peak will be shown in spectrum. Then, the distance between diffraction planes, which is called d-spacing, can be calculated based on the position of peaks and Bragg's law.

θ-2θ scan is just the basic application of x-ray diffractometer. Changing the configuration of an x-ray diffractometer, many other functions can be implemented. For example, x-ray reflectivity can be used to measure thickness and density of thin film.

1.5.2 Magnetic measurements

A magnetometer is a basic tool to study magnetic materials. In this thesis work, several types of magnetometers are used to measure hysteresis loops which provide a variety of magnetic properties, such as saturation magnetization, coercivity, remnant coercivity, switching field distribution, thermal energy barrier, and so on.

A. Vibrating sample magnetometer

The vibrating sample magnetometer (VSM) is widely used in magnetic measurements, because it is easy and fast to use. Figure 1.21 demonstrates the working principle of a VSM.

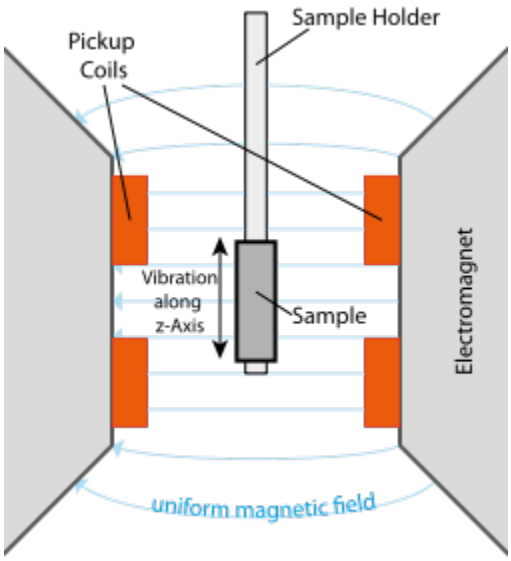

Figure 1.21 Schematic of vibration sample magnetometer.[25]

A sample is placed on a sample holder pole and inserted into a gap between two electromagnets, on which a pair of pickup coils is attached. During measurement, magnetic field is generated from the electromagnets and applied to sample. Meanwhile, the sample is vibrated by the sample holder and generates an inductive voltage in the pickup coils. Fixing the amplitude and frequency of vibration, the voltage magnitude only depends on the magnetization of sample. Therefore, the curve of magnetization (M) vs. magnetic field (H) can be produced.

B. Magneto-optic Kerr effect

The polarization angle of a polarized laser, which is reflected from a magnetic material surface, is changed. The change of polarization angle depends on the sample's magnetization. This effect is called Magneto-optic Kerr Effect (MOKE). Compared to VSM, MOKE can provide much faster measurements, such as dynamitic measurement in microsecond scale, but the sample angle in MOKE measurement is fixed by the configuration, while in VSM, it is very convenient to test the angle dependence.

1.5.3 Electron Microscopy

C. Scanning electron microscope

Scanning electron microscopy (SEM) is a very important tool to observe the morphology of sample surface in nano-scale. Typical resolution of a SEM is around 1 nm. It is not difficult to prepare thin film or a micro/nano device samples for SEM observation. A conductive surface is all you need in SEM, to neutralize the local charges in the observed area. For the samples with insulating surface, a thin conductive film, such as carbon, silver, or platinum, can be sputtered onto the surface to make it conductive.

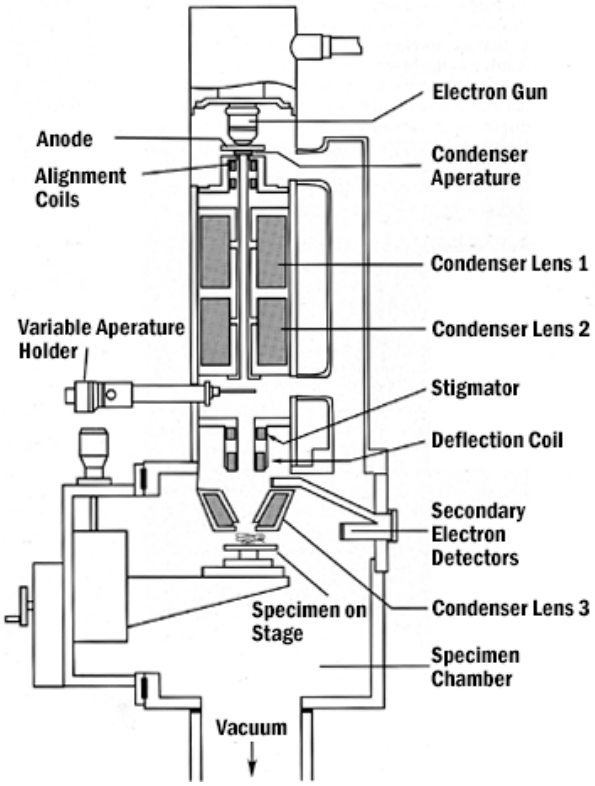

Figure 1.22 Schematic figure of a scanning electron microscopy.[26]

Figure 1.22 shows the schematic figure of a SEM. Electrons are generated from the electron gun, and accelerated to collide with the specimen surface. A set of lenses are placed at the path of electrons to control them. Unlike the optical microscope system, the lens in electron microscope is a coil, which can generate magnetic field to apply Lorenz force to electrons. When the electrons interact with the sample surface, they will generate secondary electrons. A detector will collect the secondary electrons and record the data.

However, the resolution of SEM is limited by the way it collects the information of sample surface. The secondary electrons do not only fly to the detectors, but randomly fly in any direction. Of course, some of these electrons interact with the adjacent area of the sample and also generate new secondary electrons. The detector also records these new

generated secondary electrons, but mixed them with the previous electrons which were generated at the selected area.

For micro/nano devices, SEM can provide sufficiently high resolution. But it can not differentiate the microstructure of thin film, for example granular structure.

D. TEM

It is no exaggeration to say that transmission electron microscope (TEM) is the most important characterization tool in material research. TEM can help to study microstructure, grain size, grain boundary, crystalline structure, lattice, defects, element, chemical state, composition, and so on. A powerful TEM can even differentiate the elements of alloy in atomic scale[27]. Figure 1.23 schematically shows the structure of a TEM.

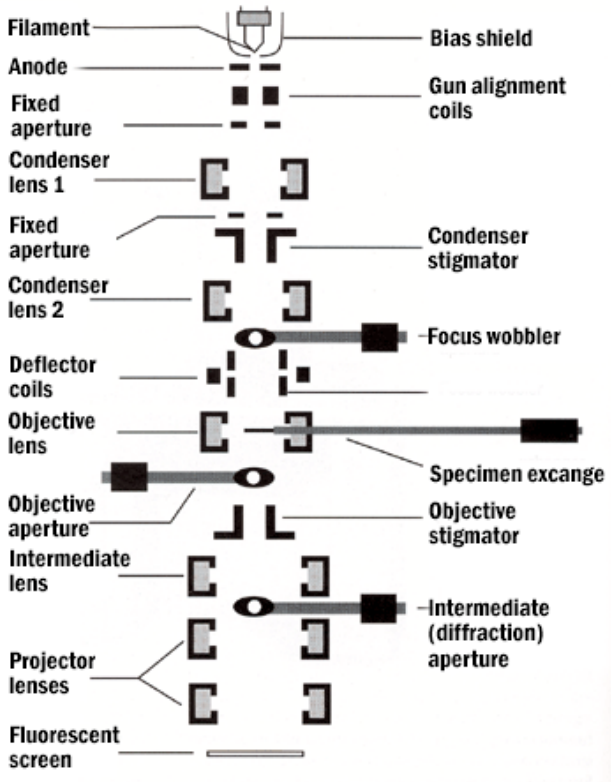

Figure 1.23 Schematic figure of a transmission electron microscopy[28]

Similar to SEM, electrons are extracted from filament and accelerated to pass through a set of lens, apertures, and stigmators, and reach the sample. But in TEM, the electrons pass through the sample and finally hit a screen, a CCD camera or a detector. While passing the sample, electrons interacted with the sample. Depends on the

interaction, the electrons are classified and used to analyze different information of the sample.

The un-diffracted or inelastic scattered electrons can be used to reproduce high resolution image. This projected image of sample is called the bright field (BF) image. In a BF image, the resolution can reach atomic scale, and its contrast reflects the information of atomic (Z) number and crystalline orientation. Typically, the higher the Z number, the darker that contrast of the BF image.

Diffracted electrons create diffraction patterns, which contain the crystalline structure information, but unlike XRD, the electron diffraction reflects the in-plane lattice planes instead of the out-of-plane lattice planes. A diffraction aperture can be placed at the electron path to only expose the sample where the researcher is interested. Thus the selected area can be analyzed independently. This technique is called select area electron diffraction (SAED). Typically, there are two kinds of diffraction: parallel electron diffraction and convergent beam electron diffraction (CBED).

In diffraction mode, an objective aperture can be placed on a single diffraction pattern, and block all the other patterns. For example, if the (001) diffraction pattern is only exposed by the objective aperture, only the electrons diffracted by the (001) plane can pass through the aperture. Then, using these electrons to reproduce the image, only (001) oriented grains can observed. This technique is call dark field (DF) imaging.

Above techniques are just the basic functions of TEM. In the TEM there are lots of advanced functions, such as scanning TEM (STEM), annular dark field (ADF), high angle ADF (HADDF). Also, more types of analysis can be performed in TEM with additional attachments, such as energy-dispersive x-ray spectroscopy and electron energy loss spectroscopy.

One of the most difficult procedures is sample preparation. The sample has to be extremely thin so than electrons can penetrate it. The thickness of sample must be smaller than 100 nm. For ultra-high resolution and advanced analysis, the sample thickness has to be within 10 nm. Sometimes one can deposit nanoparticles or thin films directly on a TEM grid carbon thin film. But in most cases, the sample has to be polished to have a thin are for TEM analysis. This is a very tedious and skillful work. Depends on the tools

used for sample preparation, usually there are three methods to prepare TEM samples: (1) Dimpling, (2) Wedge polishing, and (3) Focus Ion Beam (FIB).

1.5.4 Surface analysis

E. Atomic force microscope

Surface roughness is an important property in thin film research as well as magnetic recording media. In a hard disk drive, the head is flying on the media with a height as small as a few nanometers. Recently, the fly height was reduced within 1 nm. Therefore, the film surface has to be super flat, to prevent the head from colliding with the media. The surface roughness of recording media is required to be no larger than 0.3 nm. TEM only provides a projection view, not the surface morphology. Although SEM can provide surface image with good resolution, it cannot quantitatively evaluate the sample surface. Actually, atomic force microscopy (AFM) is the most common tool to analyze thin film surface. Figure 1.24 shows the schematic of AFM working principle.

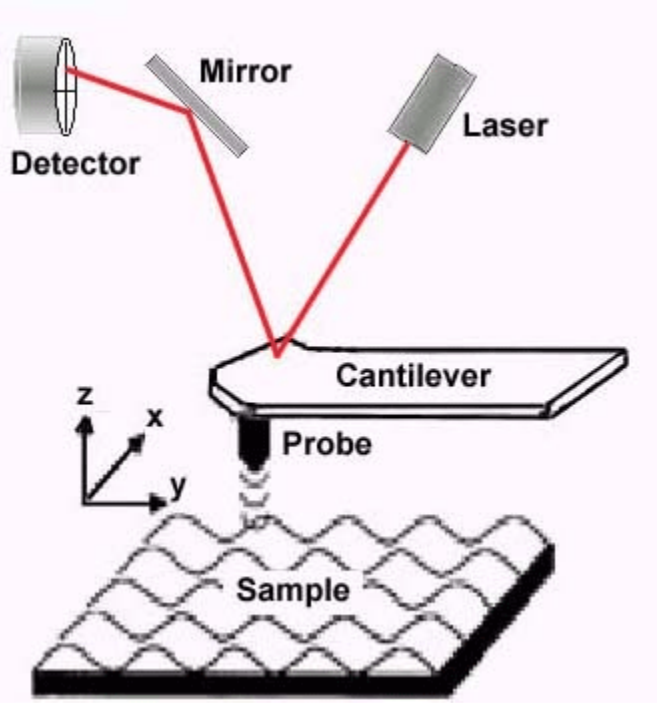

Figure 1.24 Schematic of AFM working principle [29]

As shown in Figure 1.24, in AFM, a cantilever is driven by a motor and moves across the sample surface. There is a probe at the end of the cantilever, facing the sample.

According to the interaction between the probe and sample surface, the cantilever goes up and down. A laser beam is pointed to the cantilever and reflected to a detector. The leaser point on the detector will move with the attitude change of cantilever, and of course represent the morphology of sample surface.

Typically, an AFM has two scanning modes, with different types of cantilever. One is contact mode. In contact mode, the probe attaches to sample surface and directly reproduce its morphology. The other one is called tapping mode. In tapping mode, the probe does not attach to the sample surface. The cantilever is oscillating and its frequency is affected by the atomic force interaction between sample surface and probe. Therefore, surface morphology will change the atomic force interaction and then change the oscillation frequency of cantilever. Thus the morphology can be reproduced by the AFM system.

Since there are many kinds of interaction between the sample and probe, the AFM can detect lots of information other than surface morphology. For example, the magnetic signal of recording media can be sensed by AFM with a special probe.

F. Magnetic force microscope

Magnetic force microscope (AFM) is a special mode of AFM. Besides software configuration, the only difference between MFM and normal AFM is the probe. A MFM probe is coated with magnetic material. Before analysis, the MFM probe is required to have high magnetocrystalline anisotropy and has to be magnetized using a permanent magnet, in order to prevent the magnetic state of probe being changed by the magnetic sample. Operating the MFM probe under tapping mode, the AFM system can mapping the magnetic states of sample surface based on the magnetic force interaction between sample and probe.

With MFM, it is convenient to map domain wall structures of a magnetic thin film and the recording bits of recording media. In addition, an in-plane magnetic field can be applied to the sample during MFM analysis, to observe the change of domain wall structure. However, MFM is limited in dynamic analysis of magnetic thin films with perpendicular anisotropy, because it is very difficult to apply an out-of-plane magnetic field, which is along the direction of the microscope column. Another disadvantage is

that the resolution of a normal MFM/AFM is 10 nm or larger, which is too large to observe the magnetic grains for high density recording media, but it is good enough to observe the magnetic dots of bit patterned media.

1.5.5 Composition analysis

Composition is a very critical parameter in thin film fabrication. The performance and properties of thin film samples mostly depend on its composition and fabrication process. Therefore, the analysis of composition is extremely important. In this thesis work, three methods are mainly used to determine composition. They are energy-dispersive x-ray spectroscopy, electron energy loss spectroscopy, and Rutherford backscattering spectrometry.

A. Energy-dispersive x-ray spectroscopy

Energy-dispersive x-ray spectroscopy (EDS or EDX) is normally equipped in electron microscope, either SEM or TEM. When high energy electrons interact with atoms, elemental characteristic x-ray will be generated. The energy of the x-ray depends on the energy levels of the atoms, which are excited by high energy electrons; by detecting x-ray energy, the element of the atoms can be determined. During operation, the EDS detector is placed at one side of the electron microscope column, thus it is better to slightly tilt sample toward the detector, to enhance the signal. However, EDS is not a high accuracy analysis method either in spatial resolution or in quantitative composition determination. The chemical state of element will affect the composition ratio determination and the spatial resolution of EDS mapping cannot be less than a few nanometers.

B. Electron energy loss spectroscopy

Electron energy loss spectroscopy (EELS) is an advanced application in TEM. Not all TEM systems have an EELS function. In order to do EELS analysis, an EELS detector must be placed at the bottom of TEM column. The transmitted electrons can be classified into two types: elastic scattered electrons and inelastic scattered electrons. The EELS detector only collects the inelastic scattered electrons. After penetrating the sample, inelastic scattered electrons lose a part of their kinetic energy because of the interaction

from atomic nucleus. The amount of energy loss depends on the type of nucleus which interacts with the electrons. In other words, the energy loss is elemental characteristic.

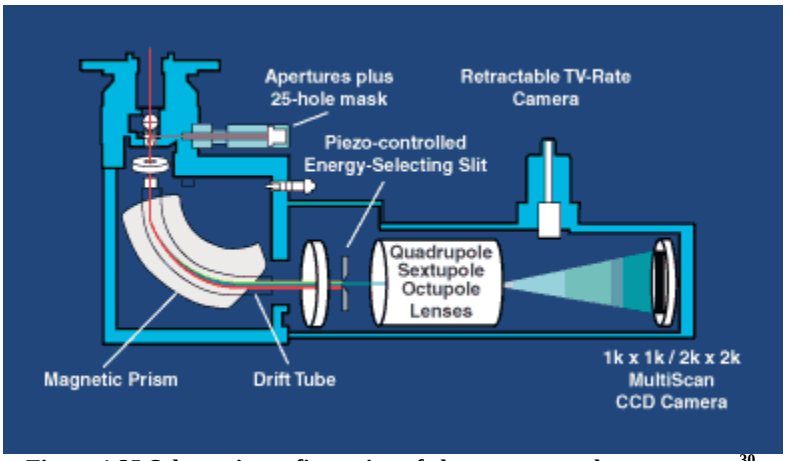

Figure 1.25 Schematic configuration of electron energy loss spectrum.[30]

Figure 1.25 shows the schematic configuration of EELS. A prism with magnetic field is placed on the path of the transmitted electrons. When electrons enter the prism, they will be deflected by the Lorenz force from the magnetic field, and finally hit a detector. However, electrons with different energy loss have different deflection angles, and will hit different positions on the detector. Based on deflection distance, the energy loss can be calculated by software, and then the element can be determined. Unlike the x-ray detected by EDS, the inelastic scattered electrons only interact with atomic nucleus and provide high accuracy in quantitative analyzing the elements of sample. With a scanning transmission microscope (STEM), EELS can reproduce an elemental mapping with very high resolution, by scanning the sample pixel by pixel. The pixel can be as small as around 1 angstrom. Additionally, EELS can be used to measure the sample thickness and valence states of the elements.

C. Rutherford backscattering spectrometry

Rutherford backscattering spectrometry (RBS) provides perhaps the highest accuracy in all common composition analysis methods. In RBS analysis, sample is placed into a vacuum chamber, and bombarded by high energy Helium ions. The high energy ions are scattered after elastic collision with nucleus in the sample; by detecting the energy of backscattered ions, elements of the sample can be determined. Since the energy of backscattered ions is mainly changed by the nucleus, the RBS result is barely affected by

valence states, and can be used for high accuracy quantitative analysis. After an appropriate simulation, the structure of a multilayer thin film can be determined. However, since only the nucleus with a certain mass can reflect high energy ions, RBS is not suitable for analysis of light elements.

1.6 Scope of this thesis

In this thesis work, FePt type recording media will be discussed and demonstrated comprehensively. Granular media, bit patterned media, ECC media, and graded media, HAMR media are all involved. Basically, recording media can be simply classified into granular media and bit patterned media. However, since a $L1_0$ ordered FePt has a very large K_U value, assistance is required to help switch the recording bit of FePt media. At least one of the ECC, graded or HAMR techniques has to be integrated to reduce switching field. There are 6 combinations. However, HAMR refers to a whole system including laser, sink layer, circuit and so on. Therefore, HAMR system will to be experimentally demonstrated in this thesis, which only contains the magnetic recording layer.

Compared to granular media, bit patterned media is more suitable to study the physics and performance of recording process, because the latter is more controllable in structure and has less mixture composition such as non-magnetic gain boundary materials. Therefore FePt type bit patterned media will occupy a large amount of this thesis. Economical and high throughput patterning processes will be demonstrated in details. Pure FePt, ECC and graded continuous films will be developed and patterned into dot arrays. Important issues, including thermal stability, chemically ordering, etching damage, switching field distribution, and so on, will be discussed, and some of them will be addressed.

However, granular media is still dominant in current recording system, and will continue its leading role at least in the near future. This thesis work will experimentally demonstrate new ideas to fabricate FePt granular media. FePt granular media with graded structure will be fabricated in a simultaneous process and FePt granular media with sub-5

nm grain size will be fabricated using a nanopatterning process, in which the hard mask will be deposited using sputtering.

Reference

[1] H. P. Myers, Introductory Solid State Physics, 2nd. Ed., Taylor & Francis, (1997).

[2] http://rondennison.com/services.htm

[3] http://www1.hgst.com/hdd/research/storage/pm/index.html

[4] http://www.xbitlabs.com/articles/storage/display/seagate-momentus-54003_2.html

[5] S. Iwasaki, and Y. Nakamura, IEEE Trans. Magn. 13, 1272 (1977).

[6] B. D. Terris and T. Thomson, J. Phys. D: Appl. Phys. 38, R199 (2005).

[7] M. H. Kryder, and R. W. Gustafson, J. Magn. Magn. Mater. 287, 449 (2005).

[8] P.H. Dederichs, R. Zeller, H. Akai, and H. Ebert, J. Magn. Magn. Mater., 100, 241(1991).

[9] J. J. M. Ruigrok, R. Coehoorn, S. R. Cumpson, and H. W. Kesteren, J. Appl. Phys. 87, 5398 (2000).

[10] A. Moser, K. Takano, D. T. Margulies, M. Albrecht, Y. Sonobe, Y. Ikeda, S. Sun and E. E. Fullerton, J. Phys. D: Appl. Phys., 35, R157 (2002).

[11] R. H. Victora and X. Shen, IEEE Trans. Magn. 41, 2828 (2005).

[12] J. P. Wang, W. K. Shen, and J. Bai, IEEE Trans. Magn. 41, 3181 (2005)

[13] D. Suess, Appl. Phys. Lett. 89, 113105 (2006).

[14] Z. Lu, P. B. Visscher, and W. H. Butler, IEEE Trans. Magn., 43, 2941 (2007).

[15] D. Weller, A. Moser, L. Folks, M. E. Best, W. Lee, M. F. Toney, M. Schwickert, J.-U. Thiele, and M. F. Doerner, IEEE Trans. Magn., 36, 10 (2000).

[16] SGTE Alloy Phase Diagrams, http://www.crct.polymtl.ca/fact/phase_diagram.php?file=Co-Sm.jpg&dir=SGTE

[17] J. Sayama, T. Asahi, K. Mizutani and T. Osaka, J. Phys. D: Appl. Phys. 37, L1 (2004).

[18] S.H. Whang, Q. Feng, Y.-Q. Gao, Acta Materialia, 46, 6485 (1998).

[19] T. Shima, K. Takanashi, Y. K. Takahashi, and K. Hono, Appl. Phys. Lett. 85, 2571 (2004).

[20] http://mysite.du.edu/~jcalvert/phys/dischg.htm

[21] http://www.angstromsciences.com/technology/sputtering.htm

[22] J. A. Thornton, Ann. Rev. Mater. Sci., 7, 239 (1977).

[23] http://www2.warwick.ac.uk/fac/sci/physics/current/postgraduate/regs/mpags/ex5/strainedlayer/surfgrwth/

[24] http://chemwiki.ucdavis.edu/Analytical_Chemistry/Instrumental_Analysis/Diffraction/Powder_X-ray_Diffraction

[25] http://en.wikipedia.org/wiki/Vibrating_sample_magnetometer

[26] http://www.uiowa.edu/~cmrf/methodology/sem/index.html

[27] K.A. Mkhoyan, P.E. Batson, J. Cha, W.J. Schaff and J. Silcox, Science, 312, 1354 (2006).

[28] http://www.uiowa.edu/~cmrf/methodology/tem/index.html

[29] http://www.mtholyoke.edu/~menunez/ResearchPage/AFM.html

[30] http://www.gatan.com/analysis/gif_2001.php

Chapter 2. PROGRESS ON FEPT RECORDING MEDIA

2.1 Introduction

In future extremely high density magnetic recording, the center to center distance between magnetic grains of hard disk media is required to be shrunk further down to sub 4 nm to support recording areal density up to 5 Terabit/in^2 while the magnetic is still kept thermally stable. FePt, which is chemically stable and has ultra-high magnetocrystalline anisotropy of $7x10^7$ erg/cc, is considered as a promising candidate for future recording media materials. In principle, a fully $L1_0$ ordered FePt grain maintains thermal stability for sizes as small as 3 nm.[1] The progress on FePt recording media in the past decade will be reviewed in this chapter.

2.2 Low temperature chemical ordering

The transformation from FePt A1 phase to $L1_0$ phase has been found to occur when it is heated to around 400 °C.[2] However, a chemically disordered A1 phase FePt thin film has to be annealed at 600 °C to form a fully ordered $L1_0$ FePt layer.[3] But for recording media fabrication, it is important to achieve (001) textured $L1_0$ FePt thin film at relatively low deposition temperature, and without post annealing. Considering that during the transformation from A1 phase to $L1_0$ phase, the FePt lattice changed from fcc structure to fct structure with shorter c axis, an in-plane strain is expected to promote the phase transformation and lower the ordering temperature. The strain comes from the lattice misfit between FePt and its underlayers. The lattice of underlayer should be slightly larger than that of the (001) plane of $L1_0$ FePt, otherwise it might match another lattice plane of FePt. The lattice misfit between Ag (001) plane and FePt (001) plane was found to be able to reduce the $L1_0$ ordering temperature, but the FePt film was not well (001) textured.[4,5]

Xu et al. successfully fabricated (001) textured $L1_0$ FePt film on $Cr_{100-x}Ru_x$ underlayer at low substrate temperature of 400 °C.[6] Since the lattice misfit is very critical, they carefully adjusted the lattice constant of CrRu underlayer by varying the composition ratio of Cr to Ru, and found that $Cr_{91}Ru_9$ is the best composition for FePt

fabrication. A Pt layer was inserted between CrRu and FePt to prevent the diffusion of Cr.[7]

Figure 2.1 (a) shows how the out-of-plane coercivity, in-plane coercivity and lattice misfit between CrRu and FePt change with the Ru content. Figure 2.1 (b) displays the XRD spectra of $Cr_{91}Ru_9$/Pt/FePt films with different deposition temperature. According to the figure, FePt was well $L1_0$ ordered at 350 °C, and its ordering and texture were greatly enhanced at 400 °C. Similar effects were found with different underlayers, such as PtMn, CrW, and RuAl.[8,9,10]

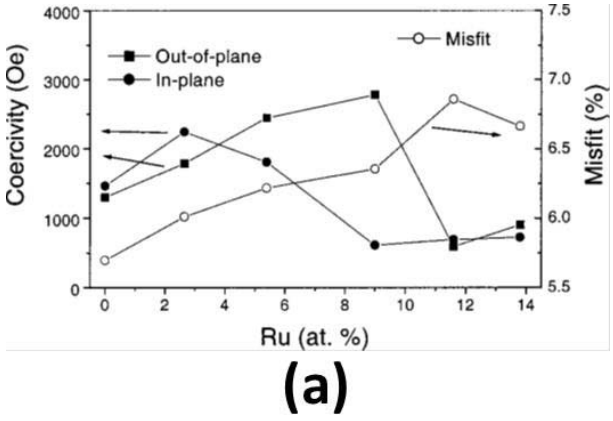

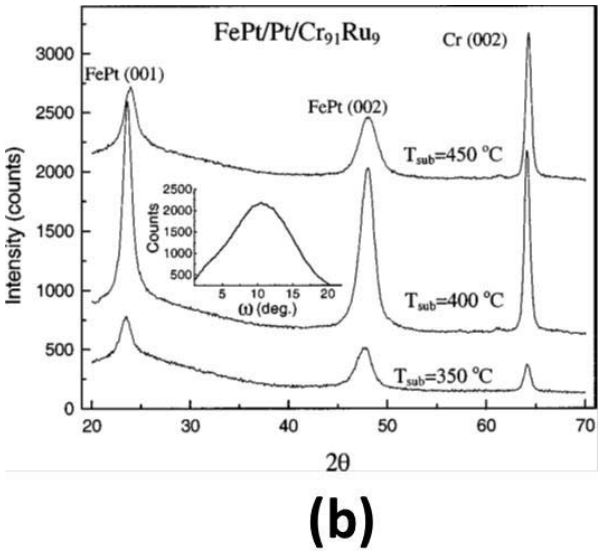

Figure 2.1 (a) How the out-of-plane coercivity, in-plane coercivity and lattice misfit between CrRu and FePt change with the Ru content. (b) displays the XRD spectra of $Cr_{91}Ru_9$/Pt/FePt films with different deposition temperature. [Ref. 6]

Besides, increasing sputtering gas pressure and adding other elements, such as C, Sb, Ag, B, Cu, Ir, were also found to effectively reduce the $L1_0$ ordering temperature of FePt.[11,12, 13,14,15] It is believed that the diffusion of small dopant atoms promotes the diffusion of Fe and Pt atoms and helps them to find low-energy sites. By post-annealing $[Fe/Pt/SiO2]_{18}$ monolayers film at 350 °C for just 60 s, Wu et al. fabricated highly ordered and (001) textured FePt film with well isolated granular structure. [16]

2.3 Grain size and distribution control for heat assisted magnetic recording.

Since FePt media has a large switching field, in order to switch an FePt recording bit, traditional techniques will not work as the head field is not large enough. Heat Assisted Magnetic Recording (HAMR) was proposed to decrease the switching field.[17, 18] It becomes more and more promising to support extremely high recording density with the recent demonstration of 1 Terabit/in^2 areal density by Seagate Technology. [19]

The key challenge of fabricating high density FePt media is to fabricate a highly $L1_0$ ordered FePt granular thin film with extremely small grain size and good (001) texture. Using RuAl as an underlayer and setting the fabrication temperature to 350 ^{o}C, Shen et al. achieved 6.6 nm FePt grains with a size distribution of 17% and a coercivity of 8 kOe.[10] The characteristic of this work is that the columnar growth was initiated from the underlayer, not FePt recording layer only. Zhang et al. fabricated FePt-Ag-C film at 550 ^{o}C and the coercivity was 35 kOe. [20] In their work, the FePt grain size was 6.2 nm. Also using 550 ^{o}C as the depositioin temperature, Mosendz et al. created FePt-Ag-C media with a coercivity of as high as 48 kOe, but the grain size increased to 7.2 nm. [21] Figure 2.2 shows the results of their work. From the cross-sectional image in Figure 2.2 (b), the spherical shape of the FePt grains can be clearly observed. This is a common draw-back of the non-columnar growth, which limits the thickness of magnetic layer. When exceeding a critical thickness, a second layer of disoriented particles would be formed.[11,21]

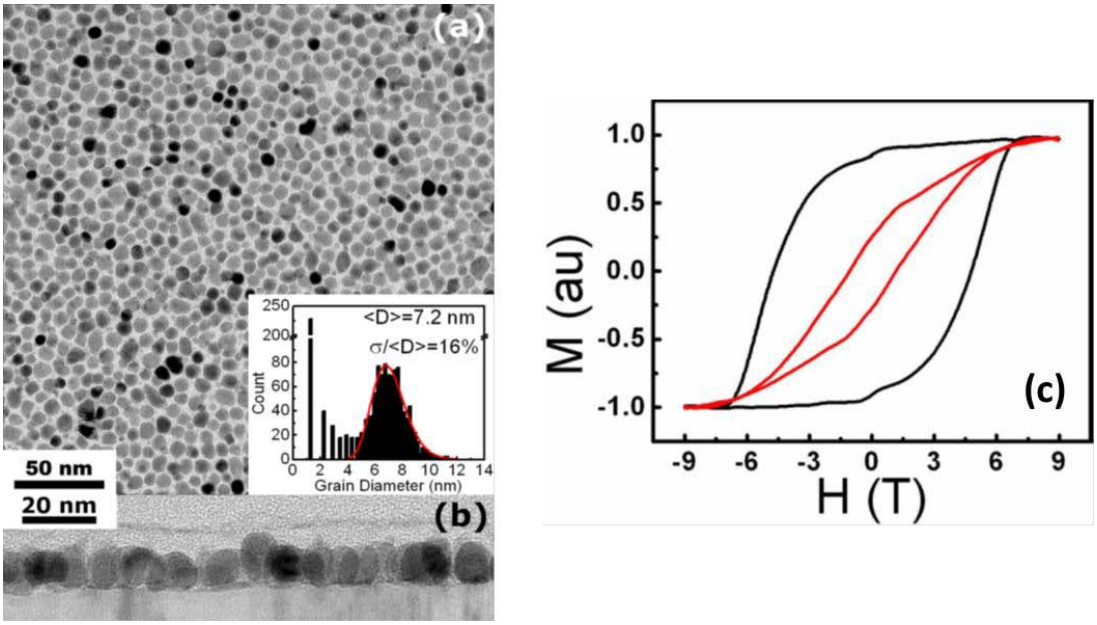

Figure 2.2 (a) plan-view TEM image, (b) cross-sectional TEM image, (c) in-plane and out-of-plane hysteresis loops of FePtAg-C granular media. [Ref. 21]

Granz et al. successfully reduced the FePt grain size down to 2.5 nm by depositing the FePtB film at room temperature, but the FePt was in disordered phase with superparamagnetic behavior. [22] Dong et al. created sub-6 nm FePt grains with a coercivity of 21.5 kOe by depositing FePt-SiN_x-C film at a relatively low temperature of 380 ^oC, however, the grains were not well isolated. [23] As shown in Table 2.1, a dilemma for the fabrication of FePt media with desirable properties is that a high temperature deposition leads to good $L1_0$ ordering thus high coercivity, but results in large grain sizes, while a low temperature deposition leads to small grain sizes, but results in poor $L1_0$ ordering thus low coercivity. Optimizing the deposition parameters and searching for doping materials may help improve the performances, but still cannot solve this dilemma completely. In order to solve this problem, a fundamentally new process is required to break down the interlock between the requirements for small grain sizes and large coercivity for FePt HAMR media.

Table 2.1 A brief summary of FePt granular media fabrication

	Grain size (nm)	H_C (kOe)	Fabrication temperature
FePt-B(-Ag)	2.5	0.05, disordered	Room temperature,.
FePt-Ag-C	6.2	35	550 ^{o}C,
FePt-Ag-C	7.2	48	500-550 ^{o}C
FePt-SiN_x-C	5.5 (not well isolated)	21.5	380 ^{o}C
FePt-Cu	6	8.0	350 ^{o}C

2.4 Bit patterned media

In conventional recording media, a single recording bit contains a certain amount of magnetic grains to maintain signal to noise ratio. Therefore, thermal fluctuation effect will become serious when further reduce the bit size and grain size. Other than simply utilizing high K_U materials, bit patterned media is another option to overcome the thermal effect issue. In bit patterned media (BPM), every single magnetic entity is exchange decoupled and can store information independently.[24] It has been considered as a promising candidate for future high areal density magnetic recording. A single magnetic entity in BPM can be as large as a recording bit in conventional recording media with same recording density, but more thermally stable. Figure 2.3 shows the comparison of conventional media and BPM.[25]

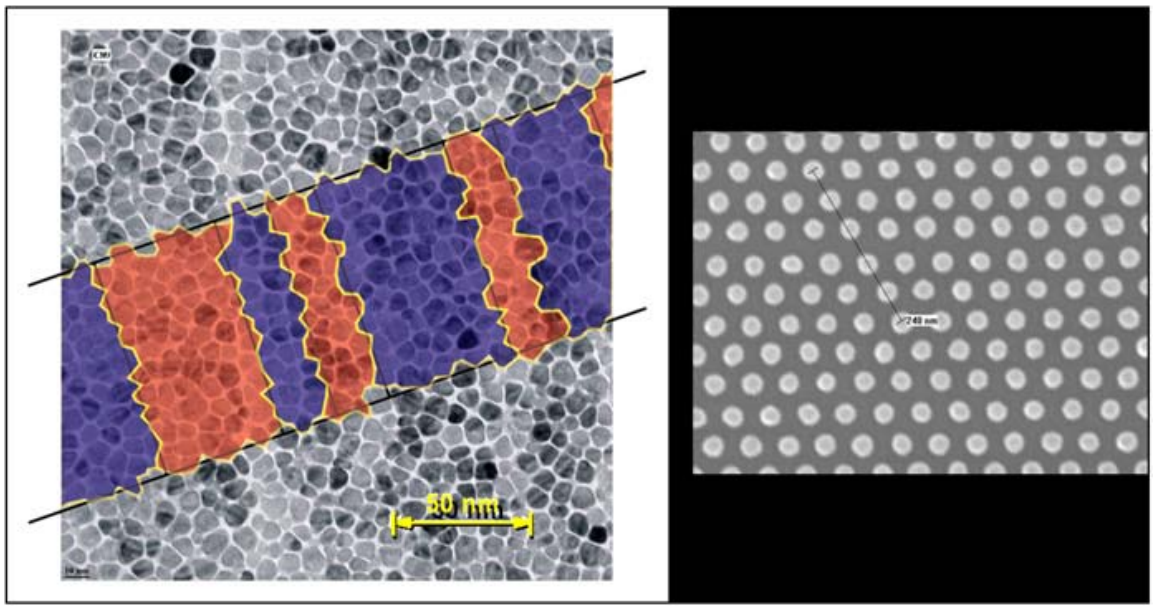

Figure 2.3 Comparison of (left) conventional media and (right) bit patterned media. [Ref. 25]

Even with BPM, to get ultra-high recording density, thermal effect is still inevitable. To achieve 10T bit/in^2 areal density in BPM, the bit size is required to be as small as 8 nm. Therefore, BPM still requires materials with very high magnetic anisotropy to guarantee thermal stability of the individual bits. $L1_0$ ordered FePt alloys was considered as one of the potential materials for the recording layer in BPM due to its large K_U.

However, the fabrication process of BPM is far more complicated and expensive than that of conventional media. Patterning process has to be employed following thin film deposition. In fact, the biggest challenge is to economically fabricate magnetic dot arrays. Typically, there are three methods to transfer the dot array patterns down to magnetic continuous films.

1) Electron beam lithography;
2) Nanoimprinting;
3) Block copolymer self-assemble.

In electron beam lithography, the nanostructures are defined by electron beam one by one. It is very accurate but costs too much. Therefore it is impossible to utilize this process on every hard disk. On the contrast, the other two processes are much more economical and feasible in media fabrication.

Several methods have been proposed for fabricating patterned structure for BPM either by depositing materials on pre-patterned substrate[26] or patterning the pre-deposited

magnetic film by e-beam lithography [27] over small area, nanoimprinting [28] and self-assembled di-block copolymer [29,30,31] over large area. Anodic Aluminum Oxide (AAO) was used as an economic mold to fabricate FePt BPM with nanoimpringting.[32] Block copolymer lithography has been considered as the most likely route to higher areal density beyond that achievable by electron beam lithography and it is economical too. Fabrication of $L1_0$ single layer FePt bit patterned media using block copolymer lithography was reported by Hieda et al.[31] They had fabricated the hole array first and filled them with spin on glass (SOG). Then, the matrix was removed and the SOG dots were used as the etching mask. Directly transferring the dot array pattern of block copolymer to FePt was demonstrated by Wang et al.[33] Figure 2.4 shows the SEM plan-view image of the block-copolymer patterned FePt dots with 31 nm dot size and 8% size distribution.

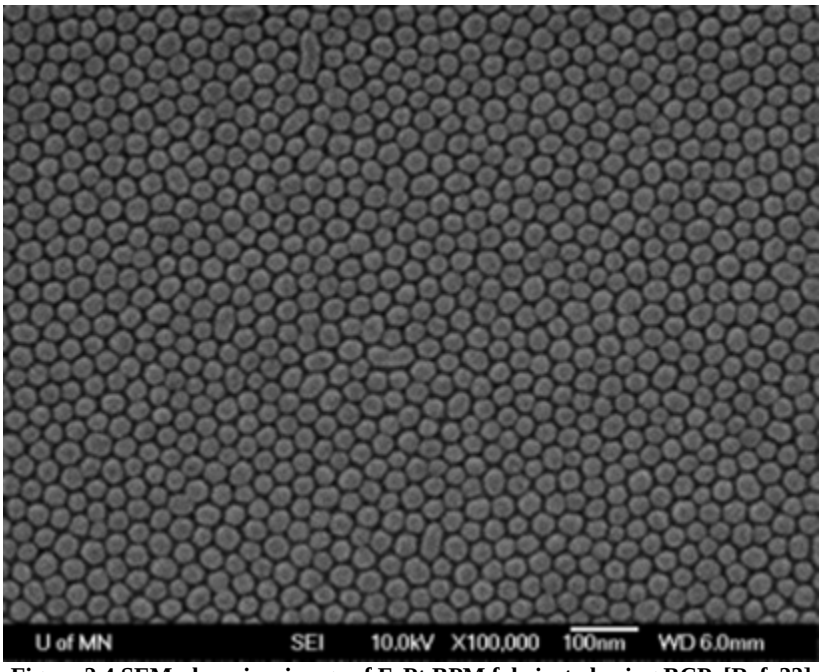

Figure 2.4 SEM plan-view image of FePt BPM fabricated using BCP. [Ref. 33]

Usually, the coercivity of the as-patterned FePt dots could not reach the expected value, which would be a few Tesla.[29,33,34,35,36,37] This fact suggests that the patterning process may cause degradation of the FePt properties. Disordered FePt phase region was found on the FePt patterned dots, and the coercivity could be significantly increased after post-annealing at a very high temperature.[36] Another key issue of the patterned media is the switching field distribution (SFD). A wide SFD seriously affects the definition of the recording bits and limits the recording density. The dot size distribution and anisotropy distribution are the major sources of the SFD. Wang et al. reported using post-annealed the patterned films at a relatively low temperature of 350 °C, to enhance the $L1_0$ ordering and reduce SFD.[38] The results are summarized in Table 2.2.

Table 2.2 Results summary of continuous film, as-patterned BPM and annealed BPM [Ref. 38]

	H_C (kOe)	Switching field distribution	Ordering parameter S	FWHM of FePt (001) rocking curve
Continuous film	3.82	-	0.72	5.95º
As-patterned BPM	16.0	34%	0.48	7.26º
Annealed BPM	17.1	15%	0.57	6.81º

2.5 Exchange coupled composite structure

Besides HAMR, exchange coupled composite (ECC) structure was proposed as an efficient way to switch high K_U media.[39,40] In ECC media, a single magnetic grain is divided into two parts with different anisotropy. One part is magnetically hard and the other part is magnetically soft. The hard part has high anisotropy and can keep the grain thermally stable, while the soft part will help reverse the magnetization of whole grain during writing process. Figure 2.5 shows how the magnetization switches in an ECC grain.

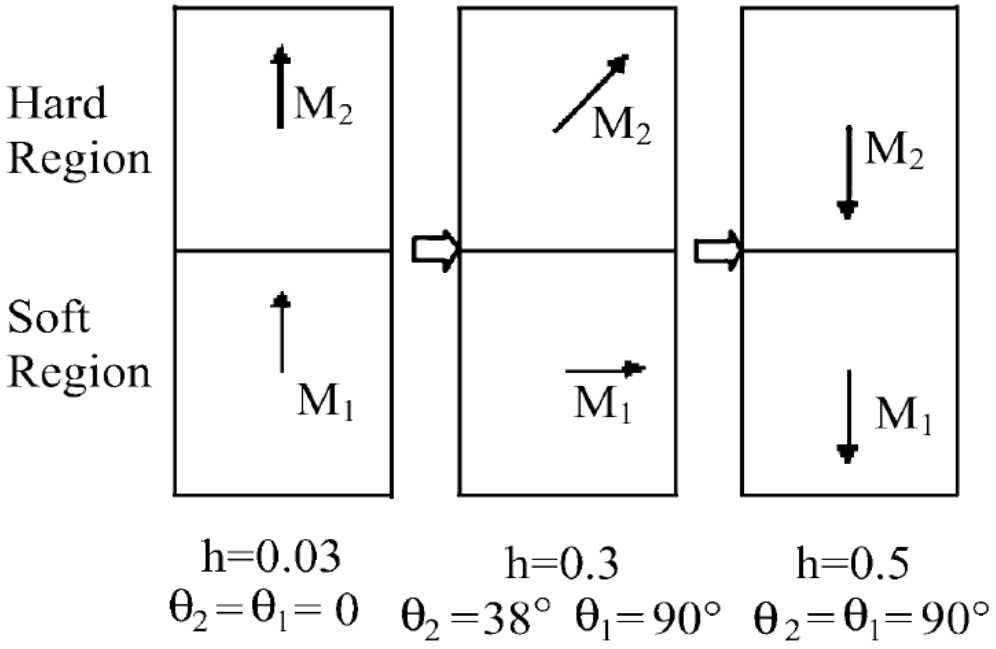

Figure 2.5 magnetization reversal in an ECC grain. [Ref. 39]

Initially, the magnetization of both hard and soft region pointed up. Then, an external magnetic field applied to the grain from up to down. The magnitude of the applied filed is smaller than the coercivity of hard region but larger than the coercivity of soft region. Therefore the magnetic moment of soft region started to rotate. The exchange coupling between the soft region and hard region make them tend to align to same direction. Therefore the moment of hard region will rotate even its coercivity is larger than the applied field. And finally, with proper magnitude of applied field and help of soft region, the magnetization of hard region will be reversed.

Basically, the soft region helps to reduce switching field while the hard region helps to maintain thermal stability. However, even though the ECC structure can make a magnetic grain switchable, it also significantly increases the volume of a single grain, which is not preferred in recording media. Actually, in conventional structure, even keep the magnetic materials unchanged, the thermal stability can be doubled by doubling the volume of grain. The ECC structure has to be carefully designed to balance this dilemma. A gain factor was defined to evaluate the advantage of an ECC media to conventional media, [39]

$$\xi = \frac{2\Delta E}{M_S \bullet H_{SW} \bullet V}$$

(3.1)

Where ξ is the gain factor, ΔE is thermal barrier of magnetic reversal, M_S is saturation magnetization, H_{SW} is switching field, and V is the volume of grain. In conventional media, $\Delta E = K_U V = (M_S \bullet H_{SW}/2) \bullet V$. Therefore its ξ equals 1. But for ECC media, its real thermal energy barrier is larger than $(M_S \bullet H_{SW}/2) \bullet V$, and its ξ is larger than 1. Theoretically, the maximum ξ of ECC structure is 2. Suess et al. used exchange spring model rather than two-spin model to demonstrate the similar structure.[41] In their model, during switching, a domain wall was initiated in the soft region of composite grains and push through the boundary of two regions.

$L1_0$ FePt based ECC media has been widely studied and experimentally demonstrated with various soft region designs. Typically there are two types of Soft layer. One type is FePt with low $L1_0$ ordering or low coercivity. The ordering or coercivity of FePt can be tuned by depositing FePt at relatively low temperature,[42] doping other elements,[43] or varying sputtering condition.[44] The other type of soft layer is other magnetic materials with relatively low coercivity than that of FePt.[45,46,47,48] In addition, FePt ECC media with ledge-type structure or core-shell structure were fabricated and found to be more efficient in switching field reduction.[49,50,51]

FePt based ECC media were also demonstrated in the form BPM.[33, 52, 53] With appropriate patterning process, the fabrication of ECC BPM is easier than that of ECC granular media, because BPM only requires continuous film stacks other than granular films with non-magnetic dopants. Therefore, in BPM, the film stacks are more controllable and have more freedom in design. Figure 2.6 shows the TEM cross-sectional image of a patterned ECC dots, whose structure is FePt/Fe/Ru(capping layer).

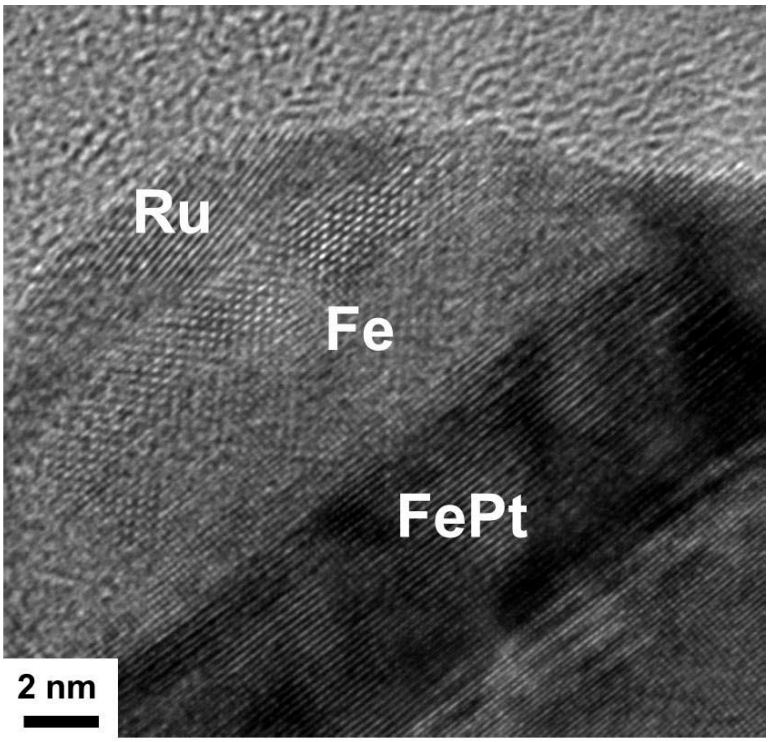

Figure 2.6 TEM cross sectional image of a patterned ECC dots with structure of FePt/Fe/Ru(capping).

2.6 Graded media

To further enhance the writability of composite structure, graded media was proposed. [54,55] In graded media, K_U value gradually changed along the grain columnar direction. Domain wall assisted switching was also suggested with a similar consideration. [56] ECC structure and graded structure are schematically compared in Figure 2.7.

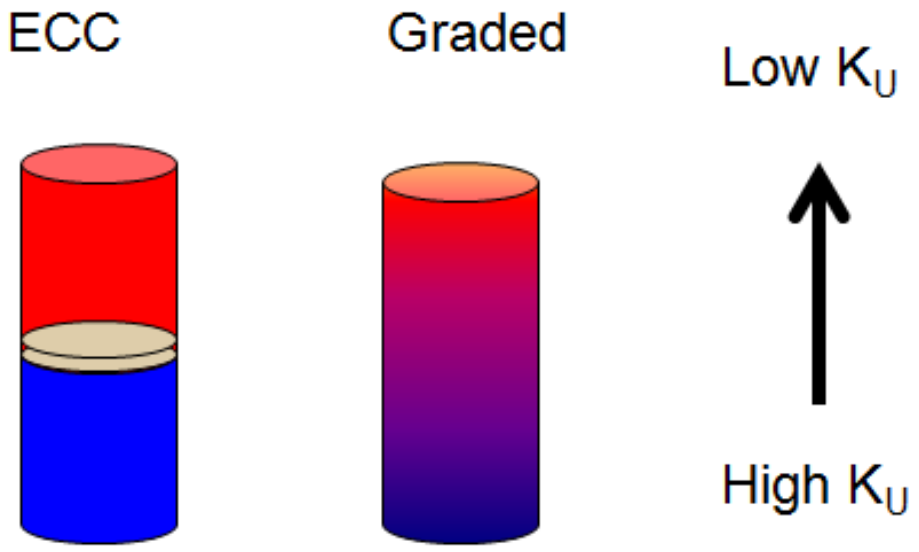

Figure 2.7 Schematic comparison of an ECC grain and a graded grain.

As mentioned above, an ECC grain is divided into two parts with different K_U value. But in a graded grain, there is no sharp interface to separate different regions. It gradually changed from magnetically hard to magnetically soft. Graded structure is expected to have better performance than ECC structure does. In other words, with proper design, graded structure can have higher thermal barrier but lower switching field than ECC structure does. Theoretically, the gain factor of a graded media can be as high as 4.[55]

In the view of fabrication, the graded structure of FePt can be achieved by annealing a FePt/Fe bilayer structure,[57] or gradually varying the dopant content.[58] Unlike ECC media, varying the sputtering condition may not be a practical way to fabricate graded media. However, since experiments are usually not ideal, FePt thin films or grains are not completely uniform. Even an FePt layer was purposely deposited as pure $L1_0$ FePt, its $L1_0$ ordering or composition always varied in the film normal direction. This imperfection provides an easy method to build up graded structure. Wang et al. found that in the structure of RuAl/Pt/FePt thin film, a compositionally graded interface was created between FePt and Pt, while deposited at 350 °C.[59] Figure 2.8 shows the Fe content distribution along the columnar direction of the grains, which was obtained from EELS line scan analysis in TEM. The designed thickness of FePt is 6 nm, but the distribution of Fe expanded to 9 nm. The graded structure was proved by the line-scan profile. The gain factor of this sample was estimated to be 3.74, which is quite close to the limit.

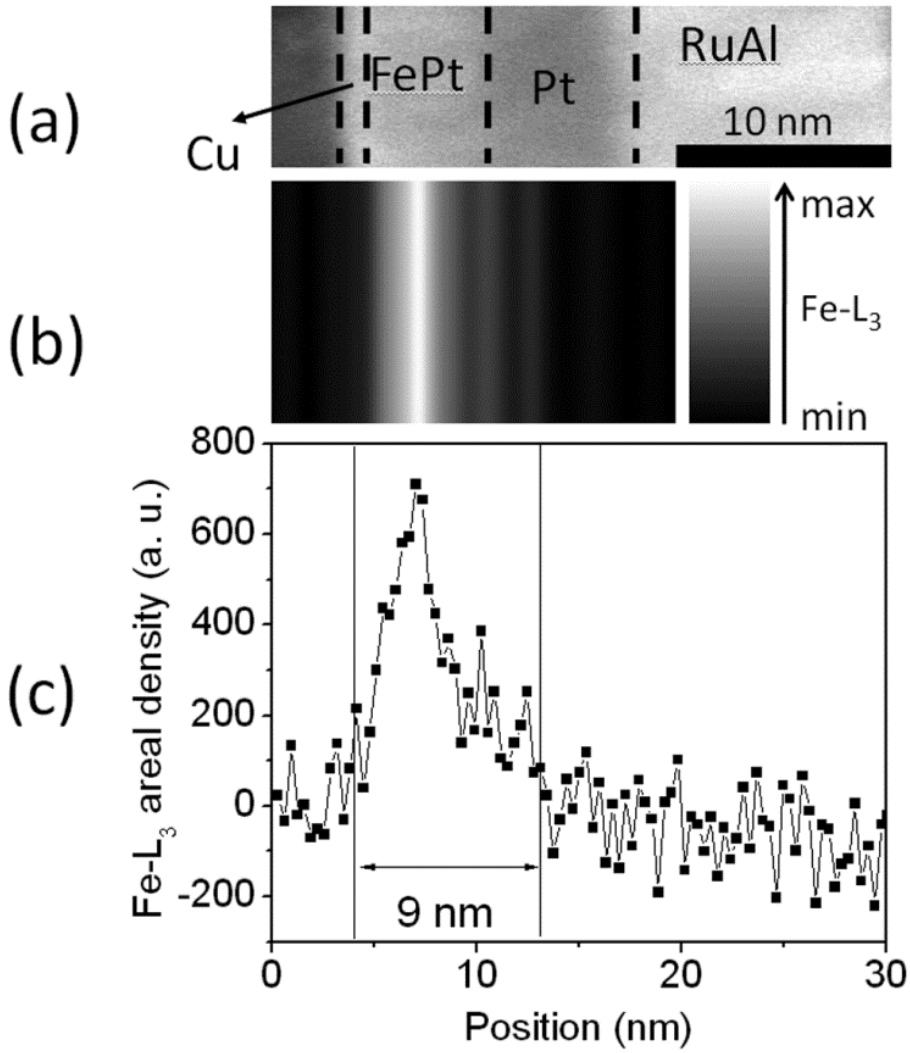

Figure 2.8 (a) Cross-sectional STEM annular dark field image of sample Pt(7 nm)/FePt(6 nm) rotated by 90 degree counterclockwise (left: film top). (b) A schematic of how the Fe composition changes with position, in which the higher the brightness, the more the Fe. (c) EELS line scan analysis of Fe content in one columnar grain along the film normal. The curve of Fe-L_3 edge areal density vs. position was plotted in (c) with associated position in (a) and (b). [Ref. 59]

FePt type graded media was also realized in BPM.[38] Unlike the granular media with graded structure, it was found that either varying deposition temperature or adjusting the composition during sputtering process is not suitable to create a graded continuous film for BPM, because both these methods caused large surface roughness. A layer inter-diffusion process is recommended for the graded continuous film fabrication, with which the thin film surface is confirmed to be flat.

2.7 Conclusion

In this chapter, the progress on FePt perpendicular recording media has been reviewed systematically.

Reference

[1] D. Weller, A. Moser, L. Folks, M. E. Best, W. Lee, M. F. Toney, M. Schwickert, J.-U. Thiele, and M. F. Doerner, IEEE Trans. Magn., 36, 10 (2000).

[2] K. Barmak, J. Kim J, A. Shell A, E. B. Svedberg, and J. K. Howard, Appl. Phys. Lett., 80, 4268 (2002).

[3] S. N. Piramanayagam, J. Appl. Phys. **102**, 011301 (2007).

[4] Y.-N. Hsu, S. Jeong, D. N. Lambeth, and D. Laughlin, IEEE Trans. Magn. 36, 2945 (2000).

[5] Y.-N. Hsu, S. Jeong, D. Laughlin, and D. N. Lambeth, J. Appl. Phys. 89, 7068 (2001).

[6] Y. Xu, J. S. Chen, and J. P. Wang, Appl. Phys. Lett., 80, 3325 (2002).

[7] J. S. Chen, Y. Xu, and J. P. Wang, J. Appl. Phys. **93**, 1661 (2003).

[8] C. C. Chiang, Chih-Huang Lai, and Y. C. Wu, Appl. Phys. Lett. 88, 152508 (2006).

[9] J. Cao, J. Cai, Y. Liu, Z. Yang, F. Wei, A. Xia, B. Han, and J. Bai, J. Appl. Phys. 99, 08F901 (2006).

[10] W. K. Shen, J. H. Judy, and J. P. Wang, J. Appl. Phys. 97, 10H301 (2005).

[11] J. S. Chen, B. C. Lim, J. F. Hu, B. Liu, G. M. Chow, and G. Ju, Appl. Phys.Lett. 91, 132506 (2007).

[12] T. Maeda, T. Kai, A. Kikitsu, T. Nagase, and J.-I. Akiyama, Appl. Phys.Lett. 80, 2147 (2002).

[13] K. Nishimur, K. Takahashi, H. Uchida, M. Inoue, J. Magn. Magn. Mater., 272-276, 2189 (2004).

[14] Q. Yan, T. Kim, A. Purkayastha, P. G. Ganesan, M. Shima, and G.Ramanath, Adv. Mater., 17, 2233 (2005).

[15] Z. L. Zhao, J. Ding, Y. Li, G. M. Chow, J.S. Chen, and J.P. Wang, Meta. and Mat. Trans. A, 38A, 811 (2007).

[16] Yun-Chung Wu, Liang-Wei Wang, and Chih-Huang Lai, Appl. Phys. Lett. 91, 072502 (2007).

[17] J. J. M. Ruigrok, R. Coehoorn, S. R. Cumpson, and H. W. Kesteren, J. Appl. Phys. 87, 5398 (2000).

[18] A. Moser, K. Takano, D. T. Margulies, M. Albrecht, Y. Sonobe, Y. Ikeda, S. Sun and E. E. Fullerton, J. Phys. D: Appl. Phys., 35, R157 (2002).

[19] T. Rausch, J. D. Trantham, A. G. Chu, H. Dakroub, C. P. Henry, E. C. Gage, J. W. Dykes, 23rd the Magnetic Recording Conference (TMRC), San Jose, CA, B2, Aug 20-22, (2012).

[20] L. Zhang, Y. K. Takahashi, K. Hono, B. C. Stipe, J.-Y. Juang, and M. Grobis, IEEE Trans. Magn., 47, 4062 (2011).

[21] O. Mosendz, S. Pisana, J. W. Reiner, B. Stipe, and D. Weller, J. Appl. Phys. 111, 07B729 (2012).

[22] S. D. Granz, K. Barmak, and M. H. Kryder, J. Appl. Phys. 111, 07B709 (2012).

[23] K. F. Dong, H. H. Li, Y. G. Peng, G. Ju, G. M. Chow, and J. S. Chen, J. Appl. Phys. 111, 07A308 (2012).

[24] B. D. Terris and T. Thomson, J. Phys. D: Appl. Phys. 38, R199 (2005).

[25] B. D. Terris, J. Magn. Magn. Mater., 321, 512 (2009)

[26] M. T. Rahman, N. N. Shams, and C. H. Lai, J. Appl. Phys. **105**, 07C112 (2009).

[27] X. Yang, S. Xiao, W. Wu, Y. Xu, K. Mountfield, R. Rottmayer, K. L. Kuo, and D. Weller, J. Vac. Sci. Technol., **25**, 2202 (2007).

[28] S. Y. Chou, P. R. Krauss, and P. J. Renstrom, J. Vac. Sci. Technol. B **14**, 4129 (1996).

[29] K. Naito, H. Hieda, M. Sakurai, Y. Kamata, and K. Asakawa, IEEE Trans. Magn. **38**, 1949 (2002).

[30] R. Ruiz, H. Kang, F. A. Detcheverry, E. Dobisz, D. S. Kercher, T. R. Albrecht, J. J. de Pablo, and P. F. Nealey, Science **321**, 936 (2008).

[31] H. Hieda, Y. Yanagita, A. Kikitsu, T. Maeda, and K. Naito, J. Photopolym. Sci. Technol. **19**, 425 (2006).

[32] T. Rahman, H. Wang, and J.P. Wang, j. nanotech., 2011, 961630 (2011).

[33] H. Wang, T. Rahman, H. Zhao, Y. Isowaki, Y. Kamata, A. Kikitsu, and J.P. Wang, J. Appl. Phys. 109, 07B754 (2011).

[34] C. Kim, T. Loedding, S. Jang, H. Zeng, Z. Li, Y. Sui, and D. J. Sellmyer, Appl. Phys. Lett. **91**, 172508 (2007).

[35] T. Bublat and D. Goll, Nanotechnology **22** 315301 (2011).

[36] T Bublat and D Goll,J. Appl. Phys. **110**, 073908 (2011).

[37] T. Shimatsu, Y. Inaba, H. Kataoka, J. Sayama, H. Aoi, S. Okamoto, and O. Kitakami, J. Appl. Phys. **109**, 07B725 (2011).

[38] H. Wang, H. Zhao, T. Rahman, Y. Isowaki, Y. Kamata, T. Maeda, H. Hieda and A. Kikitsu, H.-H. Guo, B. Ma, Y. Chen, W. Li, J. Ding, J.P. Wang, 23rd The Magnetic Recording Conference(TMRC), F-6 (invited), San Jose, 2012.

[39] R. H. Victora and X. Shen, IEEE Trans. Magn. **41**, 2828 (2005).

[40] J. P. Wang, W. K. Shen, and J. Bai, IEEE Trans. Magn. **41**, 3181 (2005)

[41] D. Suess, T. Schrefl, S. Fahler, M. Kirschner, G. Hrkac, F. Dorfbauer, and J. Fidler, Appl. Phys. Lett. **87**, 012504 (2005).

[42] L. S. Huang, J. F. Hu, G. M. Chow, and J. S. Chen, J. Appl. Phys. 109, 063910 (2011).

[43] H. Zhao, H. Wang, and J. P. Wang, J. Appl. Phys. 111, 07B732 (2012).

[44] C. J. Jiang, J. S. Chen, J. F. Hu, and G. M. Chow, J. Appl. Phys. 107, 123915 (2010).

[45] F. Wang, X. Xu, Y. Liang, J. Zhang, and H. Wu, Appl. Phys. Lett., 95, 022516 (2009).

[46] J. -L. Tsai, H. -T. Tzeng, and G. -B. Lin, Appl. Phys. Lett. 96, 032505 (2010).

[47] D. Makarov, J. Lee, C. Brombacher, C. Schubert, M. Fuger, D. Suess,J. Fidler, and M. Albrecht, Appl. Phys. Lett. 96, 062501 (2010).

[48] H. H. Guo, J. L. Liao, B. Ma, Z. Z. Zhang1, Q. Y. Jin, H. Wang, and J. P. Wang, Appl. Phys. Lett. 100, 142406 (2012).

[49] D. Goll and A. Breitling, Appl. Phys. Lett. 94, 052502 (2009).

[50] B. Ma, H. Wang, H. Zhao, C. Sun, R. Acharya, and J.P. Wang, IEEE Trans. Magn. ,46, 2345 (2010).

[51] C. J. Sun, D. Stafford, and R. Acharya, IEEE Trans. Magn., 46, 1795 (2010).

[52] A. Breitling, T. Bublat, and D. Goll, Phys. Status Solidi (RRL) **3**, 130 (2009).

[53] A. T. McCallum, P. Krone, F. Springer, C. Brombacher, M. Albrecht, E. Dobisz, M. Grobis, D. Weller, and O. Hellwig, Appl. Phys. Lett. 98, 242503 (2011).

[54] D. Suess, Appl. Phys. Lett. **89**, 113105 (2006).

[55] Z. Lu, P. B. Visscher, and W. H. Butler, IEEE Trans. Magn., **43**, 2941 (2007).

[56] A. Dobin and H. J. Richter, Appl. Phys. Lett., **89**, 062512 (2006).

[57] D. Goll, A. Breitling, L. Gu, P. A. van Aken, and W. Sigle, J. Appl. Phys. 104, 083903 (2008).

[58] T. J. Zhou, B. C. Lim, and B. Liu, Appl. Phys. Lett. 94, 152505 (2009).

[59] H. Wang, H. Zhao, O. Ugurlu, and J.P. Wang, IEEE Magn. Lett., 3, 450014 (2012).

Chapter 3. FEPT THIN FILM FABRICATION AND COMPOSITE STRUCTURE

3.1 Introduction

As mentioned previously, there is a trilemma in high density magnetic recording media design. To achieve high signal to noise ratio (SNR), a recording bit must contain a certain number of magnetic grains. Therefore, the grain size has to be reduced with the bit size. However, the thermal stability decreases with the grain size. Hence, magnetic materials with high magnetocrystalline anisotropy (K_U) are required to fabricate recording media. But high K_U leads to high switching field. To reverse a recording bit, writing field has to be larger than switching field, but the writing field is limited. Recently, $L1_0$ ordered FePt with (001) texture has been considered as the most promising candidate for future high density magnetic recording media due to its ultra-high magnetocrystalline anisotropy of ~ $7x10^7$ erg/cc.[1] However the writing capability of the recording head is among the most important concerns of future FePt recording media. Exchange coupled composite (ECC) media, which has two magnetic layers with different anisotropies and switching fields in the recording layer, was proposed theoretically[2,3] and implemented experimentally[4] as a promising solution to address this issue. Figure 3.1 shows a schematic comparison between conventional structure and ECC structure.

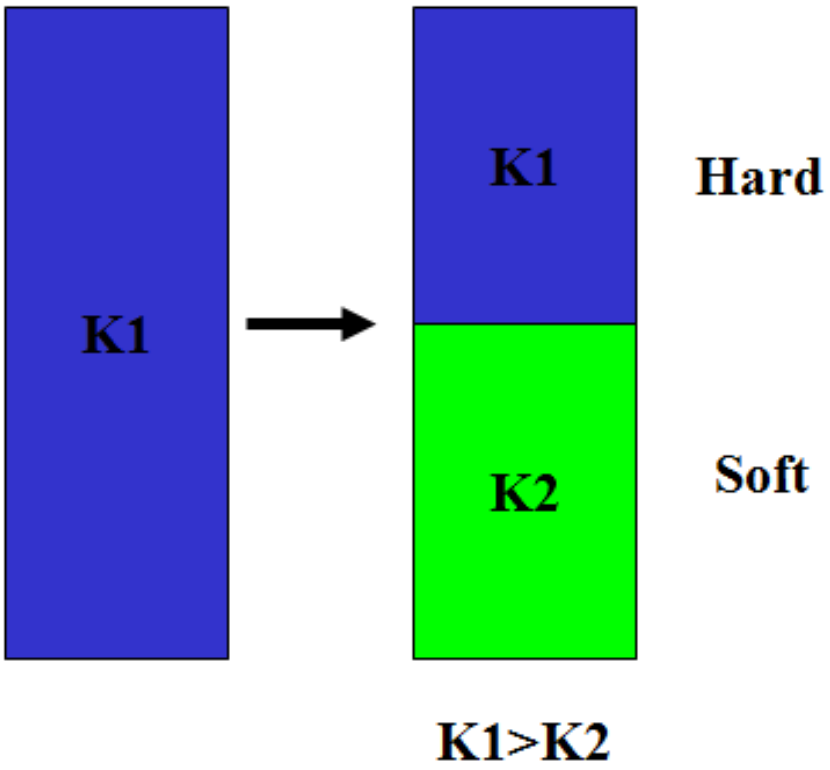

Figure 3.1 schematic comparison between conventional structure and ECC structure

The left figure in Figure 3.1 is a magnetic grain of conventional recording media with a uniform anisotropy along its columnar direction. For high density recording, it must have high anisotropy to against thermal fluctuation. In ECC media, as shown in the right figure of Figure 3.1, a single magnetic grain is divided into two parts with different anisotropy. One part is magnetically hard and the other part is magnetically soft. The hard part has high anisotropy and can keep the grain thermally stable, while the soft part will help reverse the magnetization of whole grain during writing process. However, even though the ECC structure can make a magnetic grain switchable, it also significantly increases the volume of a single grain, which is not preferred in recording media. Actually, in conventional structure, even keep the magnetic materials unchanged, the thermal stability can be doubled by doubling the volume of grain. The ECC structure has to be carefully designed to balance this dilemma. A gain factor was defined to evaluate the advantage of an ECC media to conventional media, [39]

$$\xi = \frac{2\Delta E}{M_S \bullet H_{SW} \bullet V} \quad (3.1)$$

Where ξ is the gain factor, ΔE is thermal barrier of magnetic reversal, M_S is saturation magnetization, H_{SW} is switching field, and V is the volume of grain. In conventional media, $\Delta E=K_U V=(M_S \cdot H_{SW}/2) \cdot V$. Therefore its ξ equals 1. But for ECC media, its real thermal energy barrier is larger than $(M_S \cdot H_{SW}/2) \cdot V$, and its ξ is larger than 1. Theoretically, the maximum ξ of ECC structure is 2. Although ECC structure was initially proposed as a simple columnar structure with two different layers, it is not limited to be this form. Goll et al. proposed several different types based on FePt/Fe structure[5], as shown in Figure 3.2.

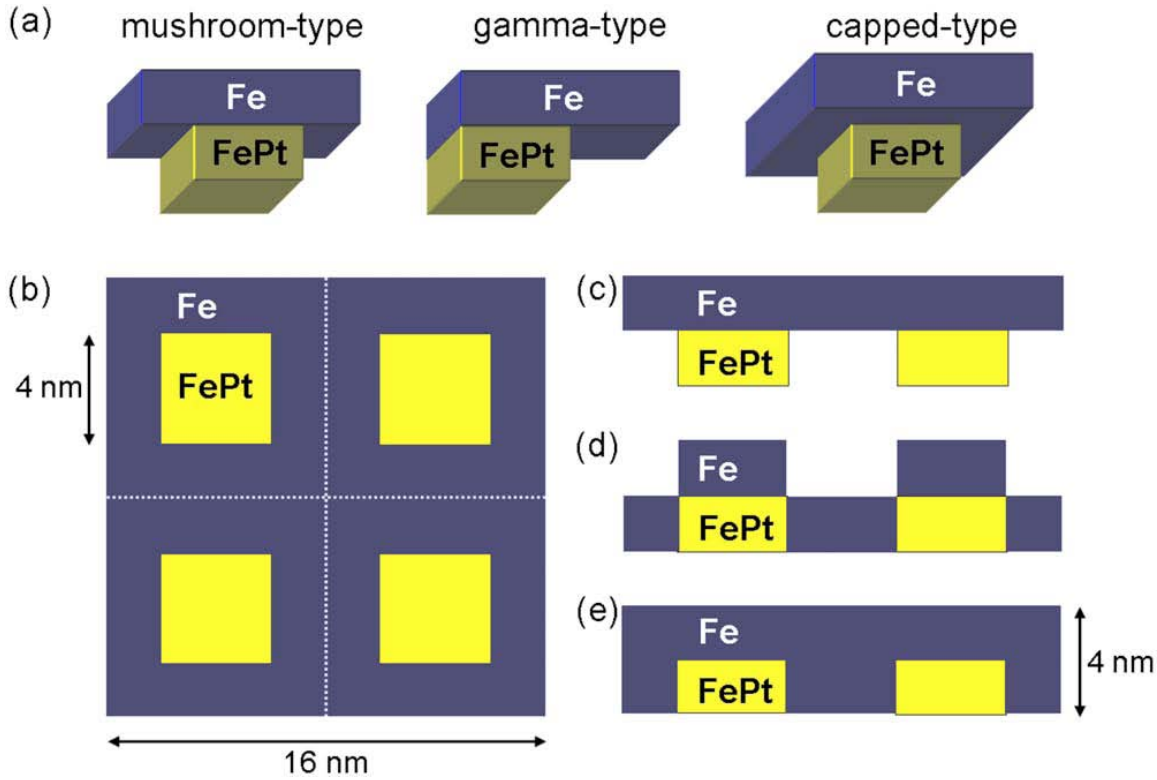

Figure 3.2 Different configurations of ECC structure (Ref. 5)

As shown in Figure 3.2 (a), depends on the shape of soft capping layer, a single ECC dot can be classified into mushroom-type, gamma-type and capped-type. In the view of whole media, the FePt dots can be connected using soft region, and can be classified based on how the Fe region surrounds FePt dots. Based on simulation results, they claimed that mushroom-type structure shows the best thermal stability ratio.

To further enhance the writability of composite structure, graded media was proposed. [6,7] In graded media, K_U value gradually changed along the grain columnar

direction. Domain wall assisted switching was also suggested with a similar consideration. [8] As mentioned above, an ECC grain is divided into two parts with different K_U value. But in a graded grain, there is no sharp interface to separate different regions. It gradually changed from magnetically hard to magnetically soft. Graded structure is expected to have better performance than ECC structure does. In other words, with proper design, graded structure can have higher thermal barrier but lower switching field than ECC structure does. It was theoretically that the gain factor of a graded media can be as high as 4^{55}. However, no experimental result approaches 4.

3.2 Core-shell type FePt ECC media

3.2.1 Experiment

Based on the ECC concept, a large coercivity reduction is seen in the FePt/Fe bilayers, FePt $L1_0/A_1$ stack[9, 10, 11], and ledge-type structure.5 As an extension of ledge-type composite, a simulation work indicates that half-filled nanopattern has the highest thermal barrier and its coercivity was decreased by a factor of 7. [12] However, because of the large volume of soft materials, its gain factor is only 1.23. Therefore, the thickness of ECC media is a drawback in magnetic recording. Is there any method to reduce its thickness but keep the advantage of switching field reduction? The answer is yes. The solution is making the soft layer cover all the surface of hard region, not only being placed on the top. This is so-called core shell structure.

Goh et al. theoretically studied this structure and provided simulation results. [13] Figure 3.3 schematically shows their model.

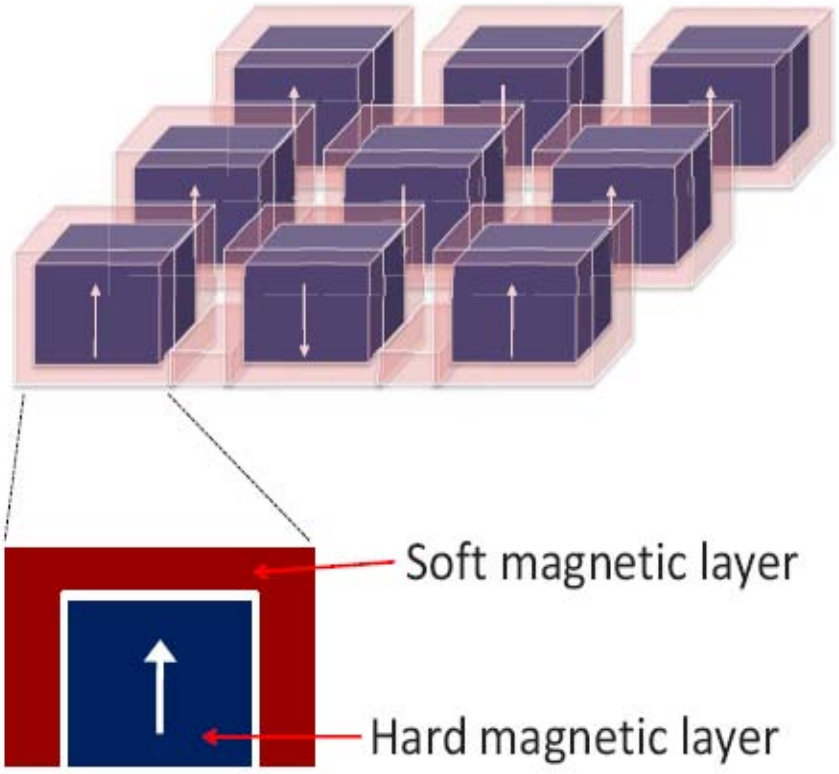

Figure 3.3 Micromagnetic simulation model in Ref. 13.

Their results showed that core-shell structure successfully caused significant reduction of switching field.

The advantage of core-shell structure was experimentally demonstrated and confirmed by Ma et al. [14]. In this work, we have prepared a set of FePt/Fe composite grain films with different Fe layer thickness. A core-shell type nanocomposite structure is developed. The switching field, thermal stability, and gain factor are studied. Compared to the original bi-layer ECC structure, the height of composite dot can be reduced to meet the requirement of recording media. In addition, a modified formula for gain factor is proposed to demonstrate the advantage of core-shell ECC structure over original ECC structure.

The $L1_0$ FePt/Fe ECC films were prepared on single crystal MgO substrate by our 8-target magnetron sputtering system. At first, substrate was heated to 450 °C for one hour. Then, FePt thin film was co-sputtered from elemental targets while maintain the high temperature. After the deposition, the substrate was cooled down to room temperature,

and finally an Fe layer was deposited on FePt. The nominal thickness of FePt layer is fixed at 3.2 nm. The composition of FePt layer was $Fe_{54.8}Pt_{45.2}$. The nominal thickness of Fe capping layer varied from 2 nm to 12 nm.

Since there is large difference between the surface energy of FePt and MgO, the thin FePt layer will form island structure to reduce the total surface energy, while deposited on MgO surface at high temperature.

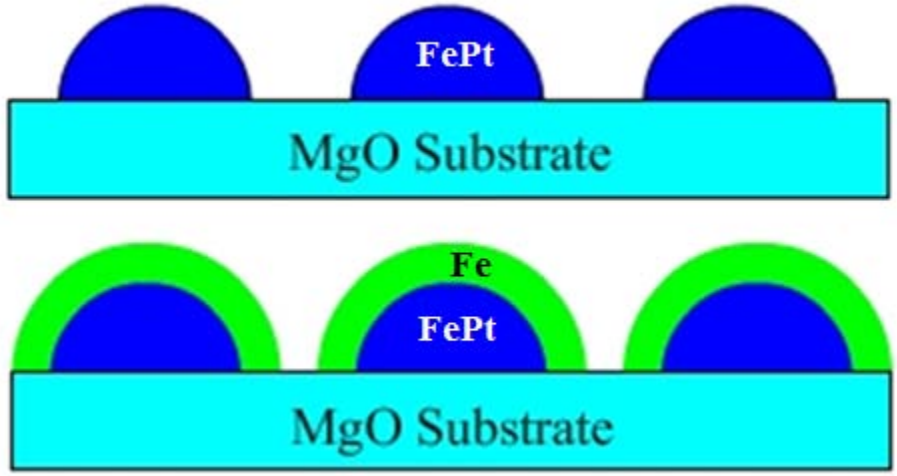

Figure 3.4 schematic figure of the morphology of FePt and FePt/Fe films on MgO substrate.

Figure 3.4 shows the schematic figure of the morphology of FePt and FePt/Fe films on MgO substrate. FePt film forms isolated islands. Fe layer tends to cover the surface of FePt islands, rather than the exposed surface of MgO substrate, because FePt has higher surface energy than MgO does. Thus the core-shell structure is created.

The structural properties are measured by x-ray diffraction (XRD), scan electronic microscopy (SEM) and high resolution transmission electronic microscopy (HRTEM). Chemical ordering parameter S of FePt is calculated by the intensity ratio of (001) peak to (002) peak, which theoretic value is 1.9 [15]. S=1 presents fully ordered, and S=0 completed disordered. The magnetic properties are measured by superconductor quantum interfere devices (SQUID) and vibrating sample magnetometry (VSM). Film composition is measured by Rutherford backscattering (RBS).

3.2.2 Results and discussion

Figure 3.5 shows the XRD θ-2θ scan spectra of the core-shell type ECC samples, including the pure FePt sample. Strong FePt (001) peaks can be observed in all films whose Fe layer thickness varies from 0 to 12 nm. According to the intensity ratio of (001) peak to (002) peak, the chemical ordering parameter S of $L1_0$ FePt is about 0.8.

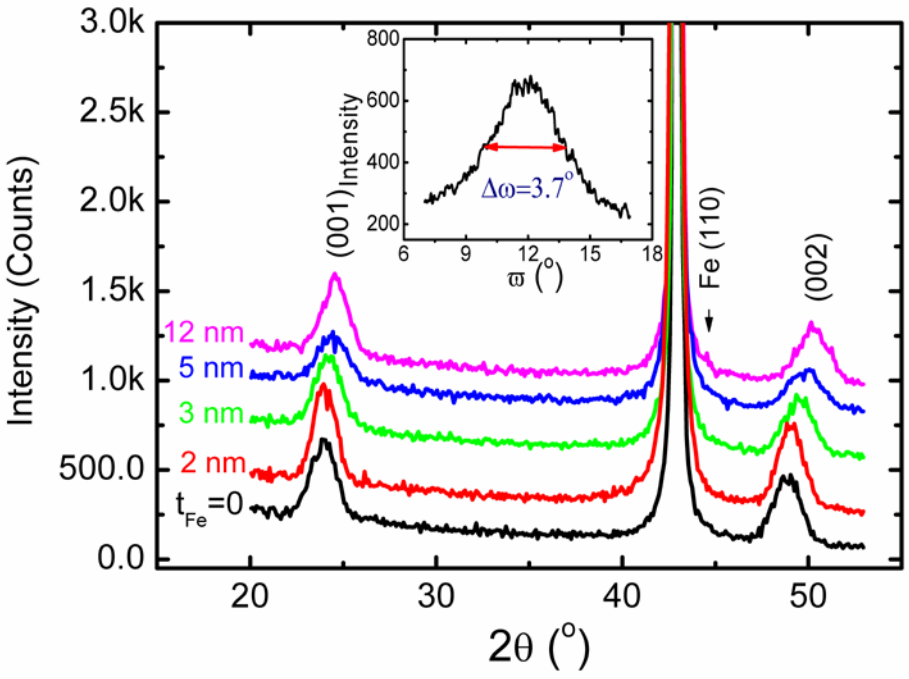

Figure 3.5 XRD θ-2θ scan spectra of the core-shell type ECC samples.

Both TEM images in Figure 3.6 (a) and SEM image inset reveal a island structure of the pure FePt film. Average grain size of these FePt islands is about 14.2 nm, and the height is 6.95 nm, which is calculated by a number of islands from the TEM cross-section images. Moreover, there is a large distance of 7 nm among them. When a 3-nm-thick Fe layer deposited on the FePt, it follows the morphology of FePt islands, and surrounds islands (Figure 3.6 (b)). The inset high resolution image shows that FePt islands are enclosed by Fe layer. Moreover, the Fe thickness is 3.05 nm, which is almost as same as the nominal thickness. Compared with conventional ECC structure, the core-shell structure has larger interface between the hard and soft regions. It is expected that the

core-shell structure has a larger domain wall area when an opposite external field is applied.

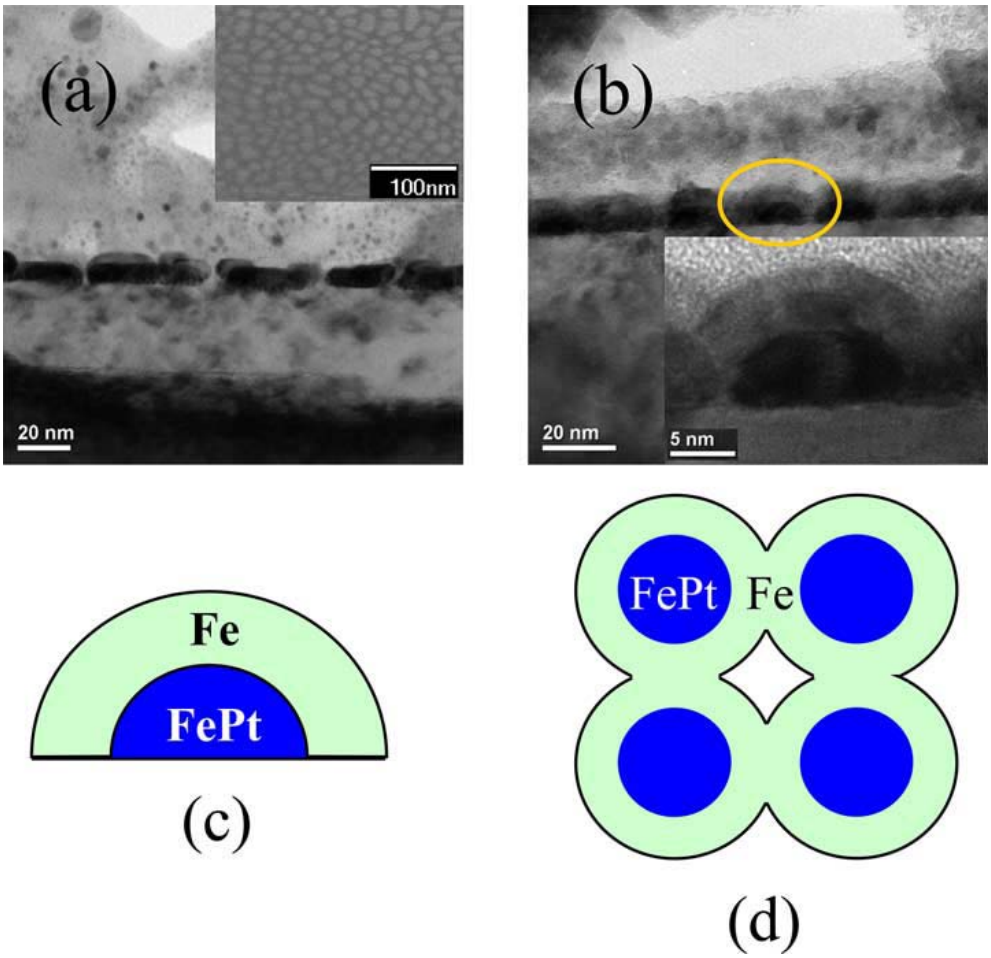

Figure 3.6 TEM cross-sectional images of (a) FePt and (b) FePt/Fe(3nm); (c), (d) schematic figures of core-shell structure

The core-shell type composite structure is again schematically illustrated in Figure 3.6 (c) and (d). The FePt island is enveloped by an Fe layer (Figure 3.6 (c)). When the Fe layer is thin as in the case of 3-nm-thick Fe, the island size of the composite nanostructure increases, but they are still isolated. The composite island size gradually increases with the increases of Fe layer thickness. When the Fe layer thickness exceeds 5 nm, adjacent islands start to connect each other (Figure 3.6 (d)).

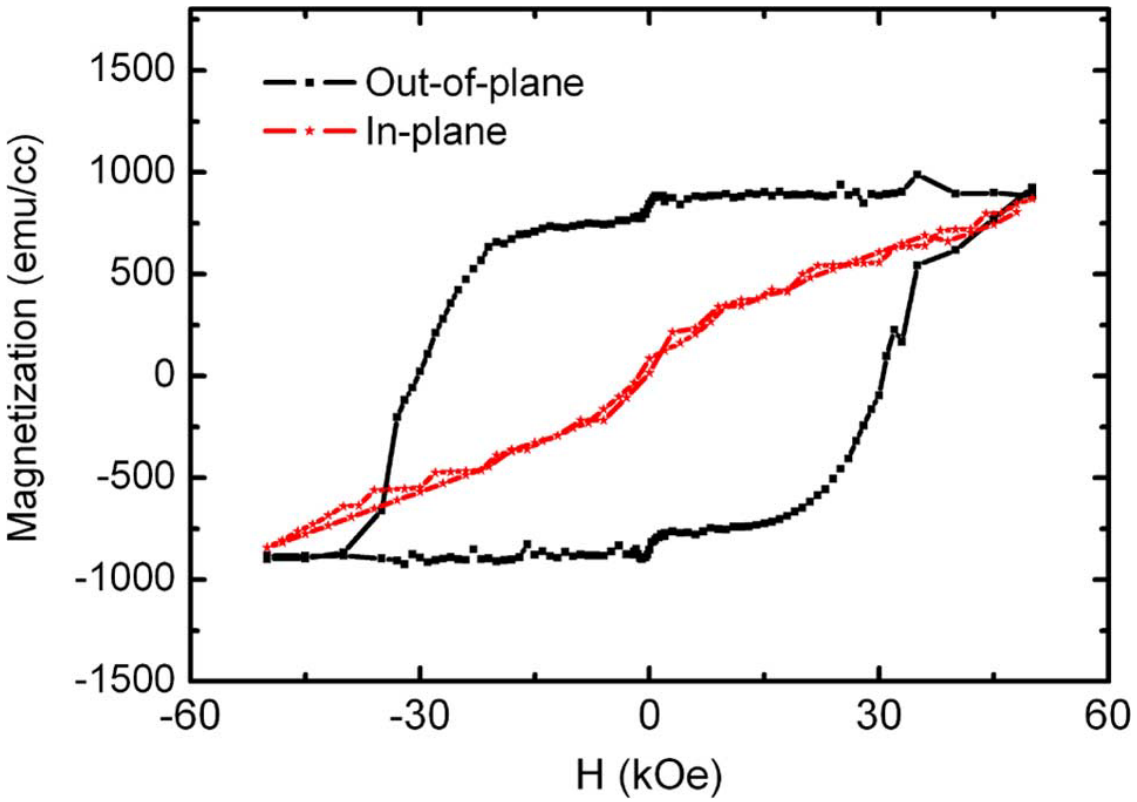

Figure 3.7 hysteresis loop of pure FePt film.

Figure 3.7 shows the hysteresis loop of pure FePt film whose nominal thickness is about 3.2 nm. The magnetic easy axis is along the normal direction of the film plane. Its coercivity is about 30.6 kOe, and the anisotropy field is beyond 40 kOe. As expected, coercivity decreases greatly when a thin Fe layers cover the FePt islands, as shown in Figure 3.8.

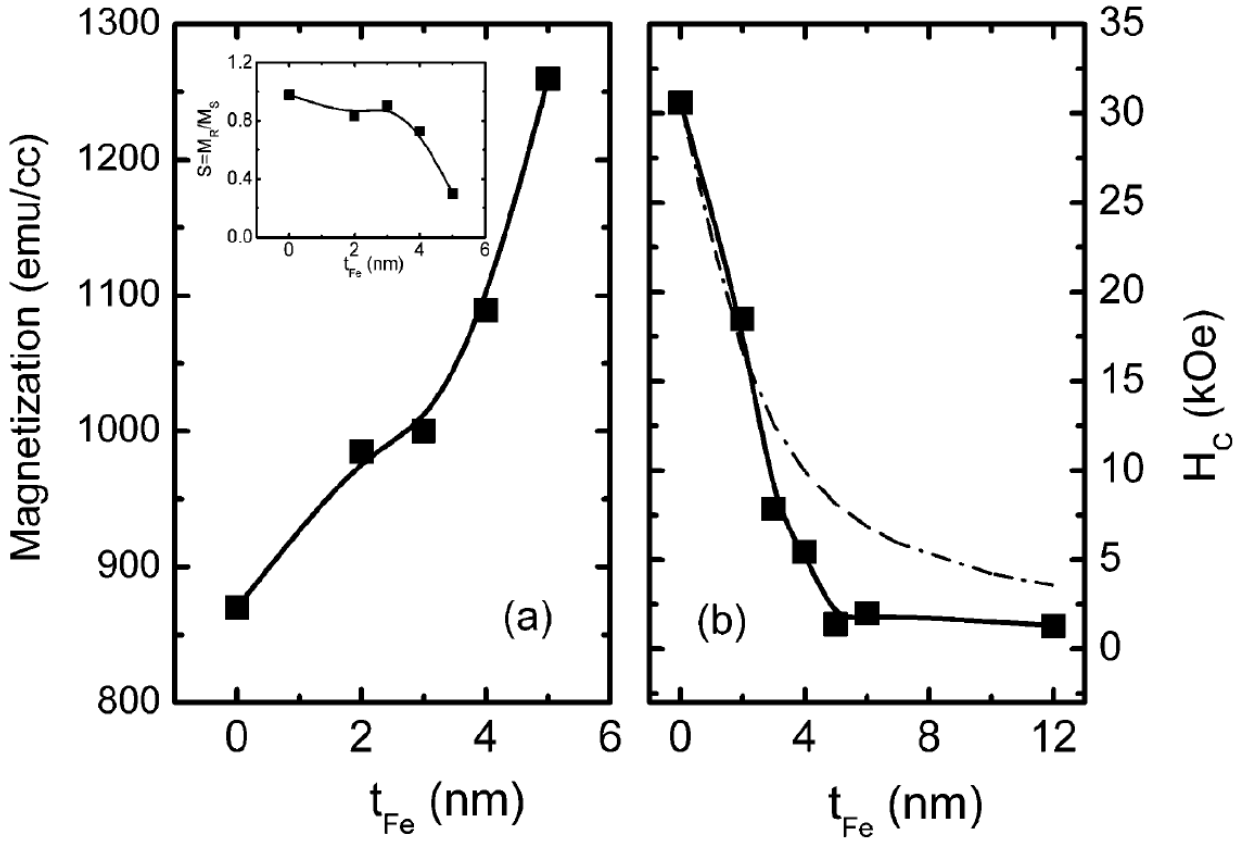

Figure 3.8 The Fe layer thickness dependence of magnetic properties: (a) the saturation magnetization. The inset is the square ratio of magnetization; (b) the coercivities.

Figure 3.8 shows the dependence of magnetic properties of core-shell- type L10 FePt/Fe composite granular film on the thickness of Fe layer. Coercivity is 7.85 kOe for FePt grains with a 3-nm-thick Fe layer, 1.45 kOe for FePt with a 5-nm-thick Fe. According to the domain wall motion assisted magnetic recording (DWAMR) model for ECC media, a power law could be used to describe the reduction of coercivity, and an exponent 1.38 is suggested by the experimental fitting, which is indicated in the figure by the dotted line[10]. However, their curve cannot simulate the current coercivity reduction. The reason is the core-shell structure has large domain wall.

As described in the DWAMR model, the domain wall gradually compressed to the interface between the hard and the soft material, and effective domain wall energy E_T accumulates, including exchange-coupling energy, anisotropy energy and Zeeman energy in the wall. At the point where the stored energy exceeds the domain wall energy of the hard region, the domain wall injects into the hard region from the interface, resulting in magnetization reversal. In an ideal cubic core-shell type composite structure, there are

four additional surfaces for the domain wall formation, which increase the effective energy ET by a factor of 5. Thus, magnetization reversal can happened at low switching field. Furthermore, wall energy decreases due to wall shrinking after its injection, and is consistent with the reversal. Hence, drastic coercivity reduction is expected.

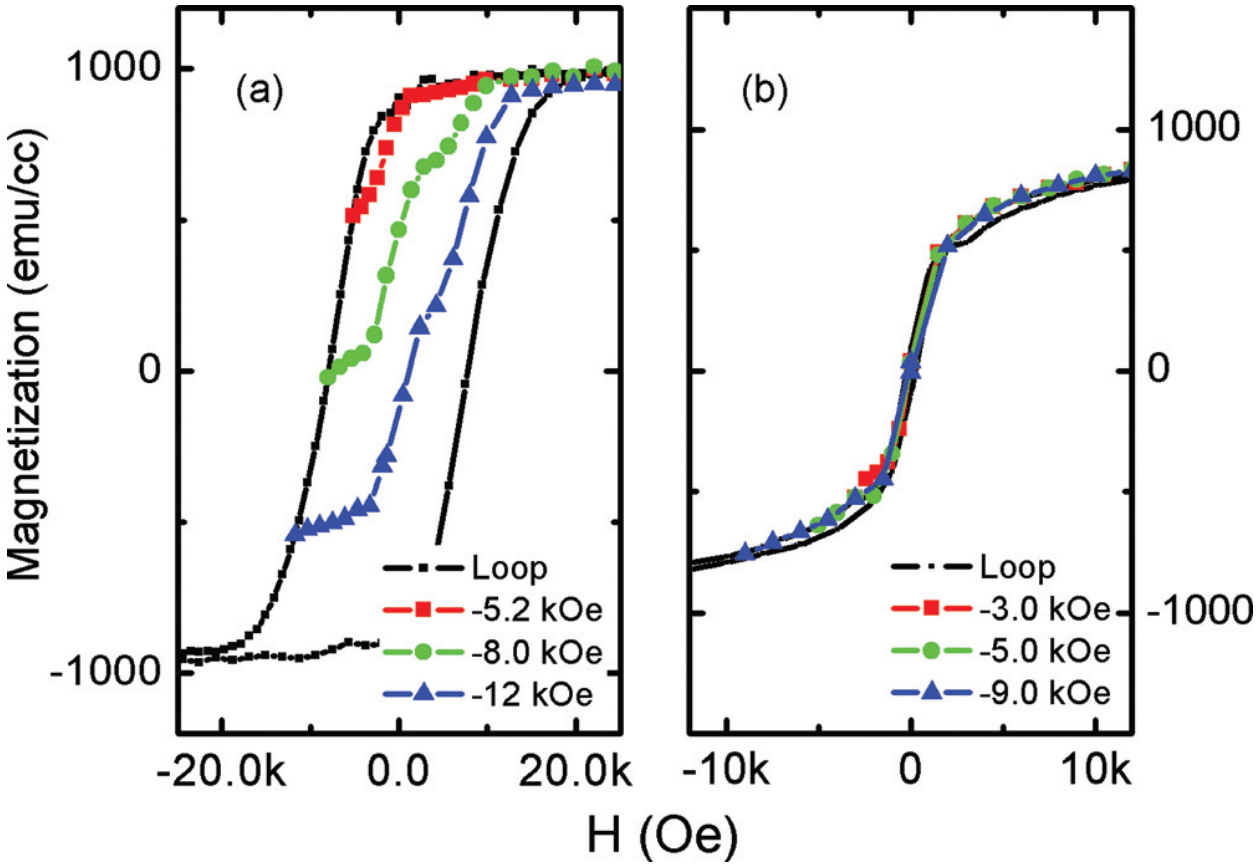

Figure 3.9 The recoil curves of FePt/Fe (3nm) nanocomposite: (a) Out-of-plane, and (b) In-plane. The fields labeled in the figures are the applied fields that start the measurements.

The ECC characteristics of magnetization reversal are demonstrated by the recoil curves in Figure 3.9 for FePt(3.2 nm)/Fe(3nm) core-shell type composites. When the opposite field is decreased from 5.2 kOe, a sharp magnetization increase which is close to hysteresis loop along perpendicular direction is observed in Figure 3.9 (a), indicating the switching mechanism is dominated by the reversible switching. Just as the exchange spring magnet, the reversed magnetization of soft Fe region returns back when the applied field is removed since magnetization of FePt grains has not been reversed.[15,16] When the opposite field is a little beyond the coercivity, a slow magnetization increase appears in the second recoil curve upon removal of the applied field, and then a sharp increase in magnetization follows. A kink marks the different variation. Obviously, the

slight magnetization increase corresponds to the reversed rotation of FePt and decompressing of domain wall, while the sharp increase is due to the Fe rotation. When the field decreased from a larger field (-12 kOe), the kink occurs at the similar applied field as that of the second recoil curve. Magnetization increases in the case much slower than in above cases. Figure 3.9 (b) shows the recoil curves along in-plane direction. After the opposite fields are removed, all the magnetization reversals are reversible and uniform. The results indicate that the easy axis of the FePt/Fe is close to the perpendicular

The energy barrier, which characterizes the thermal stability of recorded information, would decrease with the addition of a soft magnetic layer[5,17,18]. In general, measured magnetization reversal fields depend not only on temperature, but also on the duration of an applied field. The duration of an applied field, which opposes the initial saturation field, can be used to measure the energy barrier according to the Sharrock equation:

$$H_C(t) = H_0\left\{1 - \left[\frac{k_B T}{\Delta E} ln\left(\frac{t f_0}{ln2}\right)\right]^{1/\gamma}\right\} \quad (3.2)$$

where H_C (t) is the coercivity at the switching time t. H_0 is the intrinsic switching field. $f_0 = 10^{10}$ Hz is the attempt frequency. The model is demonstrated effectively for exchange-coupled composite media, replacing ΔE by ($K_H V_H + K_S V_S$). Here, the indexes H and S denote hard and soft regions, respectively. The exponent of the power decreases with the addition of the soft layer. In our measurements, γ=1.5, 1.36 and 1.33 are used for FePt, FePt/Fe (3nm) and FePt/Fe (5 nm), respectively. The dependence of the switching field of FePt/Fe (3 nm Fe) ECC media on time is shown in Figure 3.10.

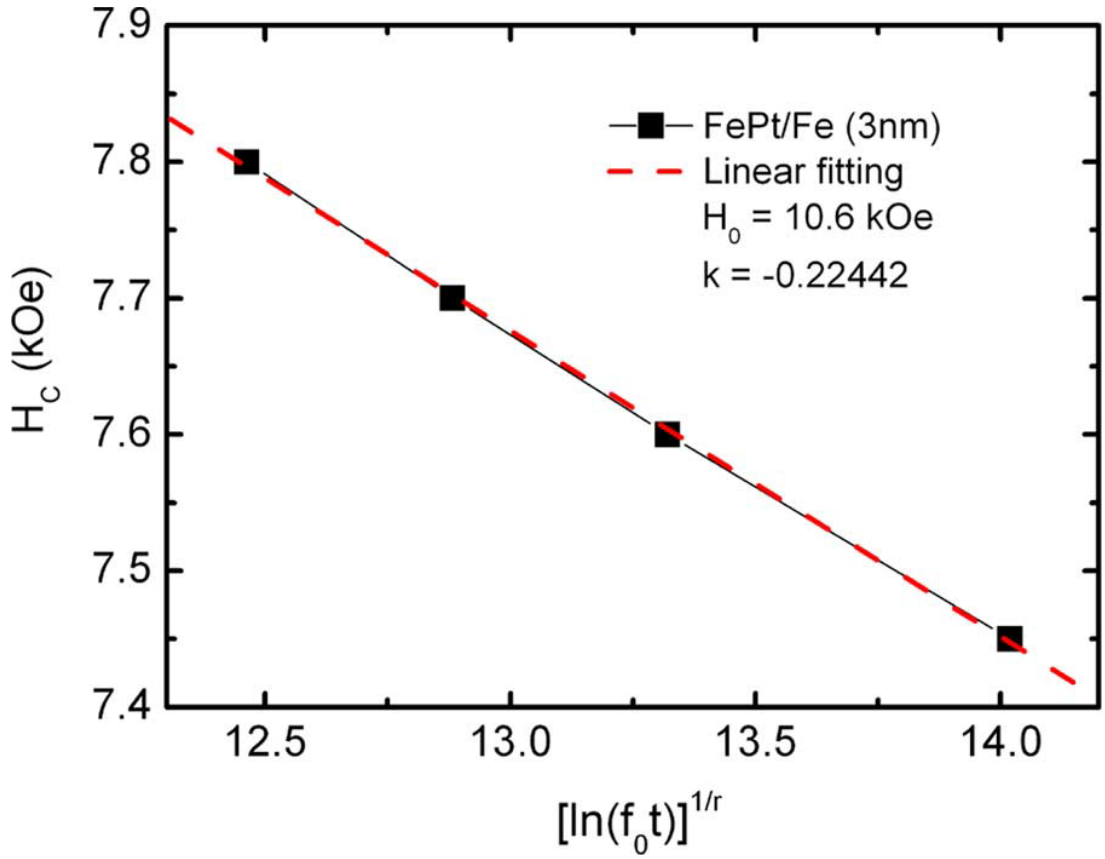

Figure 3.10 Time dependence of reverse applied field of FePt/Fe (3 nm) ECC media. The field applied opposed to saturation state, is a little smaller than coercivity measured at the normal sequense. The time is the duration through which the net magnetization is zero.

The switching field is about 10.6 kOe. Then, the energy barrier ΔE for 3-nm FePt island-like film is 216 k_BT. When FePt islands are covered by an Fe layer, the energy barrier decreases to 172 kBT and 95 kBT for Fe layer thicknesses 3 nm and 5 nm, respectively.

In the definition of gain factor ξ, both the energy required for magnetization reversal and the volume effect are considered. The gain factors of FePt/Fe core-shell type composite structure, are 1.45 and 1.82 for Fe thicknesses of 3 nm and 5 nm, respectively. However, unlike the convention ECC structure, in a core-shell type composite dot, just a small part of the soft region is placed on top of hard region. Large reduction of coercivity can be achieved in core-shell structure while its thickness does not significantly increase. Therefore the gain factor should be re-defined in the view of the real-world application. Considering the change of island's height only, the gain factor can be written in the following form, using the energy required for magnetization reversal of the hard region, and the thickness of composite media:

$$\xi = \frac{\Delta E}{M_S^H H_{SW} V^H} \cdot \frac{t^H}{t^S + t^H}$$

(3.3)

Then the modified gain factor is 1.89 and 3.55 for FePt/Fe with the Fe layer thickness of 3 nm and 5 nm, respectively.

3.2.3 Tilted axis

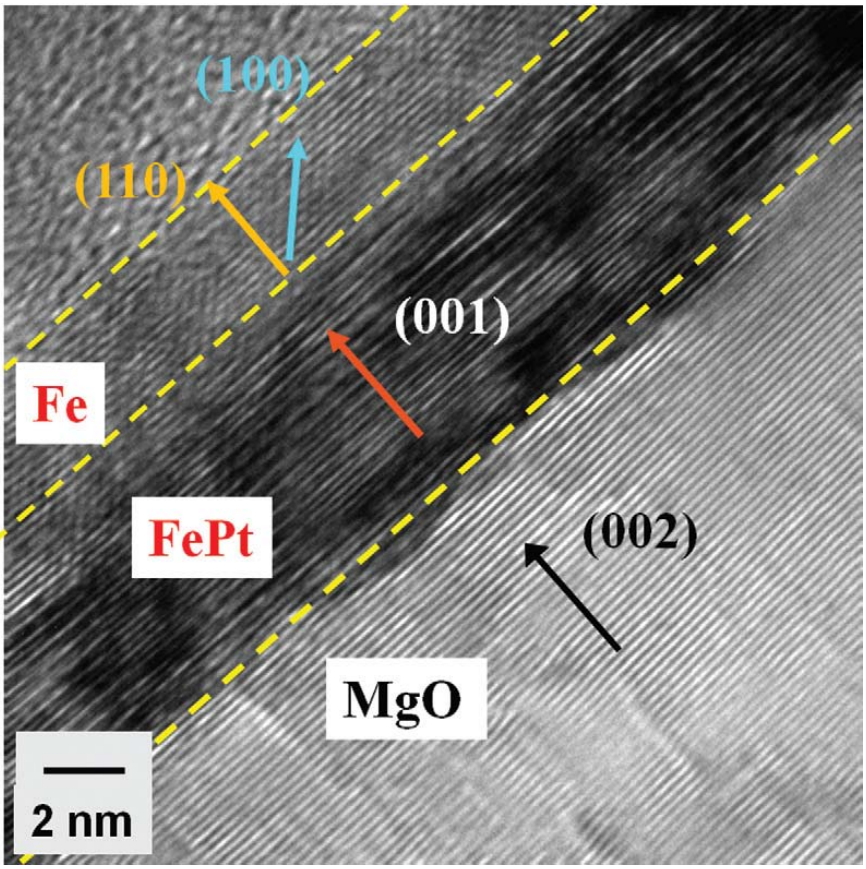

Figure 3.11 high-resolution cross-section TEM image of an FePt/Fe(3 nm) core-shell type composite island.

Figure 3.11 shows the high-resolution cross-section TEM image of an FePt/Fe(3 nm) core-shell type composite island. The FePt (001) planes are clearly seen, epitaxial growing on MgO (200) planes. However, Fe (110) planes whose spacing is 0.202 nm grows along the film normal direction on FePt (001) plane.

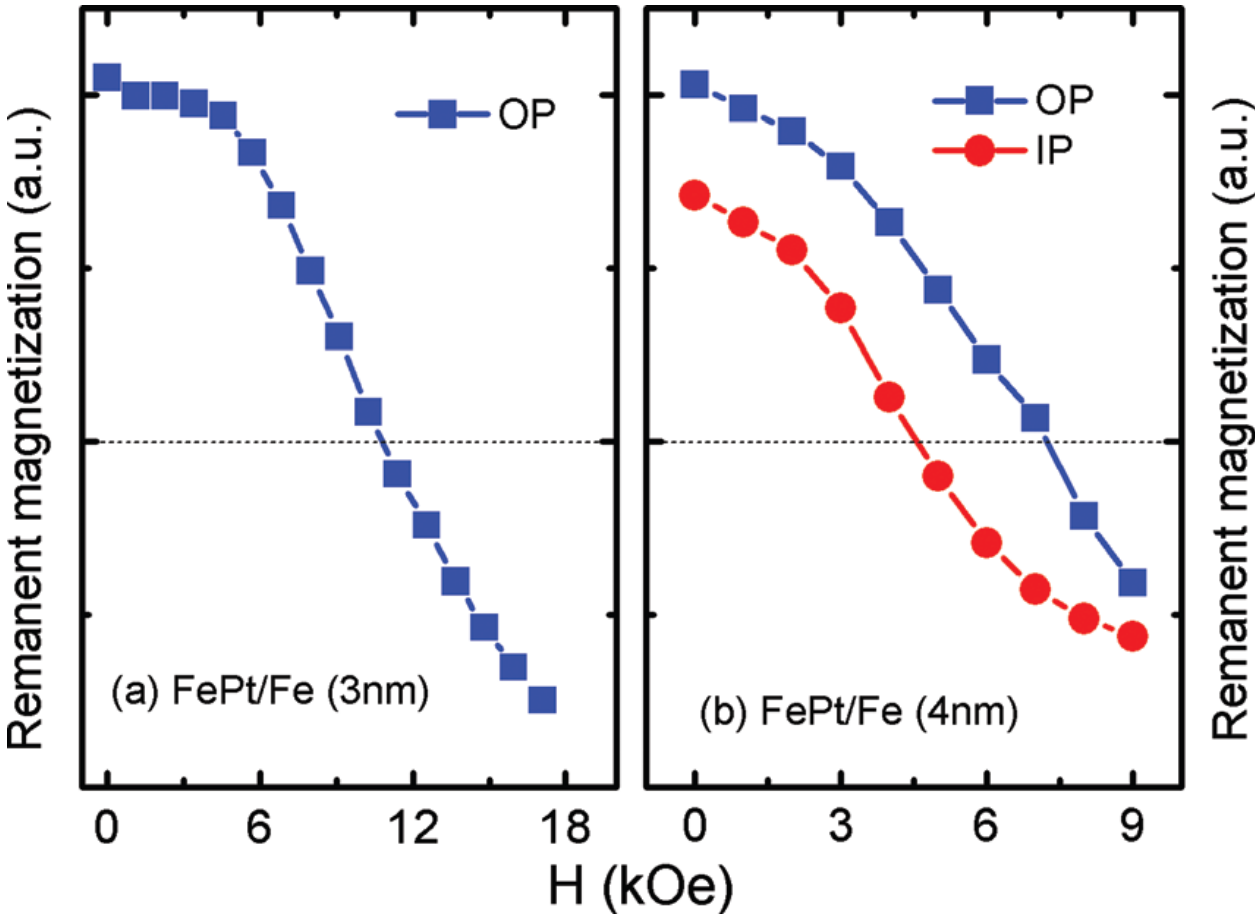

Figure 3.12 the remanence curves of the core-shell type FePt/Fe with Fe thickness of (a) 3 nm and (b) 4 nm.

Figure 3.12 (a) and (b) shows the remanence curves of the core-shell type FePt/Fe with Fe thickness of 3 nm and 4 nm, respectively. For the FePt/Fe island with 3-nm-thick Fe layer, the in-plane remanence is almost zero. However, there is an obvious remanence curve along in-plane direction for the FePt/Fe with Fe thickness of 4 nm. It implies that the effective easy axis tilts from the normal direction in the sample with thick soft layer.

In order to indentify the tilted easy axis in the core-shell nanocomposite, the angle dependences of remanent magnetizations along both the film normal and in-plane direction are measured simultaneously by using two couples of coils in a Vector VSM without any applied field. For the FePt/Fe(3 nm) core-shell islands, the maximum of the remanence is not exactly along the normal direction, but an angle of about 10o from the film normal, shown in Figure 3.13.

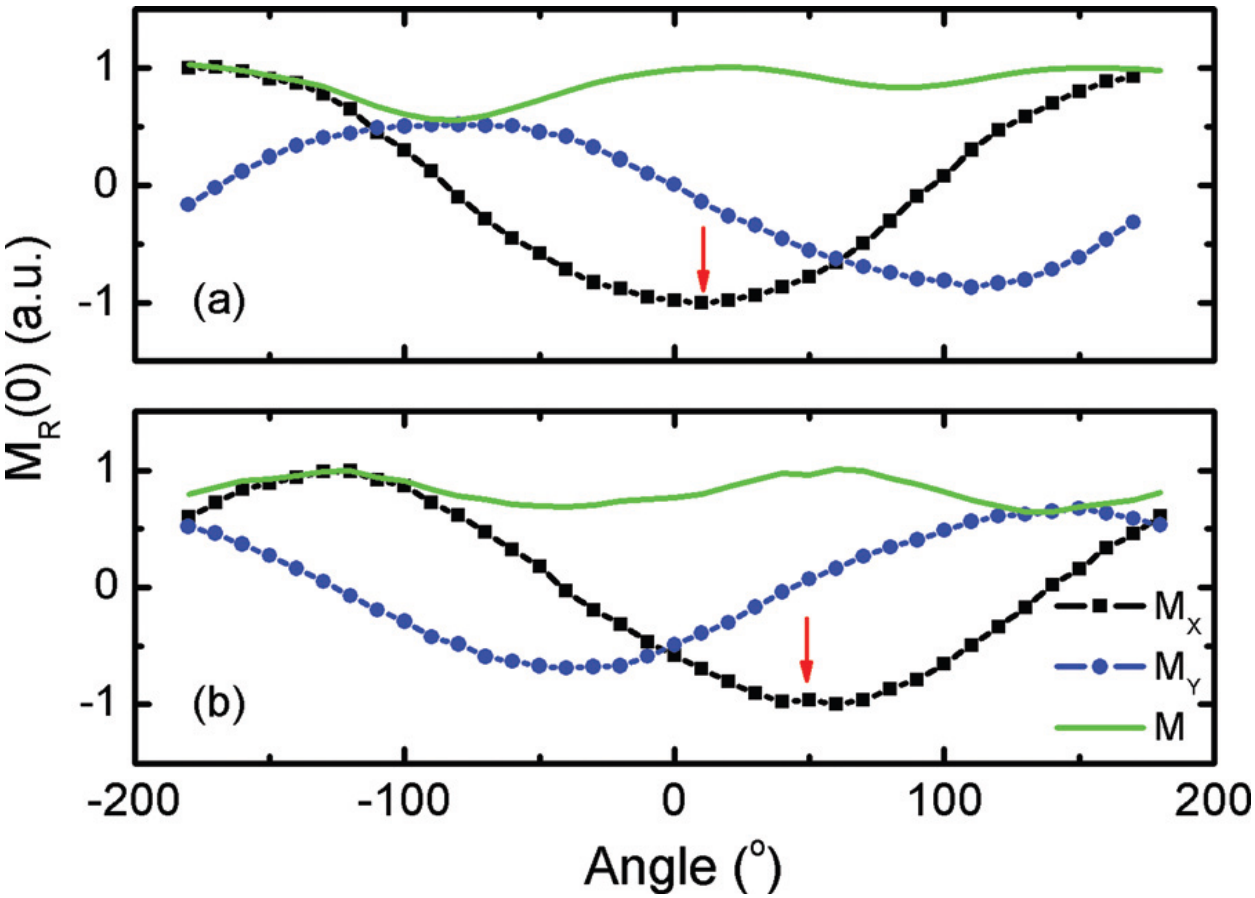

Figure 3.13 The dependence of remanent magnetization on the angle between the film normal and the direction of magnetic field in a VSM: (a) FePt/Fe(3 nm) nanocomposite; (b) FePt/Fe(5 nm) nanocomposite. The sample rotates against the magnet, and no field is applied. M_X represents the normalized magnetization along the film normal, and M_Y represents the normalized in-plane magnetization. Besides, the weak variation of total magnetization M is due to the calibration error between X and Y coils. The original direction of the film normal is set as 0. The easy axis direction is marked by the red arrow in both figures.

As described before, the FePt grains have good (001) orientation and highly chemical ordering. Its magnetization vector aligns along the perpendicular direction. Through exchange coupling the magnetization vector of Fe layer should follow that of FePt, along the film normal also. The remanence derivation indicates that the easy aixs of the FePt/Fe composites tilted from the normal direction. Larger derivation of 50° is seen in the FePt/Fe nanocomposite with thicker soft layer (5 nm). In the case, the easy axis tends to the film plane.

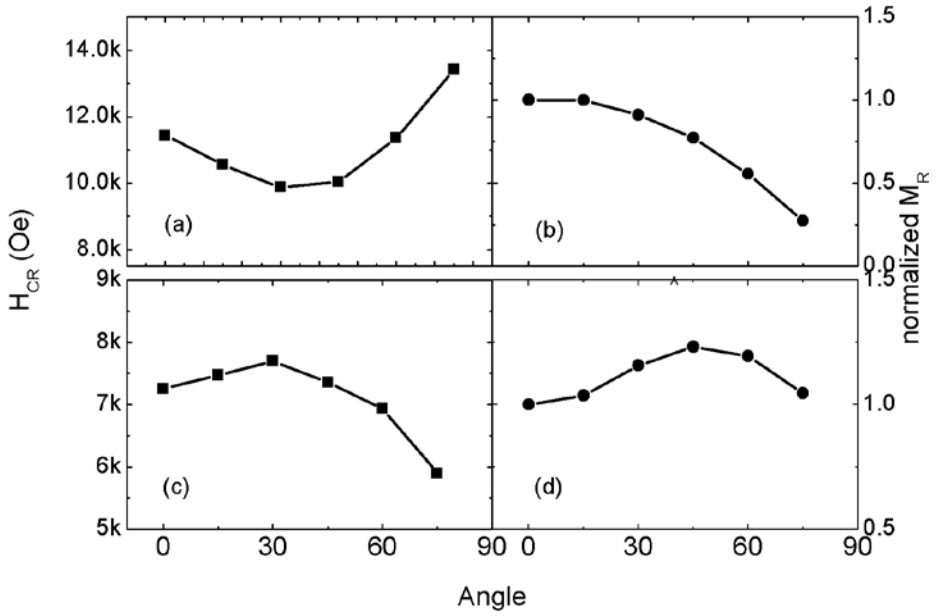

Figure 3.14 The dependence of remanent coercivity H_{CR} (left column) and magnetization M_R (right column) on the angle between the film normal and applied field, for FePt/Fe(3nm) (up row) and FePt/Fe(4nm) nanocomposite (loe row): (a) H_{CR} of FePt/Fe(3nm); (b) M_R of FePt/Fe(3nm); (c) H_{CR} of FePt/Fe(4nm); (d) M_R of FePt/Fe(4nm).

The oblique of easy axis is confirmed by the angle dependence of remanent coercivity and magnetization derived from the DCD curves (Figure 3.14). The DCD curves are measured upon different angles between the applied field and the film normal. For FePt/Fe with 3 nm Fe layer, as shown in Figure 3.14 (a), the remanent coercivity gradually decreases with the angle, reaching the minimum at 30° of 20% lower than that along the film normal, and then increases again. This is a characteristic of the exchange coupled media. Moreover, the remanence is kept until the angle increases up to 15°, and then decreases with the angle increase as shown in Figure 3.14 (b). The easy axis should be near the perpendicular direction. When the Fe layer thickness increases to 4 nm, the remanent coercivity firstly increases with the angle, reaching the maximum, and then it decreases (Figure 3.14 (c)). This is a typical feature of media with tilted easy axis[19].

The reason for the easy-axis tilt is due to the demagnetized energy and anisotropy energy. The demagnetized field is about 6 kOe, estimated by the geometry and magnetization as a homogenous dot. On the other hand, the normal direction is not the easy axis of Fe layer with (110) orientation. Hence, the effective anisotropy is not along the film normal as that of $L1_0$ FePt only, and then remanent magnetization should tilt

from the normal direction to decrease the total energy. The tilted easy-axis observed in the core-shell exchange coupled nanocomposite is assumed to initiate the nucleation and contribute to the drastic coercivity reduction.

In conclusion, Table 3.1 summarizes the experimental results of core-shell type FePt/Fe ECC media, including the original (ξ) and modified gain factor (ξ').

Table 3.1 The magnetic properties and gain factors of FePt/Fe bilayers. Two kinds of gain factor ξ are obtained. $\xi_{\Delta E}$ by measured energy barrier, and ξ' by the modified formula

FePt/Fe	**M_S** (emu/cc)	**H_{SW}** (kOe)	**ΔE** (k_BT)	**V** (10^3 nm^3)	***t*** (nm)	**$\xi_{\Delta E}$** (ECC)	**ξ'** (NP)
t_{Fe}=0	870	39.7	216	1.18	6.95	1.00	1.00
t_{Fe}=3 nm	1010	10.6	172	2.08	9.20	1.45	1.89
t_{Fe}=5 nm	1260	2.02	95	3.86	11.6	1.82	3.55
FePt/Fe	**M_S** (emu/cc)	**H_{SW}** (kOe)	**ΔE** (k_BT)	**V** (10^3 nm^3)	***t*** (nm)	**$\xi_{\Delta E}$**	**ξ'**

Core-shell structure could be potentially used in bit patented media (BPM), since there are sufficient spacing among the patterned bits. And the modified gain factor (ξ') can be used to evaluate the performance of core-shell type ECC BPM.

3.3 Spontaneously formed FePt graded granular media

So far, although CoCrPt composite media can be fabricated by varying the thickness of CoCrPt layer [20], the FePt composite media has only been fabricated by adjusting either the substrate temperature or varying the magnetic layer composition during the thin film deposition process [21,22,23,24,25,26,27,28]. Both of these two methods are time-consuming and not compatible with current hard disk media production line. Also, with these methods, it is very difficult to maintain the columnar grain structure for the graded magnetic grains. A one-step process to deposit the magnetic layer is highly demanded for the fabrication of graded media. The inter-diffusion of Mn and Cr was found in the film structure of CoCrPt/CrMn and CoCrPt/Cr, and influenced the magnetic properties of the

CoCrPt[29]. In this work, we reported a spontaneous layer inter-diffusion process to fabricate FePt graded granular media, by utilizing the compositionally graded interface between ultra thin FePt recording layer and Pt interlayer.

A relatively high deposition temperature (350 °C), which was set just around the minimum level of $L1_0$ FePt ordering temperature, enhanced the inter-diffusion between FePt and Pt layers and thus created a $Fex Pt_{100-x}$ graded structure. The graded magnetic layer was formed in one step and no multiple soft magnetic regions are required. More importantly, the switching and saturation field of the media are 5.5 kOe and 12 kOe, respectively, which are recordable using the available recording head. A large gain factor as high as 3.74 was achieved for such media with the thermal barrier around 160 kBT. It can be potentially used in conventional perpendicular recording systems or future bit patterned media (BPM) systems without integrating thermally assisted magnetic recording[30,31].

3.3.1 Experiment

Thin films with the structure of Glass substrate/Al_2O_3(3 nm)/Ta(2 nm)/RuAl(20 nm)/Pt(x nm)/FePt(y nm)/Cu(2 nm) were prepared using a DC magnetron sputtering system at 350 °C. The role of the Cu top layer was to diffuse into grain boundaries of FePt layer and exchange-decouple the FePt grains[32]. Co-sputtering of elemental targets was used to prepare both RuAl and FePt layers. The base pressure of the sputtering chamber was better than 2×10-7 torr and the substrate was heated to 350 °C before sputtering. The atomic composition ratio of FePt and RuAl layers was both 50 to 50. Two sets of samples were fabricated. In one set, the FePt layer thickness varied from 4 to 6 nm while keeping Pt layer at 7 nm. In the other set of samples, the Pt layer thickness varied from 7 to 12 nm while keeping FePt at 6 nm. The crystallographic texture of the samples was measured by an x-ray diffractometer (XRD) with Cu Kα radiation. The magnetic properties were tested using a vibrating sample magnetometer (VSM). The microstructure was observed with a FEI Tecnai F30 high-resolution (scanning) transmission electron microscope ((S)TEM). The Fe composition profile was analyzed

using the electron energy loss spectroscopy (EELS) on the F30 TEM. The sputtering rates were calibrated using TEM cross-sectional analysis.

3.3.2 Results and discussion

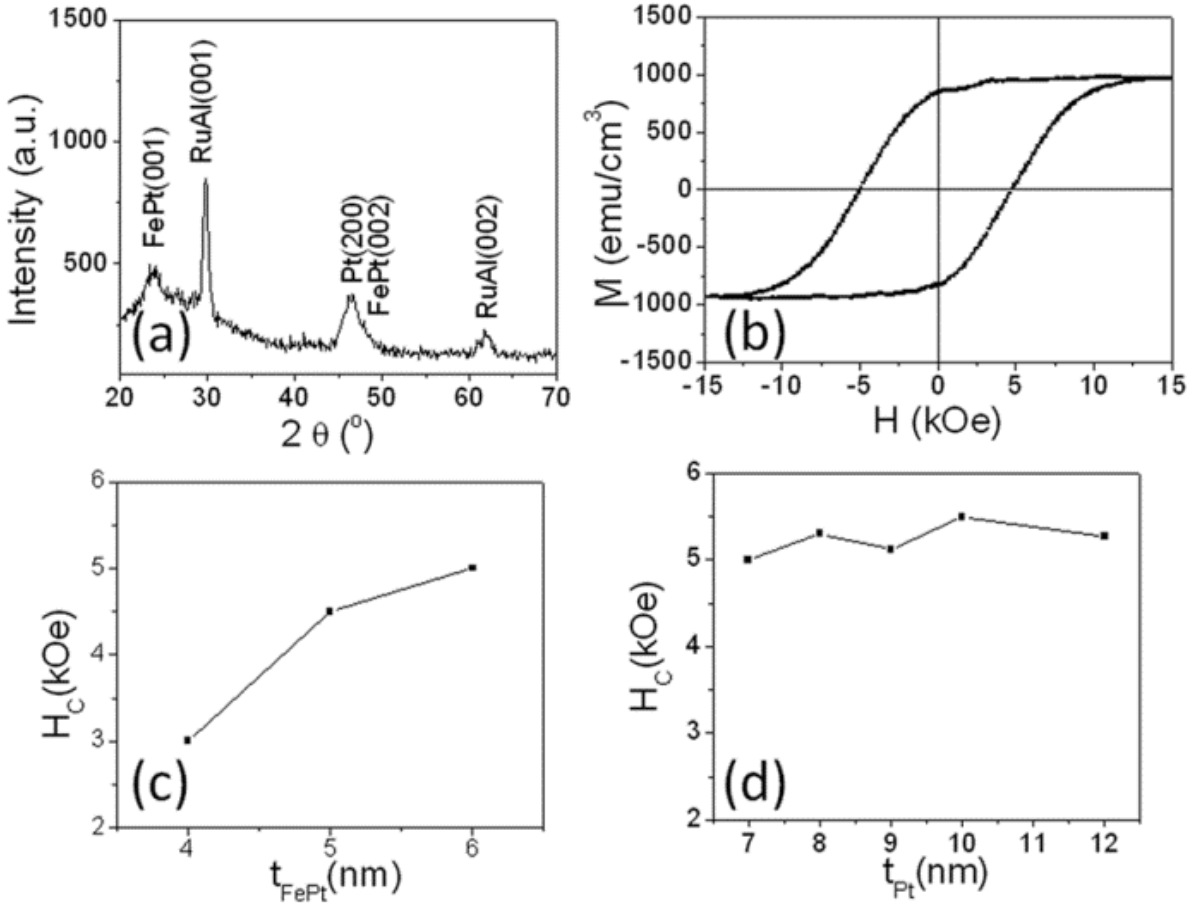

Figure 3.15 (a) XRD spectrum and (b) Out-of-plane hysteresis loop of the sample Pt(7 nm)/FePt(6 nm); (c) Coercivity vs. FePt thickness while keeping Pt as 7 nm; (d) coercivity vs. Pt thickness while keeping FePt as 6 nm. We only listed the magnetic layer in figure captions.

Figure 3.15 (a) shows the XRD spectrum of the sample Pt(7 nm)/FePt(6 nm). All the peaks were contributed by the FePt, Pt, and RuAl with good (001) texture. The out-of-plane hysteresis loop was shown in Fig. 1 (b). The coercivity is 5 kOe and the remnant squareness is 0.88, which is required to approach 1, in order to reduce the DC noise. [33] As designed, the Cu capping layer might diffuse into the grain boundary of the FePt grains,

and result in a hysteresis loop with a typical exchange-decoupled behavior. Further evidence on the exchange-decoupling of FePt grains will be provided in later section.

Keeping the Pt interlayer thickness as 7 nm, coercivity vs. FePt thickness (t_{FePt}) was plotted in Figure 3.15 (c). The coercivity dropped from 5 kOe to 3 kOe when the FePt thickness decreased from 6 nm to 4 nm. We chose the Pt layer at 7 nm based on the following experiment. Keeping the FePt thickness at 6 nm, the Pt interlayer thickness varied from 7 nm to 12 nm. Figure 3.15 (d) shows the coercivity vs. the Pt thickness (t_{Pt}). The coercivity did not show any significant change when the Pt thickness decreased from 12 nm to 7 nm.

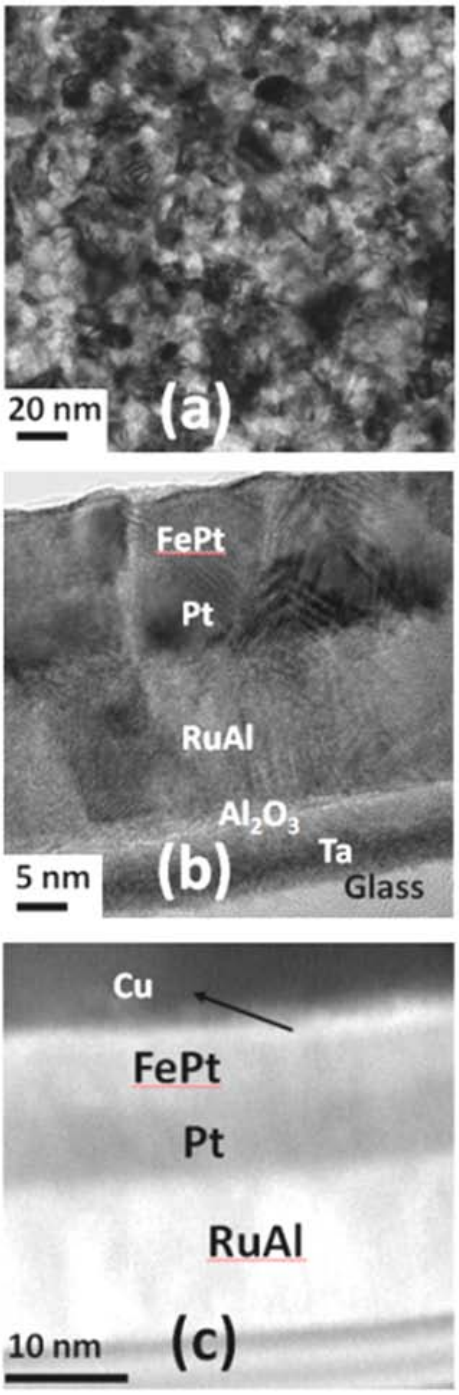

Figure 3.16 **(a) TEM plan-view image of the sample Pt(7 nm)/FePt(6 nm). The mean diameter of the grains is around 12 nm. (b) Bright field cross-sectional image clearly shows the granular structure and the different layers except the Cu capping layer. (c) STEM annular dark field cross-sectional image shows the entire layer structure including the Cu capping layer. The thicknesses of corresponding layers are: RuAl (20 nm), Pt (7 nm), FePt (6 nm), Cu (1 nm).**

Figure 3.16 (a) shows the TEM plane view image of the film Pt(7 nm)/FePt(6 nm). The average grain size is around 12 nm. Figure 3.16 (b) is the bright field TEM cross-sectional image. Clear grain boundary was shown in the Pt/FePt layer. The diameter of the grains is 12 nm, which is consistent with the plan-view TEM image. The Cu capping layer could not be seen in the bright field image. But the STEM annular dark field (ADF) image as shown in Figure 3.16 (c) displays the entire layer structure including the Cu capping layer, because the ADF technique is more sensitive to the Z number difference of elements compared to bright field technique. The thickness of Cu layer in the ADF image is only 1 nm. The rest of 1 nm Cu diffused in the FePt grain boundary and exchange-decoupled the FePt grains as evidenced in Figure 3.16 (b).

We estimated the diffusion length of Fe from FePt layer to Pt layer. The diffusion length can be written as $L=(Dt)^{0.5}$, [34] where $D=D_0\exp(-Q/(k_{BT}))$ is the diffusion coefficient and t is the annealing time. For Fe atom diffusion in Pt layer, we used the parameters of $D0=2.5\times10^{-6}$ m^2/s and the activation energy Q=2.434eV as provided by Ref. 35. The transformation from FePt A1 phase to $L1_0$ phase has been found to occur when it is heated to around 400 °C.[36] However, a chemically disordered A1 phase FePt thin film has to be annealed at 600 °C to form a fully ordered L10 FePt layer. [37] In our deposition process with in-situ substrate heating, the L10 phase FePt was formed even the substrate temperature was around 350 °C, with the assistance of the strain energy from the underlayer and the kinetic energy of the as-deposited Fe and Pt atoms. Based on this, we made the following assumptions: 1) the energy of the as-deposited Fe atoms at 350 °C in our case is under a proper strain and is close to the energy of the Fe atoms at 600 °C annealing and 2) the effective “annealing” time is close to the FePt layer sputtering time, which was around 300s. The calculated diffusion length of Fe atoms in Pt layer is 2.6 nm.

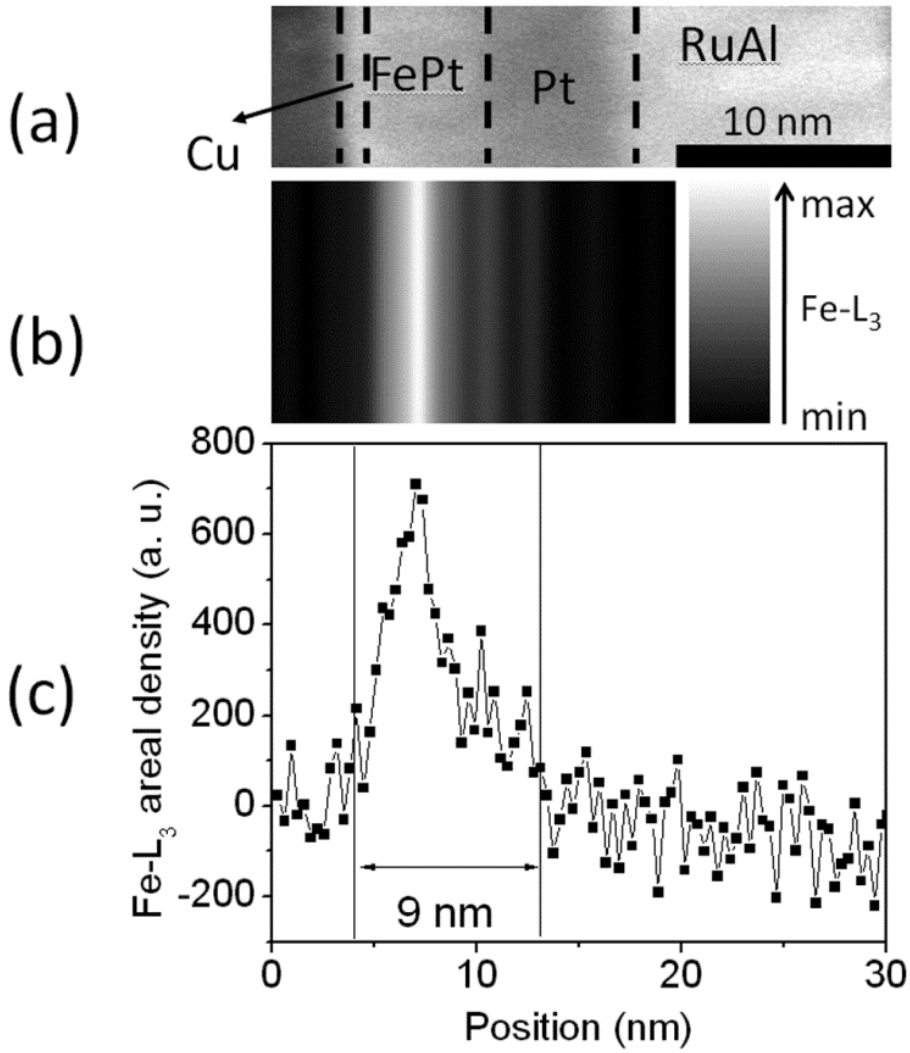

Figure 3.17 (a) Cross-sectional STEM annular dark field image of sample Pt(7 nm)/FePt(6 nm) rotated by 90 degree counterclockwise (left: film top). (b) A schematic of how the Fe composition changes with position, in which the higher the brightness, the more the Fe. (c) EELS line scan analysis of Fe content in one columnar grain along the film normal. The curve of Fe-L_3 edge areal density vs. position was plotted in (c) with associated position in (a) and (b).

EELS line scan was performed to measure the Fe distribution in a single columnar grain along the film normal. Fe-L_3 edge areal density was measured by scanning from left side (film top surface) to right side (Pt layer) in Figure 2.8 (a), which is the cross-sectional STEM ADF image of sample Pt(7 nm)/FePt(6 nm), with a step size of 0.32 nm. The profile of Fe- L_3 edge areal density is shown in Figure 2.8 (c). Figure 2.8 (b) is a schematic to guide how the Fe composition changed with position, in which the higher the brightness, the more the Fe. Comparing Figure 2.8 (b) and (c) to (a), we could see clearly that Fe elements existed in not only FePt layer but also Pt layer. The thickness of the FePt is around 6 nm, but in the Fe content profile, the Fe distribution expanded to 9

nm with a graded composition distribution, which means the Fe atoms diffused into the Pt interlayer and created a graded interface. The observed Fe diffusion length in Pt layer from Figure 2.8 (c) is about 3.0 nm, which is very close to the above calculated value (2.6 nm).

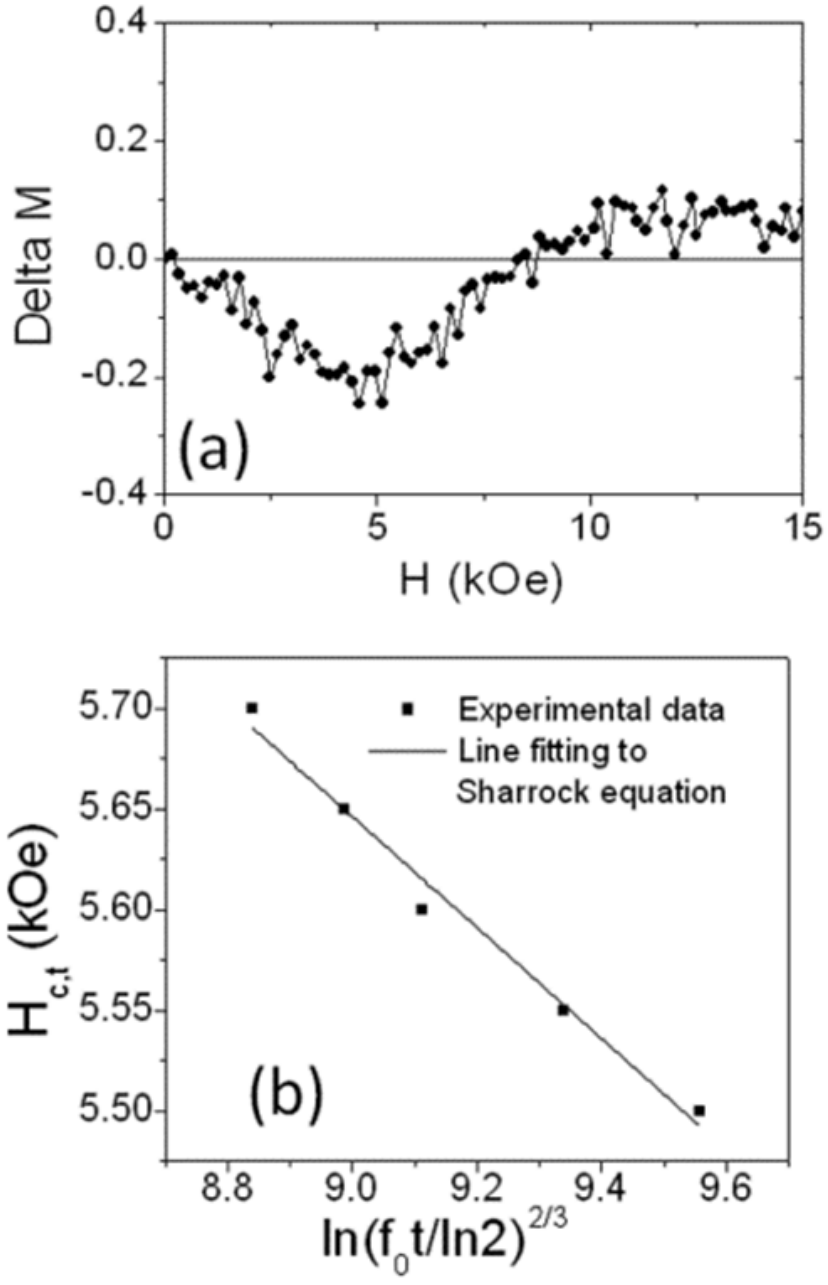

Figure 3.18 (a) Delta M curve of sample Pt(7 nm)/FePt(6 nm). The negative peak at 5 kOe field indicates the dominant dipole interaction of FePt grains. Thermal decay measurement was performed and the experimental data were shown in (b) as the scattered dots. The line was obtained by fitting the experimental data to the Sharrock equation. The thermal barrier is 160 $k_B T$.

Delta M measurement was carried out to confirm the exchange decoupling of FePt grains. The curve is shown in Figure 3.18 (a). A strong negative peak at around 5 kOe, which corresponds to the coercivity, indicates that magnetostatic interaction is dominant in the film.

Furthermore, we tested the gain factor of the fabricated FePt graded media. As mentioned before, gain factor is expressed as $\xi=2\Delta E/(M_S \bullet H_{SW} \bullet V)$, where ΔE is the thermal energy barrier, M_S is the saturation magnetization, H_{SW} is the switching field. V is the activation volume. The diffusion of Fe atoms made it almost impossible to get the accurate value of V. However, since $M_S \bullet V$=magnetic moment, which is an experimental data, this will not influence the gain factor calculation. ΔE was obtained by measuring the time-dependent switching field and fitting to the Sharrock equation (eq. 3.2). The experimental data and fitting results are shown in Figure 3.18 (b). The energy barrier ΔE is 160 k_{BT} and the gain factor ξ is 3.74.

In summary, a graded FePt granular media was fabricated at 350 °C substrate temperature without depositing any soft magnetic layers purposely. The spontaneous inter-diffusion between FePt and Pt layers enabled the FePt composition gradient, which led to the anisotropy and saturation magnetization gradient. The gain factor of the graded media was evaluated to be 3.74. Choosing proper seed layer and grain boundary materials could further reduce the FePt grain size.[38, 39] The fabrication process of this spontaneously-formed graded media is potentially compatible with today's disk media fabrication, and can be extended to other hard magnetic materials such as $L1_0$ CoPt and Co_3Pt. Considering that the deposition time in today's industrial fabrication process is much shorter than that of this work, the substrate temperature can be increased to accelerate the diffusion and improve the ordering of FePt as well.

3.4 Conclusion

In this chapter core-shell type ECC media has been experimentally demonstrated and systematically studied. It is confirmed that it has better performance than conventional bi-layer ECC structure des.

FePt based graded granular media was fabricated using a spontaneous inter-diffusion process. Its gain factor is as large as 3.74, which exceeds the limit value of ECC structure. This spontaneously-formed graded media is potentially compatible with today's disk media fabrication

Reference

[1] D. Weller, A. Moser, L. Folks, M. E. Best, W. Lee, M. F. Toney, M. Schwickert, J.-U. Thiele, and M. F. Doerner, IEEE Trans. Magn. 36, 10 (2000).

[2] R. H. Victora and X. Shen, IEEE Trans. Magn. **41**, 2828 (2005).

[3] D. Suess, T. Schrefl, S. Fahler, M. Kirschner, G. Hrkac, F. Dorfbauer, and J. Fidler, Appl. Phys. Lett. **87**, 012504 (2005).

[4] J. P. Wang, W. K. Shen, and J. Bai, IEEE Trans. Magn. **41**, 3181 (2005)

[5] D. Goll and S. Macke, Appl. Phys. Lett., 93**,** 152512 (2008)

[6] D. Suess, Appl. Phys. Lett. **89**, 113105 (2006).

[7] Z. Lu, P. B. Visscher, and W. H. Butler, IEEE Trans. Magn., **43**, 2941 (2007).

[8] A. Dobin and H. J. Richter, Appl. Phys. Lett., **89**, 062512 (2006).

[9] F. Casoli, F. Albertini, L. Nasi, S. Fabbrici, R. Cahassi, F. Bolzoni, and C. Bocchi, Appl. Phys. Lett. **92**, 142506 (2008).

[10] D. Goll and A. Breitling, Appl. Phys. Lett. **94**, 052502 (2009).

[11] Y. K. Takahashi, K. Hono, S. Okamoto, and O. Kitakami, J. Appl. Phys., **100**, 074305 (2006).

[12] D. Goll, A. Breitling, L. Gu, P. A. Van Aken, and S. Sigle, J. Appl. Phys., 104, 083903 (2008).

[13] Chi-Keong Goh,a Zhi-min Yuan, and Bo Liu, J. Appl. Phys., 105, 083920 (2009).

[14] B. Ma, H. Wang, H. Zhao, C. Sun, R. Acharya, and J. P. Wang, IEEE Trans. Magn. **46**, 2345 (2010).

[15] E. F. Kneller, IEEE Trans. Magn. 27(4), 3588 (1991).

[16] E. E. Fullerton, J. S. Jiang, M. Grimsditch, C. H. Sowers, and S. D. Bader,Phys. Rev. B 58, 12193 (1998).

[17] H. N. Bertram, and B. Lengsfield, IEEE Trans. Magn., 43, 2145 (2007)

[18] M. P. Sharrock, IEEE Trans. Magn., 35, 4414 (1999)

[19] C. L. Zha, B. Ma, Z. Z. Zhang, T. R. Gao, F. X. Gan, and Q. Y. Jin, Appl. Phys. Lett. 89, 022506 (2006).

[20] D. Vokoun, M. Beleggia, T. Rahman, H. C. Hou, C. H. Lai, J. Appl. Phys., **103**, 07F520 (2008).

[21] L. S. Huang, J. F. Hu, G. M. Chow, and J. S. Chen, J. Appl. Phys., **109**, 063910 (2011).

[22] D. Makarov, J. Lee,2, C. Brombacher, C. Schubert, M. Fuger, D. Suess, J. Fidler, and M. Albrecht, Appl. Phys. Lett., **96**, 062501 (2010).

[23] H. Wang, T. Rahman, H. Zhao, Y. Isowaki, Y. Kamata, A. Kikitsu, and J. P. Wang, J. Appl. Phys., **109**, 07B754 (2011).

[24] D. Goll and A. Breitling, Appl. Phys. Lett. **94**, 052502 (2009).

[25] B. Ma, H. Wang, H. Zhao, C. Sun, R. Acharya, and J. P. Wang, IEEE Trans. Magn. **46**, 2345 (2010).

[26] D. Goll, A. Breitling, L. Gu, P. A. van Aken, and W. Sigle, J. Appl. Phys., **104**, 083903 (2008).

[27] T. J. Zhou,B. C. Lim, and B. Liu, Appl. Phys. Lett. **94**, 152505 (2009).

[28] C. J. Jiang, J. S. Chen, J. F. Hu, and G. M. Chow, J. Appl. Phys., **107**, 123915 (2010).

[29] L. L. Lee, D. E. Laughlin and D. N. Lambeth, IEEE. Trans. Magn. **34**, 1561 (1998).

[30] J .J. M. Ruigrok, R. Coehoorn R, S. R. Cumpson, and H. W. Kesteren, J. Appl. Phys. 87, 5398 (2000).

[31] M. H. Kryder MH, E. C. Gage EC, T. W. Mcdaniel TW, W. A. Challener, R. E. Rottmayer, G. Ju, Y. T. Hsia, and M. F. Erden MF, Proceedings of the IEEE, 96, 1810 (2008).

[32] J.S. Chen, J.P. Wang, J. Magn. Magn. Mater., **284,** 423 (2004).

[33] D. Litvinov, M. H. Kryder and S. Khizroev, J. Magn. Magn. Mater., **241**, 453 (2002).

[34] M. Rennhofer, B. Sepiol, M. Sladecek, D. Kmiec, S. Stankov, G. Vogl, M. Kozlowski, R. Kozubski, A. Vantomme, J. Meersschaut, R. Rüffer, and A. Gupta, Phys. Rev. B, **74**, 104301 (2006).

[35] T. Kaiser, W. Sigle, D. Goll, N. H. Goo, V. Srot, P. A. van Aken, E. Detemple, and W. Jäger, J. Appl. Phys., **103**, 063913 (2008).

[36] K. Barmak, J. Kim J, A. Shell A, E. B. Svedberg, and J. K. Howard, Appl. Phys. Lett., 80, 4268 (2002).

[37] S. N. Piramanayagam, J. Appl. Phys. **102**, 011301 (2007).

[38] W. K. Shen, J. H. Judy, J. P. Wang, J. Appl. Phys., 97, 10H301 (2005).

[39] E. Yang, S. Ratanaphan, D. E. Laughlin, and J. Zhu, IEEE Trans. Magn., **47**, 81 (2011).

Chapter 4. FEPT BIT PATTERNED MEDIA

4.1 Introduction

In conventional recording media, a single recording bit contains a certain amount of magnetic grains to maintain signal to noise ratio. Therefore, thermal fluctuation effect will become serious when further reduce the bit size and grain size. Other than simply utilizing high K_U materials, bit patterned media is another option to overcome the thermal effect issue. In bit patterned media (BPM), every single magnetic entity is exchange decoupled and can store information independently.[1] It has been considered as a promising candidate for future extremely high areal density magnetic recording. A single magnetic entity in BPM can be as large as a recording bit in conventional recording media with same recording density. And, obviously, BPM is much more thermally stable than the conventional media. Figure 2.3 shows the comparison of conventional media and BPM.[2]

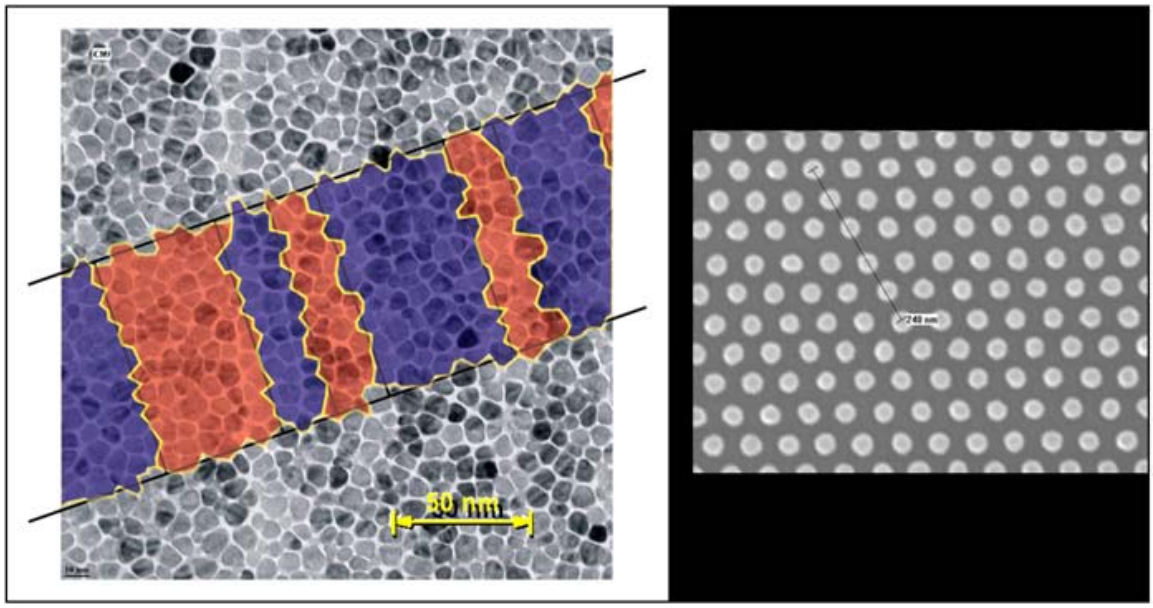

Figure 4.1 Comparison of (left) conventional media and (right) bit patterned media.

Even with BPM, to get ultra-high recording density, thermal effect is still inevitable. To achieve 10T bit/in^2 areal density in BPM, the bit size is required to be as small as 8

nm. Therefore, in future extremely high recording system, BPM still requires materials with very high magnetic anisotropy (K_u) to guarantee thermal stability of the individual bits.[3] $L1_0$ ordered FePt alloys with perpendicular anisotropy can be considered as one of the potential materials for the recording layer in BPM due to its large K_u of ~ $7x10^7$ erg/cc.[4]

However, the fabrication process of BPM is far more complicated and expensive than that of conventional media. Patterning process has to be employed following thin film deposition. In fact, the biggest challenge is to economically fabricate magnetic dot arrays. Typically, there are three methods to transfer the dot array patterns down to magnetic continuous films.

4) Electron beam lithography;
5) Nanoimprinting;
6) Block copolymer self-assemble.

In electron beam lithography, the nanostructures are defined by electron beam one by one. It is very accurate but cost too much. Therefore it is impossible to utilize this process on every hard disk. On the contrast, the other two processes are much more economical and feasible in media fabrication. In this thesis work, both nanoimpringting and block copolymer self-assemble were included.

4.2 Patterning process

4.2.1 Nanoimprinting

For modern fabrication process, high throughput and low cost are two very important requirements in both industry and academics. However, when the lithography feature sizes become extremely small, approaching sub-100 nm or even sub-10 nm, it is very difficult to meet these two requirements. The conventional optical lithography was limited by diffraction limitation. According to Rayleigh criterion, the smallest resolution of the optical lithography is $0.61\lambda/N_A$, where λ is the wave length of the exposing light and N_A is the numerical aperture. Normally the resolution is around hundreds of nanometers. With some very complicated systems, the EUV optical lithography can reach

sub-100 nm. However, it still can not fulfill the requirements to further reduce the feature size and cost. Electron beam lithography has the capability to create sub-10 nm feature size. But its high cost and low throughput make it difficult to be accepted for mass productions.

As a high throughput, high resolution parallel patterning method, nanoimprint lithography (NIL) was proposed by Chou et al.[5] and was accepted as a very promising candidate for future nanofabrication process. NIL has now passed a barrier from a laboratory scale to industrial preproduction. Data storage will most likely be the first industrial application field where replication techniques will be able to replace standard methods of lithography. Also, much interest in NIL processes comes from a large community of sensor, biochip, and nano-optics manufacturers and institutes.

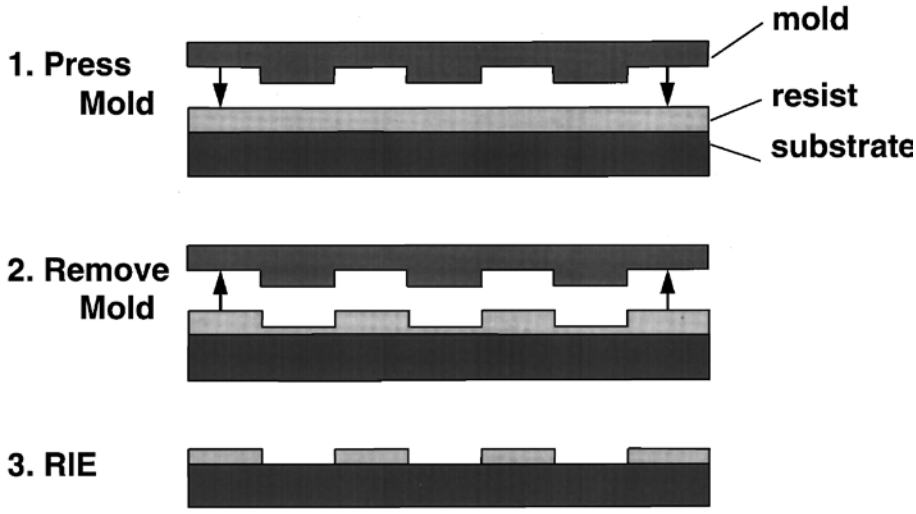

Figure 4.2 Baseic steps of nanoimprint lithography

The basic steps of nanoimprint lithography were shown in Figure 4.2.[6] The first step is pressing a mold with nanostructures on the surface into a substrate covered by a thin resist layer. The second step is removing the mold. These two steps duplicated the nanostructures on the mold surface to the resist as a mirror pattern. Height difference was built up on the resist. However residual resist layer remains on the bottom of the lowest level. Therefore, in the third step, reactive ion etching (RIE) was used to remove the residual layer. This step is quite critical. Since the goal is to just remove the residual and keep the other height contrast. Then, the substrate surface was exposed. Finally, the

pattern in the resist was transferred into the substrate by RIE, ion milling or other etching process. Compared to the conventional patterning process, nanoimprint lithography requires no any energetic beams, such as light, x-ray and electron beam. So the resolution of the nanoimprint lithography is not limited by the wave diffraction and interaction with the resist or materials. And unlike self-assembled molecules, nanoimprint is a physics process and can create any pattern provided by the mold. However, the mold itself has to be prepared by conventional lithography. Actually, most of the cost in nanoimprint lithography is the mold. Currently, there are two main types of nanoimprint lithograpy[7]. One is called thermal NIL and the other is called UV NIL.

The thermal type NIL was proposed in Chou's work.6 Temperature sensitive resist was spin coated onto the sample and post baked. After heating, the resist will be liquefied or become soft. For example, the PMMA resist has small thermal expansion coefficient and small pressure shrink coefficient. Its glass-transition temperature is about 105 ^{o}C. Lines and dots with 25nm – 30 nm feature sizes were created in their work.

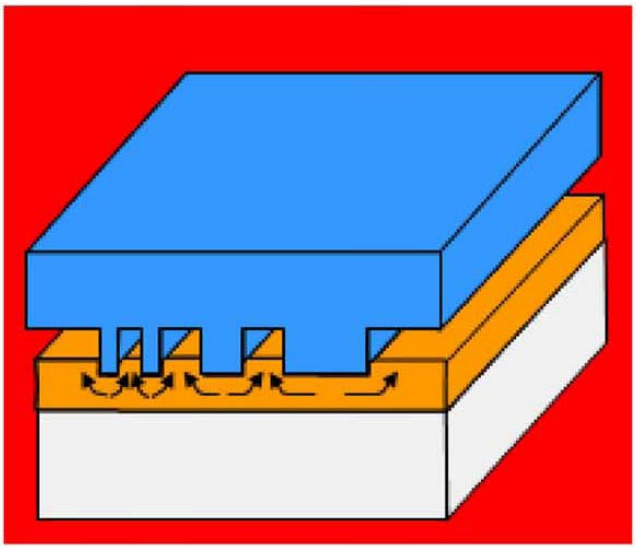

Figure 4.3 Schematic figure of the thermal type NIL process

Figure 4.3 shows the schematic figure of the thermal type NIL process. After been liquefied by heating, the resist was pressed to fill the space on the mold surface under high pressure. The pressure was kept for a while. And the temperature was reduced to room temperature. Then, the pressure was reduced to atmosphere. To perform this

process, the sample was placed between two flexible membranes. The air between the two membranes will be pumped out and high pressure gas will fill the outside space of the membranes to apply uniform pressure to the membranes, and meanwhile, to the sample. After reduced the temperature and pressure, the mold was removed. The residual layer was etched by the O2 plasma in RIE. Finally, the sample was ready for the pattern transfer.

Although this process is quite simple, there are some disadvantages. The high temperature and high pressure make it more difficult to depart the mold from the substrate after imprinting, because they may enhance the bonding between the resist and the mold. Also, the process has to be performed under high temperature. If the substrate we want to pattern has some materials sensitive to temperature, the thermal type NIL is not a good choice.

Figure 4.4 shows the schematic figure of the UV-type NIL.

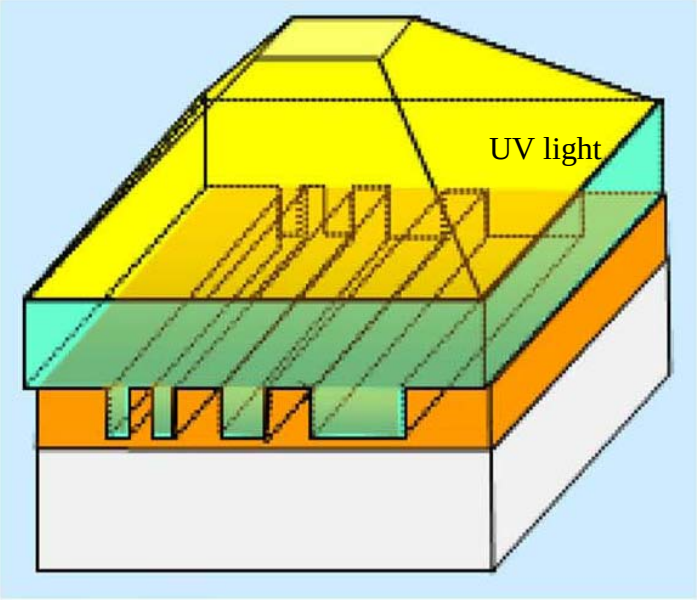

Figure 4.4 schematic figure of the UV-type NIL

A very low viscosity resist was dispensed on the substrate. Then a mold which was transparent to ultraviolet (UV) light was pressed to the substrate. Capillary forces then pulled the mold into conformal contact with the substrate. At this point the mold was exposed with UV light from back side to cure the resist. The mold was then separated

from the substrate by a reverse motion. Then the residual layer of the resist was removed by O2 RIE. Finally the pattern was transferred.

UV curable NIL resist has to be sensitive to the UV light. It is composed of a mixture of monomers or prepolymers and a suitable photoinitiator, and often chemicals are added which decrease the effect of radical scavengers on photopolymerization[8]. Immediately during contact of the mold with the liquid resist, the capillary force fills the mold with the resist, and pulls the mold toward the substrate. Therefore, the general strategy is as follows: (i) low viscosities are needed both for rapid dispensing and filling of mold. (ii) Thin resist layer are used to achieve a homogeneous film thickness. (iii) Cross-linking and photopolymer conversion are adapted to achieve high curing speed and high etch resistance in the following plasma etching process. Also, resists with adapted dielectric properties have been developed for specific applications such as the dual damascene process for the structuring of interconnects on microchips[9,10].

Compared to the thermal type NIL, UV NIL has several advantages. It does not require heating process. So the temperature sensitivity of the materials is not an issue. The resist for the UV NIL has a very low viscosity. The capillary force can play a major role in the imprinting process. Therefore high pressure is not necessary. Since the UV NIL process can be performed under room temperature and relatively low pressure, it will cost less damage to the mold and the substrate, and the mold life time will be much longer compared to the thermal type.

However, to ensure the UV light transmit through the mold and reach the resist, the mold has to be transparent. It means that we need to choose specific materials for the UV NIL mold. But for the thermal NIL, common Si wafer can be used for the mold materials.

One of the biggest issues in the nanoimprint lithography is the demolding process. During the imprinting process, the mold was pressed to the resist by a high pressure. The resist has to be contact to the mold and deform with the surface topography of the mold. However, the surface tension and the bonding between the resist and the mold have to be considered. Because the surface of the substrate is flat and the surface of the mold is very rough with the pattern, the surface area on the mold is much larger than the surface area of the substrate. This means, if the mold and the substrate have the same surface materials, the former will have higher surface energy. And the resist is tending to attach

to the mold rather than the substrate. What we expect is that, after demolding, the surface topography of the resist will not change. However, without specific treatment, the demolding is very difficult. Since the resist may attach to the mold tightly, some or even most of the resist will be peeled with the mold. The patterns on the resist will be destroyed. The smaller the feature size, the more serious the problem is. Therefore, people had to come out some method to prevent the resist from sticking to the mold.

To solve this problem, people studied the atoms and molecules in the interfaces in order to find suitable lubrication and anti-sticking materials and methods. Molecular dynamics simulation was performed to calculate the surface energy[11]. The surface modification was considered to be an ideal way of solving it. Normally, fluoroalkylsilane was coated onto the mold surface as a release agent to significantly reduce the adhesion between mold and resist[12]. To coat the release agent, the mold was put in a chamber. A small container was placed near the mold with a few drops of the fluoroalkylsilane. Then, the chamber was evacuated by a pump. And the solution will be evaporated, and form a self-assembly monolayer (SAM layer) on the mold surface. With the assist of the SAM layer, the mold surface was modified to be hydrophobic. Removing the mold in the demolding process will be much easier and will not damage the pattern on the resist.

Also, there are other methods to do the surface modification of the mold. CHF_3 and SF_6 were used as feed gases in RIE. With the plasma provided by the RIE, they will decompose and form CF_2 layer on the mold surface. The formulas were listed below,

$$CHF_3 = CF_2 + HF \quad (1)$$

$$CHF_3 = C + 2F + HF \quad (2)$$

$$SF_6 = S + 6F \quad (3)$$

$$C + 2F = CF_2 \quad (4)$$

Using 1H,1H,2H,2H-perfluorooctyl-trichlorosilane trichlorosilane,CF_3–$(CF_2)_5(CH_2)_2$–$SiCl_3$, or F_6 liquids solution to coat SAM layer are all good choices for nanoimprinting mold anti-sticking treatment. The advantage of using SAM layer as release agent is that it has good stability and easy fabrication.

4.2.2 Block copolymer self-assemble

Block copolymer (BCP) lithography[13,14,15] could have been considered as the most likely route to higher areal density beyond. As a chemical method, BCP is economical and easy to form nanostructures over large area. Figure 4.5 shows how to form a nanodot array using BCP.

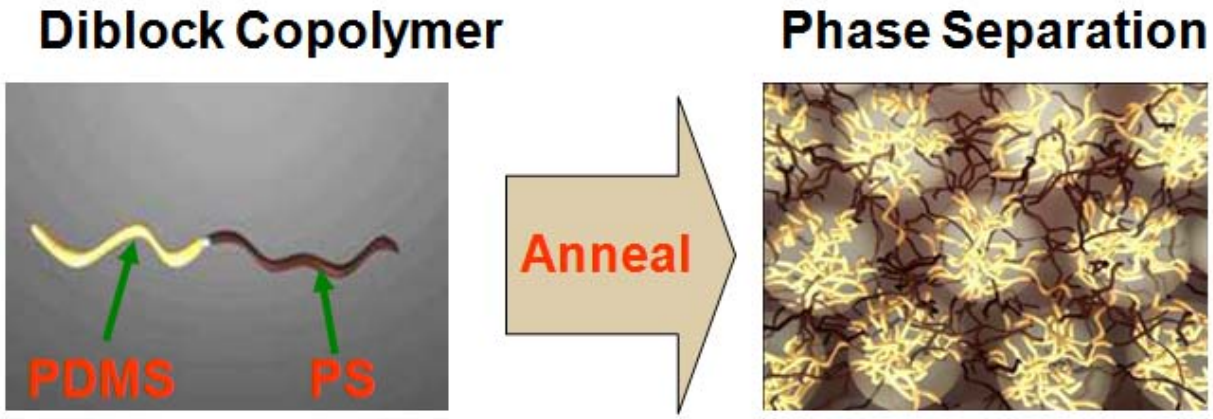

Figure 4.5 Phase transformation and nanodot array formation of block copolymer

A typical di-block copolymer molecular is combined by two types of polymers, which are polystyrene (PS) and polydimethylsiloxane (PDMS), respectively. The copolymer can be dissolved in solution such as toluene. The volume ratio of PDMS to PS has to be carefully designed. After annealing, which can be either thermal annealing or vapor annealing, phase separation will happen and the PDMS will form dots while PS will form matrix as a self-assemble process. The PDMS dot array can be used as the hard mask of pattern transfer process to create dot array on magnetic thin film.

Figure 4.6 shows the typical process of BCP lithography.

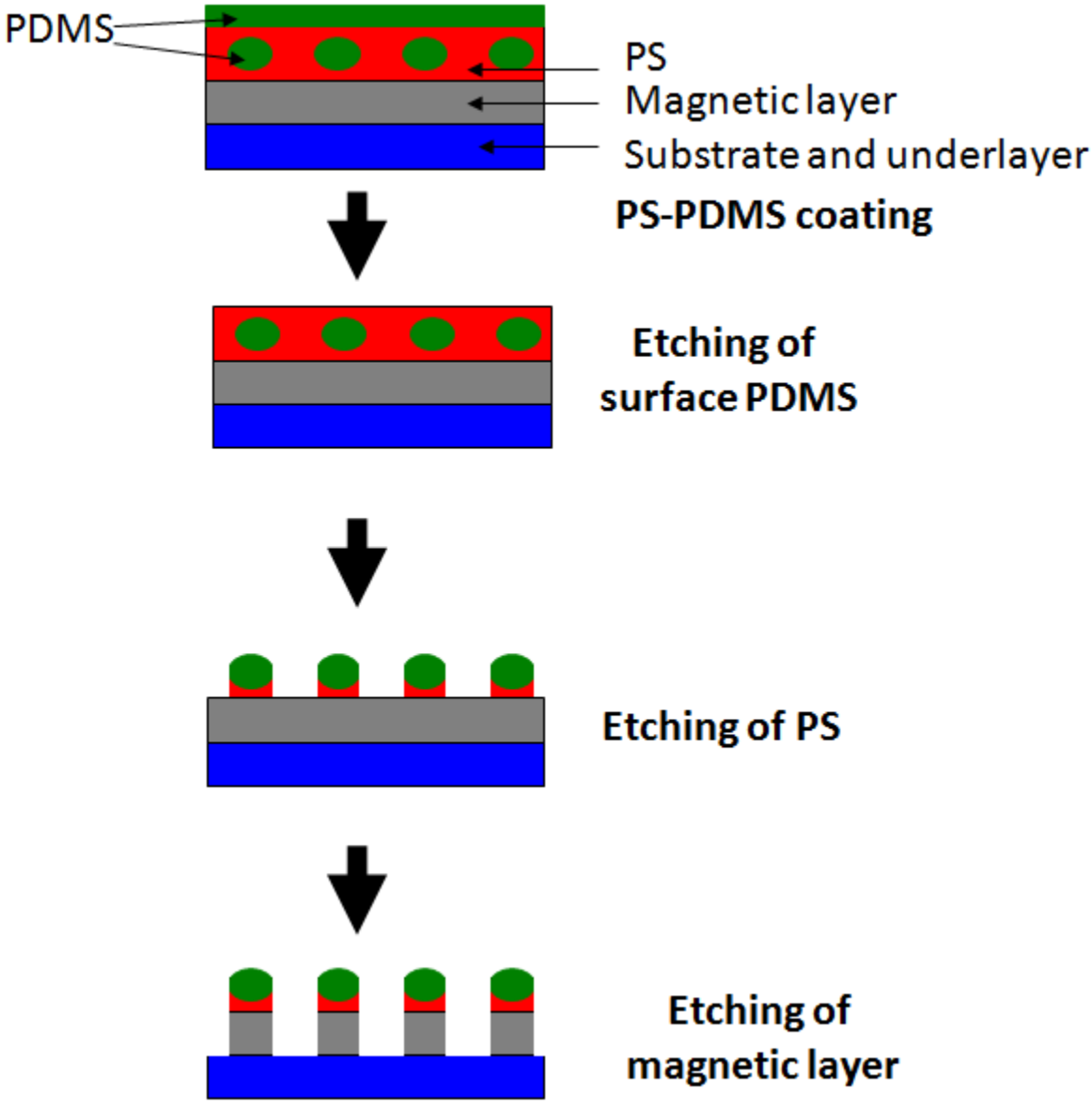

Figure 4.6 Schematic diagram of fabrication process of block-copolymer lithography.

As shown in Figure 4.6, the BCP was spin coated onto the sample and annealed. Then, the surface PDMS was selectively etched using reactive ion etching with proper recipe. The PS matrix was removed by oxygen plasma. The PDMS dots were left as masks. Then the pattern was transferred into the magnetic layer using ion milling. Finally the residual BCP was removed. In this thesis work, most patterning processes were done by using BCP.

4.3 $L1_0$ FePt type bit patterned media

4.3.1 Development of FePt continuous film

FePt thin films are required to be flat and continuous for pattern transfer. The films were deposited on single crystal MgO substrates using an eight-target magnetron sputtering system. The base pressure was lower than $5x10^{-8}$ torr. The full structure of the composite medium was CrRu(30nm)/Pt(3nm)/FePt(10nm)/Ru(3nm). At first, the substrate was heated to 350 °C. Then, CrRu underlayer was co-sputtered with atomic ratio of 9 (Cr) to 1 (Ru), followed by the deposition of Pt interlayer. We used Pt interlayer instead of commonly used MgO interlayer to ensure continuous film microstructure in this ultra-thin FePt layer. The FePt would form discontinuous island structure on MgO when the FePt layer were very thin and deposited at a relatively high temperature.[16] Fe and Pt were co-sputtered onto the Pt layer to get $L1_0$ FePt. Finally the samples were capped with 3 nm Ru at room temperature for protection.

Figure 4.7 shows the AFM image of FePt continuous film. Its surface roughness is 0.218 nm.

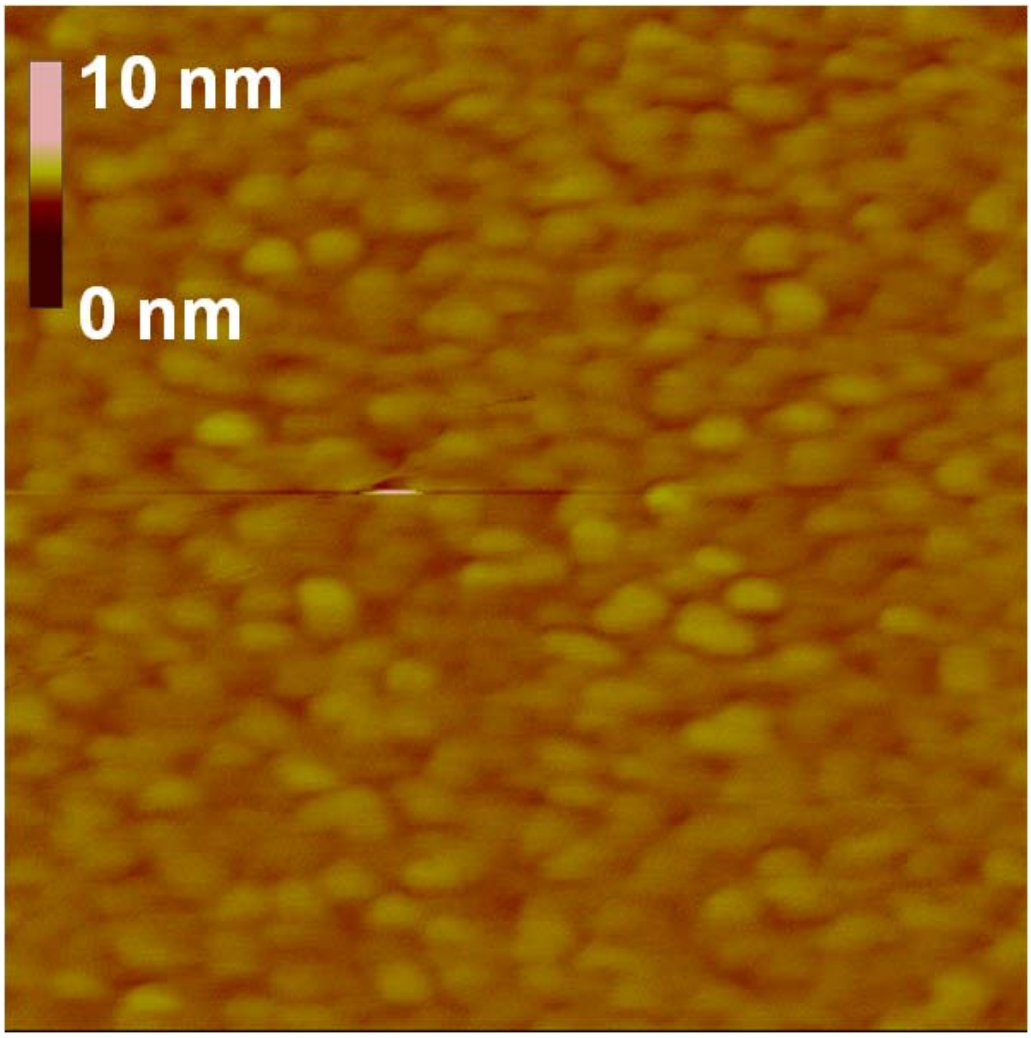

Figure 4.7 The AFM images of FePt continuous film, with surface roughness of 0.218 nm

Figure 4.8 (a) shows the XRD spectra of FePt continuous film, and confirms it is well ordered and has (001) texture. According to the intensity ratio of (001) peak to (002) peak, its ordering parameter S is 0.72,[17] but we need to consider that the 3 nm Pt interlayer generates a weak Pt (200) peak overlapped with the FePt (002) peak, and contributes to the intensity of the latter. Therefore, the calculated S value is a underestimated one. The inset in Figure 4.8 (a) is FePt (001) rocking curve. Its FWHM is 5.95º. The out-of-plane hysteresis loops of continuous film are shown in Figure 4.8 (b). The H_C of the continuous film is 3.82 kOe.

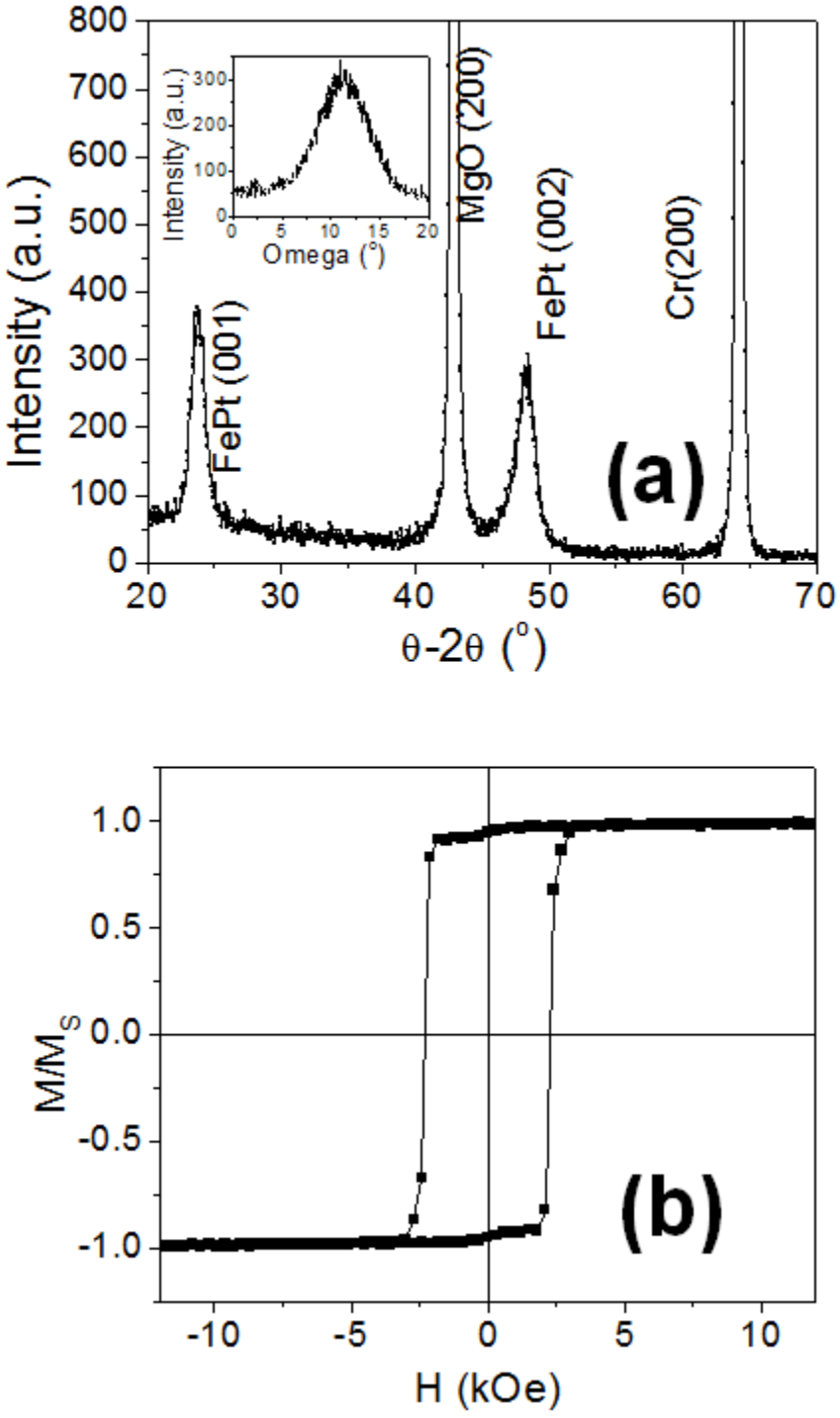

Figure 4.8 (a) XRD spectra and (b) Out-of-plane hysteresis loop of FePt continuous film. Its H_C value is 3.82 kOe.

4.3.2 FePt BPM fabricated using nanoimpringting lithography

The mold (also called as template or stamp) is the crucial part of the NIL that determines the throughput and resolution of the later in practical applications. Usually electron beam lithography or focused ion beam lithography followed by the pattern transfer using reactive ion etching (RIE) is used for making the mold. The high cost and low throughput of these methods limit the usefulness of the NIL for fabricating nano-patterns over large area for the research and also practical applications. Therefore, exploring the fabrication of low- cost and highly robust large area mold is a must to enjoy the full potential of the NIL. However, to date, only very few works have been reported in this highly demanding area. Park et al.[18] fabricated the large area mold by using block-copolymer lithography that involved an extra pattern transfer step. Kim et al. [19] and Lee et al. [20], used AAO membrane filled with carbon and aluminum respectively, that also involved number of harsh steps like, fabrication of AAO membrane that is difficult to handle due its brittle nature, attaching that AAO membrane with another rigid substrate, deposition of carbon or aluminum, heat treatment, ion milling and chemical etching.

The fabrication procedure is schematically shown in Figure 4.9 (a-f). The procedure consists of two main processes: (i) preparation of the AAO mold with different hole diameter, coating it with thin SiO_2 followed by SAM layer deposition and (ii) nanoimprinting. At first, a 500 nm Al film with a thin Ti underlayer is deposited on a 4 inch (~10.2cm) circular disc of a Si wafer by thermal evaporation [Figure 4.9 (a)]. This Al film is anodized in phosphoric and Oxalic acid by a two- step anodization process as described elsewhere to get the AAO with pore diameter of 160 nm and 75 nm respectively.[21,22] Then the AAO mold is coated with a very thin~ 2-3 nm SiO_2 layer by atomic layer deposition (ALD) technique followed by the coating with commonly used silane based SAM (Heptadecafluro 1,1,2,2-Tetra-Hydrodecyl Trichlorosilane) layer [Figure 4.9 (b)]. The surface modification of the AAO by SiO_2 is the key to the success of the direct use of AAO mold for NIL. Either Si wafer or FePt film grown on Si wafer is coated with nanonex-1050 thermal resist by spin coating [Figure 4.9 (c)]. Then thermal nanoimprinting has been performed by using nanonex BX200 nanoimprinter on Si wafer and FePt thin film spin coated with thermal resist [Figure 4.9 (d)]. The resist flown into

the AAO holes remain as pillars after demolding [Figure 4.9 (e)]. The FePt film is patterned by RIE and Ar ion milling using the resist pillars as mask [Figure 4.9 (f)]. The remaining resist pillars are removed by chemical etching in acetone and RIE that leaves FePt pillars on the substrate [Figure 4.9 (g)].

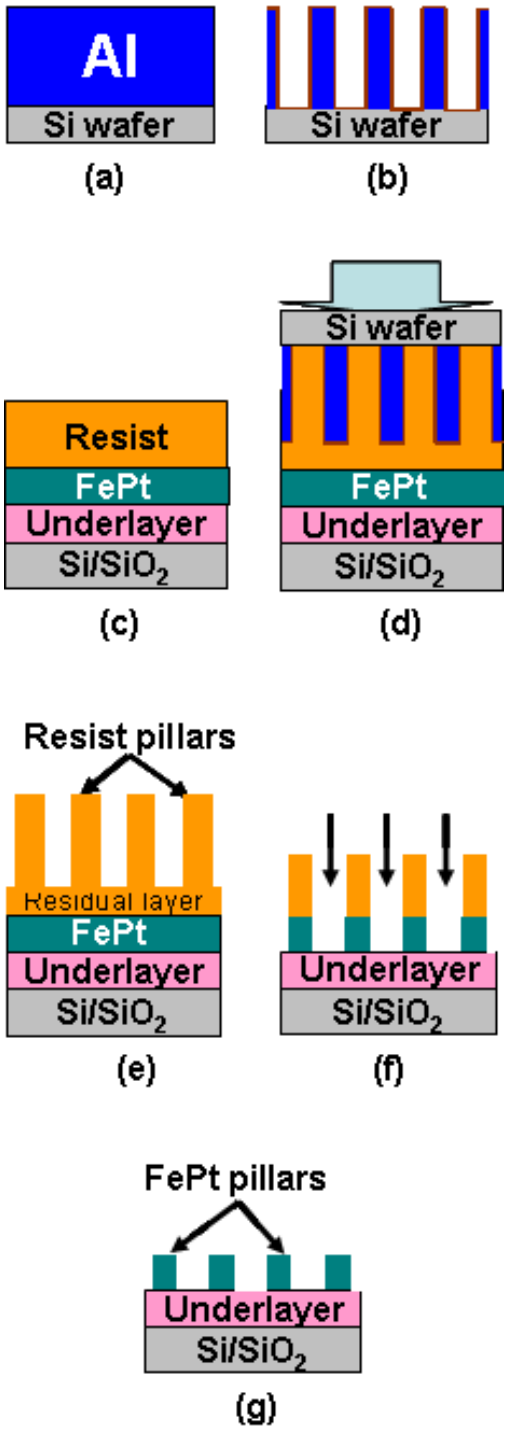

Figure 4.9 Schematic drawing of the fabrication of FePt patterned structure by using anodize alumina (AAO) mold. (a) deposition of Al film on Si wafer, (b) fabrication of AAO and coated it with thin SiO_2 and SAM layer, (c) spin coating of the resist on FePt thin film, (d) nanoimprinting, (e) demolding, (f) removal of the residual layer by reactive ion etching (RIE) and transfer the pattern into FePt film by Ar ion milling (f) removal of the resist to leave the FePt pillars on substrate.

We have started with a mold with large feature size. Figure 4.10 (a) shows the AAO mold fabricated in phosphoric acid. The diameter of the AAO holes is varied from about

80 nm to 160 nm and the height of the holes is about 400 nm. We do not pay attention to the ordering and size distribution of the AAO pores that can be achieved very easily by optimizing the anodization parameters.[23] Figure 4.10 (b) shows the SEM image of the imprinted resist on Si wafer by using the mold shown in Figure 4.10 (a) coated with SAM layer only without any SiO_2 coating. The resist over more than 50% area are peeled off with the mold as represented by the bright areas. Although resist remain adhered on the rest part of the substrate but no features are observed as indicated by the high magnification image of the corresponding area shown in the inset. The friction and sticking problem between the mold and the resist is one of the main challenges in nanoimprinting technology. With the nanostructure size becoming smaller and smaller, the surface to volume ratio increases dramatically and the fiction and sticking problem become more severe. When the mold makes contact with the substrate coated with resist, the high surface energy produces a large amount of surface force. With the interaction between surfaces, the profile of the two surfaces changes and reestablishes a new energy equilibrium state that produces sticking. Due to the sticking forces between surfaces, the nano system produces a big friction force, especially during the demolding process. Among the several options,[24,25,26] application of the silane based hydrophobic self-assembled monolayer (SAM), namely, "Heptadecafluro 1,1,2,2-Tetra-Hydrodecyl Trichlorosilane" has been reported as the most successful lubrication method. We do not get any imprinting result by using this silane based SAM layer directly on our AAO mold as shown in Figure 4.10 (b) due to the inferior bonding between Al_2O_3 and the SAM layer. We modify the surface of the AAO mold by coating it with a very thin~ 2-3 nm SiO_2 by ALD followed by the deposition of SAM layer on it. Eventually, we achieve excellent imprinting over more than 1 cm^2 area with almost 100% replication of the mold as shown in Figure 4.10 (c). The imprinting from even the smallest features is also clearly shown in the inset of Figure 4.10 (c). The imprinted feature size is reduced by about 45% after removal of the residual layer by RIE due to the lateral etching. The coating of the AAO mold with SiO_2 layer reduces the surface energy of the mold and enhances the bonding with SAM layer, which is the key of getting successful imprinting.

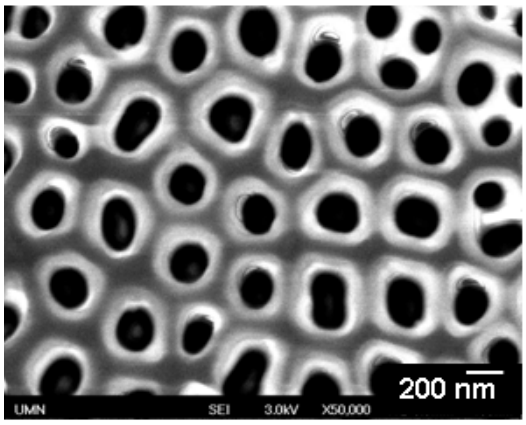

(a)

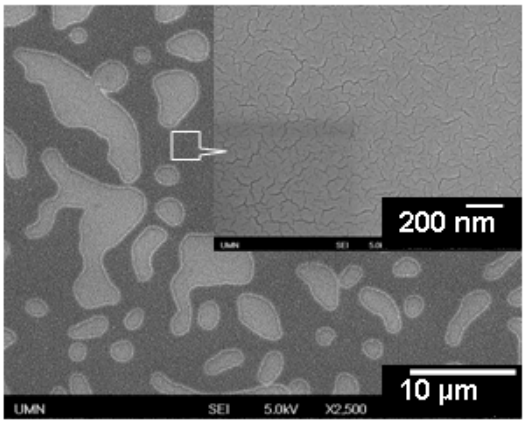

(b)

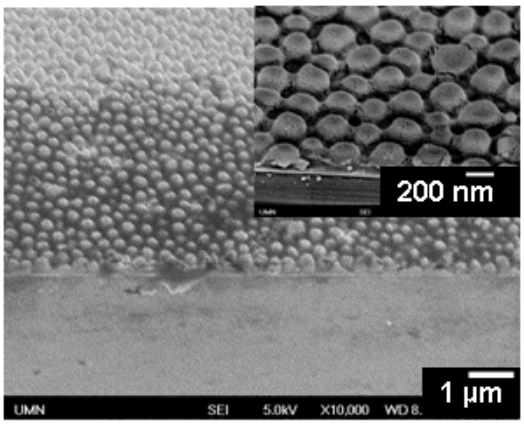

(c)

Figure 4.10 SEM plane -view images of (a) AAO mold, (b) as-imprinted image of resist by using mold without SiO_2 coating, inset is the magnified view of the indicated area, and SEM cross-sectional image of (c) as-imprinted image of resist pillars by using the mold with thin ~ 2-3 nm SiO_2 coating.

After achieving very good imprinting of resist pillars with large feature size on Si wafer, we concentrate our effort to reduce the feature size and fabricate $L1_0$ FePt patterned structure. The FePt continuous thin film was spin- coated with 150 nm thick thermal resist (PMMA) and patterned by using an AAO mold with smaller feature size.

Figure 4.11 (a) shows the plan-view SEM images of the mold. This mold is fabricated by anodizing the Al film in oxalic acid to get smaller hole diameter.[27] The area of the mold is about 1 cm^2. The diameter and height of the AAO holes in the mold is 75 and 150 nm, respectively. The imprinting is done at 350 psi, 175 °C for 3 minutes. Figure 4.11 (b) shows the SEM cross-sectional image of as imprinted resist pillars on FePt thin film. The diameter of the most of the resist pillars isare almost same as the diameter of the mold but the height of the some of them isare smaller than the corresponding depth of the mold's features. This is may be due to the lack of sufficient flatness of the mold and insufficient initial resist thickness. Figure 4.11 (c) shows the plan-e view SEM image of the FePt dots on the Si wafer after removing the residual layer and transferring the pattern by Ar ion milling using the resist pillars as mask. The average diameter of the FePt dots is about 40 nm with a size distribution of about 10 %. The size of the dots is about 45% smaller than the mold feature size as well as as-imprinted resist pillars. This size reduction is good in agreement with the reduction of size for the large feature sized mold as described in previous section and indicates that the size of imprinted features again can be tuned by controlling the depth of the mold's features and residual layer thickness. Some of the dots as indicated by the black arrows in the inset of Figure 4.11 (c) are almost etched away due to the smaller mask height onto it as indicated by the white arrows in Figure 4.11 (b). As a result, the density of the FePt dots is somewhat smaller than the density of the holes in the mold. The magnetic properties of this patterned FePt structure is measured by using SQUID at room temperature. The perpendicular coercivity of the patterned structure is about 12 kOe that is about 3.5 times larger than that of the continuous film. This H_C value is much lower than that of the isolated FePt islands on MgO.[28] Several mechanisms can be considered for this low Hc value of the patterned structure. First, diffusion may occur at the interface between the Pt layer and the FePt layer as Pt is used as interlayer, therefore the composition and switching field at the

interface may differ with the other part. The FePt at the interface with smaller switching field may be exchange coupled with the adjacent part with larger switching field and reduce the Hc. Second, the re-deposition effect may add some disordered FePt onto outer surface of the pillars. This re-deposited disordered FePt may act as nucleation sites to start the magnetization switching at low field that can reduce the coercivity.

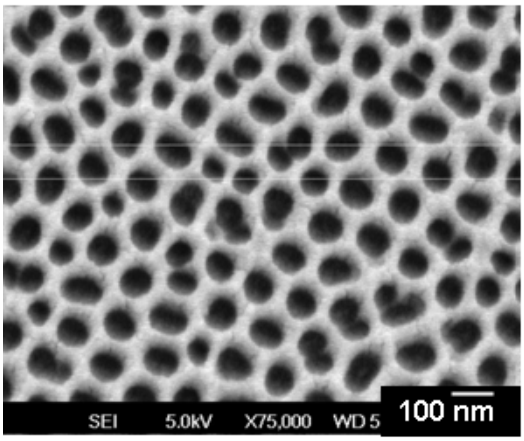

(a)

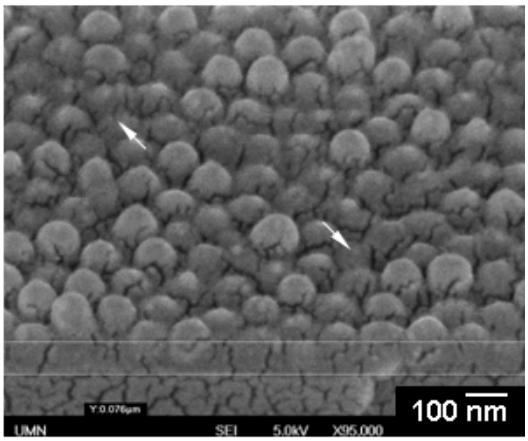

(b)

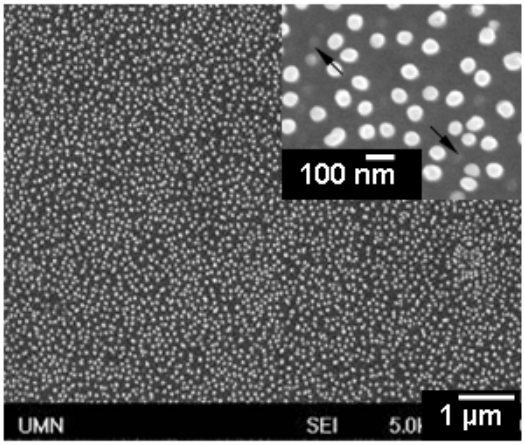

(c)

Figure 4.11 SEM plane view images of (a) AAO mold coated with thin SiO2 layer. The average hole diameter is about 75 nm. (b) the cross-sectional SEM image of as-imprinted resist pillars. Some pillars with smaller height are indicated by white arrows and (c) plan-e view SEM image of FePt dots on Si wafer. Some dots with reduced height are indicated by black arrows.

To summary, we have demonstrated the direct use of anodize alumina (AAO) fabricated on Si wafer as a large area mold for nanoimprinting. The sticking problem

between the mold and the resist has been overcome by modifying the AAO surface by coating it a very thin SiO_2 layer. Moreover, we successfully fabricate $L1_0$ FePt patterned structure with 40 nm feature size over large area with a size distribution below 10%. Optimization of naonimprinting parameters and flatness of the mold may open the path to fabricate patterned magnetic nanostructures with reduced feature size and high density for practical applications.

4.3.3 FePt BPM fabricated using block copolymer self-assemble

Fabrication of $L1_0$ single layer FePt bit patterned media using block copolymer lithography has been reported by Hieda et al. [29], where they have fabricated the hole array first and filled them with spin on glass (SOG). Then, the matrix has been removed and the SOG dots have been used as the etching mask. In this work, BCP was used as hard mask for pattern transfer directly to fabricate FePt BPM.[30] Figure 4.12 shows the SEM plan view image of BCP-fabricated FePt BPM. The FePt bit size is around 31 nm and the pitch size is around 37 nm.

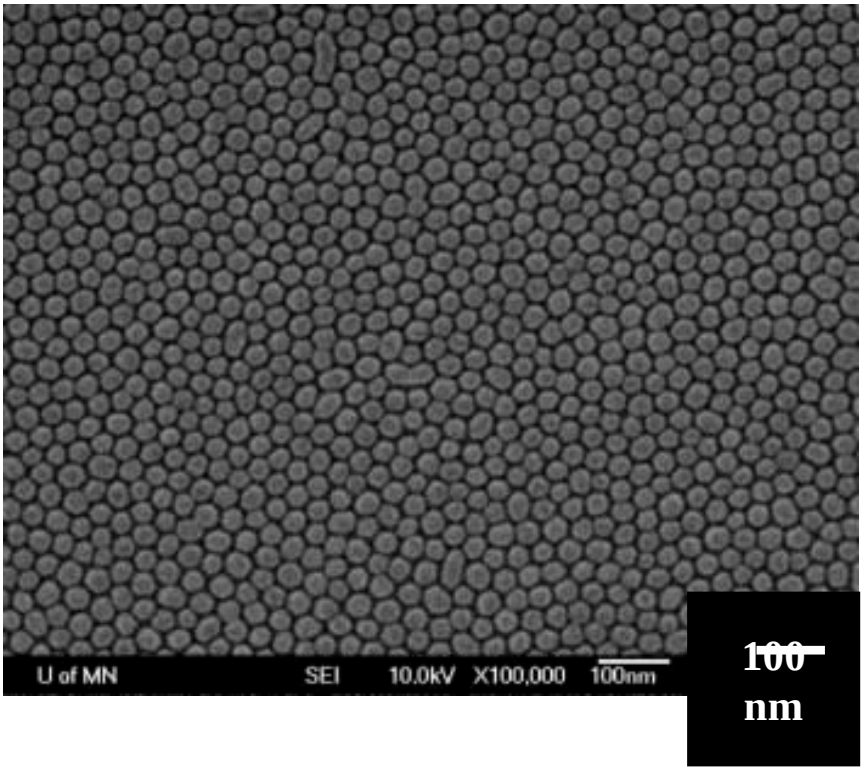

Figure 4.12 SEM plan-view image of FePt BPM fabricated using BCP.

Figure 4.13 shows the TEM cross-sectional image of the FePt BPM. The physical isolation of the FePt bits can be clearly observed in the TEM images. Thus the exchange-decoupling between adjacent bits is realized and confirmed.

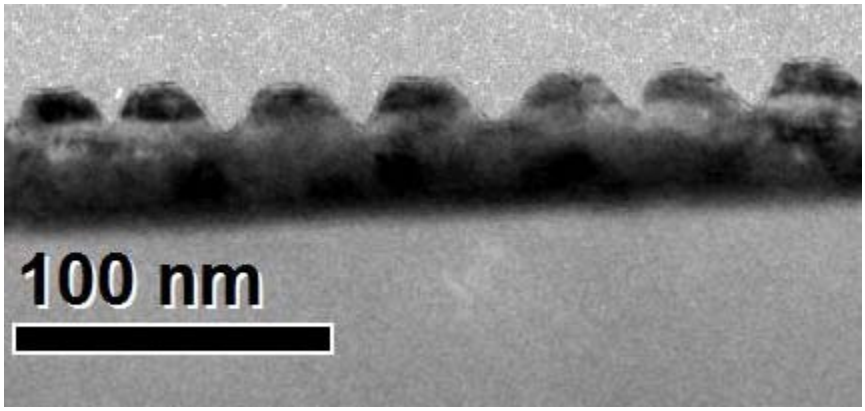

Figure 4.13 TEM cross-sectional image of FePt BPM fabricated using BCP.

Figure 4.14 (a) is the XRD spectra of the as-patterned FePt BPM. After patterning, the ordering parameter S of FePt decreases from 0.72 to 0.48. And the FWHM of FePt (001) rocking curve, which is shown as the inset of Figure 4.14 (a), increases from 5.95º

to 7.26º, compared to the continuous film, the as-patterned film has lower FePt chemical ordering and broader distribution of easy axis orientation.

Figure 4.14 (b) shows the out-of-plane hysteresis loop of the patterned sample and its recoil loop, which starts from the coercivity point. The coercivity is 16.0 kOe. The recoil curve demonstrates an ECC-characteristic magnetization reversal. When the applied field decreases from the coercive field, an increase of magnetization is observed, indicating a reversible switching. The following part of the recoil loop is flat, suggesting that irreversible switching mechanism also exists. This serious non-uniformity, which was created during the pattern transfer process, broadened the switching field distribution (SFD). According to the ΔH_C method,[31] SFD was calculated by $\Delta H_C/1.35H_C$. ΔH_C was defined as the difference between the field positions of recoil loop and major loop at the point of $M=0.5M_S$. This is a rough estimation of intrinsic SFD. Here ΔH_C is 7.3 kOe and H_C is 16.0 kOe. Therefore the SFD of this as-patterned sample is 34%. Although dot size distribution is an important source of SFD, it is probably not the reason for a large SFD, because the size distribution is less than 10%.

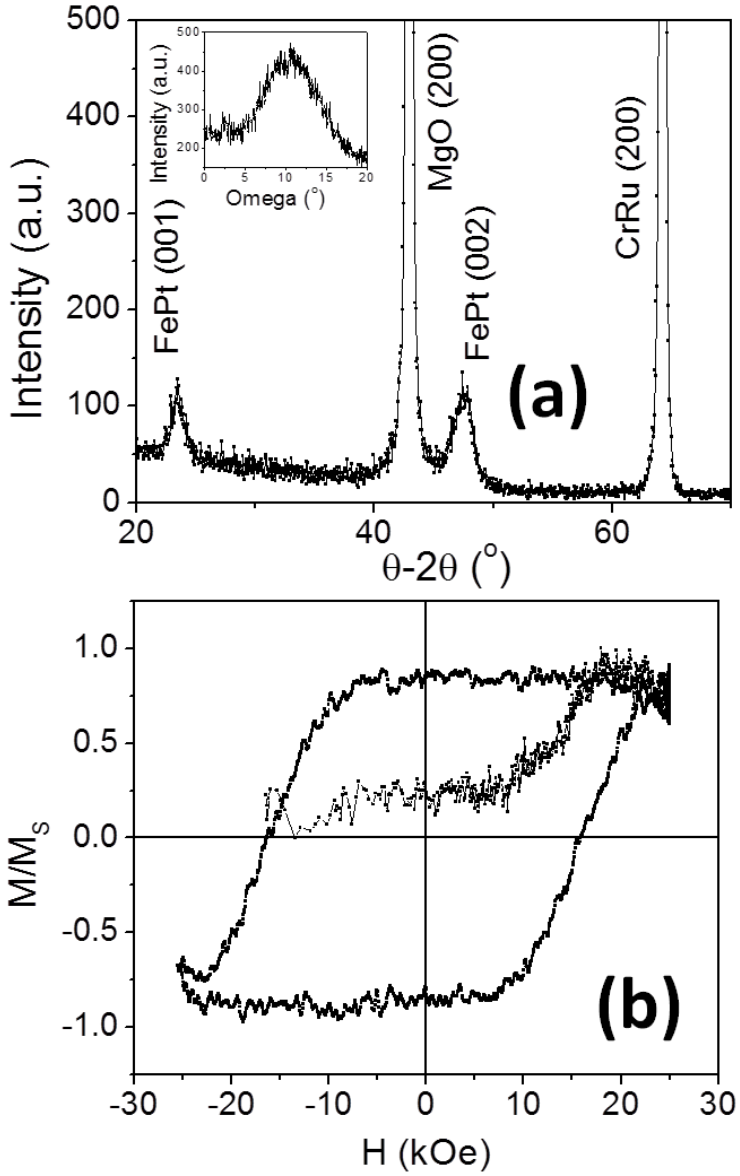

Figure 4.14 (a) XRD spectra, (b) out-of-plane hysteresis loop and recoil loop of the as-patterned FePt BPM. The inset in (a) is FePt (001) rocking curve, whose FWHM is 7.26°. The ordering parameter of FePt is 0.48, and coercivity is 16.0 kOe. Delta H_C is 7.3 kOe and SFD is 34%.

There are limited papers related to the degradation of FePt films after patterning. Usually, the coercivity of the as-patterned FePt dots could not reach the expected value, which would be a few tesla. This fact suggests that the patterning process may cause degradation of the FePt properties. Disordered FePt phase region was found on the FePt patterned dots, and the coercivity could be significantly increased after post-annealing at a very high temperature.[32] Another key issue of the patterned media is the SFD. A wide

SFD seriously affects the definition of the recording bits and limits the recording density. The dot size distribution and anisotropy distribution are the major sources of the SFD. Exchange coupled composite (ECC)[33,34] effect could help narrowing the SFD of FePt BPM,[35] but the problem was sidestepped that the FePt dots were still far from uniform in properties.

To study the degradation of FePt dots caused by the pattern transfer process, we proposed and demonstrated that annealing the patterned samples in vacuum can increase the crystallinity of FePt and reduce its SFD.

The patterned sample was then annealed in vacuum for one hour at 350 ºC, which is the same as the deposition temperature for the continuous thin film. Although annealing the sample at higher temperature may further increase the ordering of FePt, it may also significantly change other properties of the film and the comparison would be invalid. Figure 4.15 (a) displays the XRD pattern and FePt (001) rocking curve of the annealed sample. Compared to the as-patterned one, ordering parameter increases from 0.48 to 0.57, and the FWHM of the FePt(001) rocking curve decreases from 7.26º to 6.81 º. Quality improvement is observed in the annealed FePt patterned dots, though it is still not as good as the continuous film.

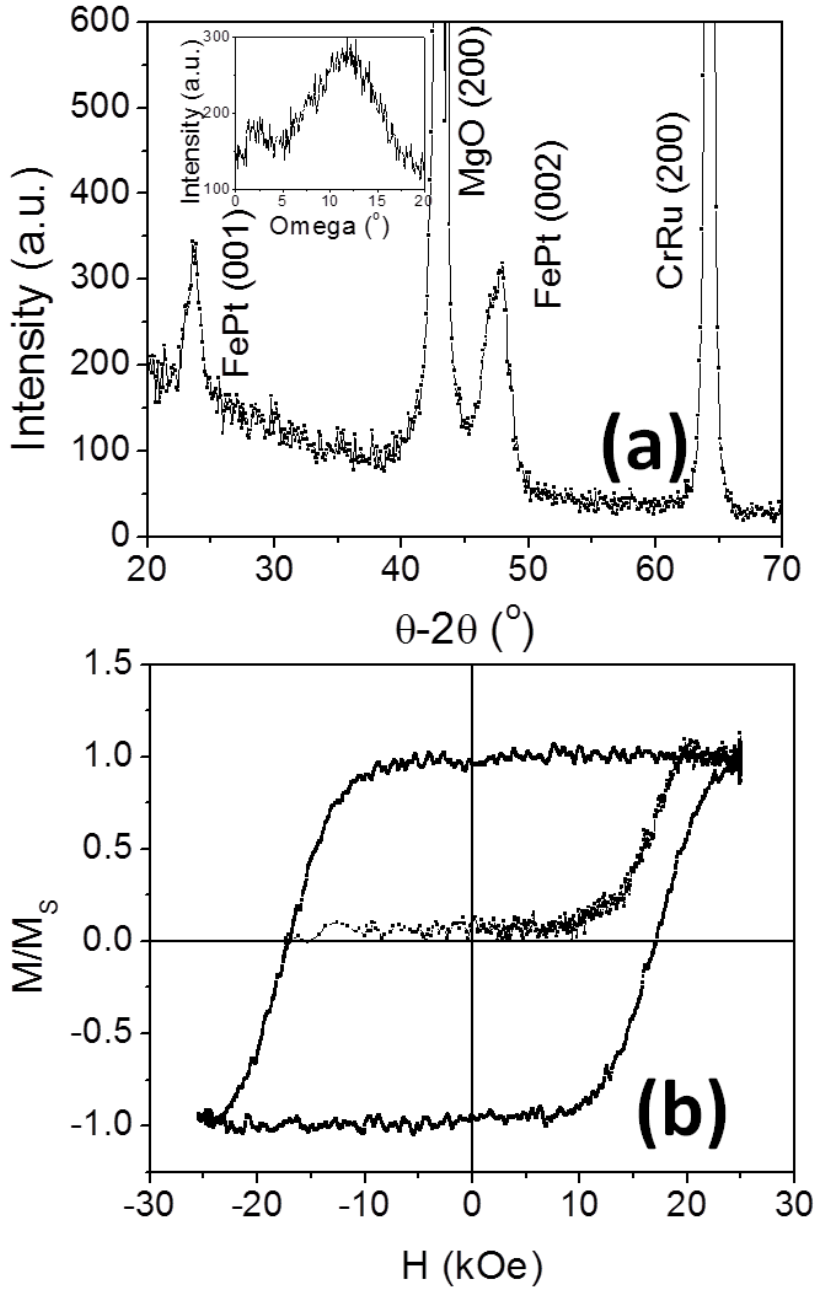

Figure 4.15 (a) The XRD spectra, (b) out-of-plane hysteresis loop and recoil loop of the annealed FePt BPM. The inset in (a) is FePt (001) rocking curve. The ordering parameter of FePt is 0.57, the FWHM of the rocking curve is 6.81°, and coercivity is 17.1 kOe. Delta HC is 3.4 kOe and SFD is 15%.

The out-of-plane hysteresis loop and recoil loop of the annealed sample are shown in Figure 4.15 (b). The coercivity is 17.1 kOe, but the ECC characteristic in the recoil loop is completely eliminated. The typical irreversible magnetization behavior observed is evidence of single domain switching. This may not imply that the FePt is fully $L1_0$

ordered. A possible explanation is that the soft regions of these dots are small in volume and they are fully exchange-coupled by the hard regions on the same FePt dot. ΔH_C is reduced from 7.3 kOe to 3.4 kOe and SFD drops from 34% to 15%. SFD is significantly decreased while the $L1_0$ ordering of FePt is increased and its easy-axis orientation distribution is reduced. These results demonstrate that post-annealing is an effective way to address the etching damage problem and could be a necessary step for FePt BPM fabrication in future.

All the data of the continuous film, as-patterned BPM and annealed BPM provided above are summarized in Table 2.2. Please note that all the listed S values should be smaller than the real values because of the existence of Pt (200) peak, which is partially overlapped with FePt (002) peak. Also, the real coercivity should be larger than 17.1 kOe, because the sample was not fully saturated at 25 kOe, which is the highest magnetic field of the measurement system in this work.

Table 4.1 Results summary of continuous film, as-patterned BPM and annealed BPM

	H_C (kOe)	Switching field distribution	Ordering parameter S	FWHM of FePt (001) rocking curve
Continuous film	3.82	-	0.72	5.95º
As-patterned BPM	16.0	34%	0.48	7.26º
Annealed BPM	17.1	15%	0.57	6.81º

4.4 Conclusion

In this chapter, FePt bit patterned media has been fabricated using nanoimprinting and block copolymer self-assemble, with dot size of sub-50 nm and sub-30 nm, respectively. AAO was used as a mold of nanoimprinting process to pattern FePt for the first time.

The crystallinity of FePt was partially damaged during patterning processes, e.g. the ion milling process. Annealing the patterned samples at 350 ºC, the $L1_0$ ordering of FePt was improved and SFD was narrowed. Using partially ordering FePt as the magnetic soft region for either ECC or graded BPM was not recommended.

Reference

[1] B. D. Terris and T. Thomson, J. Phys. D: Appl. Phys. 38, R199 (2005).

[2] B. D. Terris, J. Magn. Magn. Mater., 321, 512 (2009)

[3] D. Weller, and A. Moser, IEEE. Trans. Magn., 35, 4423 (1999).

[4] D. Weller, A. Moser, L. Folks, M. E. Best, W. Lee, M. F. Toney, M. Schwickert, J.-U. Thiele, and M. F. Doerner, IEEE Trans. Magn. 36, 10 (2000)

[5] S. Y. Chou, P. R. Krauss, and P. J. Renstrom, Appl. Phys. Lett., 67, 3114(1995).

[6] S. Y. Chou, P. R. Krauss, and P. J. Renstrom, J. Vac. Sci. Technol. B, 14,4129(1996).

[7] H. Schift, J. Vac. Sci. Technol. B, 26, 458(2008).

[8] L. J. Guo, Adv. Mater., 19, 495(2007).

[9] G. M. Schmid et al., J. Vac. Sci. Technol. 24, 1283(2006).

[10] W. L. Jen et al., Proc. SPIE, 6517, 6517 (2007).

[11] H. Sun, J. Liu, and et al.,Applied Surface Science, 254, 2955(2008).

[12] H. Ge,W. Wu,and et al., Nano Lett., 5, 179(2005).

[13] K. Naito, H. Hieda, M. Sakurai, Y. Kamata, and K. Asakawa, IEEE Trans. Magn. **38**, 1949 (2002).

[14] R. Ruiz, H. Kang, F. A. Detcheverry, E. Dobisz, D. S. Kercher, T. R. Albrecht, J. J. de Pablo, and P. F. Nealey, Science **321**, 936 (2008).

[15] H. Hieda, Y. Yanagita, A. Kikitsu, T. Maeda, and K. Naito, J. Photopolym. Sci. Technol. **19**, 425 (2006).

[16] B. Ma, H. Wang, H. Zhao, C. Sun, R. Acharya, and J. P. Wang, IEEE Trans. Magn. **46**, 2345 (2010).

[17] H. Wang, H. Zhao, O. Ugurlu, and J.P. Wang, , IEEE Magn. Lett., **3**, 450014 (2012).

[18] H. J. Park, M.G. Kang, and L.J. Guo, ACS nano, 3, 2601 (2009).

[19] Y.S. Kim, K. Lee, J.S. Lee, G.Y. Jung, and W.B. Kim, Nanotechnology, **19**, 365305, (2008).

[20] P.S. Lee, O.J. Lee, S.K. Hwang, S.H. Jung, S.E. Jee, and K.H. Lee, Chem. Mater, 17, 6181 (2005).

[21] M.T. Rahman , N.N. Shams, and C.H. Lai, Nanotechnology 19, 325302 (2008).

[22] M.T. Rahman , N.N. Shams, C.H. Lai, J. Fidler, and D. Suess, Phys. Rev. B, 81, 014418 (2010).

[23] H. Masuda, K. Yada, and A. Osaka, Jpn. J. Appl. Phys., 37, L1340 (1998).

[24] N. Roos, H. Schulz, M. Fink, K. Pfeiffer, F. Osenberg and H.-C. Scheer, Proceedings of SPIE-Emerging Lithographic Technologies VI, 4688 ,232 (2002).

[25] K.I. Nakamatsu, N. Yamada, K. Kanda, Y. Haruyama and S. Matsui, Jpn. J. Appl. Phys., 45, L954 (2006).

[26] K.J. Byeon, K.-Y. Yang and H. Lee, Microelectron. Eng. 84, 1003 (2007).

[27] A.P. Li, F. Muller, A. Birner, K. Nielsch, and U. gosele, J. Appl. Phys. 84, 6023 (1998).

[28] B. Ma, H. Wang, H. Zhao, C. Sun, R. Acharya, and J.P. Wang, J. Appl. Phys. 109, 083907 (2011).

[29] H. Hieda, Y. Yanagita, A. Kikitsu, T. Maeda, and K. Naito, J. Photopolym. Sci. Technol. **19**, 425 (2006).

[30] H. Wang, T. Rahman, H. Zhao, Y. Isowaki, Y. Kamata, A. Kikitsu, and J.P. Wang, J. Appl. Phys. 109, 07B754 (2011).

[31] I. Tagawa and Y. Nakamura, IEEE Trans. Magn. , 27, 4975 (1991).

[32] T Bublat and D Goll,J. Appl. Phys. **110**, 073908 (2011).

[33] R. H. Victora and X. Shen, IEEE Trans. Magn. 41, 2828 (2005).

[34] J. P. Wang, W. K. Shen, and J. Bai, IEEE Trans. Magn. **41**, 3181 (2005).

[35] A. T. McCallum, P. Krone, F. Springer, C. Brombacher, M. Albrecht, E. Dobisz, M. Grobis, D. Weller, and O. Hellwig, Appl. Phys. Lett. **98**, 242503 (2011)

Chapter 5. FEPT TYPE ECC AND GRADED BIT PATTERNED MEDIA

5.1 Introduction

Bit patterned media (BPM) with exchange coupled composite (ECC) or graded structure has been widely studied to improve the writing capability. [1,2,3,4,5] As shown in Figure 5.1, the fabrication of ECC or graded FePt BPM contains several major stages. First step is the fabrication of the continuous film. Its quality is so critical that it substantially determines the magnetic properties of BPM. The surface roughness of recording media is required to be no larger than 0.3 nm. A planarization process can be employed to improve the flatness of media surface. However, it may not work for ECC or graded type BPM, if the film surface is not flat enough before patterning. Every single bit has to be kept intact; otherwise its properties may change significantly. For example, if two graded bits are not at the same height level, after planarization, the upper one will lose part of its graded region and its switching field will be different from the other bit. Therefore, for ECC or graded BPM, the continuous film must have a sufficiently flat surface, however, there is no report focusing on the continuous magnetic thin film designed for BPM.

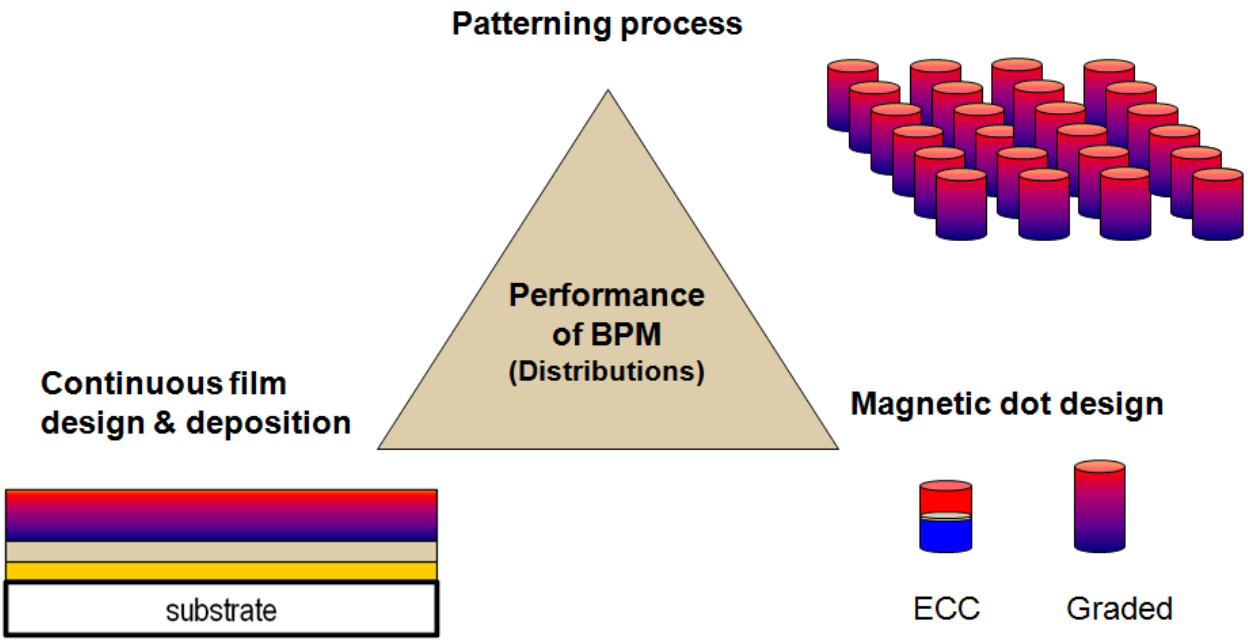

Figure 5.1 Major stages and trilemma of FePt ECC or graded BPM fabrication

In this work, FePt-type BPM with both ECC and graded structures with 25 nm dot size are fabricated and studied. Several challenges have been addressed in fabricating FePt BPM, including the ways to prepare the FePt continuous films with a well-controlled graded anisotropy and small surface roughness. Di-block copolymer lithography was used to pattern the FePt based continuous films over 2-inch-diameter substrates. One of the key findings of this work is that either varying deposition temperature or adjusting the composition during sputtering process is not suitable to create a graded continuous film for BPM, because both these methods caused large surface roughness. A layer inter-diffusion process is recommended for the graded continuous film fabrication, with which the thin film surface is confirmed to be flat. Figure 5.2 schematically demonstrate this process.

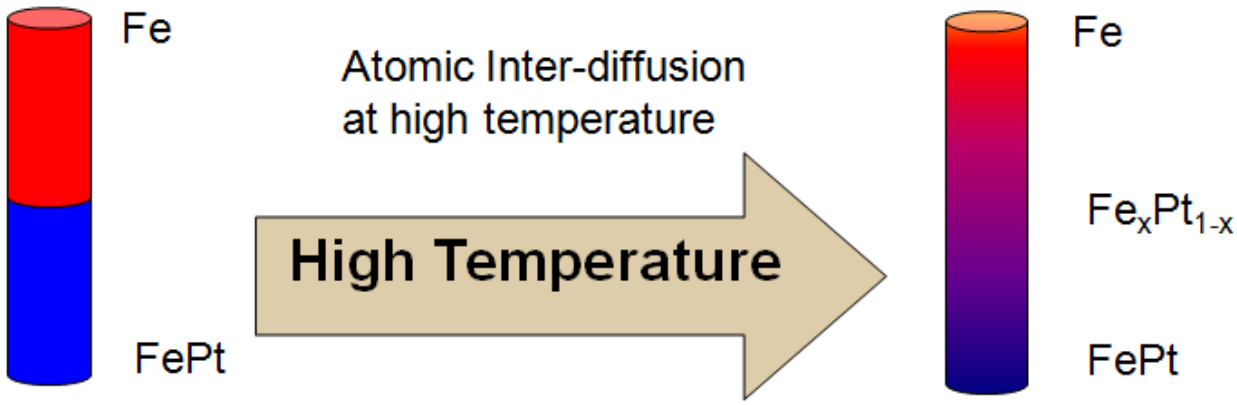

Figure 5.2 Formation of FePt/Fe graded interface.

As shown in Figure 5.2, an FePt/Fe bi-layer ECC continuous film was fabricated at first. Then, post anneal this film at high temperature to make the Fe and FePt inter-diffused between each other and create a compositionally graded interface.

5.2 Development of FePt type continuous film with composite structure

The continuous FePt film and graded films were deposited on single crystal MgO substrates using a DC magnetron sputtering system with base pressure better than $1x10^{-7}$ torr. The structure of the samples are MgO sub/Cr/Pt/recording layer/Ru(3 nm). Each layer was sputtered from an elemental target. The Ru layer was deposited at room temperature to protect against oxidation. Cr/Pt underlayer was fabricated at 350 ºC. Cr was deposited as a seed layer to ensure the epitaxial growth of FePt continuous film, because the FePt forms an island-like structure when it is directly sputtered on MgO substrate at high temperature. [6] The Pt interlayer was designed to prevent the inter-diffusion between Cr and FePt.[7] The structure of recording layer varies according to the types of samples. For all samples, FePt hard magnetic layer was fabricated at 350 ºC with an atomic ratio of 1 : 1.

The sample names and magnetic layer structures of all samples are listed in Table 5.1.

Table 5.1 The recording layer structure and fabrication condition of all continuous films.

continuous films	FePt layer thickness	Soft\graded layer fabrication temperature	Annealing temperature
Hard I	10nm	N	N
Hard II	5nm	N	N
ECC	5nm	Fe(5nm), Room temperature	N

Graded I-200	5nm	Fe(5nm), Room temperature	200 °C
Graded I-300	5nm	Fe(5nm), Room temperature	300 °C
Graded II	5nm	Fe(5nm), 350°C	N
Graded III	5nm	Fe_xPt_{1-x}(5nm), 350°C (x gradually increased from 0 to 1)	N

Sample 'Hard I' and 'Hard II' are hard magnetic films. They only have FePt as recording layer, with thickness of 10 nm and 5 nm only. Sample 'ECC' has FePt(5 nm)/Fe(5 nm) bi-layer structure, in which the Fe soft layer was deposited at room temperature. There are three types of graded films, whose recording layer's thicknesses are all 10 nm. The basic structure of the graded recording layers is FePt (5 nm)/ graded layer (5 nm). For Graded I type, a 5-nm-thick Fe layer was deposited on FePt at room temperature. Then, the sample was annealed in vacuum for one hour to create the graded structure between Fe and FePt layers. [8] In other words, 'Graded I' was achieved by annealing the 'ECC' sample for one hour. 'Graded I-200' was annealed at 200 ºC. 'Graded I-300' was annealed at 300 ºC. Different annealing temperature creates different graded FePt/Fe structures. For 'Graded II', 5 nm-thick Fe layer was deposited right after the deposition of FePt at 350 ºC. In this case, the Fe ad-atoms have much more energy and longer diffusion length compared to the case of 'Graded I', because of the kinetic energy of as-deposited Fe atoms. Thicker graded region was expected in Graded II. For 'Graded III', its recording layer's structure is FePt (5 nm)/Fe_xPt_{1-x} (5 nm). During the deposition of Fe_xPt_{1-x} layer, the temperature was maintained at 350 ºC, and the value of x was gradually increased from 0.5 to 1 by adjusting the sputtering power of Fe and Pt, which means the composition of the graded layer gradually changed from $Fe_{50}Pt_{50}$ to Fe.

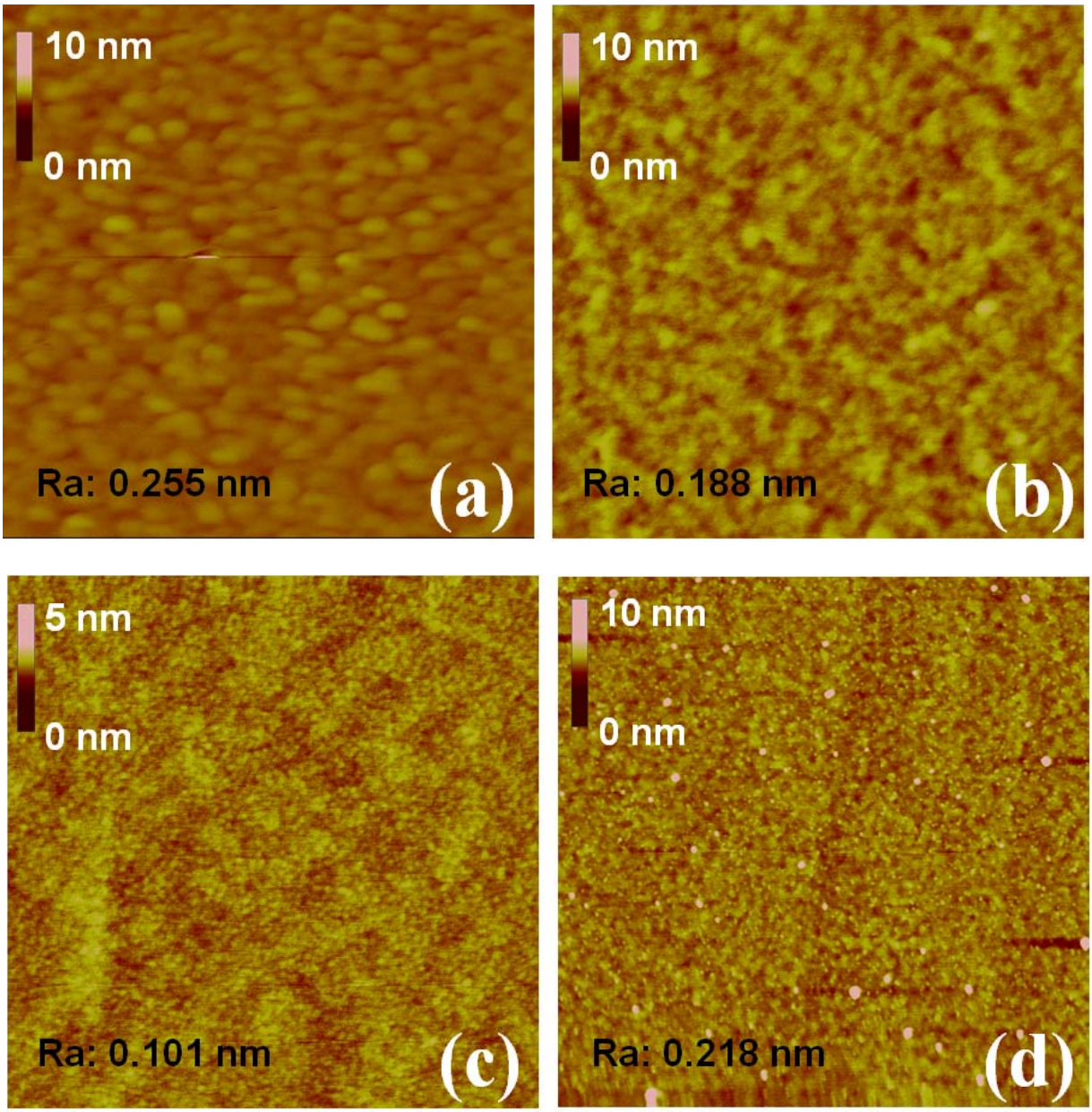
10 nm
0 nm
Ra: 0.255 nm
(a)
10 nm
0 nm
Ra: 0.188 nm
(b)
5 nm
0 nm
Ra: 0.101 nm
(c)
10 nm
0 nm
Ra: 0.218 nm
(d)

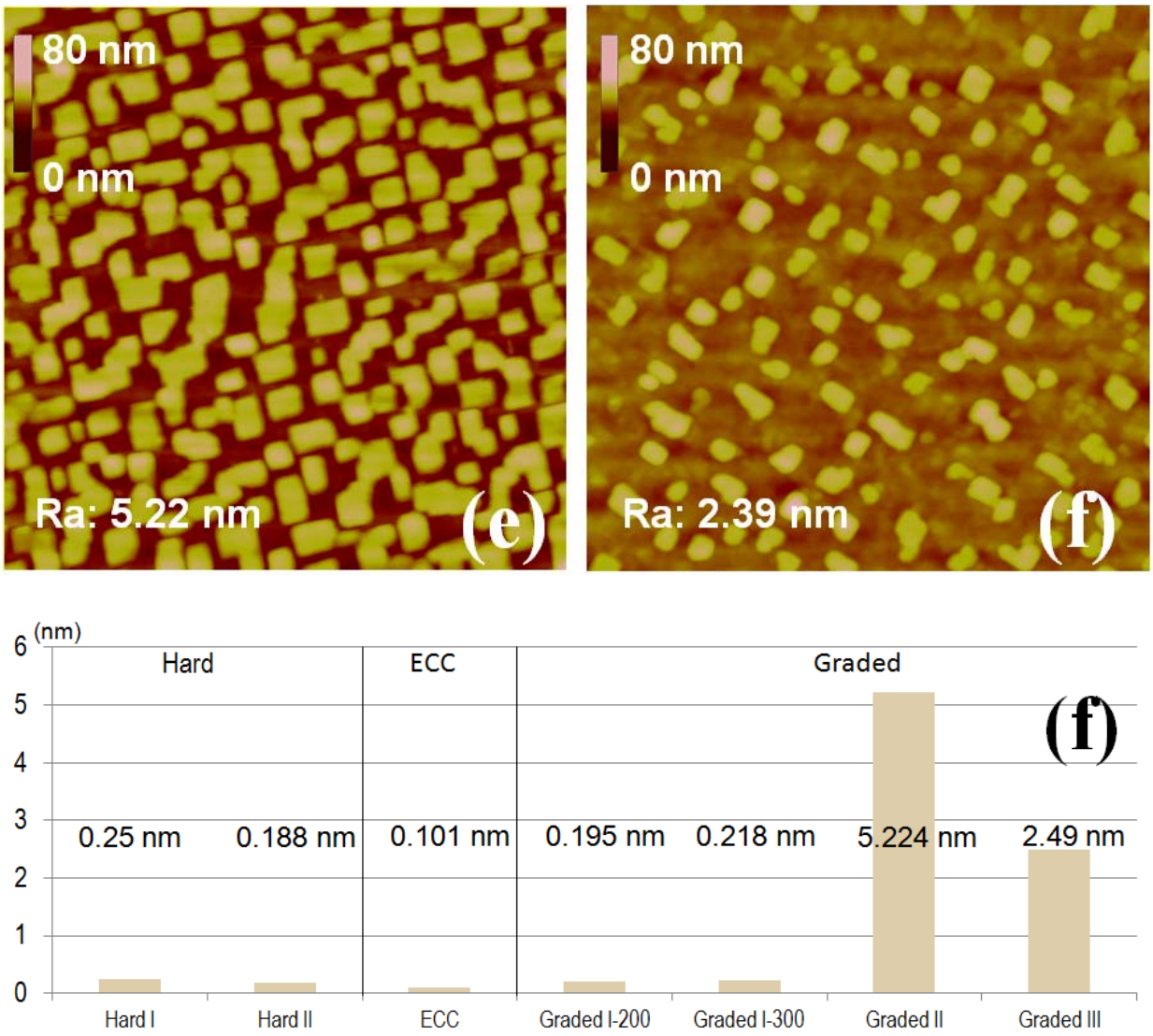

Figure 5.3 The AFM images of (a) 'Hard I', (b) 'Hard II', (c) 'ECC', (d) 'Graded I-300', (e) 'Graded II' and (f) 'Graded III'. (e) Surface roughness of all continuous films.

The surface roughness of sample 'Hard I', 'Hard II', 'ECC', 'Graded I-200', 'Graded I-300', 'Graded II' and 'Graded III' are 0.25 nm, 0.188nm, 0.101 nm, 0.195 nm, 0.218 nm, 5.224 nm and 2.49 nm, respectively. The chart in Figure 5.3 (e) shows these values corresponding to the samples and reveals the huge difference of surface roughness. Sample 'Hard I', 'Hard II', 'ECC' and 'Graded I' type have relatively small roughness while 'Graded II' and 'Graded III' have very rough surfaces, especially 'Graded II'. The AFM topography images of sample 'Hard' and 'Graded I-300' are shown in Figure 5.3 (a) and (b), respectively. Depositing 5 nm Fe on 5 nm FePt to fabricate 'ECC' sample reduced the surface roughness to 0.101 nm. The 'Graded I-300', which was annealed at 300 °C, is still smoother than sample 'Hard I'.

'Graded II' and 'Graded III' are very rough and their Fe layers may not even be continuous. Large isolated grains are observed in the AFM image of 'Graded II' in Figure 5.3 (e). The height of the islands is as large as tens of nanometers. The large roughness of 5.224 nm makes it impossible for recording media application. 'Graded III', whose AFM image is shown in figure 2 (d), also has large islands, compared to 'Graded II', its islands are smaller and the spacing between the islands is larger. Since the Fe_xPt_{1-x} layer of 'Graded III' has more Fe near the surface, the island structure could be formed when the Fe concentration exceeded a certain level. A conclusion can be drawn that Fe-rich film formed large islands on FePt when deposited at high temperature. A possible explanation is that Fe layer could be BCC structure, whose surface energy is much larger than that of FePt[9]. The surface energy of $L1_0$ FePt and bcc Fe are summarized in Table 5.2, according to Ref. 9.

Table 5.2 Surface energy of $L1_0$ FePt and bcc Fe.

	Surface energy (eV/atom)		
	(001)	(111)	(110)
$L1_0$ FePt	0.991	0.675	1.440
Fe (bcc)	1.261	2.355	0.872

The surface energy of $L1_0$ FePt (001) plane is 0.991 eV/atom. When Fe was deposited at low temperature, it formed (110) texture,[10] whose surface energy is lower than that of FePt (001) plane. To minimize the energy of whole system, Fe smoothly covered the surface of (001) textured FePt. But high temperature deposition would induce the epitaxial growth of Fe on (001) textured FePt. Hence, when Fe was deposited at high temperature, it formed (001) texture, whose surface energy is higher than that of FePt (001) plane. Fe atoms formed island-like structure to minimize the surface energy. Therefore, to fabricate FePt/Fe continuous film, Fe has to be deposited at a relatively low temperature.

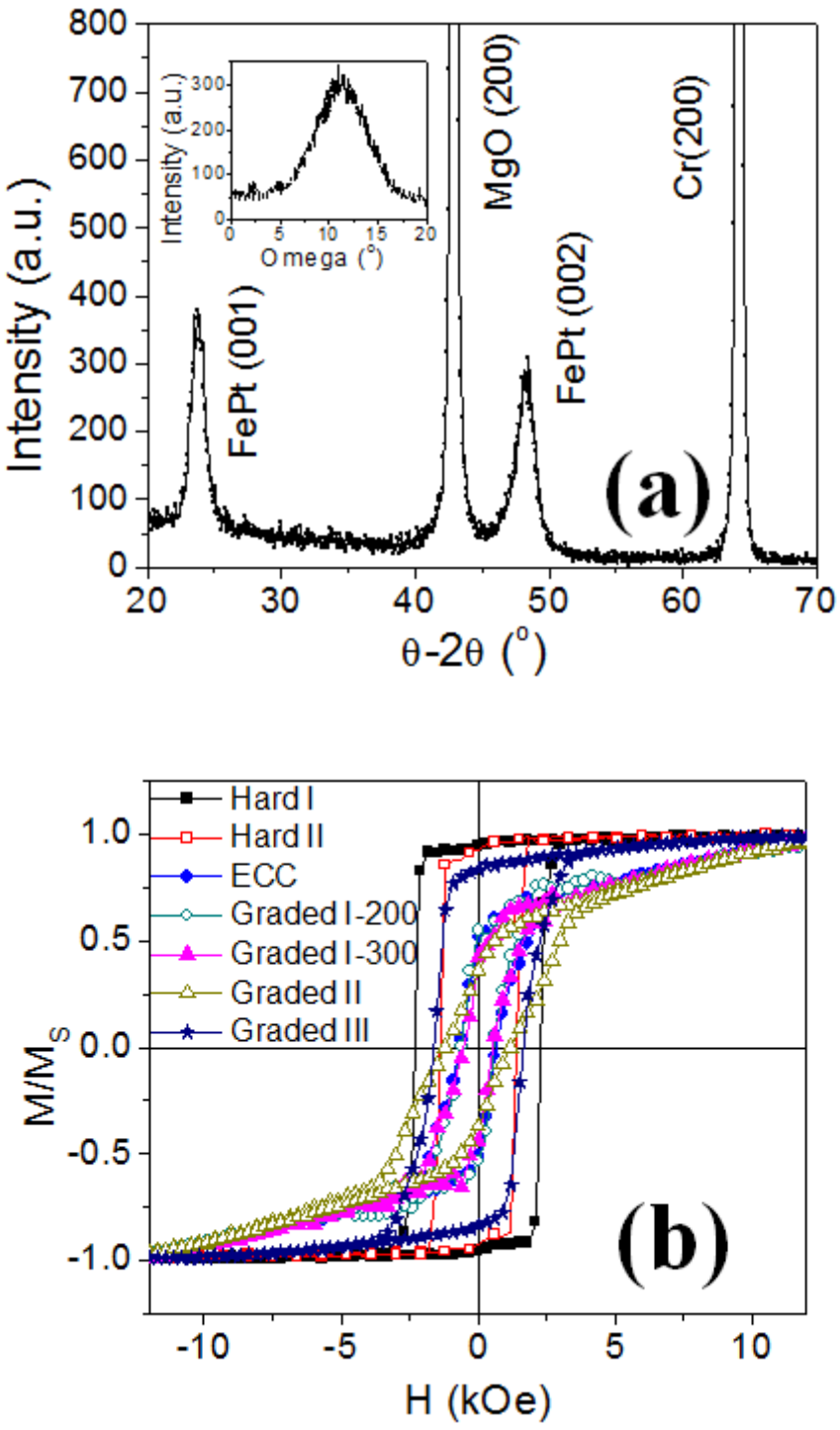

Figure 5.4 (a) XRD spectra of sample 'Hard I'; (b) Out-of-plane hysteresis loops of the continuous films sample 'Hard I', 'Hard II', 'ECC', 'Graded I-200', 'Graded I-300', 'Graded II' and 'Graded III'. Their HC values are 2.28 kOe, 1.38 kOe, 0.66 kOe, 0.59 kOe, 0.52 kOe, 1.18 kOe, and 1.62 kOe respectively.

Figure 5.4 (a) shows the XRD spectra of sample 'Hard I', and confirms that it is well ordered and has (001) texture. According to the intensity ratio of (001) peak to (002) peak, its ordering parameter S is 0.72, [11] but we need to consider that the 3 nm Pt interlayer generates a weak Pt (200) peak overlapped with the FePt (002) peak, and contributes to the intensity of the latter. Therefore, the calculated S value is underestimated. The inset in Figure 5.4 (a) is FePt (001) rocking curve. Its FWHM is 5.95º. The out-of-plane hysteresis loops of continuous films are shown in figure 2 (b). The HC of the continuous films of sample 'Hard I', 'Hard II', 'ECC', 'Graded I-200', 'Graded I-300', 'Graded II, and 'Graded III' are 2.28 kOe, 1.38 kOe, 0.66 kOe, 0.59 kOe, 0.52 kOe, 1.18 kOe, and 1.62 kOe respectively.

5.3 FePt type ECC and graded bit patterned media

The continuous films were then patterned to dot arrays using di-block copolymer self-assemble masks followed by an ion milling etching process as described in reference 1.

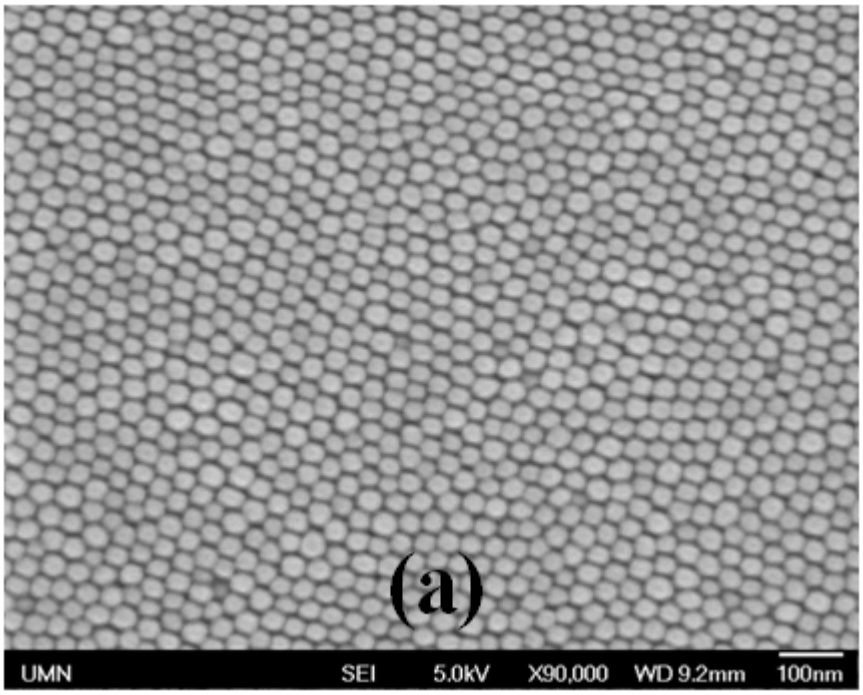

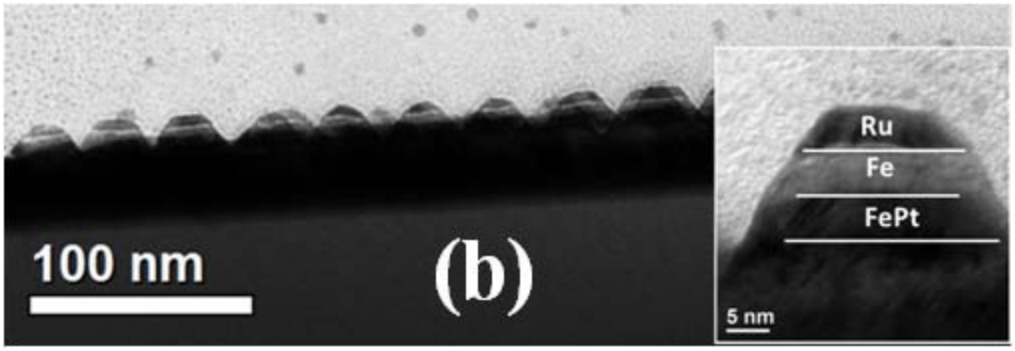

Figure 5.5 SEM plan-view image of the patterned 'ECC' film. The inset is a cross-sectional TEM image of a single ECC dot.

Figure 5.5 shows the SEM plan-view image of the patterned 'ECC' sample, and the inset is a cross-sectional TEM image of a single ECC dot. The center to center distance of the magnetic dots is 37 nm, and the dot size is around 25 nm. The cross-sectional image shows that a patterned dot is conical frustum. Therefore the dot size in the plan-view image is around 30 nm. The other patterned samples are structurally similar to patterned 'ECC' sample.

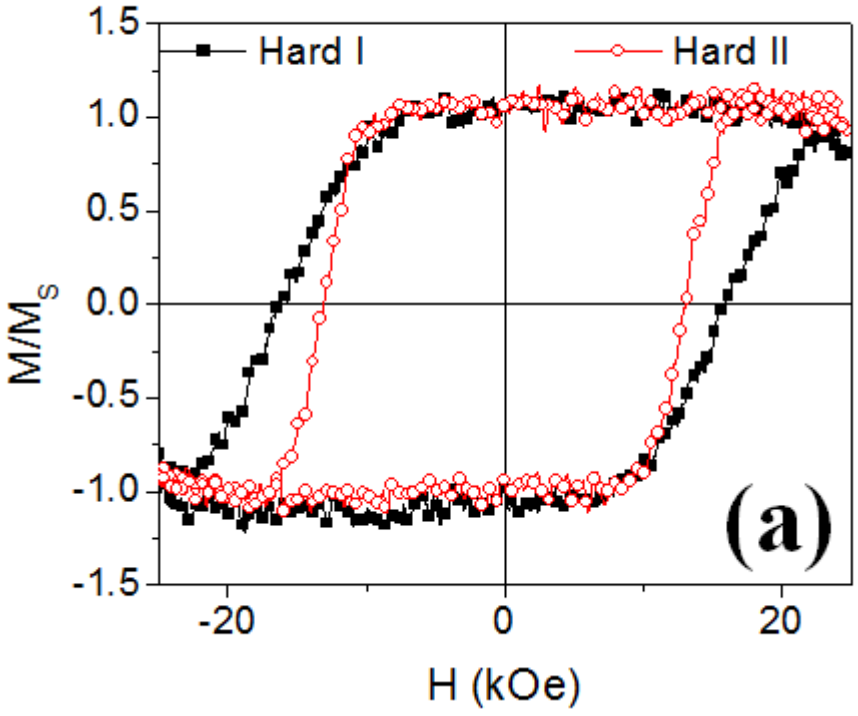

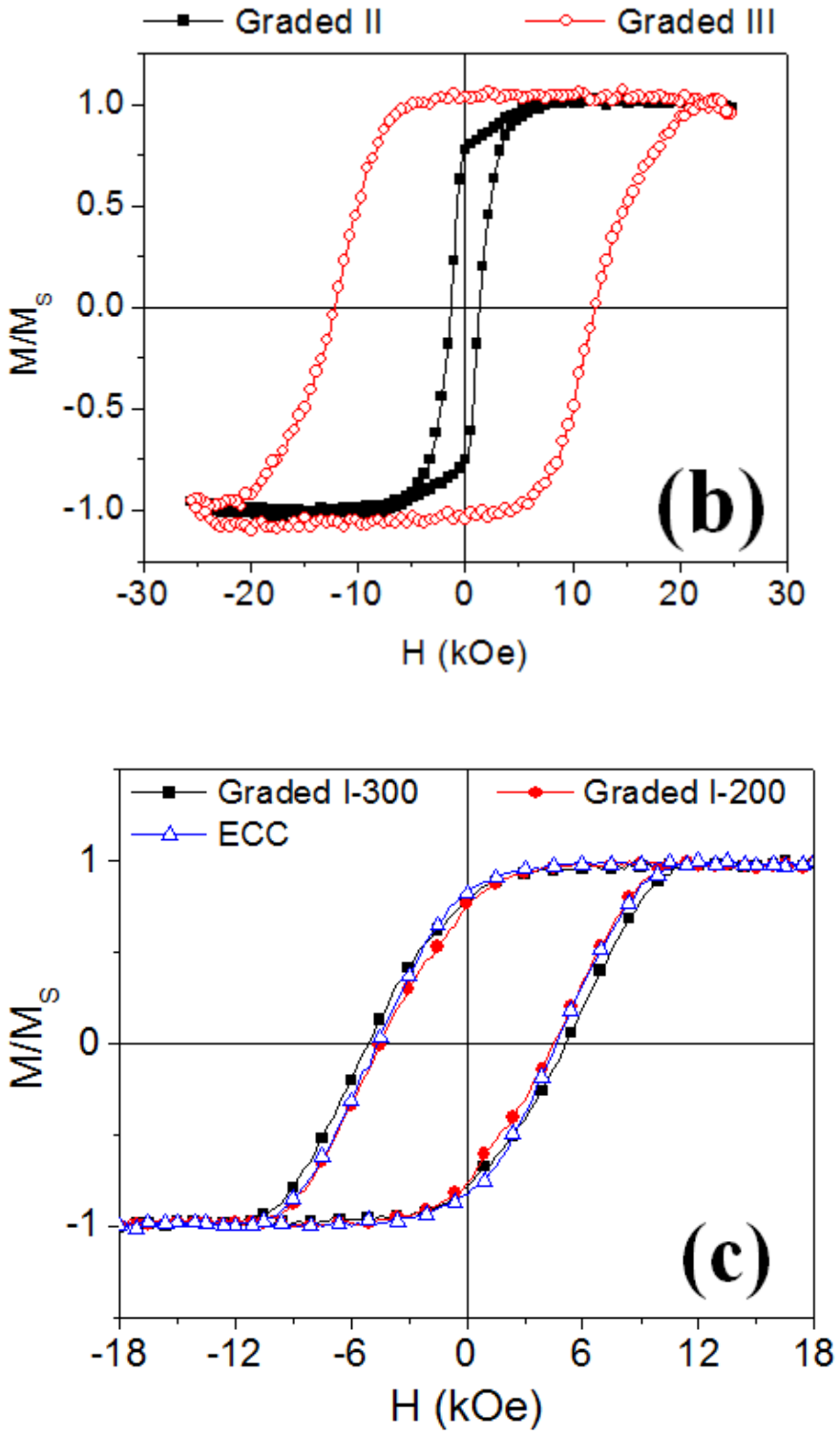

Figure 5.6 The out-of-plane hysteresis loops of (a) patterned 'Hard I' and 'Hard II', (b) patterned 'Graded II' and 'Graded III', (c) patterned 'ECC', 'Graded I-200', and 'Graded I-300'. Their H_C are 16 kOe, 13 kOe, 1.3 kOe, 12.1 kOe, 4.64 kOe, 4.47 kOe and 5.08 kOe, respectively.

The H_C of the patterned 'Hard I', 'Hard II', 'ECC', 'Graded I-200', 'Graded I-300', 'Graded II, and 'Graded III' are 16 kOe, 13 kOe, 1.3 kOe, 12.1 kOe, 4.64 kOe, 4.47 kOe and 5.08 kOe, respectively. Their out-of-plane hysteresis loops are shown in Figure 5.6. The H_C of these the patterned 'ECC', 'Graded I-200' and 'Graded I-300', whose continuous films had flat surface, are less than one third of the patterned 'Hard I' sample's H_C, and also less than half of the patterned 'Hard II' sample's H_C. However, the condition of patterned 'Graded II' and 'Graded III', whose continuous films were extremely rough, is totally different. For 'Graded II', both coercivity and the shape of MH loop did not significantly change after patterning. It suggests that the even exchange decoupling is not realized in the patterned 'Graded II'. For patterned 'Graded III', its coercivity is as large as pattered 'Hard II'. It indicates that the expected graded structure has no effect on this sample. It is again confirmed that a rough continuous film is not suitable for BPM fabrication, and the inter-layer diffusion process works very well.

The thermal energy barrier (ΔE) values of patterned 'ECC', 'Graded I-200' and 'Graded I-300' are obtained by measuring the time-dependant switching field from thermal decay and fitting to Sharrock equation. The results are listed in Table 5.3. The ΔE of the patterned Hard sample was not obtained because it could not be saturated. It should be pointed out that the error bar for the estimation of the thermal energy barrier is large based on this available method. In future, to find an accurate measurement method is highly desirable for this research.

Table 5.3 H_C and ΔE of patterned 'ECC', 'GRADED I-200' and 'GRADED I-300'

Sample	H_C (kOe)	Energy barrier ΔE (k_BT)
Patterned ECC	4.64	190
Patterned Graded I-200	4.47	230
Patterned Graded I-300	5.08	234

The H_C of these three patterned samples are very close to each other. But the ΔE of the patterned graded samples is significantly larger than that of the patterned 'ECC' sample. This is reasonable, because the annealing process created a compositionally graded interface between FePt and Fe, and the volume ratio of the relatively hard region increased. Therefore the graded samples are more thermally stable than the ECC sample.

Although the ΔE values of the two patterned graded samples are almost the same, patterned 'Graded I-200' has a smaller H_C than patterned 'ECC' does, while patterned 'Graded I-300' has a larger H_C. It is clear that different annealing process created different graded structures.

Figure 5.7 shows the DCD curve of the patterned 'ECC' sample obtained from MFM analysis. The MFM images were taken after saturating the sample followed by applying different reverse fields, ranging from 0 to -15 kOe.[12] The numbers of bright and dark dots were counted and converted to the Mr/Ms value by calculating the portion of the reversed dots. Then the Mr/Ms vs. reversed fields was plotted as the DCD curve. The MFM images of -1 kOe, -6 kOe and -9 kOe reverse fields are shown in Figure 5.7 (b), (c) and (d), respectively.

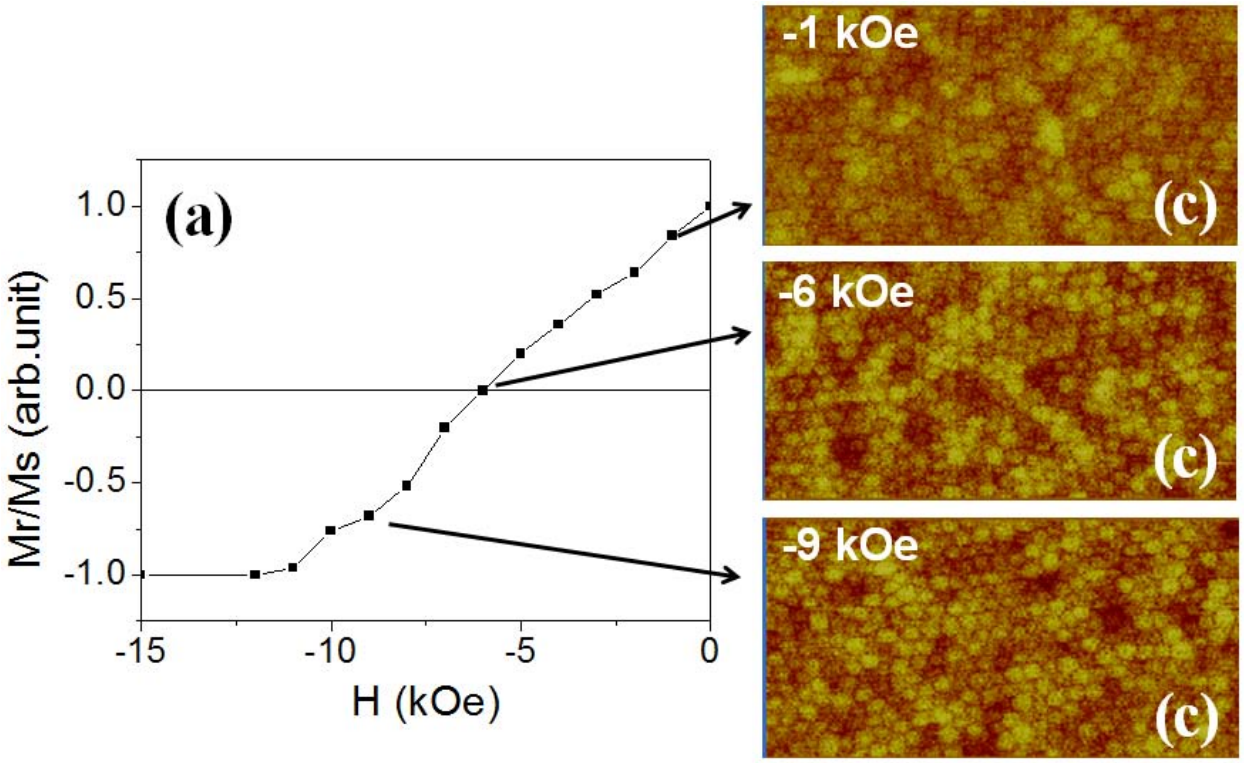

Figure 5.7 (a) DCD curve obtained from MFM images of patterned 'ECC' sample, and MFM images with different remanent states: after applied reverse field (b) -1 kOe, (c) -6 kOe and (d) -9 kOe, respectively. The DCD curve was plotted by counting the number of the reversed magnetic islands under different remanent states from MFM images.

From these MFM images, we can find that the irreversible switching, which was represented by the bright dots in the MFM pattern, happened even when the reverse field was just -1 kOe. As the reverse field increasing to -6 kOe, lots of small clusters appeared, in which the adjacent bits have the similar contrast, indicating the strong interaction between the bits. According to the two-spin model10, when the reverse field was applied to the ECC bit, the magnetization of the soft region fell down before the magnetization of the hard region started to rotate. At this stage, the soft region had a lateral dipole field which might be applied to the neighbors. Therefore, when the external field was smaller than its intrinsic switching field, the ECC bit generated lateral dipole field to its neighbors and assisted the switching. Meanwhile, its own switching was helped by the neighbors too. This phenomenon suggests that the dipole interaction from neighboring bits may play an important role in the reversal process of the bit patterned media and increase the switching field distribution (SFD). The saturation magnetization (MS) of this sample was 810 emu/cm^3 before patterning. The inter-diffusion between Pt layer and FePt layer made the Ms value lower than expected. The maximum demagnetization field can be roughly estimated as large as around $4\pi[M_S \bullet (d^2/D^2)]$= 7141 Oe, where d is the bit size and D is the pitch size. It is desirable to further reduce the M_S in order to reduce the magnetostatic interaction.

5.4 Conclusion

In this work, depositing Fe on FePt at room temperature and then annealing it to create graded anisotropy through the layer inter-diffusion process was proposed and demonstrated to fabricate FePt graded BPM. An Fe-rich film would form a very rough surface with extremely large grains when deposited onto FePt at high temperature. Annealing the FePt/Fe film, whose Fe layer was deposited at room temperature, didn't increase the surface roughness, and was recommended for the fabrication of future FePt bit patterned media with graded structure. Compared to the FePt BPM with ECC structure, FePt BPM with graded structure showed smaller H_C and larger thermal energy barrier. In ECC BPM, the dipole interaction may play an important role in the switching process of the sample.

Reference

[1] H. Wang, T. Rahman, H. Zhao, Y. Isowaki, Y. Kamata, A. Kikitsu, and J.P Wang, J. Appl. Phys. **109**, 07B754 (2011).

[2] P. Krone, D. Makarov, T. Schrefl, and M. Albrecht, Appl. Phys. Lett. **97**, 082501 (2010).

[3] A. T. McCallum, P. Krone, F. Springer, C. Brombacher, M. Albrecht, E. Dobisz, M. Grobis, D. Weller, and O. Hellwig, Appl. Phys. Lett. **98**, 242503 (2011)

[4] P. Sharma, N. Kaushik, A. Makino, M. Esashi, and A. Inoue, J. Appl. Phys. **109**, 07B908 (2011).

[5] J. E. Davies, P. Morrow, C. L. Dennis, J. W. Lau, B. McMorran, A. Cochran, J. Unguris, R. K. Dumas, P. Greene, and K. Liu, J. Appl. Phys. **109**, 07B909 (2011).

[6] B. Ma, H. Wang, H. Zhao, C. Sun, R. Acharya, and J. P. Wang, J. Appl. Phys. **109**, 083907 (2011).

[7] J. S. Chen, Y. Xu, and J. P. Wang, J. Appl. Phys. **93**, 1661 (2003).

[8] D. Goll, A. Breitling, L. Gu, P. A. van Aken, and W. Sigle, J. Appl. Phys. **104**, 083903 (2008).

[9] A. Dannenberg, M. E. Gruner, A. Hucht, and P. Entel, Phys. Rev. B, 80, 245438 (2009).

[10] B. Ma, H. Wang, H. Zhao, C. Sun, R. Acharya, and J. P. Wang, J. Appl. Phys. vol. 109, pp. 083907, 2011.

[11] S. Okamoto, N. Kikuchi, O. Kitakamo, T. Miyazaki, Y. Shimada, and K. Fukamichi, Phys. Rev. B. **66**, 024413 (2002).

[12] H. Wang, W. Li, T. Rahman, H. Zhao, J. Ding, Y. Chen, and J.P. Wang, J. Appl. Phys., 111, 07B914 (2012).

Chapter 6. EMBEDDED MASK PATTERNING: A NANOPATTERNING PROCESS TO FABRICATE FEPT GRANULAR

6.1 Introduction

In future extremely high density magnetic recording, the center distance between magnetic grains of hard disk media is required to be shrunk further down to sub 4 nm to support recording areal density up to 5 Terabit/in^2 while the magnetic is still kept thermally stable. FePt, which is chemically stable and has ultra-high magnetocrystalline anisotropy of $7x10^7$ erg/cc, is considered as a promising candidate for future recording media materials. In principle, a fully $L1_0$ ordered FePt grain maintains thermal stability for sizes as small as 3nm. [1] Since the FePt media has a large switching field, in order to switch a FePt recording bit, traditional techniques will not work as the head field is not large enough. Heat Assisted Magnetic Recording (HAMR), [2, 3] Exchange Couple Composite (ECC) media [4, 5], and graded media [6, 7], were proposed to decrease the switching field, and experiments have confirmed their effectiveness. HAMR has been more promising to support extremely high recording density with the recent demonstration of 1 Terabit/in^2 areal density by Seagate Technology. [8]

The key challenge of fabricating high density FePt media is to fabricate a highly $L1_0$ ordered FePt granular thin film with extremely small grain size and good (001) texture. As shown in Table 2.1, Granz et al. successfully reduced the FePt grain size down to 2.5 nm by depositing the FePtB film at room temperature, but the FePt was in disordered phase with superparamagnetic behavior. [9] Zhang et al. fabricated FePt-Ag-C film at 550 ^oC and the coercivity was 35 kOe. [10] In their work, the FePt grain size was 6.2 nm. Also using 550 ^oC as the depositioin temperature, Mosendz et al. created FePt-Ag-C media with a coercivity of as high as 48 kOe, but the grain size increased to 7.2 nm [11]. Dong et al. created sub-6 nm FePt grains with a coercivity of 21.5 kOe by depositing FePt-SiN_x-C film at a relatively low temperature of 380 ^oC, however, the grains were not well isolated [12]. Using RuAl as an underlayer and setting the fabrication temperature to 350 ^oC, Shen et al. achieved 6.6 nm FePt grains with a coercivity of 8 kOe. [13] A dilemma for the fabrication of FePt media with desirable properties is that a high temperature deposition

leads to good $L1_0$ ordering thus high coercivity, but results in large grain sizes, while a low temperature deposition leads to small grain sizes, but results in poor $L1_0$ ordering thus low coercivity. Optimizing the deposition parameters and searching for doping materials may help improve the performances, but still cannot solve this dilemma completely. In order to solve this problem, a fundamentally new process is required to break down the interlock between the requirements for small grain sizes and large coercivity for FePt HAMR media.

Table 6.1 A brief summary of FePt granular media fabrication

	Grain size (nm)	**H_C (kOe)**	**Fabrication temperature**
FePt-B(-Ag)	2.5	0.05, disordered	Room temperature,.
FePt-Ag-C	6.2	35	550 ^{o}C,
FePt-Ag-C	7.2	48	500-550 ^{o}C
FePt-SiN_x-C	5.5 (not well isolated)	21.5	380 ^{o}C
FePt-Cu	6	8.0	350 ^{o}C

In this work, we propose and experimentally demonstrate an Embedded Mask Patterning (EMP) process which can solve this dilemma. Figure 6.1 schematically shows the steps for EMP process. The basic four steps of this process are as follows:

1) deposit a highly L10 ordered FePt continuous film at high temperature;

2) tdeposit an embedded mask layer (e.g. Ru-SiO2) with ultra small grain size and short center to center distance on top of the FePt continuous film;

3) remove the SiO_2 grain boundary and form Ru dot array mask layer using a reactive etching process;

4) transfer the Ru dot array pattern of the mask layer down to highly ordered FePt layer and form the FePt layer with large coercivity and small grain size;

This process has several advantages over the conventional media fabrication process. In this EMP process, the definition of the properties of the magnetic layer is disconnected from the definition of the grain size and grain boundary, while still using the sputtering process. The mean grain size of the embedded layer could be reduced to sub-3 nm by optimizing the granular structure. More importantly, unlike other processes to prepare the hard mask by spin-coating or other wet process, this process is compatible with today's

media fabrication process since the whole process can be done in vacuum. In principle, the etching rate could be as fast as the deposition rate, which will at least maintain the hard disk fabrication yield (number of disks per hour).

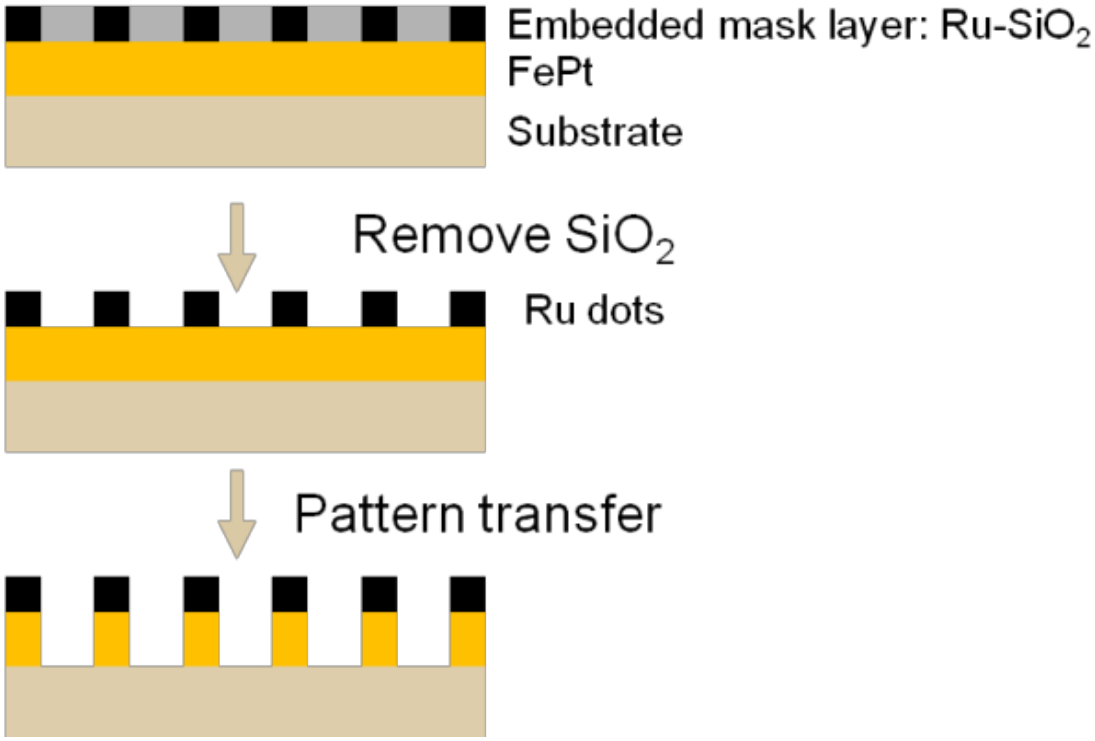

Figure 6.1 The schematic drawing of the EMP process. Step one: Highly $L1_0$ ordered FePt continuous layer was deposited on the substrate; Step two: The embedded mask layer (Ru-SiO_2) with a fine granular structure was deposited on the $L1_0$ ordered FePt continuous film. Step three: The SiO_2 of hard mask layer was removed using a reactive ion etching process (RIE). Step four: The Ru dots array pattern was transferred to FePt layer using a RIE process. All four steps could be done in vacuum.

6.2 Experiments and discussion

The complete stack structure of the sample is (001) MgO substrate/Cr(12nm)/Pt(3nm)/FePt(5nm)/Ru-SiO_2(3nm), which was prepared by an eight-target ultra high vacuum magnetron sputtering system with a base pressure better than $1x10^{-7}$ Torr. Cr layer was deposited as a seed layer to ensure the epitaxial growth of the continuous film, [14] because the FePt layer tends to form an island-like structure when it is directly deposited on MgO substrate at high substrate temperature. [15,16] The Pt interlayer was designed to prevents the interlayer diffusion between the Cr and FePt layer. [17] The atomic ratio of Fe and Pt was set as 1:1 for FePt layer. The substrate was heated to 450 oC before the deposition. The Ru-SiO2 embedded mask layer was then deposited on top of the FePt layer by co-sputtering Ru and SiO2 targets with volume ratio of 1:1.

Then the SiO_2 boundary was selectively removed using a reactive ion etching (RIE) process with CF_4 and CHF_3. The embedded mask layer was converted to a dot array hard mask. Then the dot array pattern was transferred to FePt film using a methanol gas combined with argon gas.

Figure 6.2 (a) shows the granular structure of Ru-SiO_2 embedded mask layer which was directly deposited on the carbon film of a TEM grid. The Ru grains are well separated by the SiO_2 grain boundary. In this work, the grain boundary was purposely made wide to ensure the pattern transfer process successful. Figure 6.2 (b) shows the out-of-plane hysteresis loop of the FePt continuous film of the sample with the stack structure described above. It shows a typical loop of a continuous film with a sharp switching.

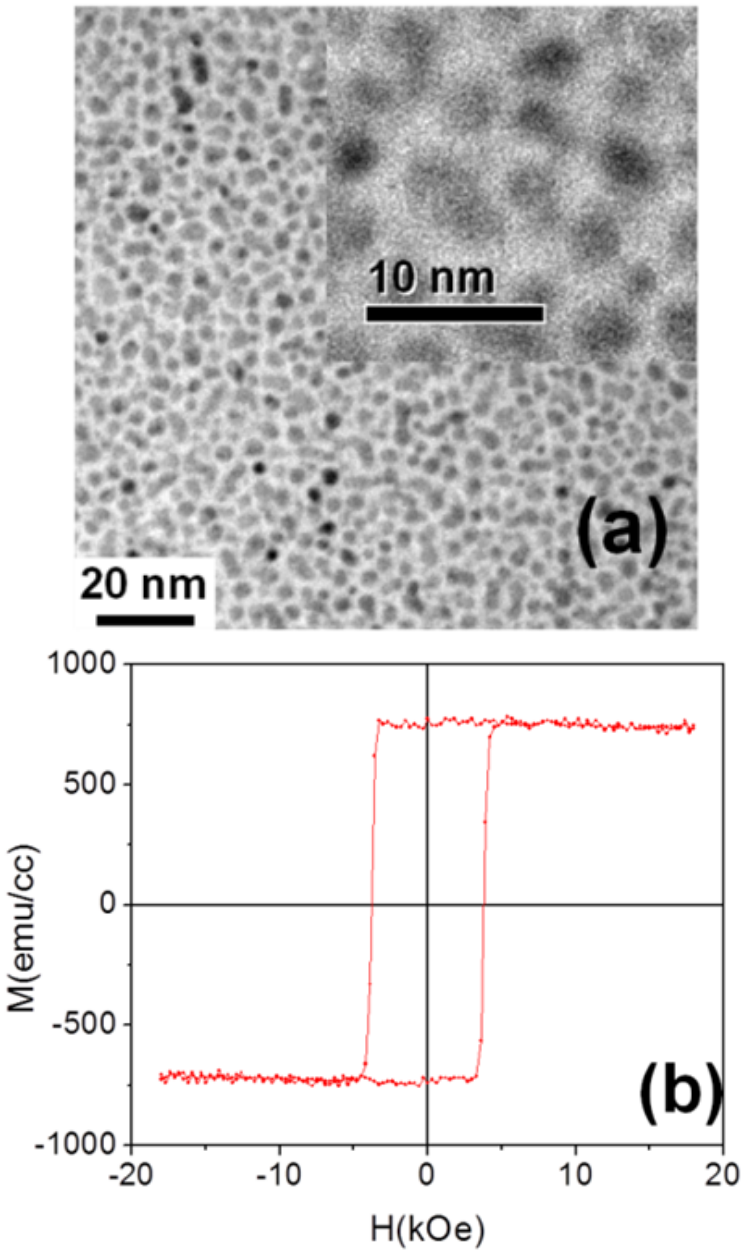

Figure 6.2 (a) TEM plan-view image of Ru-SiO_2 mask layer on the carbon film of a TEM grid; (b) the out-of-plane hysteresis loop of FePt continuous film of the sample with full structure.

The sample was then patterned using the EMP process described above. The hysteresis loops of the as-prepared continuous film, the as-patterned film, and the annealed patterned film are shown in Figure 6.3.

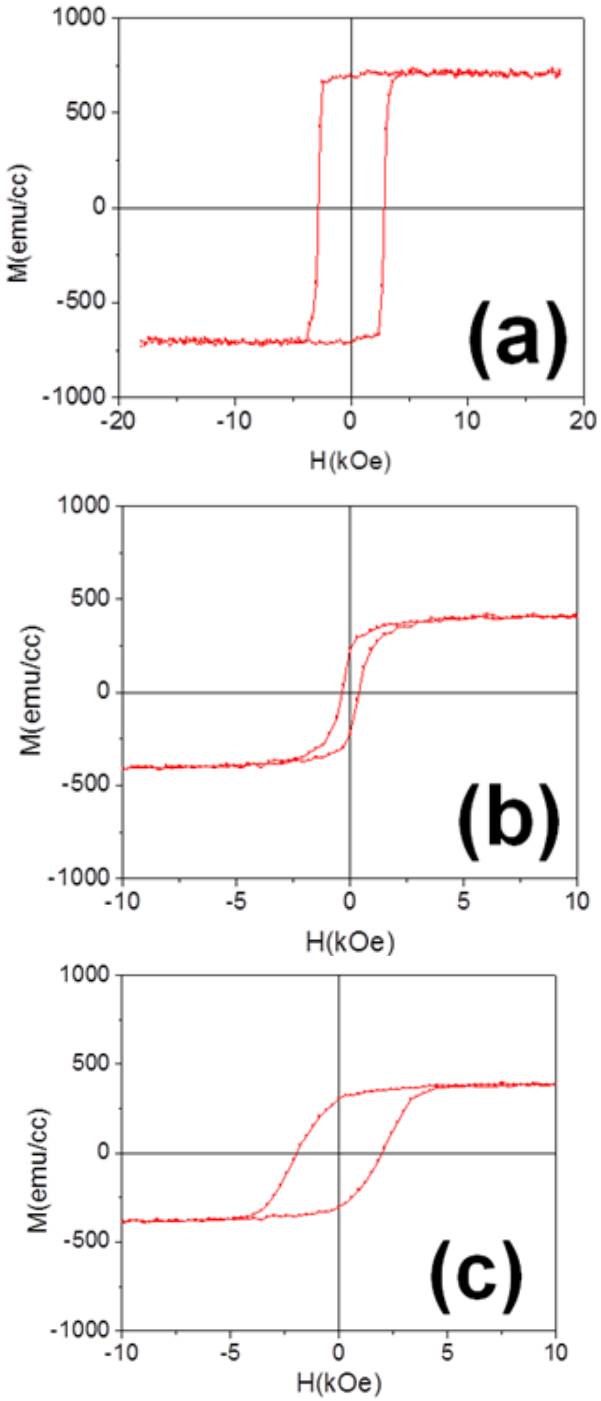

Figure 6.3 The out-of-plane hysteresis loops of the (a) continuous film, (b) as-etched film, and (c) annealed film with coercivity of 2.8 kOe, 350 Oe and 2 kOe, respectively.

Figure 6.3 (a) is the out-of-plane hysteresis loop for the as-prepared continuous film before patterning. The sharp switching at the nucleation point indicates a domain wall motion type magnetization switching mechanism, which is typical for the continuous film with perpendicular anisotropy. After EMP process, the hysteresis loop of the as-patterned

film no longer possesses a sharp switching. However, its coercivity is also reduced as low as 350 Oe, as shown in Figure 6.3 (b). As we know, the etching damage is a common problem in the fabrication of FePt bit patterned media, which typically leads to a low coercivity than expected. We believe that etching process for this EMP process may induce the phase transformation of the continuous FePt film from the magnetic hard $L1_0$ phase to magnetic soft A1 phase or partially ordered phase, which leads to the lower coercivity of the as-patterned film. However this kind of phase transformation should not lead to significant texture change. Therefore the original (001) texture of $L1_0$ FePt can be transformed into (002) texture of A1 FePt. This is a major difference between the EMP patterned FePt and other FePt layers with extremely small but randomly oriented grains. In order to improve the $L1_0$ ordering of as-patterned FePt film, the as-patterned sample was then annealed in vacuum at 550 ^{o}C for 1 hour. The hysteresis loop of the annealed sample is shown in Figure 6.3 (c). Its coercivity was increased to 2 kOe and the loop shows a typical single-domain switching behavior.

In order to further verify the real cuase for the change of the coercivity, XRD spectra were collected for the as-prepared continuous film, the as-patterned and the annealed sample.

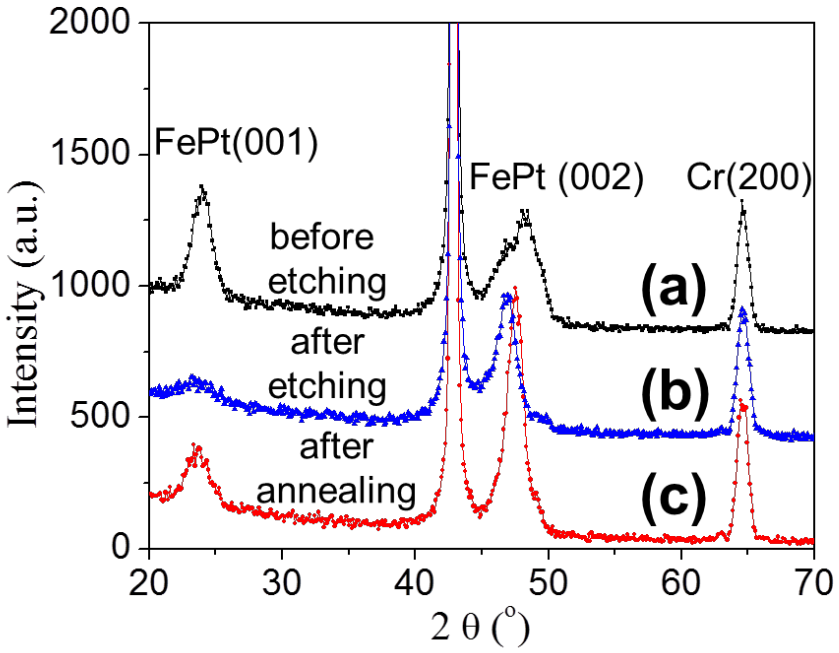

Figure 6.4 XRD spectra of the (a) as-prepared continuous film, (b) as-patterned film, and (c) annealed film.

Figure 6.4 shows the XRD spectra of (a) the as-prepared continuous film, (b) the as-patterned film and (c) the annealed film. Since the Pt (200) peak overlaps with FePt (002) peak, and the Pt peak was greatly enhanced after annealing, it is impossible to compare the $L1_0$ FePt ordering parameter for the samples. Considering that the intensity of the Cr (200) peak did not change at all for all samples, it is reasonable to use the FePt (001) peak for comparison. For the as-patterned sample (immediately after etching and pattern transfer), the FePt (001) peak almost disappeared, and its (002) peak shifted to a smaller angle, which suggests that the FePt became more disordered after the patterning process. However, after annealing at 550 ^{o}C for 1 hr, the FePt (001) peak became much stronger as shown in Figure 6.4 (c). This implies that the $L1_0$ ordering and the crystallinity of FePt grains were improved after annealing, although not as good as the as-prepared continuous FePt film. The FePt (002) peak not only shifted to a high angle, but also became stronger, because the crystallinity and texture of Pt was improved during annealing. Although the annealed sample is $L1_0$ ordered as indicated by its XRD pattern, its coercivity is still low. There could be several reasons for this. Firstly, the annealed sample is still not fully ordered, considering the FePt (001) peak of the annealed sample is still much weaker

than that of the continuous film. Secondly, the real FePt grains after patterning could be very small and hence could not be thermally stable with a low ordering parameter. Thirdly, depositing Ru-SiO_2 on the FePt continuous layer at high temperature might creat a soft magnetic layer at the interface between FePt and Ru-SiO_2. This could be resulted from the reaction between iron and oxygen. This soft magnetic interface could reduce its coercivity further. To clarify this, we purposely varied the FePt thickness while keeping the other layers of the stack unchanged. We found that when the FePt layer thickness was no more than 2 nm, the FePt (001) peak was very weak and the continuous film was almost magnetic soft. Therefore, the oxidation region could be as thick as 2 nm out of the total FePt layer thickness of 5 nm. This soft region may significantly reduce the coercivity of the FePt grain through an exchange-coupled composite effect.

To improve the portion of the magnetic hard region, we prepared samples with a thick FePt layer. A sample with 12 nm-thick FePt layer was patterned using the same EMP process, and then was annealed at 550 ^{o}C for 1 hr. The hysteresis loops of the as-patterned and annealed samples are shown in Figure 6.5. For the as-patterned sample before annealing, its coercivity is 0.5 kOe. After annealing, its coercivity is increased to 3.7 kOe, and the hysteresis loop also has a single-domain switching behavior with a relatively large nucleation field (2 kOe).

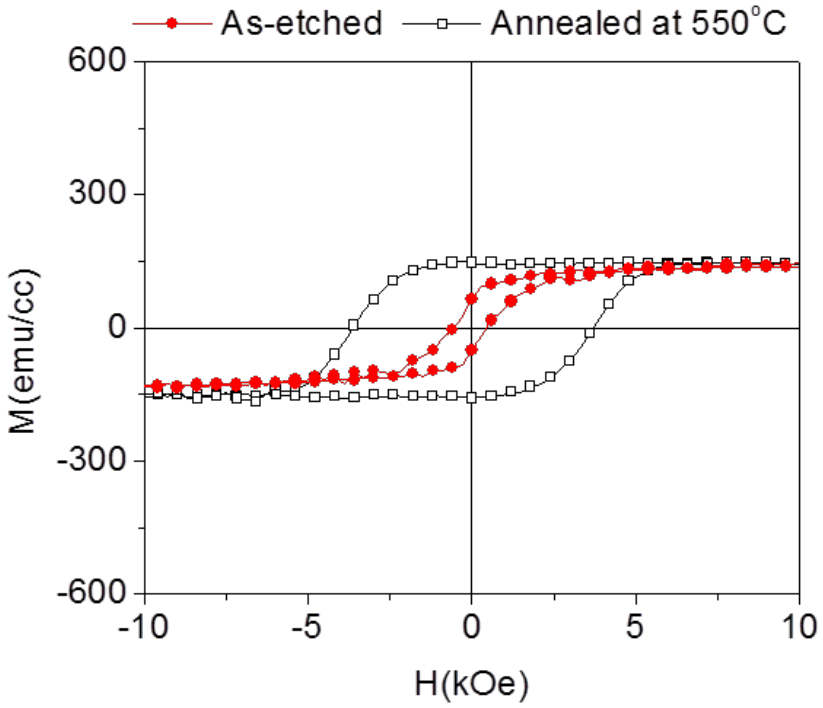

Figure 6.5 Hysteresis loops of as-patterned and annealed 12nm-thick FePt sample.

Figure 6.6 shows the TEM plan-view image of the annealed 5nm-thick FePt sample after the EMP patterning process. Isolated FePt grains can be clearly observed. The mean grain size is 4.6 nm and the center to center distance is 6.3 nm. The FePt grain packing density is only defined by the Ru-SiO_2 embedded mask layer. The grain size was determined not only by the Ru grain packing density, but also by the width of the SiO_2 grain boundary. The FePt grain size and packing density can be adjusted and optimized by changing the sputtering conditions of the embedded mask layer, i.e. sputtering gas pressure, substrate temperature and composition ratio. Furthermore, Ru-SiO_2 also can be replaced with other materials to further reduce the grain size and thus increase the grain packing density. For example, Yuan et al. fabricated NiAl-SiO_2 granular film with mean grain size of 2.5 nm and center to center distance of 4 nm. [18]

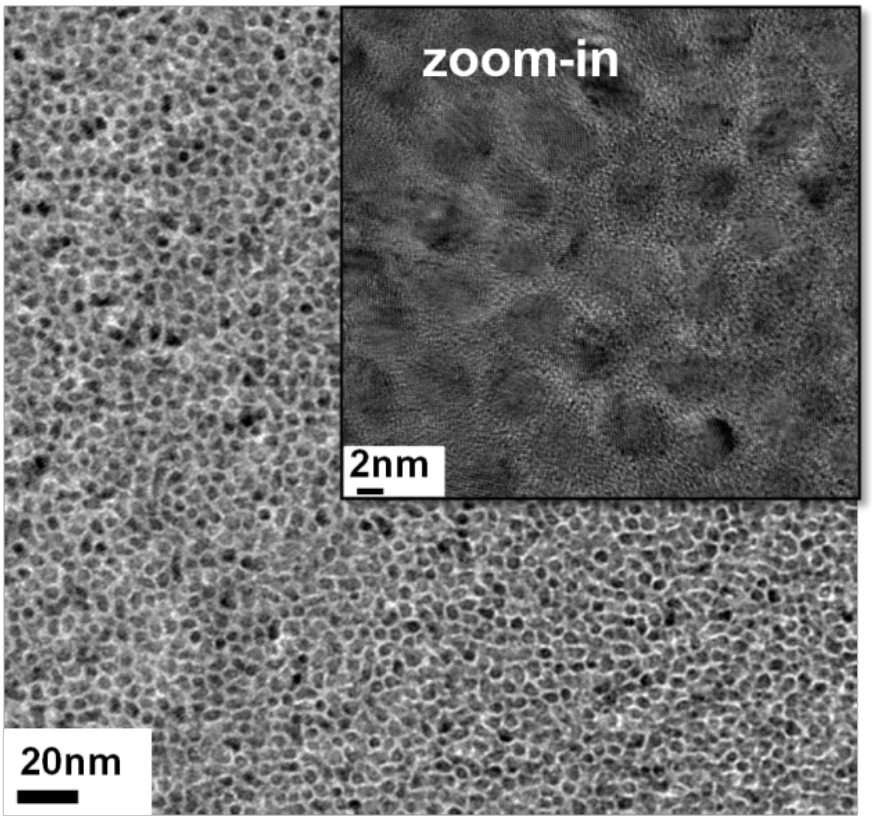

Figure 6.6 TEM plan-view image of the annealed 5nm-thick FePt sample. The grain size is 4.6 nm and the center to center distance is 6.3 nm.

6.3 Conclusion

In summary, we proposed and experimentally demonstrated a media fabrication process, named as the embedded mask patterning (EMP), to fabricate FePt granular media for future HAMR application. In this EMP process, the definition of the properties of the magnetic layer is disconnected from the definition of the grain size and grain boundary, while still using the sputtering process. The FePt grain size is only determined by the embedded mask layer and etching processes, and in principle can be reduced down to sub-3 nm. This EMP process is compatible with today's media manufacturing line because each step could be completed in vacuum without taking the disc out of the chamber.

Reference

[1] D. Weller, A. Moser, L. Folks, M. E. Best, W. Lee, M. F. Toney, M. Schwickert, J.-U. Thiele, and M. F. Doerner, IEEE Trans. Magn., 36, 10 (2000).

[2] J. J. M. Ruigrok, R. Coehoorn, S. R. Cumpson, and H. W. Kesteren, J. Appl. Phys. 87, 5398 (2000).

[3] A. Moser, K. Takano, D. T. Margulies, M. Albrecht, Y. Sonobe, Y. Ikeda, S. Sun and E. E. Fullerton, J. Phys. D: Appl. Phys., 35, R157 (2002).

[4] R. H. Victora and X. Shen, IEEE Trans. Magn., 41, 2828 (2005).

[5] J. P. Wang, W. K. Shen, and J. Bai, IEEE Trans. Magn., 41, 3181 (2005).

[6] D. Suess, Appl. Phys. Lett., 89, 113105 (2006).

[7] Z. Lu, P. B. Visscher, and W. H. Butler, IEEE Trans. Magn., 43, 2941 (2007).

[8] T. Rausch, J. D. Trantham, A. G. Chu, H. Dakroub, C. P. Henry, E. C. Gage, J. W. Dykes, 23rd the Magnetic Recording Conference (TMRC), San Jose, CA, B2, Aug 20-22, (2012).

[9] S. D. Granz, K. Barmak, and M. H. Kryder, J. Appl. Phys. 111, 07B709 (2012).

[10] L. Zhang, Y. K. Takahashi, K. Hono, B. C. Stipe, J.-Y. Juang, and M. Grobis, IEEE Trans. Magn., 47, 4062 (2011).

[11] O. Mosendz, S. Pisana, J. W. Reiner, B. Stipe, and D. Weller, J. Appl. Phys. 111, 07B729 (2012).

[12] K. F. Dong, H. H. Li, Y. G. Peng, G. Ju, G. M. Chow, and J. S. Chen, J. Appl. Phys. 111, 07A308 (2012).

[13] W. K. Shen, J. H. Judy, and J. P. Wang, J. Appl. Phys. 97, 10H301 (2005).

[14] Y. Xu, J. S. Chen and J. P. Wang, Appl. Phys. Lett., 80, 3325 (2002).

[15] Z. L. Zhao, J. S Chen, J. Ding and J. P. Wang, Appl. Phys. Lett., 88, 052503 (2006).

[16] B. Ma, H. Wang, H. Zhao, C. Sun, R. Acharya, and J. P. Wang, J. Appl. Phys. 109, 083907 (2011).

[17] J. S. Chen, Y. Xu, and J. P. Wang, J. Appl. Phys., 93, 1661 (2003).

[18] H. Yuan, Y. Qin, and D. E. Laughlin, Thin Solid Films, 517, 990 (2008).

Chapter 7. SURFACE ANISOTROPY EFFECT IN $L1_0$ FEPT NANOPARTICLES

7.1 Introduction

Surface atoms play an important role in determining the physical performance of nanostructured materials, as they have increased overall fraction of total volume. The study of surface effects on magnetic phenomena is especially interesting and important. The continued shrinkage of feature sizes in magnetic recording devices [1] and for the emergence of spintronics [2] may be fundamentally limited by surface effects. Surface magnetism has inspired tremendous interest since the early work of Louis Néel [3] and remains as an important research topic [4]. However, very few results have been reported on direct measurement of the surface anisotropy of magnetic nanoparticles because of accessibility issues [5]. Consequently, most of the treatments were done theoretically, except for certain thin film cases-- in which large and repeatable surfaces can be constructed experimentally [6]. In the case of nanoparticles, it is even difficult to determine the direction of the magnetic easy axis on the surface [7]. Simulation results have shown that the surface contribution to the effective anisotropy of magnetic nanoparticles depends on both the orientation and magnitude of surface anisotropy, while the latter is usually an estimation based on the strength of exchange interaction [8].

FePt binary alloys with composition of approximately equal atomic ratios have two crystal phases at room temperature--the chemically disordered A1 phase and the chemically ordered $L1_0$ phase. The latter has huge magnetocrystalline anisotropy (MCA, 7×10^7 erg/cc) with an easy axis along the [001] direction [9]. $L1_0$ FePt nanoparticles have great potential in future information storage media [10] and permanent magnets [11]. The

large bulk anisotropy could keep the magnetization thermally stable at a size as small as 3 nm in diameter before becoming superparamagnetic. This size calculation is based on the assumption that the bulk anisotropy is independent of particle size, and any particle size reduction will not introduce additional physical effects. However, this is not true, since roughly half of all the atoms are on the surface for a 3-nm particle; thus significant surface effects are expected. Here we use $L1_0$ FePt nanoparticles and thin films with island structure to experimentally demonstrate the observation and elimination of surface anisotropy effect.

7.2 Experiments and discussion

A 'kink' was observed in the hysteresis loop of $L1_0$ FePt nanoparticles, as shown in Figure 7.1 (c). The $L1_0$ FePt nanoparticles were prepared using a gas-phase condensation technique [12], which can selectively make single-crystalline FePt nanoparticles with either A1 or $L1_0$ phases [13]. Statistical analysis of more than 2800 particles from 50 different transmission electron microscopy (TEM) micrographs shows that these $L1_0$ FePt nanoparticles have a Gaussian distribution with a mean effective size of 5.8 nm and standard deviation of 11%. The octahedral shape is clearly visible from the TEM image in Figure 7.1 (a). The corresponding 3-D particle model, as shown in Figure 7.1 (b), illustrates the packing sequence of Fe and Pt atoms and all the surface atoms sit on (111) planes, which are most closely packed with lowest surface energy. This model was built based on the TEM image in Figure 7.1 (a). At this size, surface atoms on the eight equivalent (111) planes have an overall volume fraction of 28.3%. [12, 13, 14]

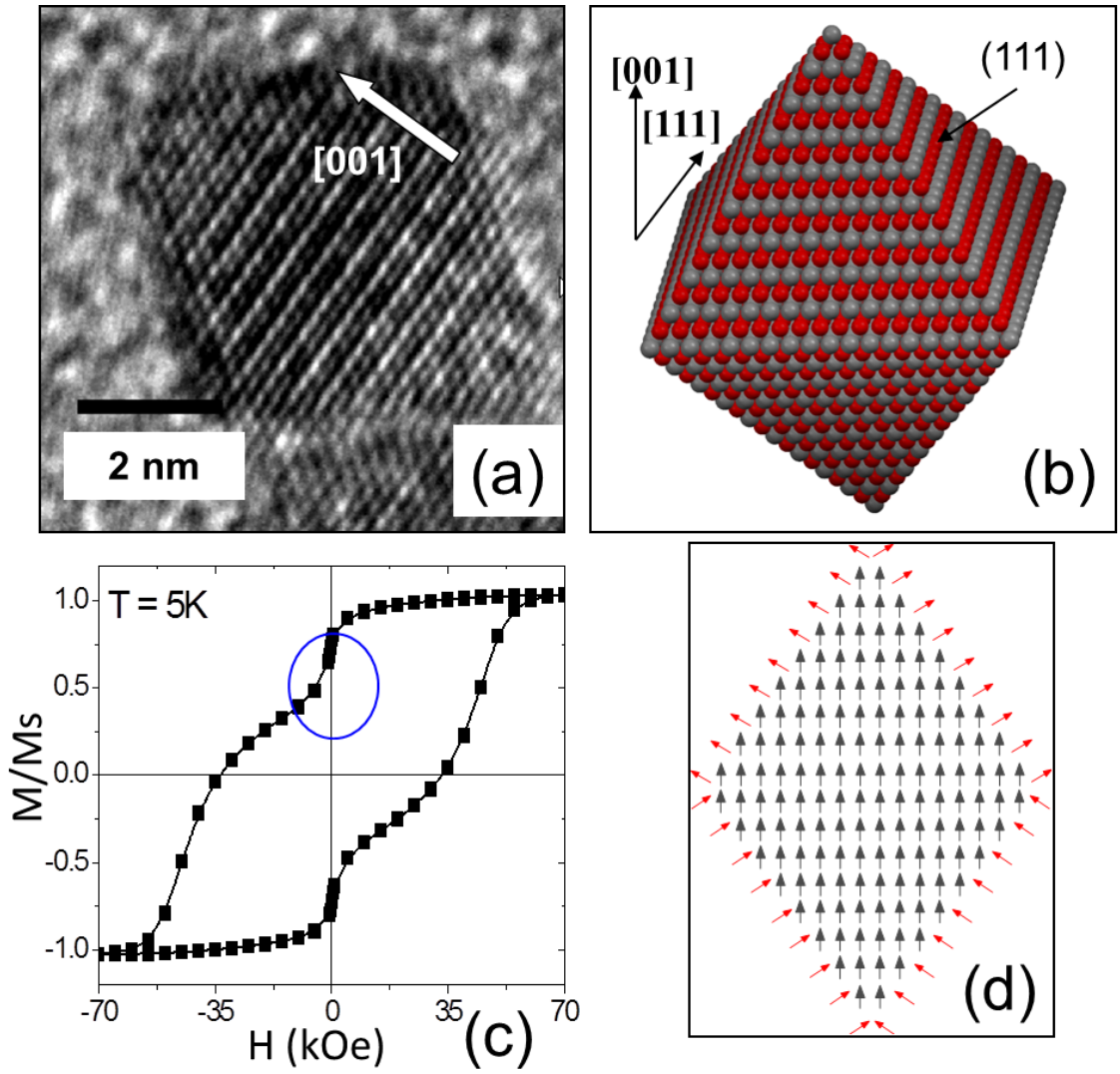

Figure 7.1 Directly ordered $L1_0$ FePt nanoparticles prepared using a gas-phase aggregation technique at room temperature. (Ref. 12) (a) TEM image of one chemically ordered particle with its c-axis (the magnetic easy axis) lying in-plane; (b) a 3-D atomic reconstruction of the $L1_0$ FePt particle. (c) Hysteresis loop of 30 layers of mono-dispersed $L1_0$ FePt nanoparticles, with a coercivity of 33.4 kOe at temperature of 5 Kelvin. (d) The remanence state of one octahedral $L1_0$ FePt nanoparticle. Here arrows represent the spins from iron atoms and all platinum atoms have been omitted for clarity. Red arrows are surface spins and black arrows are interior spins, respectively.

The magnetization reversal process of 30 layers of mono-dispersed $L1_0$ FePt nanoparticles was measured. The easy axes of over 75% particles were aligned parallel in the plane. The samples were prepared through 'in-flight guided landing' method by applying in-situ magnetic field, which was applied directly over the substrate [14]. The measurement fields were applied parallel to the easy axis direction. As shown in Figure

7.1 (c), the sample has a coercivity value of 33.4 kOe at a measurement temperature of 5 K. Clearly, there is a kink in the hysteresis loop around zero field region. Similar behavior has been found for: highly ordered FePt particulate films [15], octahedral-shaped FePt nanoparticles formed using FePt and MgO alternate deposition [16] at substrate temperature as high as 780 °C, and FePt-Ag-C recording media fabricated at 550 °C [17]. The kink was attributed to the existence of poorly ordered phase due to size effect, but surface effects were not mentioned. However, considering all the FePt samples listed above were highly $L1_0$ ordered, it is more likely that the kink came from surface spin reversal governed by surface anisotropy. These spins experience an anisotropy associated with the broken symmetry of their crystal environment. When this surface anisotropy is comparable to, or larger than exchange coupling interaction, the surface spins will favor a full alignment along the surface anisotropy direction. Consequently, there will be jumps on magnetization curves [18]. The validity of the surface anisotropy assumption also lies in such an understanding that the bulk anisotropy energy in an FePt system is not simply a result of the Néel model or directly due to tetragonal distortion. Instead, the magnetocrystalline anisotropy energy comes from the polarization of the Pt 5d electrons by the Fe 3d electrons, and the strong spin-orbit coupling in 5d electrons of Pt [19]. Every Fe atom in the interior part of the nanoparticle has eight Pt atoms as its nearest neighbors, but surface Fe atoms have at most six Pt atoms as its nearest neighbors as shown in Figure 7.1 (b), four of which are surface Pt atoms. Therefore, the symmetry between Fe and Pt is different from the interior to the surface. Since each surface has different normal direction, which is structurally associated with the broken symmetry, each surface should have its own anisotropy direction. This may cause atoms on different surface to have

different remanent states, as shown in Figure 7.1 (d). Also, the exchange coupling in the surface portion has to be relatively weak, otherwise the surface spins would be coupled with the internal spins, and there would be no kink in the hysteresis loop.

Based on the discussion above, the most direct approach to overcome the surface effect is epitaxially covering the particle surface with Pt atoms, but unfortunately, it is difficult demonstrate this process using nanoparticles. It is required to not only embed the particles in a Pt matrix, but also induce epitaxial growth at the interface between FePt and Pt. In this work, FePt thin films with island-like structure were prepared to address the issue.

It was confirmed that a ultra-thin FePt film formed island-like structure when deposited on single crystal MgO (100) substrate at high temperature [15,20], because of the difference of surface energy. An FePt island is schematically illustrated in Figure 7.2 (a); the island has a (001) texture, which was induced by MgO. It has a uniaxial anisotropy with an easy axis perpendicular to the film plane. Similar to the (111) surface of FePt nanoparticles, the side wall of FePt island also has broken symmetry and a kink should be observed in its hysteresis loop. In order to fix the broken symmetry, we propose coating the FePt islands with a Pt thin film that completely covers the surface, as shown in Figure 7.2 (b). Pt can have lattice matching with FePt and induce epitaxial growth.[21] If the Pt layer repairs the symmetry, then the exchange coupling should be enhanced.

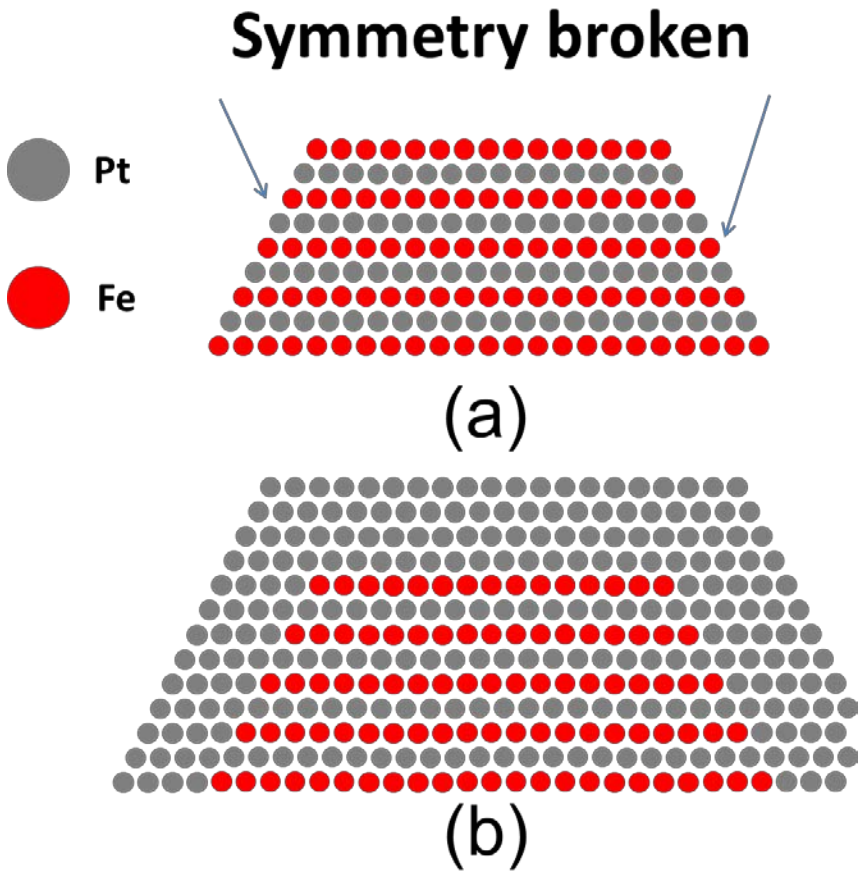

Figure 7.2 (a) The schematic of an FePt island with (001) texture. (b) The FePt island is covered by Pt atoms epitaxially.

The samples were prepared using a magnetron sputtering system. First, a single crystal MgO substrate was heated to 500 °C then an FePt thin film with 4 nm nominal thickness was deposited while maintaining the high temperature. The TEM cross-sectional images of the FePt film are shown in Figure 7.3. Both TEM cross-sectional image in Figure 7.3 (a) and SEM plan-view image inset reveal an island-like structure of a $L1_0$ FePt film. The average grain size of these islands is about 14 nm, and the height is approximately 7 nm. The distance between two adjacent islands is on order of a few

nanometers. Figure 7.3 (b) displays the zoom-in cross-sectional image of a single island, which exactly match the schematic model in Figure 7.2 (a).

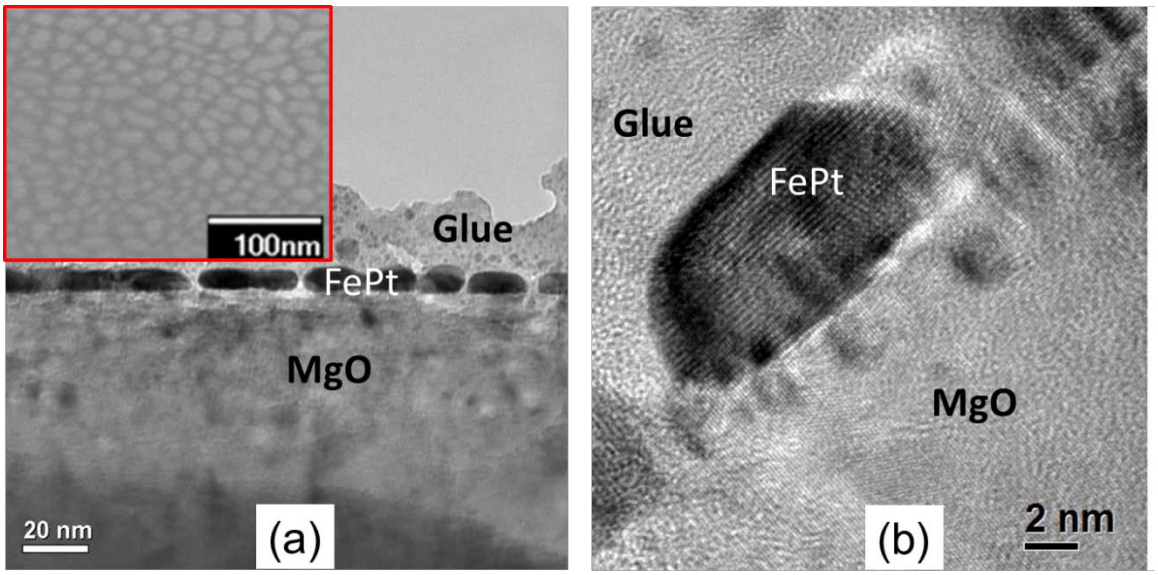

Figure 7.3 (a) The TEM cross-section image of $L1_0$ FePt island-structural film. The plan-view image of the island-like structure is shown in the SEM image inset. (b) The zoom-in cross-section image of a single FePt island, which exactly matches the model in Figure 7.2 (a).

Then, two samples were prepared by depositing Pt on top of the FePt film after cool the sample down to room temperature to avoid the inter-diffusion between FePt and Pt. The sample structures of these two samples are MgO sub/FePt(4nm)/Pt(3nm) and MgO sub/FePt(4nm)/Pt(8nm), respectively. The TEM cross-sectional images of FePt(4nm)/Pt(8nm) sample are shown in Figure 7.4.

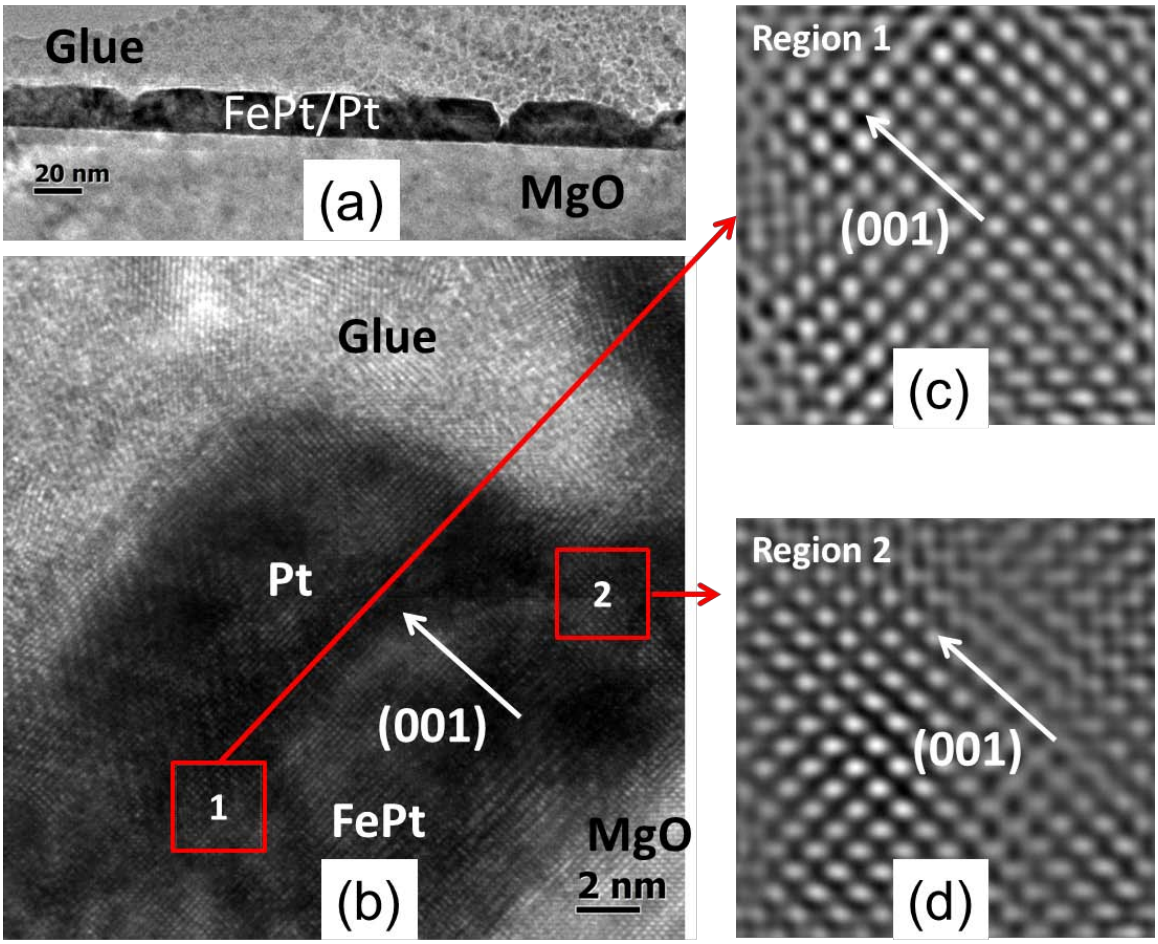

Figure 7.4 (a) The TEM cross-section image of FePt/Pt(8nm) island-structural film. (b) The zoom-in cross-section image of a single FePt/Pt(8nm) island. The region 1 and region 2 are located at the top and side wall of an FePt island, respectively. The enlarged and filtered images are shown in (c) region 1 (top part) and (d) region 2 (side wall), to confirm the epitaxial growth and lattice match of Pt on FePt.

As shown in Figure 7.4 (a), the islands became much larger after coating with an 8nm-Pt layer because the Pt layer was so thick that adjacent FePt islands were connected by Pt. A single FePt/Pt island is enlarged in Figure 7.4 (b), and confirmed that the surface of an FePt island is covered by Pt. In Figure 7.4 (b), two regions at FePt-Pt interface are marked as #1 and #2, which are located at the top and side wall of an FePt island, respectively. Both region 1 and region 2 are enlarged and filtered in Figure 7.4 (c) and (d) to confirm the epitaxial growth and lattice match of Pt on FePt. The TEM images in

Figure 7.4 suggest that the FePt/Pt sample matches the model, which was proposed earlier and is illustrated in Figure 7.2 (b).

The XRD spectra and hysteresis loops of all three samples are displayed and compared in Figure 7.5. The $L1_0$ ordering and (001) texture of FePt was confirmed using XRD spectra, as shown in Figure 7.5 (a). After coating a 3nm-Pt layer on top of the FePt islands, very weak Pt (200) peak and Pt (111) peak appear but are hardly observed. Both of these two peaks become much stronger, after increasing the thickness of Pt layer to 8 nm. This suggests that Pt layer has two textures when deposited on MgO/FePt film at room temperature, this is because the FePt film has island-like structure, and the surface of MgO substrate exposes between adjacent FePt islands. When the Pt layer was deposited, it covered not only the surface of FePt islands, but also the surface of the exposed MgO substrate. Without substrate heating, the epitaxial growth of Pt layer cannot be guaranteed; as a result, the Pt layer formed (111) textured on MgO surface, while formed (001) texture on (001)-textured FePt surface and displayed (200) peak in XRD spectrum.

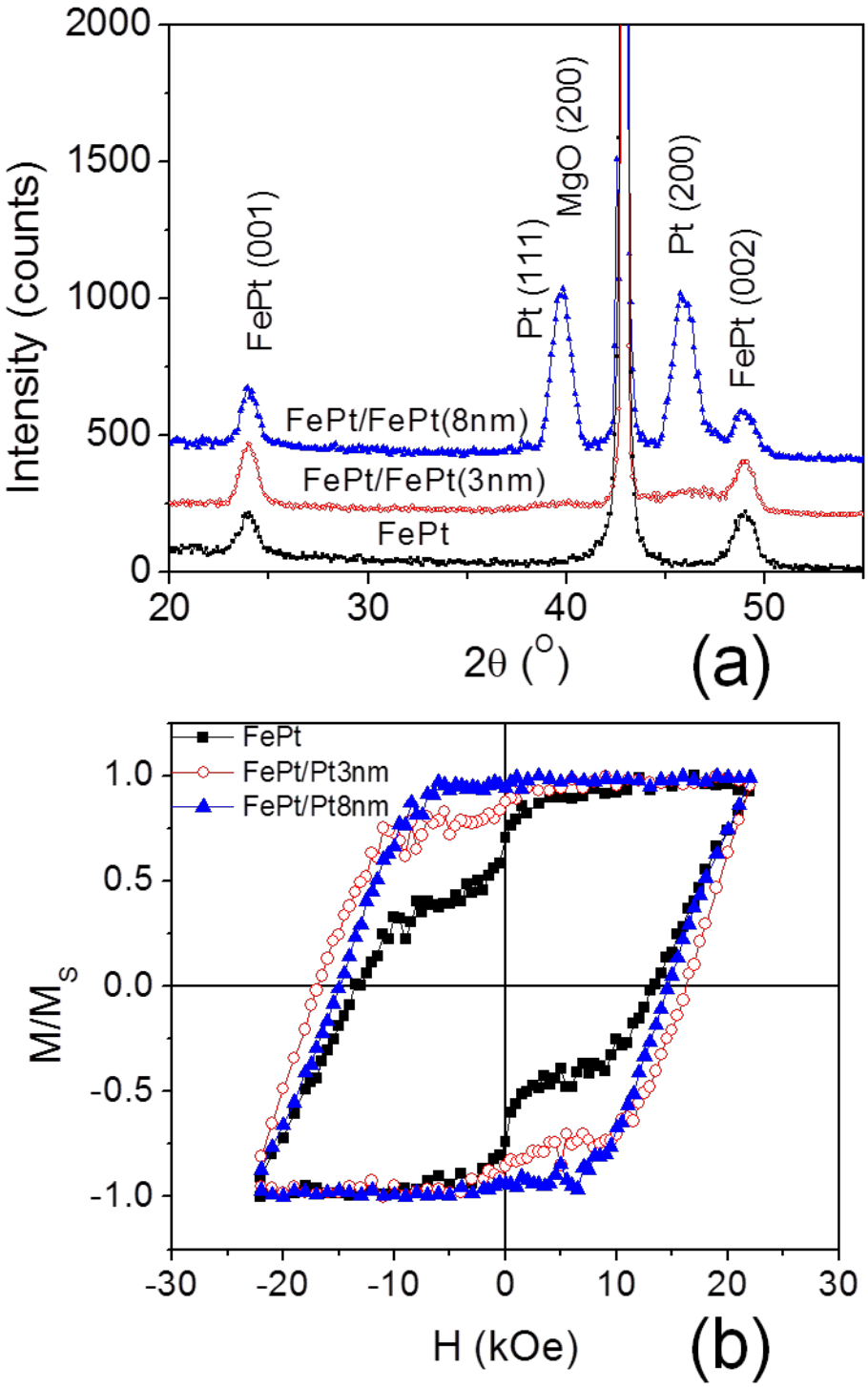

Figure 7.5 (a) XRD spectra of FePt, FePt/Pt(3nm), and FePt/Pt(8nm) samples. All of them show good (001) texture and $L1_0$ ordering of FePt. Pt layer has both (200) texture and (111) texture. (b) The hysteresis loops of all three samples. The coercivity of FePt, FePt/Pt(3nm), and FePt/Pt(8nm) are 13.5 kOe, 15 kOe and 17 kOe, respectively. A kink is obviously visible in FePt sample, but weaker in FePt/Pt(3nm), and disappears in FePt/Pt(8nm).

The key results of this work are demonstrated using hysteresis loops as shown in Figure 7.5 (b). The coercivity of FePt, FePt/Pt(3nm), and FePt/Pt(8nm) are 13.5 kOe, 15 kOe and 17 kOe, respectively, but the hysteresis loop of the pure FePt sample has an obvious kink. Although a kink is visible in the hysteresis loop of FePt/Pt(3nm) sample, it is much smaller than the kink of pure FePt sample's hysteresis loop, and as expected, the kink disappeared in the hysteresis loop of FePt/Pt(8nm) sample. Since the FePt film formed island-like structure, the superficial area of the sample is much larger than that of a flat surface. The Pt layer with 3-nm nominal thickness cannot completely cover the sample surface. Therefore the kink became weaker, but was not removed. However, after increasing the nominal thickness of Pt layer to 8 nm, all the surface of FePt and MgO are covered, and the kink of hysteresis loop can be thoroughly eliminated.

In order to further discuss the surface effect, it should be noted that the existence of kink implies two facts:

(1) The surface portion looks soft magnetic or superparamagnetic. The direction of surface anisotropy is related to the surface plane normal due to the broken symmetry, and when considering a macroscopic view, the nanoparticles have countless surface plane normals that are pointing in all directions. Therefore, the surface portion of the whole sample has a randomly oriented anisotropy. Thus, a behavior similar to a superparamagnetic material was observed in macroscopic measurement.

(2) The exchange coupling between internal portion and surface portion is weak, but it became stronger after fixing the broken symmetry. There has been no report about the exchange coupling constant for a monolayer, or several atomic layers, of FePt films. It has been reported that the exchange constant in 14-nm thick epitaxially grown $L1_0$ FePt

film is about 1×10^{-6} erg/cm [22] or 2×10^{-14} erg/atom. However, the exchange constants in ultra-thin films can be much smaller than that in thick films or bulk phases. It is reasonable to expect a further reduced exchange interaction when surface reconstruction happens and iron-iron distances are enlarged [23], since the exchange constant approximately varies as d^{-5}, where d is inter-atomic distance [24]. Similar behavior is expected on the surface Fe atoms of FePt nanoparticles and island-structure thin films.

After coating a Pt layer on the FePt islands, all the Fe atoms are embedded as internal atoms, which repairs the symmetry. It must be noted that, even with Pt capping, the crystal environment of the surface Fe atoms is still different from that of the internal Fe atoms. Compared to the internal Fe atoms, the surface Fe atoms have two more Pt neighbors, which are located at the same atomic layer of Fe. Considering that the anisotropy of $L1_0$ FePt comes from the Pt 5d electrons which are polarized by Fe, the anisotropy orientation at the lateral interface between FePt and Pt is still different from the film plane normal. The only explanation for the disappearance of the kink is that the exchange coupling was largely enhanced and the surface magnetic spins are strongly exchange coupled with the internal spins.

7.3 Conclusion

In conclusion, we provided an experimental evidence of the existence of surface anisotropy in both 5.8 nm octahedral $L1_0$ FePt nanoparticles and $L1_0$ FePt thin film with island structure. Surface spins are decoupled from the internal spins due to the broken symmetry at surface, and so surface spins switch independently upon applying reversal magnetic fields. The surface effect was overcome by coating an epitaxial Pt layer on the FePt islands. The origin of the kink in hysteresis loop is not only due to the surface

anisotropy, but also the weak exchange coupling in surface portion. By embedding the surface atoms as internal atoms, their exchange coupling is enhanced and the kink disappeared. The method could be useful in ultra-high density FePt recording media, in which the surface atoms of each FePt grain may play an important role in magnetic reversal.

Reference

[1] D. Weller and A. Moser, IEEE Trans. Magn. **35**, 4423 (1999)

[2] I. Zutic, J. Fabian, S. Das Sarma, Rev. Mod. Phys. **76**, 323 (2004)

[3] L. Néel, J. Phys. Radium, **15**, 225 (1954)

[4] S. D. Bader, Rev. Mod. Phys. **78**, 1 (2006)

[5] M. Jamet, W. Wernsdorfer, C. Thirion, D. Mailly, V. Dupuis, P. Mélinon, and A. Pérez, Phys. Rev. Lett., **86**, 4676 (2001)

[6] For example, see C. Liu, E. R. Moog, and S. D. Bader, Phys. Rev. Lett. **60**, 2422 (1988); H. C. Mireles, and J. L. Erskine, Phys. Rev. Lett. **87**, 037201 (2001)

[7] H. Kachkachi, H. Mahboub, J. Mag. Mag. Mater. **278**, 334 (2004)

[8] D. A. Garanin and H. Kachkachi, Phys. Rev. Lett. **90**, 065504 (2003)

[9] O. A. Ivanov, L. V. Solina, V. A. Demshina, L. M. Magat, Fiz. Metal. Metalloved. **35**, 92 (1973)

[10] S. Sun, C. B. Murray, D. Weller, L. Folks, A. Moser, Science **287**, 1989 (2000)

[11] H. Zeng, J. Li, J. P. Liu, Z. L. Wang, S. Sun, Nature **420**, 395 (2002)

[12] J. M. Qiu, J. P. Wang, Appl. Phys. Lett., **88**, 192505 (2006)

[13] J. M. Qiu, J. P. Wang, Adv. Mater., **19**, 1703 (2007)

[14] J. M. Qiu, J. M. Bai, J. P. Wang, Appl. Phys. Lett. **89**, 222506 (2006)

[15] T. Shima, K. Takanashi, Y. K. Takahashi, K. Hono, Appl. Phys. Lett. **85**, 2571 (2004)

[16] T. Shima, K. Takanashi, Y. K. Takahashi, K. Hono, Appl. Phys. Lett. **88**, 063117 (2006)

[17] O. Mosendz, S. Pisana, J. W. Reiner, B. Stipe, and D. Weller, J. Appl. Phys. **111**, 07B729 (2012).

[18] H. Kachkachi and M. Dimian, Phys. Rev. B. **66**, 174419 (2002)

[19] G. H. O. Daalderop, P. J. Kelly, and M. F. H. Schuurmans, Phys. Rev. B. **44**, 12054 (1991)

[20] B. Ma, H. Wang, H. Zhao, C. Sun, R. Acharya, and J. P. Wang, J. Appl. Phys. **109**, 083907 (2011).

[21] J. S. Chen, Y. Xu, and J. P. Wang, J. Appl. Phys. **93**, 1661 (2003).

[22] S. Okamoto, N. Kikuchi, O. Kitakami, T. Miyazaki, Y. Shimada, K. Fukamichi, Phys. Rev. B. **66**, 024413 (2002)

[23] J. L. Rodríguez-López, J. M. Montejano-Carrizales, U. Pal, J. F. Sánchez-Ramírez, H. E. Troiani, D. García, M. Miki-Yoshida, and M. José-Yacamán, Phys. Rev. Lett. **92**, 196102 (2004)

[24] F. Gautier in Magnetism of Metals and Alloys, edited by M. Cryo (North-Holland, Amsterdam1982)

Chapter 8. CONCLUSION AND OUTLOOK

8.1 Conclusion

(1) FePt based ECC media with core-shell structure has been systematically studied, and proved to have large gain factor. It could be potentially used in bit patented media (BPM), because there is sufficient spacing among the patterned bits. And the modified gain factor can be used to evaluate the performance of core-shell type ECC BPM.

(2) A graded FePt granular media was fabricated at 350 °C substrate temperature without depositing any soft magnetic layers purposely. The spontaneous inter-diffusion between FePt and Pt layers enabled the FePt composition gradient, which led to the anisotropy and saturation magnetization gradient. The gain factor of the graded media was evaluated to be 3.74. The fabrication process of this spontaneously-formed graded media is potentially compatible with today's disk media fabrication. Considering that the deposition time in today's industrial fabrication process is much shorter than that of this work, the substrate temperature can be increased to accelerate the diffusion and improve the ordering of FePt as well.

(3) The direct use of anodize alumina (AAO) fabricated on Si wafer as a large area mold for nanoimprinting has been demonstrated. The sticking problem between the mold and the resist has been overcome by modifying the AAO surface by coating it a very thin SiO_2 layer. Moreover, we successfully fabricate $L1_0$ FePt patterned structure with 40 nm feature size over large area with a size distribution below 10%. Optimization of naonimprinting parameters and flatness of the mold may open the path to fabricate patterned magnetic nanostructures with reduced feature size and high density for practical applications.

(4) FePt BPM with dot size of sub-30 nm and size distribution of 8% has been fabricated using di-block copolymer. The crystallinity of FePt was partially damaged during patterning processes, e.g. the ion milling process. Annealing the

patterned samples at 350 ºC, the $L1_0$ ordering of FePt was improved and SFD was narrowed.

(5) Depositing Fe on FePt at room temperature and then annealing it to create graded anisotropy through the layer inter-diffusion process was proposed and demonstrated to fabricate FePt graded BPM. An Fe-rich film would form a very rough surface with extremely large grains when deposited onto FePt at high temperature. Annealing the FePt/Fe film, whose Fe layer was deposited at room temperature, didn't increase the surface roughness, and was recommended for the fabrication of future FePt bit patterned media with graded structure. Compared to the FePt BPM with ECC structure, FePt BPM with graded structure showed smaller HC and larger thermal energy barrier. In ECC BPM, the dipole interaction may play an important role in the switching process of the sample.

(6) We proposed and experimentally demonstrated a media fabrication process, named as the embedded mask patterning (EMP), to fabricate FePt granular media for future HAMR application. In this EMP process, the definition of the properties of the magnetic layer is disconnected from the definition of the grain size and grain boundary, while still using the sputtering process. The FePt grain size is only determined by the embedded mask layer and etching processes, and in principle can be reduced down to sub-3 nm. This EMP process is compatible with today's media manufacturing line because each step could be completed in vacuum without taking the disc out of the chamber.

(7) We provided an experimental evidence of the existence of surface anisotropy in both 5.8 nm octahedral $L1_0$ FePt nanoparticles and $L1_0$ FePt thin film with island structure. Surface spins are decoupled from the internal spins due to the broken symmetry at surface, and so surface spins switch independently upon applying reversal magnetic fields. The surface effect was overcome by coating an epitaxial Pt layer on the FePt islands. The origin of the kink in hysteresis loop is not only due to the surface anisotropy, but also the weak exchange coupling in surface portion. By embedding the surface atoms as internal atoms, their exchange coupling is enhanced and the kink disappeared. The method could be

useful in ultra-high density FePt recording media, in which the surface atoms of each FePt grain may play an important role in magnetic reversal.

8.2 Outlook

(1) According to the study of FePt granular media with spontaneously formed graded structure, similar phenomena should be found in FePt BPM, and similar method should be effective in FePt graded BPM fabrication. This work has already been started. FePt BPM with 1.5 nm thickness FePt layer just has a coercivity of 3 kOe, which is much smaller than that of FePt BPM with 5 nm thickness FePt layer.

(2) The ordering of the patterned dots, which were fabricated using BCP, is quite bad. With pre-patterned guided tracks, the ordering should be improved significantly.

(3) The core-shell ECC structure could be used in BPM. Its effectiveness can be demonstrated and proved by depositing a thin Fe layer on top of a patterned FePt dot array at room temperature.

(4) Currently, the EMP process is far from practical. Lots of work has to be done to optimize both the layer structure and etching process. The coercivity is low. Post-annealing with higher temperature but shorter process time should be considered. It also can be potentially used to fabricate nanoparticles with complex stacks with high throughput.

Conference presentations

1. **H. Wang**, H. Zhao, T. Rahman, Y. Isowaki, Y. Kamata, T. Maeda, H. Hieda and A. Kikitsu, H.-H. Guo, B. Ma, Y. Chen, W. Li, J. Ding, and J. P. Wang, '***Fabrication and Characterization of FePt Exchange Coupled Composite and Graded Bit Patterned Media***', 23rd The Magnetic Recording Conference(TMRC), F-6 (invited), San Jose, 2012.

2. **H. Wang**, W. Li, T. Rahman, H. Zhao, J. Ding, Y. Chen, and J. P. Wang, "***Characterization of $L1_0$-FePt based exchange coupled composite bit pattern media***". 56th Annual Conference on Magnetism & magnetic Materials, DQ-08, Scottsdale, USA, 2011.

3. **H. Wang**, T. Rahman, H. Zhao, Y. Isowaki, Y. Kamata, A. Kikitsu, and J. P Wang, "***Fabrication of FePt Type Exchange Coupled Composite Bit Patterned Media by Block-copolymer Lithography***". 55th Annual Conference on Magnetism & magnetic Materials, AR-13, Atlanta, USA, 2010.

4. **H. Wang**, H. Zhao, A. Das, M. Racine, M. Imakawa, and J. P. Wang, "***A Nature Method to Fabricate Exchange Coupled Composite Media***",53rd Annual Conference on Magnetism & magnetic Materials, CC-09, Austin, USA, 2008.

5. J. P. Wang, **H. Wang** and H. Zhao, "***FePt type exchange coupled composite media and multi-level recording***", 19th Magnetic Recording Conference(TMRC), BB-3 (invited), Singapore, 2008

Patent

J. P. Wang, **H. Wang**, H. Zhao, “Embedded mask patterning process for fabricating magnetic media or other structures”, U.S. Appln. No. 61/691,681

Publications

1. **H. Wang**, H. Zhao, T. Rahman, Y. Isowaki, Y. Kamata, T. Maeda, H. Hieda and A. Kikitsu, and J. P. Wang, "*Fabrication and Characterization of FePt Exchange Coupled Composite and Graded Bit Patterned Media*", (invited), IEEE trans. Magn., 49, 707 (2013).
2. **H. Wang**, H. Zhao, P. Quarterman, and J. P. Wang, "*Embedded mask patterning: A nanopatterning process to fabricate FePt magnetic media*", Appl. Phys. Lett., 102, 052406 (2013).
3. **H. Wang**, H. Zhao, O. Ugurlu, and J. P. Wang, "*Spontaneously-formed FePt graded granular media with a large gain factor*", IEEE Magn. Lett., 3, 450014 (2012).
4. **H. Wang**, W. Li, T. Rahman, H. Zhao, J. Ding, Y. Chen, and J. P. Wang, "*Characterization of $L1_0$-FePt based exchange coupled composite bit pattern media*", J. Appl. Phys., 111, 07B914 (2012).
5. **H. Wang**, T. Rahman, H. Zhao, Y. Isowaki, Y. Kamata, A. Kikitsu, and J. P. Wang, "*Fabrication of FePt Type Exchange Coupled Composite Bit Patterned Media by Block-copolymer Lithography*", J. Appl. Phys. 109, 07B754 (2011).
6. **H. Wang**, X. Liu, J. M. Qiu, P. Quarterman, H. Guo, B. Ma and J. P. Wang, "*Observation and elimination of surface anisotropy effect in L10 phase FePt nanoparticles and island-structural films*", Phys. Rev. Lett., in preparation.
7. T. Rahman, **H. Wang**, and J. P. Wang, "*Exploration of the Direct Use of Anodized Alumina as a Mold for Nanoimprint Lithography to Fabricate Magnetic Nanostructure over Large Area*", journal of nanotechnology, 961630 (2011).
8. S. Yin, **H. Wang**, H. Zhao, Y. Jiang, J. P. Wang, "*The effects of Cu doping on crystalline structure and magnetic properties of SmCo5-xCux thin films grown on Ru (0002)*", J. Appl. Phys., in press.
9. H. Zhao, **H. Wang**, and J. P. Wang, "*Fabrication of Ultra Thin $L1_0$-FePt Based Exchange Coupled Composite Media*", J. Appl. Phys., 111, 07B732 (2012).

10. H. Zhao, **H. Wang**, and J. P. Wang, "*Microstructure Study of Pinning Sites of Highly (0001) Textured Sm(Co,Cu)$_5$ Thin Films Grown on Ru Underlayer*", J. Appl. Phys., 111, 07B730 (2012).
11. B. Ma, **H. Wang**, H. Zhao, C. Sun, R. Acharya, and J. P. Wang, "*Structural and magnetic properties of a core-shell type L1$_0$ FePt/Fe exchange coupled nanocomposite with tilted easy axis*", J. Appl. Phys. 109, 083907 (2011).
12. H. Zhao, **H. Wang**, X. Liu, T. Zhang, and J. P. Wang, "*Chemical Stability of Highly (0001) Textured Sm(CoCu)$_5$ Thin Films with a Thin Ta Capping Layer*", J. Appl. Phys. 109, 07B715 (2011).
13. B. Ma, **H. Wang**, H. Zhao, C. Sun, R. Acharya, and J. P. Wang, "*L1$_0$ FePt/Fe Exchange Coupled Composite Structure on MgO Substrates*", IEEE Trans. Magn. ,46, 2345 (2010).

Reference list

[1] H. P. Myers, Introductory Solid State Physics, 2nd. Ed., Taylor & Francis, (1997).

[2] http://rondennison.com/services.htm

[3] http://www1.hgst.com/hdd/research/storage/pm/index.html

[4] http://www.xbitlabs.com/articles/storage/display/seagate-momentus-54003_2.html

[5] S. Iwasaki, and Y. Nakamura, IEEE Trans. Magn. 13, 1272 (1977).

[6] B. D. Terris and T. Thomson, J. Phys. D: Appl. Phys. 38, R199 (2005).

[7] M. H. Kryder, and R. W. Gustafson, J. Magn. Magn. Mater. 287, 449 (2005).

[8] P.H. Dederichs, R. Zeller, H. Akai, and H. Ebert, J. Magn. Magn. Mater., 100, 241(1991).

[9] J. J. M. Ruigrok, R. Coehoorn, S. R. Cumpson, and H. W. Kesteren, J. Appl. Phys. 87, 5398 (2000).

[10] A. Moser, K. Takano, D. T. Margulies, M. Albrecht, Y. Sonobe, Y. Ikeda, S. Sun and E. E. Fullerton, J. Phys. D: Appl. Phys., 35, R157 (2002).

[11] R. H. Victora and X. Shen, IEEE Trans. Magn. 41, 2828 (2005).

[12] J. P. Wang, W. K. Shen, and J. Bai, IEEE Trans. Magn. 41, 3181 (2005)

[13] Suess, Appl. Phys. Lett. 89, 113105 (2006).

[14] Z. Lu, P. B. Visscher, and W. H. Butler, IEEE Trans. Magn., 43, 2941 (2007).

[15] Weller, A. Moser, L. Folks, M. E. Best, W. Lee, M. F. Toney, M. Schwickert, J.-U. Thiele, and M. F. Doerner, IEEE Trans. Magn., 36, 10 (2000).

[16] http://www.crct.polymtl.ca/fact/phase_diagram.php?file=Co-Sm.jpg&dir=SGTE

[17] J. Sayama, T. Asahi, K. Mizutani and T. Osaka, J. Phys. D: Appl. Phys. 37, L1 (2004).

[18] S.H. Whang, Q. Feng, Y.-Q. Gao, Acta Materialia, 46, 6485 (1998).

[19] T. Shima, K. Takanashi, Y. K. Takahashi, and K. Hono, Appl. Phys. Lett. 85, 2571 (2004).

[20] http://mysite.du.edu/~jcalvert/phys/dischg.htm

[21] http://www.angstromsciences.com/technology/sputtering.htm

[22] J. A. Thornton, Ann. Rev. Mater. Sci., 7, 239 (1977).

[23] http://www2.warwick.ac.uk/fac/sci/physics/current/postgraduate/regs/mpags/ex5/strainedlayer/surfgrwth/

[24] http://chemwiki.ucdavis.edu/Analytical_Chemistry/Instrumental_Analysis/Diffraction/Powder_X-ray_Diffraction

[25] http://en.wikipedia.org/wiki/Vibrating_sample_magnetometer

[26] http://www.uiowa.edu/~cmrf/methodology/sem/index.html

[27] K.A. Mkhoyan, P.E. Batson, J. Cha, W.J. Schaff and J. Silcox, Science, 312, 1354 (2006).

[28] http://www.uiowa.edu/~cmrf/methodology/tem/index.html

[29] http://www.mtholyoke.edu/~menunez/ResearchPage/AFM.html

[30] http://www.gatan.com/analysis/gif_2001.php

[31] K. Barmak, J. Kim J, A. Shell A, E. B. Svedberg, and J. K. Howard, Appl. Phys. Lett., 80, 4268 (2002).

[32] S. N. Piramanayagam, J. Appl. Phys. 102, 011301 (2007).

[33] Y.-N. Hsu, S. Jeong, D. N. Lambeth, and D. Laughlin, IEEE Trans. Magn. 36, 2945 (2000).

[34] Y.-N. Hsu, S. Jeong, D. Laughlin, and D. N. Lambeth, J. Appl. Phys. 89, 7068 (2001).

[35] Y. Xu, J. S. Chen, and J. P. Wang, Appl. Phys. Lett., 80, 3325 (2002).

[36] J. S. Chen, Y. Xu, and J. P. Wang, J. Appl. Phys. 93, 1661 (2003).

[37] C. C. Chiang, C. –H. Lai, and Y. C. Wu, Appl. Phys. Lett. 88, 152508 (2006).

[38] J. Cao, J. Cai, Y. Liu, Z. Yang, F. Wei, A. Xia, B. Han, and J. Bai, J. Appl. Phys. 99, 08F901 (2006).

[39] W. K. Shen, J. H. Judy, and J. P. Wang, J. Appl. Phys. 97, 10H301 (2005).

[40] J. S. Chen, B. C. Lim, J. F. Hu, B. Liu, G. M. Chow, and G. Ju, Appl. Phys.Lett. 91, 132506 (2007).

[41] T. Maeda, T. Kai, A. Kikitsu, T. Nagase, and J.-I. Akiyama, Appl. Phys.Lett. 80, 2147 (2002).

[42] K. Nishimur, K. Takahashi, H. Uchida, M. Inoue, J. Magn. Magn. Mater., 272-276, 2189 (2004).

[43] Q. Yan, T. Kim, A. Purkayastha, P. G. Ganesan, M. Shima, and G.Ramanath, Adv. Mater., 17, 2233 (2005).

[44] Z. L. Zhao, J. Ding, Y. Li, G. M. Chow, J.S. Chen, and J.P. Wang, Meta. and Mat. Trans. A, 38A, 811 (2007).

[45] Yun-Chung Wu, Liang-Wei Wang, and Chih-Huang Lai, Appl. Phys. Lett. 91, 072502 (2007).

[46] T. Rausch, J. D. Trantham, A. G. Chu, H. Dakroub, C. P. Henry, E. C. Gage, J. W. Dykes, 23rd the Magnetic Recording Conference (TMRC), San Jose, CA, B2, Aug 20-22, (2012).

[47] L. Zhang, Y. K. Takahashi, K. Hono, B. C. Stipe, J.-Y. Juang, and M. Grobis, IEEE Trans. Magn., 47, 4062 (2011).

[48] O. Mosendz, S. Pisana, J. W. Reiner, B. Stipe, and D. Weller, J. Appl. Phys. 111, 07B729 (2012).

[49] S. D. Granz, K. Barmak, and M. H. Kryder, J. Appl. Phys. 111, 07B709 (2012).

[50] K. F. Dong, H. H. Li, Y. G. Peng, G. Ju, G. M. Chow, and J. S. Chen, J. Appl. Phys. 111, 07A308 (2012).

[51] B. D. Terris, J. Magn. Magn. Mater., 321, 512 (2009)

[52] M. T. Rahman, N. N. Shams, and C. H. Lai, J. Appl. Phys. 105, 07C112 (2009).

[53] X. Yang, S. Xiao, W. Wu, Y. Xu, K. Mountfield, R. Rottmayer, K. L. Kuo, and D. Weller, J. Vac. Sci. Technol., 25, 2202 (2007).

[54] S. Y. Chou, P. R. Krauss, and P. J. Renstrom, J. Vac. Sci. Technol. B 14, 4129 (1996).

[55] K. Naito, H. Hieda, M. Sakurai, Y. Kamata, and K. Asakawa, IEEE Trans. Magn. 38, 1949 (2002).

[56] R. Ruiz, H. Kang, F. A. Detcheverry, E. Dobisz, D. S. Kercher, T. R. Albrecht, J. J. de Pablo, and P. F. Nealey, Science 321, 936 (2008).

[57] H. Hieda, Y. Yanagita, A. Kikitsu, T. Maeda, and K. Naito, J. Photopolym. Sci. Technol. 19, 425 (2006).

[58] T. Rahman, H. Wang, and J.P. Wang, J. Nanotech., 2011, 961630 (2011).

[59] H. Wang, T. Rahman, H. Zhao, Y. Isowaki, Y. Kamata, A. Kikitsu, and J.P. Wang, J. Appl. Phys. 109, 07B754 (2011).

[60] C. Kim, T. Loedding, S. Jang, H. Zeng, Z. Li, Y. Sui, and D. J. Sellmyer, Appl. Phys. Lett. 91, 172508 (2007).

[61] T. Bublat and D. Goll, Nanotechnology 22 315301 (2011).

[62] T. Bublat and D Goll,J. Appl. Phys. 110, 073908 (2011).

[63] T. Shimatsu, Y. Inaba, H. Kataoka, J. Sayama, H. Aoi, S. Okamoto, and O. Kitakami, J. Appl. Phys. 109, 07B725 (2011).

[64] H. Wang, H. Zhao, T. Rahman, Y. Isowaki, Y. Kamata, T. Maeda, H. Hieda and A. Kikitsu, H.-H. Guo, B. Ma, Y. Chen, W. Li, J. Ding, J.P. Wang, 23rd The Magnetic Recording Conference(TMRC), F-6 (invited), San Jose, 2012.

[65] D. Suess, T. Schrefl, S. Fahler, M. Kirschner, G. Hrkac, F. Dorfbauer, and J. Fidler, Appl. Phys. Lett. 87, 012504 (2005).

[66] L. S. Huang, J. F. Hu, G. M. Chow, and J. S. Chen, J. Appl. Phys. 109, 063910 (2011).

[67] H. Zhao, H. Wang, and J. P. Wang, J. Appl. Phys. 111, 07B732 (2012).

[68] C. J. Jiang, J. S. Chen, J. F. Hu, and G. M. Chow, J. Appl. Phys. 107, 123915 (2010).

[69] Wang, X. Xu, Y. Liang, J. Zhang, and H. Wu, Appl. Phys. Lett., 95, 022516 (2009).

[70] J. -L. Tsai, H. -T. Tzeng, and G. -B. Lin, Appl. Phys. Lett. 96, 032505 (2010).

[71] D. Makarov, J. Lee, C. Brombacher, C. Schubert, M. Fuger, D. Suess,J. Fidler, and M. Albrecht, Appl. Phys. Lett. 96, 062501 (2010).

[72] H. Guo, J. L. Liao, B. Ma, Z. Z. Zhang1, Q. Y. Jin, H. Wang, and J. P. Wang, Appl. Phys. Lett. 100, 142406 (2012).

[73] D. Goll and A. Breitling, Appl. Phys. Lett. 94, 052502 (2009).

[74] B. Ma, H. Wang, H. Zhao, C. Sun, R. Acharya, and J.P. Wang, IEEE Trans. Magn. ,46, 2345 (2010).

[75] C. J. Sun, D. Stafford, and R. Acharya, IEEE Trans. Magn., 46, 1795 (2010).

[76] A. Breitling, T. Bublat, and D. Goll, Phys. Status Solidi (RRL) 3, 130 (2009).

[77] T. McCallum, P. Krone, F. Springer, C. Brombacher, M. Albrecht, E. Dobisz, M. Grobis, D. Weller, and O. Hellwig, Appl. Phys. Lett. 98, 242503 (2011).

[78] A. Dobin and H. J. Richter, Appl. Phys. Lett., 89, 062512 (2006).

[79] D. Goll, A. Breitling, L. Gu, P. A. van Aken, and W. Sigle, J. Appl. Phys. 104, 083903 (2008).

[80] T. J. Zhou, B. C. Lim, and B. Liu, Appl. Phys. Lett. 94, 152505 (2009).

[81] H. Wang, H. Zhao, O. Ugurlu, and J.P. Wang, IEEE Magn. Lett., 3, 450014 (2012).

[82] D. Goll and S. Macke, Appl. Phys. Lett., 93, 152512 (2008)

[83] F. Casoli, F. Albertini, L. Nasi, S. Fabbrici, R. Cahassi, F. Bolzoni, and C. Bocchi, Appl. Phys. Lett. 92, 142506 (2008).

[84] Y. K. Takahashi, K. Hono, S. Okamoto, and O. Kitakami, J. Appl. Phys., 100, 074305 (2006).

[85] D. Goll, A. Breitling, L. Gu, P. A. Van Aken, and S. Sigle, J. Appl. Phys., 104, 083903 (2008).

[86] Chi-Keong Goh,a Zhi-min Yuan, and Bo Liu, J. Appl. Phys., 105, 083920 (2009).

[87] B. Ma, H. Wang, H. Zhao, C. Sun, R. Acharya, and J. P. Wang, IEEE Trans. Magn. 46, 2345 (2010).

[88] E. F. Kneller, IEEE Trans. Magn. 27(4), 3588 (1991).

[89] E. E. Fullerton, J. S. Jiang, M. Grimsditch, C. H. Sowers, and S. D. Bader,Phys. Rev. B 58, 12193 (1998).

[90] N. Bertram, and B. Lengsfield, IEEE Trans. Magn., 43, 2145 (2007)

[91] M. P. Sharrock, IEEE Trans. Magn., 35, 4414 (1999)

[92] C. L. Zha, B. Ma, Z. Z. Zhang, T. R. Gao, F. X. Gan, and Q. Y. Jin, Appl. Phys. Lett. 89, 022506 (2006).

[93] D. Vokoun, M. Beleggia, T. Rahman, H. C. Hou, C. H. Lai, J. Appl. Phys., 103, 07F520 (2008).

[94] D. Makarov, J. Lee,2, C. Brombacher, C. Schubert, M. Fuger, D. Suess, J. Fidler, and M. Albrecht, Appl. Phys. Lett., 96, 062501 (2010).

[95] L. L. Lee, D. E. Laughlin and D. N. Lambeth, IEEE. Trans. Magn. 34, 1561 (1998).

[96] M. H. Kryder MH, E. C. Gage EC, T. W. Mcdaniel TW, W. A. Challener, R. E. Rottmayer, G. Ju, Y. T. Hsia, and M. F. Erden MF, Proceedings of the IEEE, 96, 1810 (2008).

[97] J.S. Chen, J.P. Wang, J. Magn. Magn. Mater., 284, 423 (2004).

[98] D. Litvinov, M. H. Kryder and S. Khizroev, J. Magn. Magn. Mater., 241, 453 (2002).

[99] M. Rennhofer, B. Sepiol, M. Sladecek, D. Kmiec, S. Stankov, G. Vogl, M. Kozlowski, R. Kozubski, A. Vantomme, J. Meersschaut, R. Rüffer, and A. Gupta, Phys. Rev. B, 74, 104301 (2006).

[100] T. Kaiser, W. Sigle, D. Goll, N. H. Goo, V. Srot, P. A. van Aken, E. Detemple, and W. Jäger, J. Appl. Phys., 103, 063913 (2008).

[101] W. K. Shen, J. H. Judy, J. P. Wang, J. Appl. Phys., 97, 10H301 (2005).

[102] E. Yang, S. Ratanaphan, D. E. Laughlin, and J. Zhu, IEEE Trans. Magn., 47, 81 (2011).

[103] D. Weller, and A. Moser, IEEE. Trans. Magn., 35, 4423 (1999).

[104] S. Y. Chou, P. R. Krauss, and P. J. Renstrom, Appl. Phys. Lett., 67, 3114(1995).

[105] S. Y. Chou, P. R. Krauss, and P. J. Renstrom, J. Vac. Sci. Technol. B, 14,4129(1996).

[106] H. Schift, J. Vac. Sci. Technol. B, 26, 458(2008).

[107] L. J. Guo, Adv. Mater., 19, 495(2007).

[108] G. M. Schmid et al., J. Vac. Sci. Technol. 24, 1283(2006).

[109] W. L. Jen et al., Proc. SPIE, 6517, 6517 (2007).

[110] H. Sun, J. Liu, and et al.,Applied Surface Science, 254, 2955(2008).

[111] H. Ge,W. Wu,and et al., Nano Lett., 5, 179(2005).

[112] H. J. Park, M.G. Kang, and L.J. Guo, ACS nano, 3, 2601 (2009).

[113] Y.S. Kim, K. Lee, J.S. Lee, G.Y. Jung, and W.B. Kim, Nanotechnology, 19, 365305, (2008).

[114] P.S. Lee, O.J. Lee, S.K. Hwang, S.H. Jung, S.E. Jee, and K.H. Lee, Chem. Mater, 17, 6181 (2005).

[115] M.T. Rahman , N.N. Shams, and C.H. Lai, Nanotechnology 19, 325302 (2008).

[116] M.T. Rahman , N.N. Shams, C.H. Lai, J. Fidler, and D. Suess, Phys. Rev. B, 81, 014418 (2010).

[117] H. Masuda, K. Yada, and A. Osaka, Jpn. J. Appl. Phys., 37, L1340 (1998).

[118] N. Roos, H. Schulz, M. Fink, K. Pfeiffer, F. Osenberg and H.-C. Scheer, Proceedings of SPIE-Emerging Lithographic Technologies VI, 4688 ,232 (2002).

[119] K.I. Nakamatsu, N. Yamada, K. Kanda, Y. Haruyama and S. Matsui, Jpn. J. Appl. Phys., 45, L954 (2006).

[120] K.J. Byeon, K.-Y. Yang and H. Lee, Microelectron. Eng. 84, 1003 (2007).

[121] A.P. Li, F. Muller, A. Birner, K. Nielsch, and U. gosele, J. Appl. Phys. 84, 6023 (1998).

[122] B. Ma, H. Wang, H. Zhao, C. Sun, R. Acharya, and J.P. Wang, J. Appl. Phys. 109, 083907 (2011).

[123] I. Tagawa and Y. Nakamura, IEEE Trans. Magn. , 27, 4975 (1991).

[124] P. Krone, D. Makarov, T. Schrefl, and M. Albrecht, Appl. Phys. Lett. 97, 082501 (2010).

[125] P. Sharma, N. Kaushik, A. Makino, M. Esashi, and A. Inoue, J. Appl. Phys. 109, 07B908 (2011).

[126] J. E. Davies, P. Morrow, C. L. Dennis, J. W. Lau, B. McMorran, A. Cochran, J. Unguris, R. K. Dumas, P. Greene, and K. Liu, J. Appl. Phys. 109, 07B909 (2011).

[127] B. Ma, H. Wang, H. Zhao, C. Sun, R. Acharya, and J. P. Wang, J. Appl. Phys. 109, 083907 (2011).

[128] A. Dannenberg, M. E. Gruner, A. Hucht, and P. Entel, Phys. Rev. B, 80, 245438 (2009).

[129] S. Okamoto, N. Kikuchi, O. Kitakamo, T. Miyazaki, Y. Shimada, and K. Fukamichi, Phys. Rev. B. 66, 024413 (2002).

[130] H. Wang, W. Li, T. Rahman, H. Zhao, J. Ding, Y. Chen, and J.P. Wang, J. Appl. Phys., 111, 07B914 (2012).

[131] Z. L. Zhao, J. S Chen, J. Ding and J. P. Wang, Appl. Phys. Lett., 88, 052503 (2006).

[132] H. Yuan, Y. Qin, and D. E. Laughlin, Thin Solid Films, 517, 990 (2008).

[133] I. Zutic, J. Fabian, S. Das Sarma, Rev. Mod. Phys. 76, 323 (2004)

[134] L. Néel, J. Phys. Radium, 15, 225 (1954)

[135] S. D. Bader, Rev. Mod. Phys. 78, 1 (2006)

[136] M. Jamet, W. Wernsdorfer, C. Thirion, D. Mailly, V. Dupuis, P. Mélinon, and A. Pérez, Phys. Rev. Lett., 86, 4676 (2001)

[137] For example, see C. Liu, E. R. Moog, and S. D. Bader, Phys. Rev. Lett. 60, 2422 (1988); H. C. Mireles, and J. L. Erskine, Phys. Rev. Lett. 87, 037201 (2001)

[138] H. Kachkachi, H. Mahboub, J. Mag. Mag. Mater. 278, 334 (2004)

[139] D. A. Garanin and H. Kachkachi, Phys. Rev. Lett. 90, 065504 (2003)

[140] O. A. Ivanov, L. V. Solina, V. A. Demshina, L. M. Magat, Fiz. Metal. Metalloved. 35, 92 (1973)

[141] S. Sun, C. B. Murray, D. Weller, L. Folks, A. Moser, Science 287, 1989 (2000)

[142] H. Zeng, J. Li, J. P. Liu, Z. L. Wang, S. Sun, Nature 420, 395 (2002)

[143] J. M. Qiu, J. P. Wang, Appl. Phys. Lett., 88, 192505 (2006)

[144] J. M. Qiu, J. P. Wang, Adv. Mater., 19, 1703 (2007)

[145] J. M. Qiu, J. M. Bai, J. P. Wang, Appl. Phys. Lett. 89, 222506 (2006)

[146] T. Shima, K. Takanashi, Y. K. Takahashi, K. Hono, Appl. Phys. Lett. 88, 063117 (2006)

[147] H. Kachkachi and M. Dimian, Phys. Rev. B. 66, 174419 (2002)

[148] G. H. O. Daalderop, P. J. Kelly, and M. F. H. Schuurmans, Phys. Rev. B. 44, 12054 (1991)

[149] J. L. Rodríguez-López, J. M. Montejano-Carrizales, U. Pal, J. F. Sánchez-Ramírez, H. E. Troiani, D. García, M. Miki-Yoshida, and M. José-Yacamán, Phys. Rev. Lett. 92, 196102 (2004)

[150] F. Gautier in Magnetism of Metals and Alloys, edited by M. Cryo (North-Holland, Amsterdam1982).